

# **Development of Porous Material Dual-Functional Reactors for the Facile Synthesis of Sustainable Chemicals**

Von der NATURWISSENSCHAFTLICHEN FAKULTÄT der  
GOTTFRIED WILHELM LEIBNIZ UNIVERSITÄT HANNOVER

zur Erlangung des Grades

**DOKTOR der NATURWISSENSCHAFTEN**

**(Dr. rer. nat.)**

genehmigte Dissertation  
von

**M. Sc. Felix Rieck genannt Best**

2022

Referent: Prof. Dr. rer. nat. Jürgen Caro

Korreferent: apl. Prof. Dr. rer. nat. Claus Rüscher

Tag der Promotion: 15.07.2022

“All models are  
wrong ...

... but some are  
useful”

- George E.P. Box

# Abstract

With the depleting deposits of crude oil and the progressive change of mind to intensify environment protection, the search for new reaction routes for the production of sustainable compounds is constantly evolving and propelled. For most reactions, promising approaches have already been proposed, but their lack of efficiency and insufficient legal provisions are responsible that petrochemical cracking processes still prevail as the source of choice for energy production and the formation of a variety of basic chemicals. A further issue considering undesirable energy consumption, is the necessity of product separation.

In this thesis, the task to improve reactions that are already established or on the brink of commercialization is tackled in three different ways with the help of porous materials to develop dual-functional reactor systems, that improve not only the synthesis reaction itself, like the reaction rate or the selectivity, but also serve a secondary purpose as they improve product separation and longevity or are simultaneously used for waste removal. The first reaction discussed is the methylamine synthesis from methanol and ammonia at high temperatures. The addition of a highly hydrophilic, water removing Na-LTA zeolite membrane led to increased methylation rates in the product distribution. By choosing a size selective catalyst a high selectivity towards the desired product dimethylamine could be achieved, while the extraction of the by-product water pre-emptively decreased the need for post-synthesis product separation. With post-synthesis ion exchange, K-LTA membranes were achieved to further improve the methanol conversion rate. The methanol-to-olefins (MTO) reaction is a promising alternative for small olefin production. By applying the aforementioned Na-LTA to the MTO reaction, the varying product composition could be stabilized over a long period of time, while also providing product separation and an enhanced catalyst longevity. Besides the dualfunctional production/separation reactors, production/decomposition experiments were conducted with the utilization of the (dotted variant) porous monolayer carbon graphene, the durability of the important cocatalyst  $\text{Cu}^0$  in  $\text{TiO}_2$  photocatalysis was achieved and improved the yield of hydrogen in photochemical water splitting and facilitated the concurrent decomposition of the pollutant 2-chlorophenol.

**Keywords:** dual-functional reactors, sustainable chemicals, porous materials, zeolites, methylamine, methanol-to-olefins, photocatalysis

# Zusammenfassung

Durch die unaufhaltsame Erschöpfung der Erdölvorkommen und das zunehmende Bewusstsein zum Umweltschutz wird die Suche nach neuen Reaktionswegen für die Produktion von nachhaltigen Chemikalien stetig vorangetrieben. Viele Chemikalien besitzen bereits Alternativrouten zur Synthese, jedoch mangelt es diesen oft an Effizienz, während geringe gesetzliche Auflagen dazu beitragen, dass der Großteil der Energie und viele Grundchemikalien weiterhin durch Verbrennen fossiler Energieträger und petrochemische Prozesse bereitgestellt werden, während auch die Produkttrennung einen hohen Energiebedarf besitzt.

In dieser Arbeit wird die Aufgabe Prozesse, die vielsprechend oder bereits etabliert sind, zu verbessern in drei Variationen angegangen. Dies geschieht mit der Hilfe von porösen Materialien und ihrem Einsatz in Reaktoren, die simultan zwei Aufgabengebiete adressieren: Zum einen die Reaktion selbst, wie den Umsatz oder die Selektivität und zum anderen Probleme wie Produktseparation, Langlebigkeit und Zersetzung von schädlichen Abfallprodukten. Die erste Reaktion im Fokus ist die Methylaminsynthese aus Methanol und Ammoniak. Durch das Integrieren von hydrophilen, Na-LTA Zeolithmembranen zur Extraktion von Wasser konnte der Methylierungsgrad in der Produktverteilung erhöht werden. Mit der Wahl eines adäquaten Katalysators wurde die Selektivität des gewünschten Dimethylamin deutlich verbessert, während der Wasserentzug zudem die Notwendigkeit der Produktseparation verringerte. Durch einen Kalium-Ionenaustausch wurde die Wasserselektivität erhöht und der Methanolumsatz verbessert. Die Methanol-zu-Olefin-Reaktion erweist sich zunehmend als ernstzunehmende Alternative für die Produktion von kurzkettigen Olefinen. Durch den Einsatz der oben genannten Na-LTA-Membran wurde die variierende Produktverteilung stabilisiert und gleichzeitig eine in-situ Produkttrennung, sowie eine Verbesserung der Katalysatorlebensdauer erreicht. Neben den dualfunktionalen Synthese/Separations-Versuchen wurden noch Synthese/Dekompositions-Reaktoren getestet, dazu wurde der dotierte poröse Kohlenstoff Graphen verwendet um die Langlebigkeit des Co-Katalysators  $\text{Cu}^0$  in der  $\text{TiO}_2$  Photokatalyse und die Ausbeute an Wasserstoff in der photochemischen Zersetzung von Wasser zu erhöhen, während zusätzlich der Umweltschadstoff 2-Chlorphenol abgebaut wurde.

**Schlagworte:** dualfunktionale Reaktoren, nachhaltige Chemikalien, poröse Materialien, Zeolithe, Methylamin, Olefine, Photokatalyse

# Table of Content

Abstract.....	4
Zusammenfassung.....	5
List of abbreviations.....	8
1. Introduction.....	10
1.1. Motivation.....	10
2. Porous materials .....	13
2.1. Graphene.....	13
3. Zeolites .....	14
3.1. Zeolite membranes .....	18
4. Membrane reactors.....	19
5. Examples for zeolites.....	24
5.1. Mordenite (MOR) .....	27
5.2. Zeolite A (LTA).....	30
5.3. Chabazite (CHA).....	35
5.3.1. H-SSZ-13 .....	36
5.3.2. SAPO-34.....	37
6. Methylamine synthesis .....	40
7. Methanol-to-olefins .....	45
8. Photocatalytic water splitting .....	49
9. Measurement setup and membrane separation principle .....	52
9.1. Membrane separation .....	52
9.2. Quantities in catalysis .....	55
10. Published results.....	57

10.1.	Methanol-to-Olefins in a Membrane Reactor with in Situ Steam Removal – The Decisive Role of Coking.....	57
10.2.	Boosting Dimethylamine Formation Selectivity in a Membrane Reactor by In Situ Water Removal .....	71
10.3.	Controlled methylamine synthesis in a membrane reactor featuring a highly steam selective K <sup>+</sup> -LTA membrane .....	92
10.4.	Bridging the interface between Metallic Copper and TiO <sub>2</sub> via B/N-graphene for enhanced Photocatalytic H <sub>2</sub> Production and 2-Chlorophenol Degradation: A DFT, experimental and mechanistic investigation .....	105
11.	Summary .....	120
12.	Conclusion & outlook .....	124
	List of References.....	126
	Appendix.....	144
	Danksagung .....	144
	List of publications.....	145
	Curriculum vitae .....	146

## List of abbreviations

<b>2-CP</b>	2-chlorophenol
<b>ALPO</b>	aluminiumphosphate
<b>ATR</b>	attenuated total reflection
<b>BEA</b>	beta (zeolite)
<b>CBU</b>	composite building unit
<b>CHA</b>	chabazite
<b>CMR</b>	catalytic (permselective) membrane reactor
<b>CNMR</b>	catalytic nonpermselective membrane reactor
<b>DFT</b>	density functional theory
<b>DMA</b>	dimethylamine
<b>DME</b>	dimethylether
<b>DSC</b>	differential scanning calorimetry
<b>EDXS</b>	energy dispersive X-ray spectroscopy
<b>FAU</b>	faujasite
<b>FBCMR</b>	fluidized bed catalytic (permselective) membrane reactor
<b>FBMR</b>	fluidized bed (permselective) membrane reactor
<b>FCC</b>	fluid catalytic cracking
<b>FER</b>	ferrite
<b>FTIR</b>	Fourier transform infrared spectroscopy
<b>GC</b>	gas chromatography
<b>HCP</b>	hydrocarbon pool
<b>IR</b>	infrared spectroscopy
<b>IUPAC</b>	International Union of Pure and Applied Chemistry
<b>IZA</b>	International Zeolite Association
<b>LTA</b>	Linde type A
<b>MFI</b>	mordenite framework inverted
<b>MMA</b>	monomethylamine
<b>MOF</b>	metal organic framework
<b>MOR</b>	mordenite
<b>MS</b>	mass spectroscopy
<b>MTH</b>	methanol-to-hydrocarbons
<b>MTO</b>	methanol-to-olefins
<b>PBCMR</b>	packed-bed catalytic (permselective) membrane reactor
<b>PBMR</b>	packed-bed (permselective) membrane reactor



<b>PBU</b>	primary building unit
<b>QMS</b>	quadrupole mass spectrometry
<b>SAPO</b>	silicoaluminophosphate
<b>SBU</b>	secondary building unit
<b>SCR</b>	selective catalytic reduction
<b>SDA</b>	structure directing agent
<b>SEM</b>	scanning electron microscopy
<b>SOD</b>	sodalite
<b>SSZ</b>	Standard Oil Synthetic Zeolite
<b>TEM</b>	transmission electron microscopy
<b>TGA</b>	thermal gravimetric analysis
<b>TMA</b>	trimethylamine
<b>UV</b>	ultraviolet spectroscopy
<b>WHSV</b>	weight hourly space velocity
<b>XPS</b>	X-ray photoelectron spectroscopy
<b>XRD</b>	X-ray diffraction
<b>ZIF</b>	zeolitic imidazolate framework

# 1. Introduction

## 1.1. Motivation

It was merely around 100 years ago, when Fritz Haber received the Nobel prize in chemistry in 1918.<sup>1</sup> His development of the Haber-Bosch process paved the way for the large-scale production of ammonia, still a cornerstone of today's chemical industry with a production capacity of 290 million metric tons per year. The only notable change to Haber's initial concept was the implementation of an  $\alpha$ -Fe catalyst by BASF in the early 20<sup>th</sup> century. Since then the actual catalysis process remained unchanged for the most part and is still in use at BASF as of today.<sup>2</sup> It's an example of how little has changed in, especially inorganic, catalytic chemistry over the past decades. The hunt for the next big thing has slowed down tremendously, new breakthroughs are relying on exotic materials and systems, which mostly can't justify their price/performance ratio to find utilization and replace the current catalysts in real industrial applications. Modern chemistry turned to the idea of assistance and optimization of already established processes. The most prominent example is the history of the gasoline automobile catalyst and its astonishing improvement over the last 50 years. The initial Pt/Pd catalyst is still the material of choice for CO and hydrocarbon oxidation. Since then the addition of Rh to build a three-way catalyst for the NO<sub>x</sub> reduction, a reduction in material through improved distribution in porous materials, O<sub>2</sub> or lambda membrane sensors with CeO<sub>2</sub>-ZrO<sub>2</sub> oxygen storages, particle filters and NO<sub>x</sub> traps all found its way into the exhaust system.<sup>3</sup> It's a good example for the extraordinary results of interdisciplinary research and development, with innovations in heterogeneous catalysis, sensory, porous materials, membrane technology and chemical engineering. However, this development was induced by constant new legal provisions, but how do innovations fare in free market economy? The answer is the aforementioned price/performance ratio. Do the new advancements bring enough of an improvement to the table compared to the established systems, that a complete or gradual conversion is profitable after a certain point of time?

Based on this overall development in industrial chemistry, the cross-disciplinary application of porous material dual-functional reactors is tested as an additional tool in two proven syntheses of sustainable chemicals with acidic, porous catalysts:

- (i) The methylamine synthesis from methanol and ammonia
- (ii) The methanol-to-olefins (MTO) reaction

The two reactions are separated by their longevity as an established chemical process and by their primary weak points, which allow room for improvement.

The methylamine synthesis goes back to the early 1920s when methylamines were first produced commercially by the Commercial Solvents Corporation and offers three different main products: monomethylamine (MMA), dimethylamine (DMA) and trimethylamine (TMA).<sup>4</sup> With an overall production of aliphatic amines in general of 1.9 million metric tons in 2013<sup>5</sup>, the methylamines belong to the more important nitrogen-based source materials. MMA, DMA and TMA all have different applications, with DMA having the highest demand. TMA is generally tried to be suppressed as it forms an azeotropic mixture with ammonia.<sup>6</sup> Since product separation has generally a high cost factor and the individual formation of each methylamine is not possible, synthesis conditions in which one amine, preferably DMA, takes up most of product share are highly desirable. Consequently, methylamine research primarily focuses on the alteration of the product selectivities with a variety in-situ and post synthesis catalyst modifications with dwindling room for improvements due to the time and resources already spent on the topic.<sup>7,8</sup>

The methanol-to-olefins reaction on the other hand is a fairly new synthesis route to the ever important base chemicals ethylene and propylene. The two light olefins bring along a production capacity of 150 million and 80 million metric tons, respectively, per year.<sup>9</sup> Steam cracking, where larger hydrocarbons get broken down into the light olefins, was the lone player for a long time in the production of ethylene and propylene. With the discovery of the methanol-to-olefins process in 1977 by Mobil Oil Corporation another viable synthesis route had been found.<sup>10</sup> In 2010 with the accumulated knowledge from the Dalian Institute for Chemical Physics (DICP), the first large-scale MTO unit was successfully launched in Baotou, China. Since this process is still considered new on the large scale, considerable catalyst enhancements are still possible in future work. The two biggest problems of the MTO reaction are attrition, since the porous catalyst particles frequently collide in the fluidized bed reactor, and catalyst deactivation through coke deposition.<sup>11</sup>

The methylamine synthesis and methanol-to-olefins possess many differences, but what about its similarities? First, the type of required catalyst as they both share the use of a porous, mild-acidic zeolite or zeolite-type material. The second one are their most common by-product: water.

The questions regarding these reactions: which types of membranes are practical for an application? The immediate answer, are hydrophilic separation membranes, which withstand harsh conditions, while in situ extracting any water formed in the reaction. Based on LeChatelier's principle, the removal of a product leads to an equilibrium shift towards the reaction product site. Adding water removal membranes to already established reactions may be a facile way to improve synthesis routes and implement the membrane separation research results as a viable alternative in a variety of catalytic reactions.

Turning the tables and regarding water not as the useless by-product but as the star of the show, the track leading to water splitting to produce the increasingly important hydrogen is inevitable. The cross-interdisciplinary research is the combination of TiO<sub>2</sub> based photocatalysis reaction with the addition of doped porous graphene layers. TiO<sub>2</sub> photocatalysis came a long way since its discovery in 1972 and is one of the more promising systems for the sustainable production of H<sub>2</sub>. The estimated demand for hydrogen in 2024 is over 120 million metric tons.<sup>12</sup> Even though hydrogen is the most abundant element in the universe, its production is still heavily depending on fossil fuels. Only a few percent of the consumed hydrogen are not produced based on the processing of fossil fuel, which is inevitably interconnected with high numbers of carbon dioxide emissions.<sup>13</sup> Alternative production routes are taken into consideration, the most promising involves the catalytic decomposition of water into hydrogen and oxygen. This process can either be performed via electrocatalysis or directly using the (sun-)light for photocatalysis with TiO<sub>2</sub> semiconductors.<sup>14</sup> To harvest as much light as possible the photochemical systems are constantly evolving, the use of cocatalysts showed an immense improvement in the water conversion rate was achieved. As the best cocatalyst materials are both scarce and expensive, elements with similar photochemical properties, in our case Cu<sup>0</sup>, are utilized.<sup>15</sup> To stabilize the Cu<sup>0</sup> phase and to further improve the reaction rate of hydrogen production and simultaneous organic waste decomposition in a dual-functional photocatalysis reaction, the application of doped graphene will be tested.

## 2. Porous materials

Dating back almost 3500 years ago, porous charcoal found use as a digestive aid, marking the earliest effort to capitalize on the benefits of porous networks in solid materials.<sup>16</sup> Today, porous substances are found in nearly every branch of chemical research: pure classic carbon- or silica based inorganic materials, organic polymers or hybrid inorganic-organic composite materials, even single organic molecules<sup>17</sup> and ionic liquids<sup>18</sup> can claim the term “porous” nowadays.

The term “porosity” is, thereby, per definition “the ratio of total pore volume to the volume of the particle or agglomerate”<sup>19</sup>, with IUPAC further distinguishing the pores in nanometre-scale into micropores (< 2 nm pore width), mesopores (between 2 - 50 nm) and macropores (> 50 nm).<sup>20</sup>

Combining large inner surface areas with small overall material volumes already opens up a wide variety of application possibilities, as the porosity e.g. facilitates the distribution of particles as a carrier substrate but the real strength of porous materials only emerges when long range ordered 3-D porous networks made of the appropriate material are taking into consideration. With tuneable pore sizes and channel dimensions, LEWIS- and BRØNSTED-acid sites, metallic-ion centres or polar/nonpolar pores, the porosity can be exploited to its fullest extent. A range of interactions of the novel porous materials with guest atoms, ions or molecules led to the rapid increase in chemical and technological utilization ranging from heterogeneous catalysis, sensors, gas storage, compound separations to environmental remediation, green energy transition and drug delivery, tissue engineering and wound healing in the field of medicine<sup>21</sup>.

### 2.1. Graphene

With the discovery and correct representation of graphene in 2004, KONSTANTIN NOVOSELOV and ANDRE GEIM not only secured their NOBEL PRIZE in physics in 2011, they opened up the door for the nearly infinite number of possibilities graphene might offer.<sup>22</sup> Sometimes, graphene is referred to as the “dream material”, as it possesses a completely unique combination of characteristics: a rigid pore system, high thermal<sup>23</sup> and electrical conductivity<sup>24</sup> in a 2D plane, unmatched room temperature charge carrier mobility<sup>25</sup>, excellent mechanical strength<sup>26</sup>,

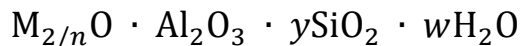
large specific surface areas<sup>27</sup> with high adsorption capacities<sup>28</sup>, low production cost<sup>29</sup> and all of that while being only composed of carbon atoms. Graphene is basically just a planar sp<sup>2</sup>-bonded monolayer of high ordered graphite, therefore, the first repeatable synthesis method was an exfoliation of highly oriented pyrolytic graphite, but also multilayers up to 10 still are considered as (few-layer) graphene. Additionally, synthesis methods via vapour deposition or chemical/thermal decomposition are possible.<sup>30</sup> Since graphene is such a new material, most of work done is limited to fundamental research of how the extraordinary graphene properties can be utilized and large-scale applications have not been realized. This is reflected by the enormous numbers of published research paper in recent years.<sup>31</sup> They focus on possible applications for graphene field emission, sensoring, battery development, photocatalysis, biomedicine and as transistors and electrode material.<sup>30,32</sup> For certain applications, a modification of the electric properties of graphene is necessary, hence, doping with e.g. nitrogen or boron is required.<sup>33</sup> Even graphene membranes have been taken into consideration, since it displays a rigid nanopore system, it is technically a porous material, thus an application as a pure molecular sieve without diffusion issues is within the realms of possibility.<sup>34</sup>

### 3. Zeolites

One of the most important representatives of porous materials in research and industrial application are the zeolites, which are microporous aluminosilicates. Their first reference goes back to 1756 to the Swedish mineralogist AXEL F. CRONSTED, who discovered the first natural zeolite and is responsible for its name, labelled after the Greek words *zeo* (“to boil”) and *lithos* (“stone”), because the mineral released steam when heated. Around 40 different natural zeolite minerals have been found until today. In 1948 the first zeolite was synthesized in lab scale by RICHARD M. BARRER<sup>35</sup>, a pioneer in zeolite chemistry and later that year he successfully found and described the first purely synthetic zeolite.<sup>36</sup> From this point, the numbers of synthetic zeolite exceeded the number of natural zeolites many times over, with 255 different zeolite types have been synthesized until 2021, while each structure is given a three-lettered code by the International Zeolite Association (IZA).<sup>37</sup> Synthetic zeolites often require structure-directing agents (SDAs), which promote the zeolite crystal structure formation, with high-silica zeolites typically rely on SDAs with quaternary ammonium cations. The overall demand of

zeolites was estimated to be around 5 million metric tons per year in 2012, while the share of synthetic zeolites makes up around 36%.<sup>38</sup>

Zeolite composition is often shown in its empirical formula<sup>39</sup>:



with  $n$  describing the cation valence,  $\gamma$  the ratio of Si to Al and  $w$  the water content. However, this expression does not represent the zeolite structure satisfyingly, as zeolites consist of tetrahedral  $AlO_4$  and  $SiO_4$  primary building units (PBUs). On account of lacking thermodynamic stability compared to Si-O-Si bondings<sup>40</sup>, an avoidance of Al-O-Al connections can be observed, known as the LOEWENSTEIN rule<sup>41</sup>, which concludes that the smallest possible Si/Al ratio in zeolites is 1.

Secondary building units (SBUs) describe the conjunction of the  $AlO_4$  and  $SiO_4$  tetrahedra, as their extensive combination possibilities are the reason for the large number of different zeolite structure types. They are small units, composed of several tetrahedra and their nearly infinite combination possibilities allow the formation of each specific zeolite structure. SBUs are often just described as a combination of two numbers:  $x$ - $y$ , where  $x$  is the number of members in the ring and  $y$  the number of additional members attached to this ring.<sup>42</sup>

In the next step to build a zeolite structure, these SBUs form polyhedral structures or composite building units (CBUs) that can be labelled in three different ways: 1. with common names, 2. with three letter codes or 3. with face symbols following the scheme:  $n1^{m1} n2^{m2} \dots$  with  $m1$  describing the number of  $n1$ -rings,  $m2$  the number of  $n2$ -rings and so on.<sup>43,44</sup>

Another approach to visualize zeolite structures is that they can be derived from pure silicates, which are likewise build from  $SiO_4$  tetrahedra. By exchanging Si with Al, a negative charge is generated as Al not possesses enough electrons. For charge balance purposes a cation is introduced into the structure, but it is considered a non-framework building component, in laboratory synthesis this is usually sodium. With post-synthesis ion exchange of the extra framework cation, a wide variety of alkali, alkaline earth metals and metals are utilized and open the door for widespread applications of zeolite materials. If the ion exchange is performed with  $NH_4^+$  salts and the exchanged zeolite is calcinated afterwards, the protonated

form of certain zeolites can be achieved and BRØNSTED-sites are created, giving the zeolite valuable acidic properties for catalysis.

Zeolite structures are not only limited to zeolites themselves, as they can be found in so-called zeolite-like structures as well. The most prevalent examples are ALPOs, three-dimensional aluminophosphates constructed from  $\text{AlO}_4$  and  $\text{PO}_4$  tetrahedra, while SAPO consists of the corresponding  $\text{SiO}_4$ ,  $\text{AlO}_4$  and  $\text{PO}_4$  tetrahedra, as they share the same tetrahedra connections to form secondary building units structurally equivalent to the SBUs found in zeolites. Even inorganic-organic composite materials like the zeolitic imidazolate frameworks (ZIFs), a subclass of metal-organic frameworks (MOFs), can display topologically isomorphic structures to zeolites, as the metal-imidazole-metal bonding angle ranges in similar values as the Si-O-Si angle in zeolites.

Figure 1 gives an overview over possible applications of zeolites (natural and synthetic) and zeolite-like materials.



Figure 1. Application overview of zeolite and zeolite-like materials divided into five major subgenres: catalysis, separation, environment, agriculture, construction and medicine.

Due to the huge variety of available zeolite structure types, counter ions, and its high inner surface have zeolites found wide-spread applications. Most-common are zeolites known for their use in water softening<sup>45</sup>. Hard water exhibits higher concentrations of magnesium ( $\text{Mg}^{2+}$ )



and calcium ( $\text{Ca}^{2+}$ ) ions, which can cause inconveniences in industrial processes, as both cations tend to form insoluble salts, leading to clogged pipes and connection parts.<sup>46</sup> Further application as a laundry detergent to soften water works with the same principle: zeolites with sodium as its extra-framework cation remove the alkaline earth metals by integrating them into their structure, while releasing the sodium into the water, which is not able to form insoluble compounds. The usage as a detergent takes up 73% of the total worldwide consumption of synthetic zeolites<sup>38</sup>, as they provide a non-toxic, environment-friendly and effective laundry additive.

Even though the largest share is used as an ion exchanger, the fastest growing and most-profitable market value wise is the catalysis branch. Especially in petrochemistry, zeolite catalysts have found its way into extensive industrial application. The most important process, the fluid catalytic cracking (FCC), is based on the catalytic degradation, which replaced the thermal cracking due to its improved conversion rate, where high-molecular crude oil gets subsequently split into smaller, more valuable olefins (like propylene), gasoline and more. The first commercial success was initiated by the French engineer EUGÈNE HOUDRY in the 1920s with the VACUUM OIL COMPANY.<sup>47</sup> Today's FCC catalysts provide zeolite, in its protonated form, as its centrepiece, because they possess the catalytic acid sites necessary for the cracking and combine it with excellent hydrothermal stability and the appropriate hierarchical micropore systems to provide product selectivity towards the desired gasoline molecules.<sup>48</sup> Further examples of zeolite catalysis include hydroxylation (to phenol)<sup>49</sup>, oximation (cyclohexanone oxime)<sup>50</sup>, alkylation (ethylbenzene<sup>51</sup>, cumene<sup>52</sup>) and epoxidation (propylene oxide)<sup>53</sup>. The role of the zeolite varies based on its application as it can be used on its own like in the FCC reaction, in a metal ion-exchanged form, as in the hydroxylation, or simply as a carrier material for better catalyst distribution.

Another rising issue tackled by zeolite catalysts is the selective catalytic reduction (SCR) of  $\text{NO}_x$  by  $\text{NH}_3$  in gasoline automobile exhaust gas.<sup>3</sup> Metal-ion exchanged zeolites are a promising material for low-temperature conversion required in the upcoming problems of cold-start car emissions.<sup>54</sup>

Due to the simple non-toxic components, zeolites have been increasingly taken into consideration in bio-compatible materials and medicine.<sup>55,56</sup> One of zeolites oldest known usage is the

utilization for detoxification because of its large surface area and excellent adsorption properties.<sup>57</sup> In addition, zeolites are considered for drug delivery<sup>58,59</sup>, implant coating<sup>60</sup>, tissue engineering<sup>61</sup> and biosensors<sup>62</sup>. Based on the huge variety of zeolites, a few selected ones have even found usage as an additive on construction in concrete production<sup>63</sup> and in agriculture as an alternative for soil treatment<sup>64</sup> and animal nutrition<sup>65</sup>.

### 3.1. Zeolite membranes

With rigid pores and channels, tuneable pore sizes and varieties in hydrophilicity / hydrophobicity, zeolites are ideal materials for film and membrane growth with further possible applications, see Figure 1.<sup>66</sup> Since the first successful growth of a zeolite composite membrane on a porous support by HIROSHI SUZUKI in 1987<sup>67</sup>, the formation of zeolite membranes has been extensively researched and resulted in astonishing results<sup>68</sup>: as the overall quality of the membranes could be improved, the preferred crystal orientation was controlled<sup>69,70</sup>, improvements in the grain boundary connections<sup>71</sup> and overall successive elimination of defects<sup>72</sup> have been accomplished, while pushing down the limits of how thick a zeolite membrane must be, surpassing the  $\mu\text{m}$ -barrier<sup>73</sup> and synthesizing zeolite nanosheets<sup>74</sup>.

Zeolite membrane growth can be achieved via different methods:

- (i) By primary crystallization, where the zeolite membrane either grows as self-supported or directly on the support<sup>75</sup>,  $\alpha\text{-Al}_2\text{O}_3$  is here the widespread material of choice
- (ii) By secondary growth, where ex-situ produced zeolite seeds are placed on the support with the help of electrostatic<sup>76</sup>, covalent<sup>77</sup> or capillary forces<sup>78</sup> to aid the growth and control the orientation of the thin, homogenous membrane.

Even double-layered zeolite membranes have successfully been synthesized.<sup>79</sup> The growth itself is either performed as a classic, hydrothermal autoclave synthesis<sup>80</sup> or via microwave synthesis<sup>81</sup>.

Zeolite membrane applications are mainly focused on separation of gas and/or liquid mixtures. Those membranes usually combine different techniques, as they work as molecular sieves, completely excluding larger molecules from entering their pores or by adsorbing compounds differently strong, based on the zeolites acid strength and pore hydrophilicity. Separation is an increasingly important process, since most reactions in heterogeneous catalysis

produce compound mixtures. It is estimated that the product separation of C<sub>2</sub>-C<sub>4</sub> paraffins/olefins through cryogenic distillation takes up to 85% of the total energy of the entire production line.<sup>82</sup>

The most prevalent example, which has already been established in industrial processes, is the solvent or gas drying. Hereby, water is removed by a strongly hydrophilic zeolite, which adsorbs the water molecules, while excluding larger molecules from entering the pore because of size restrictions. However, one of the biggest obstacles with zeolite membranes is the up-scaling into large-scale applications.<sup>83</sup> The only successful implemented zeolite is zeolite A or LTA (LINDE Type A), which will be discussed in detail later. The first large-scale plant was put into operation in Kariya City, Japan by MITSUI ENGINEERING AND SHIPBUILDING CO. LTD. in 2000 and operated after the pervaporation principle to remove water from organic solvents like methanol, ethanol and *i*-propanol, while exhibiting superior separation factors and water fluxes compared to the previously established polymer membranes.<sup>84</sup> LTA membranes have been popularized since then for the dehydration of isopropyl alcohols<sup>85</sup>, ethylene glycol<sup>86</sup> and tetrahydrofuran<sup>87</sup>. Furthermore, important work has been done in the field of zeolites for bio-ethanol dehydration to gain easier access to fuel-grade ethanol by BUSSAN NANOTECH RESEARCH INSTITUTE INC. in Japan.<sup>88</sup> Working with similar parameters but with all gaseous mixtures, zeolite membranes have been used for gas purification to separate otherwise difficult to isolate gas mixtures, which includes CO<sub>2</sub>/CH<sub>4</sub>, CO<sub>2</sub>/N<sub>2</sub> or olefin/paraffin mixtures, like propylene/propane<sup>89,90</sup> and ethylene/ethane<sup>91</sup>, as they rely on the strong adsorption interaction of the zeolite cationic sites and the olefin  $\pi$ -bonds.<sup>92</sup> However, industrial scaled gas separation has yet to exceed the pilot plant status.<sup>66,93</sup>

## 4. Membrane reactors

Zeolite membranes can not only be used for post reaction product separation, their ability for limiting or enhancing diffusion of certain compounds can also be taken advantage of to influence reactions in situ, otherwise known as chemical process intensification.<sup>94</sup> Therefore, the membrane reactor is a “device for simultaneously carrying out a reaction and membrane-based separation in the same physical enclosure”, as IUPAC states<sup>95</sup>. There are many different types of membrane reactors, including catalytic permselective membrane reactors (CMR), catalytic nonpermselective membrane reactors (CNMR), packed-bed permselective membrane

reactors (PBRM), packed-bed catalytic permselective membrane reactors (PBCMR), fluidized bed permselective membrane reactors (FBMR) and fluidized bed catalytic permselective membrane reactors (FBCMR).<sup>96</sup> Choosing the membrane material can be made based on the function required and ranges from polymers to zeolites, perovskites, inorganic-organic hybrid materials and thin metal films.<sup>97</sup> They can function in three different ways, see Figure 2:

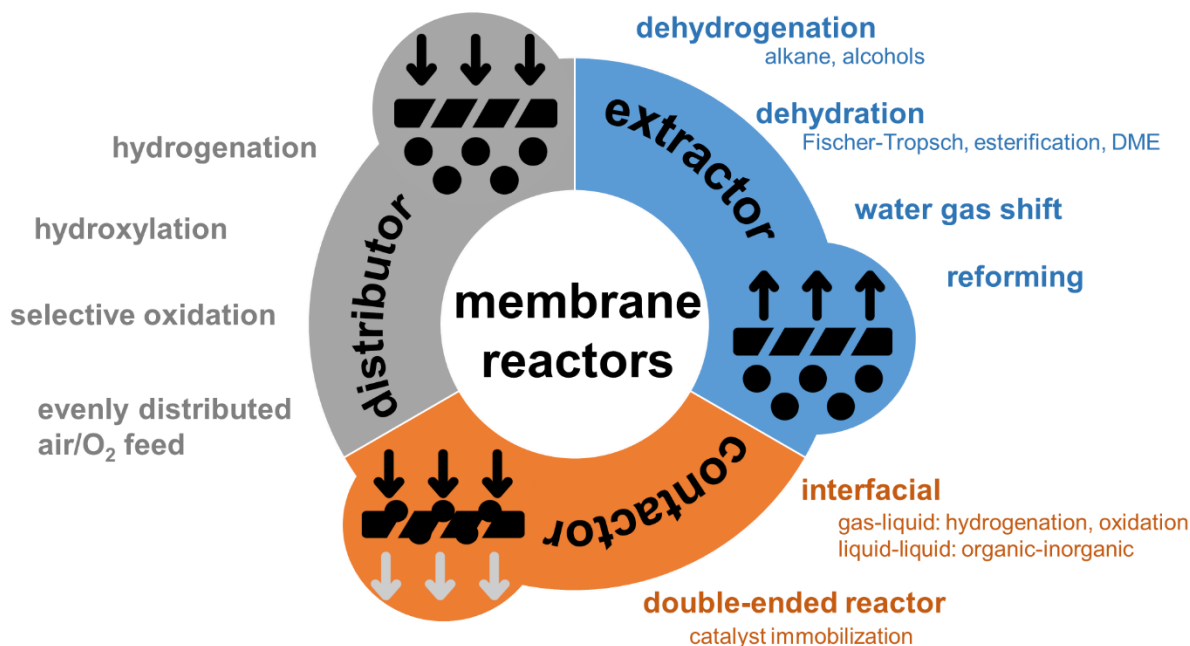


Figure 2. Overview of the three types of membrane reactors: 1. extractor, 2. distributor, 3. contactor, with examples of each type already under study.

- As an extractor, to most popular type of membrane reactors, where preferably one product is selectively removed from the reaction environment. This can be used to shift reaction equilibriums further to the product site and help exceed the equilibrium limitations, while also altering product composition. Furthermore, in situ extraction can help preventing expensive post-synthesis product separation. One of the first successful experiments goes back to 1987, when NAOTSUGU ITOH removed hydrogen through a thin dense palladium membrane in the dehydrogenation of cyclohexane to cyclohexene to help boost the conversion rate to nearly 100%.<sup>98</sup> The results could be repeated ten years later, with the application of porous materials like Vycor glass and microporous ceramics<sup>99</sup> and later with a zeolite membrane.<sup>100</sup> Since then dehydrogenation boosted by zeolite membrane reactors has been additionally performed for the

dehydrogenation of alkanes (ethane<sup>101</sup>, propane<sup>102</sup>, butanes<sup>103</sup>, and ethylbenzene<sup>104</sup>). For alcohol dehydrogenation (methanol to methyl formate<sup>105,106</sup>, ethanol to acetaldehyde<sup>107</sup>, 2-butanol to methyl-ethyl-ketone<sup>108</sup>) Pd or Pd/Ag alloys as a thin film on ceramic supports are more common than porous membranes. Furthermore, zeolite could not make the cut in the water gas shift reaction (an equilibrium of carbon monoxide and water with hydrogen and carbon dioxide), as they lack the necessary H<sub>2</sub>O/CO selectivity<sup>109,110</sup>, or the methane steam reforming<sup>111</sup> due to the instability at such high temperatures in the presence of water.<sup>112</sup>

The other common application for extractor-type membrane reactors is the in situ dehydration or water/steam removal, for which zeolite are well suited. Zeolites with high aluminium content (Si/Al ~ 1) exhibit a high hydrophilicity, with additional strong acidic adsorption sites for water. Combining this with the fact that water is one of the smallest molecules ( $d = 2.6 \text{ \AA}$ ), zeolite membranes can simultaneously act both as a molecular sieves and as a separator by preferred adsorption.

In situ water removal is most commonly used in pervaporation experiments. In pervaporation, a liquid mixture is placed on one side of the membrane, which is only selective for one compound of the mixture. Single molecules can diffuse through the membrane, get heavily diluted and can get removed as a low-pressure vapour on the permeate side.<sup>113</sup> Vacuum pervaporation can be used to avoid condensation of the permeate. Pervaporation zeolite membrane reactors are utilized to continuously dry organic solvents, as this variant prevents the need for repetitive zeolite activation. Newer applications use pervaporation membranes for desalination of salt water to find alternative ways to affordable, low cost access to fresh water.<sup>114</sup> Applying water extraction membrane reactors to remove water from the corresponding reaction environment results in an equilibrium shift towards the product side, similar to dehydrogenation in membrane reactors. The most prominent examples for reactions that benefits from the water extraction are esterifications from alcohols and carboxyl acids, which sometimes suffer from low conversion rates and ester yields. However, the esterification in a membrane reactor was mainly performed in smaller acids (like acetic<sup>115</sup> or lactic acid<sup>116</sup>) and smaller alcohols (like ethanol and butanol<sup>115</sup>), while the rising relevance of intensifying the esterification of fatty acid for important industrial applications as biodiesel<sup>117</sup> or in

food industry<sup>118</sup> leads to increasing interdisciplinary efforts in membrane reactor research. As esterifications commonly require homogenous catalysts on form of protons, zeolite stability becomes a relevant topic, as they tend to disintegrate in solution with lower pH values. Conclusively, only stable mild acidic conditions can be applied or switching to heterogeneous catalysis in form of acidic ion exchange resins is necessary.<sup>119</sup> Alternatively, hydrophobic membranes have been researched to extract the ester instead of water.<sup>120</sup>

The results of steam removal in heterogeneous catalysis gets increasingly difficult to predict as not only the influence of the water extraction is of importance, while a multitude of side reactions can occur and catalyst deactivation and diffusion limitation also play a role. The FISCHER-TROPSCH (FT) synthesis, is one of most important chemical process for the production of liquid, synthetic hydrocarbons from differently composed syngas (carbon monoxide and hydrogen) mixtures. The reaction is, depending on the desired outcome, performed with Fe- or Co-based catalysts, while the most common by-product is water.<sup>121</sup> Removing water in situ through an hydrophilic zeolite membrane reactor had an influence on (i) catalyst deactivation and diffusion, (ii) the reaction conversion and (iii) the displacement of the competing water gas shift to maintain a reactive syngas mixture.<sup>122</sup> Consequently, the water extraction had a positive influence on the longevity, conversion rate and yield in the FT synthesis.

Further examples of the beneficial appliance of extraction membrane reactors are DME synthesis from methanol<sup>123</sup> and the CO<sub>2</sub> hydrogenation<sup>124</sup>.

- As a distributor, in which the membrane is responsible for the dosing of one or more reactants. This may help to evenly distribute the compound over the whole catalytic bed and thus preventing concentration gradients and hot spots, while helping to optimize the selectivity of kinetically controlled reactions.<sup>125</sup> Distribution membrane reactors provide exceptional usefulness as they separate dangerous reactant mixtures like hydrocarbons and oxygen. By applying an oxygen selective (and electron conducting) membrane, the oxygen can be transferred as the O<sup>2-</sup> species and is able the react with ethene to form ethylene without recombination to O<sub>2</sub>. This does not only prevent the formation of highly explosive ethane/oxygen mixtures, it also largely suppresses the further oxidation of ethylene.<sup>126</sup> The same membrane reactor type can be applied to sup-

port the partial oxidation of methane to syngas.<sup>127</sup> Similar materials, Pd-based membranes<sup>128</sup> or zeolites<sup>129</sup>, used in the extraction membranes for dehydrogenation reactions, can be utilized to control and evenly distribute a hydrogen feed into the reactor for the hydrogenation of hydrocarbons. However, in extraction based membrane reactors, its usually the best strategy to maximize the permeation flux of the removed compound while maintaining a high selectivity. In membrane reactors for reactant distribution additional studies on the optimal feed flux are required, while taking the diffusion limitations of the membrane into consideration to maintain the desired reactant composition.

- As a contactor membrane reactor, which can be used in two different ways:
  - (i) The interfacial membrane reactor as a way to facilitate contact between two phases, which are otherwise insoluble and separated. The membrane pores itself works as the reaction environment, setting a defined reaction volume and limiting certain reactions due to space restrictions. Usually catalytic nanoparticles are deposited into the pores to add appropriate catalytic properties to the porous membrane, as shown in the cyclohexane oxidation by tert-butyl hydroperoxide with a polymer membrane.<sup>130</sup> The membrane reactor removed the necessity of a solvent, while simultaneously controlling the reactant concentration and reactant contact time. Environmental benefits were achieved using a contactor membrane reactor in the “Watercatox” process, in which organic compounds in waste water are oxidized using oxygen from air. The tubular ceramic membrane is modified with Pt-catalyst particles and is filled with the contaminated water, while oxygen is applied on the outside and functions as the interface contactor between liquid and gas phase. The oxidation occurs inside the pores while the partially oxidized organics are returned into the waste water. The membrane based “Watercatox” procedure can be performed at lower temperatures than comparable water oxidation purification processes and the transition from lab-scale to a pilot plant was already achieved.<sup>131</sup>
  - (ii) The flow-through membrane reactor, where the reactants are guided to the membrane, while narrow pores and channels force intermolecular interactions between the reactants and the pore system, which is either catalytic itself or made due to immobilized catalyst particles. Afterwards, the products leave the

system on the permeate side. The pore system can prevent the occurrence of undesired side reactions and by-products. Regulating the fluxes and optimizing the membrane structure based on the reaction kinetics results in an easy solution to influence contact times, potentially further improving conversion and product selectivities.<sup>125</sup> This principle was successfully applied on the partial hydrogenation of propyne to propene with Pd-particles in a polymer membrane. The control over diffusion, mass-transfer and contact time allowed the balancing of the system to largely inhibit the complete hydrogenation to propane.<sup>132</sup>

In the following, specific, industrially important and the in this study used zeolites will be discussed.

## 5. Examples for zeolites

Even though around 20 different zeolites have found usage in industrial applications, the five most important zeolites acquired the simple term “Big Five”.<sup>133</sup> They are comprised of the following structural types:

- **MFI** (Mordenite Framework Inverted): The most prominent representative is H-ZSM-5 (Zeolite Socony Mobil-5), a synthetic zeolite first patented by MOBIL OIL COMPANY in 1975 with high Si/Al ratios usually above 20.<sup>39</sup> Based on the pentasil sub unit, it forms two types of 10-membered 2D-channels with dimensions of  $5.2 \text{ \AA} \times 5.7 \text{ \AA}$  and  $5.3 \text{ \AA} \times 5.6 \text{ \AA}$ .<sup>134</sup> It is used as a heterogeneous catalyst in acidic-based petrochemistry, while it is most famous for its success in the size-selective isomerization of meta-xylene to para-xylene<sup>135</sup>. Further applications include the alkylation of hydrocarbons<sup>136</sup> and the methanol-to-gasoline (MTG)<sup>137</sup> process.
- **BEA** (Beta Zeolite): Zeolite  $\beta$  exhibits a complex structure, as it can possess three different types of channel, each with 12-membered rings along, but different channel orientations along the  $c$  axis.<sup>138</sup> The three different types are called polymorphs and tend to inter grow in a single (disordered type) BEA structure. Even though pure polymorphs are highly desirable, they have not been synthesized successfully.<sup>139</sup> BEA structures have found their niche in particular in emission control.



Here there are used in NO<sub>x</sub> reduction in automobile catalysts or for volatile organic compounds (VOC) and N<sub>2</sub>O in industry exhaust gas.

- **FAU** (Faujasite): The faujasite structure consists of sodalite sub units, which form 12-membered rings, containing “super cages” with a diameter of 11.2 Å (window diameter 7.4 Å) and 6-membered non-accessible sodalite cages.<sup>140</sup> These broad cages allow the adsorption of large molecules, making the FAU representative Zeolite Y one the most important catalysts in petrochemistry with its utilization in the fluid catalytic cracking of large hydrocarbons into valuable gasoline components.<sup>141</sup> The isostructural, but less staple due to the lower Si/Al ratio, Zeolite X is used for CO<sub>2</sub> adsorption from exhaust gas.<sup>142</sup>
- **FER** (Ferrierite): Even though the FER structure looks like a 3D-structure, it is considered as 2D, because two 2D-channels (10- and 8-membered ringed) intersect each other.<sup>143</sup> It is the zeolite with the smallest channel dimensions in the “Big Five”, but exhibits superior activity in the selective isomerization of 1-butene to isobutene, an important base chemical for polymers, rubber, acrylate and methyl tertiary-butyl ether (MTBE).<sup>144</sup> It is also considered for high-pressure water/alcohol separation.<sup>145</sup>
- **MOR** (Mordenite) will be discussed later in detail, as it was used in this study.

Table 1. Overview of structures, applications and pore systems of the industrially most important zeolites: the “Big Five” and, additionally, the zeolites used in parts of this work.

	<b>IZA code*</b>	<b>example</b>	<b>application</b>	<b>pore size [Å]**</b>	<b>channel sizes [Å]</b>	<b>ring size</b>
<b>Big Five</b>	<b>MFI</b>	H-ZSM-5	isomerization al- kylation	-	5.2 x 5.7 5.3 x 5.6	10
	<b>BEA</b>	Zeolite $\beta$	emission control	-	5.6 x 5.6 6.6 x 6.7	12
	<b>FAU</b>	Zeolite Y	fluid catalytic cracking	11.2 x 11.2 6.3 x 6.3	7.4 x 7.4	12 6
	<b>FER</b>	H-ZSM-35	isomerization	-	4.2 x 5.4 3.5 x 4.8	10 8
	<b>MOR</b>	H-MOR	isomerization	-	6.5 x 7.0 2.6 x 5.7	12 8
<b>studied</b>	<b>LTA</b>	Zeolite A	water softener	11.4 x 11.4	4.1 x 4.1	8
	<b>CHA</b>	H-SSZ-13 H-SAPO-34***	NO <sub>x</sub> reduction MTO catalyst	6.5 x 11.0 6.5 x 11.0	3.8 x 3.8 3.8 x 3.8	8 8

\* based on the three-lettered notation of the International Zeolite Association (IZA)<sup>37</sup>

\*\* when no pore size value is given, the zeolite consists of 2D-channel pores

\*\*\* H-SAPO-34 is not a zeolite, but a silico-aluminophosphate, which adopts the CHA structure

Interestingly, while laundry detergents make up over 70% of the total worldwide consumption of zeolites, neither the commonly used Zeolite A, nor the emerging alternative Zeolite P are regarded part of the “Big Five”. All members of the “Big Five” are part of petrochemical processes, which only contribute around 10% of consumption but exceeding more than half of the revenue of zeolite based process, making these zeolites more valuable compared to the detergent business.<sup>38,146</sup>

## 5.1. Mordenite (MOR)

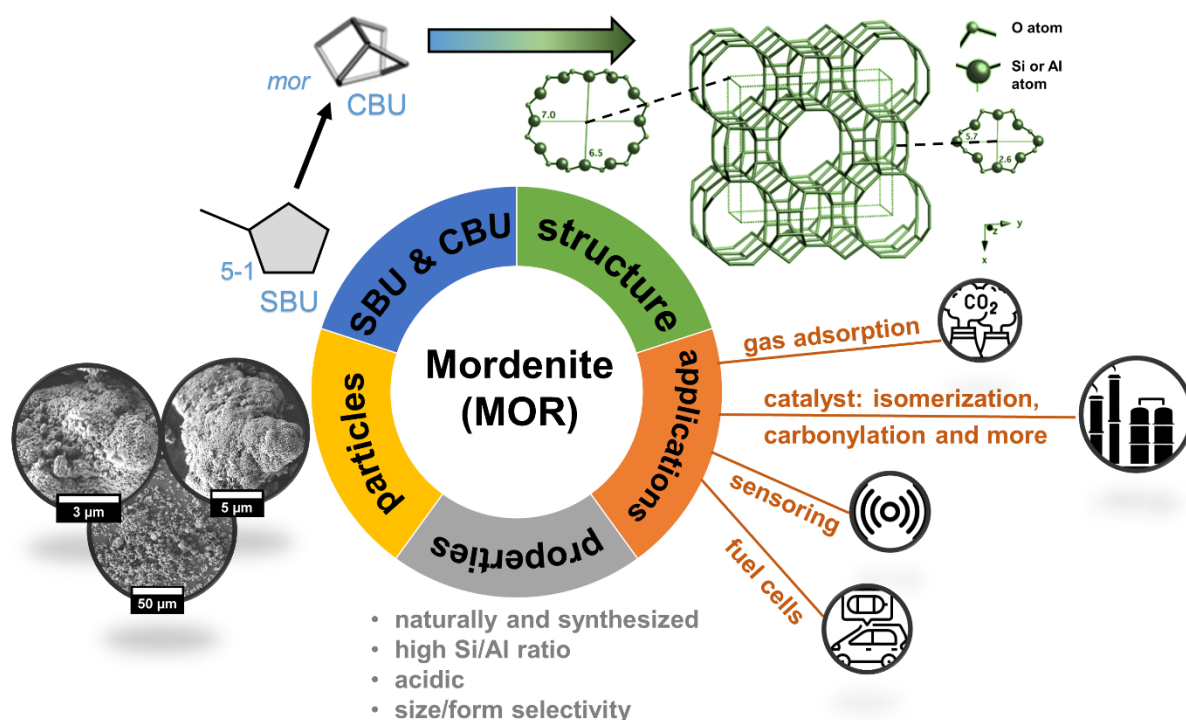


Figure 3. Overview of mordenite structure, properties and possible applications.

Mordenite is both a naturally occurring mineral, as well as a synthetic zeolite. It was first discovered by HENRY HOW in 1864 in Morden, Nova Scotia (Canada), from which the name “Mordenite” is derived.<sup>147</sup> A few years later in 1886, a mineral was described with the name “Ptilolte”, which later was discovered to be isostructural with mordenite, since then the term “Ptilolte” is occasionally used as a synonym for the mineral. Due its volcanic origin, overall mordenite occurrences are rare, however, there are a few exploitable deposits.<sup>148</sup> The first successful synthesis goes back to the founding father of synthetic zeolite chemistry, RICHARD M. BARRER in 1948 from an aqueous suspension of sodium aluminosilicate gels.<sup>35</sup> Mordenite has the following ideal composition<sup>149</sup>:



The structure possesses an orthorhombic framework system with the IZA code: MOR. The secondary building unit (SBU) is a 5-1 building block, with the composite building unit (CBU) labelled *mor* after the framework type, see Figure 3.<sup>150</sup> The resulting structure can be described as a sheet-like arrangement of six-membered rings (made of SiO<sub>4</sub> or AlO<sub>4</sub> tetrahedra) with the sheets connected by four-membered rings (side pockets). In the end, the mordenite framework

has two types of parallel main channels: one twelve-membered ring (12mR) ( $6.5 \times 7.0 \text{ \AA}$ ) and one smaller eight-membered ring channel (8mR) ( $2.6 \times 5.7 \text{ \AA}$ )<sup>151</sup> and is therefore classified as a large-pore zeolite. The main channels are interconnected through small side channels ( $3.4 \times 4.8 \text{ \AA}$ ) with eight-membered ring (8mR) windows. Overall, the mordenite framework is considered a one-dimensional framework, as the 8mR small channels are not accessible for molecules, except the smallest ones. The extra framework cations  $\text{Na}^+$  or  $\text{K}^+$  or  $\text{Ca}^{2+}$  can be located at several positions<sup>149</sup>:

- (i) inside the 8mR side pockets
- (ii) inside of either the 12mR and 8mR channels
- (iii) in the centre of the 8mR main channels at the position where the 12mR main channel and the side pockets intersect

While  $\text{Na}^+$ ,  $\text{K}^+$  or  $\text{Ca}^{2+}$  are the main counter cations in the mineral, samples with  $\text{Mg}^{2+}$ ,  $\text{Sr}^{2+}$  and  $\text{Ba}^{2+}$  also have been found. In synthetic mordenite, usually only  $\text{Na}^+$  ions are integrated.<sup>152</sup> However, by post synthesis ion exchange  $\text{NH}_4^+$ -MOR can be achieved and by subsequent calcination protons are brought into the structure as the cation. Giving that the protons can be located directly inside the main channels, valuable acidic catalytic sites are created, which are easily accessible and establish H-MOR as one of the most important acidic zeolite catalysts. The Si/Al ratio in MOR normally ranges between 5 – 20, making it moderately stable at higher temperatures. Zeolites with higher Al contents are often vulnerable to dealumination at temperatures above  $200^\circ\text{C}$  when water is present, as Si-O-Al bondings can hydrolyse irreversibly.<sup>66</sup>

Due to the aforementioned acidic sites, synthetic H-MOR has its highest usage found in the petrochemistry as a catalyst, most commonly as a low cost variant for isomerization of *n*-butane to *iso*-butane. *n*-Butane accounts for up to 5% of the cracking products in petroleum refineries, however, its demand is rather underwhelming, so a conversion into *iso*-butane for MTBE or tertiary butyl alcohol (TBA) is desirable.<sup>153</sup> H-MOR offers strong acidic sites for the adsorption of *n*-butane, further dealumination can increase the acid strength and it is a more environmentally friendly variant compared to the afore used Pt/chloride alumina catalyst, which boasts leaching of toxic  $\text{Cl}_2$  gas.<sup>151</sup> The exact reaction mechanism on H-MOR is still subject of discussion, as it is apparently depending on the number of acid sites and the *n*-butane

concentration, if the catalytic reaction is performed in a mono- or bi-molecular mechanism.<sup>154,155</sup> In both types a dehydrogenation to butene is performed, so Pt particles can be added to control the alkene concentration.<sup>155</sup> Furthermore, the shape of the mordenite channels help to suppress the formation of unwanted by-products, thus increasing the *iso*-butane selectivity. Isomerization of *n*-pentane and *n*-hexane was also reported.<sup>156</sup> An emerging application of H-MOR is the carbonylation of dimethyl ether (DME) as a green alternative synthesis route to the more than ever important ethanol. H-MOR again exhibits an excellent DME selectivity and high reaction rates due to its structure. Interestingly, the formation is one of the only few reactions in H-MOR that occur in the 8mR side channel and not in the 12mR main channel, because of their increased acid site density and strength (due to higher concentrations of Al in the 8mR channels).<sup>157</sup> Therefore, it is even tried to deactivate the 12mR channel acid sites through selective pyridine adsorption.<sup>158</sup> Recently, zeolites again resurfaced as a carbon capturing method to relief the atmosphere from carbon dioxide. The first carbon dioxide adsorption experiments on natural and treated mordenite zeolites have been promising.<sup>159</sup> More niche application of mordenite include the sensing of Hg<sup>2+</sup> ions with dealuminated, Pt-loaded zeolites<sup>160</sup> and as a composite membrane with Nafion in direct methanol fuel cells. Consistently evolving ideas like these are the reason mordenite is still subject of research with steadily above 100 publications per year related to mordenite.<sup>151</sup>

## 5.2. Zeolite A (LTA)

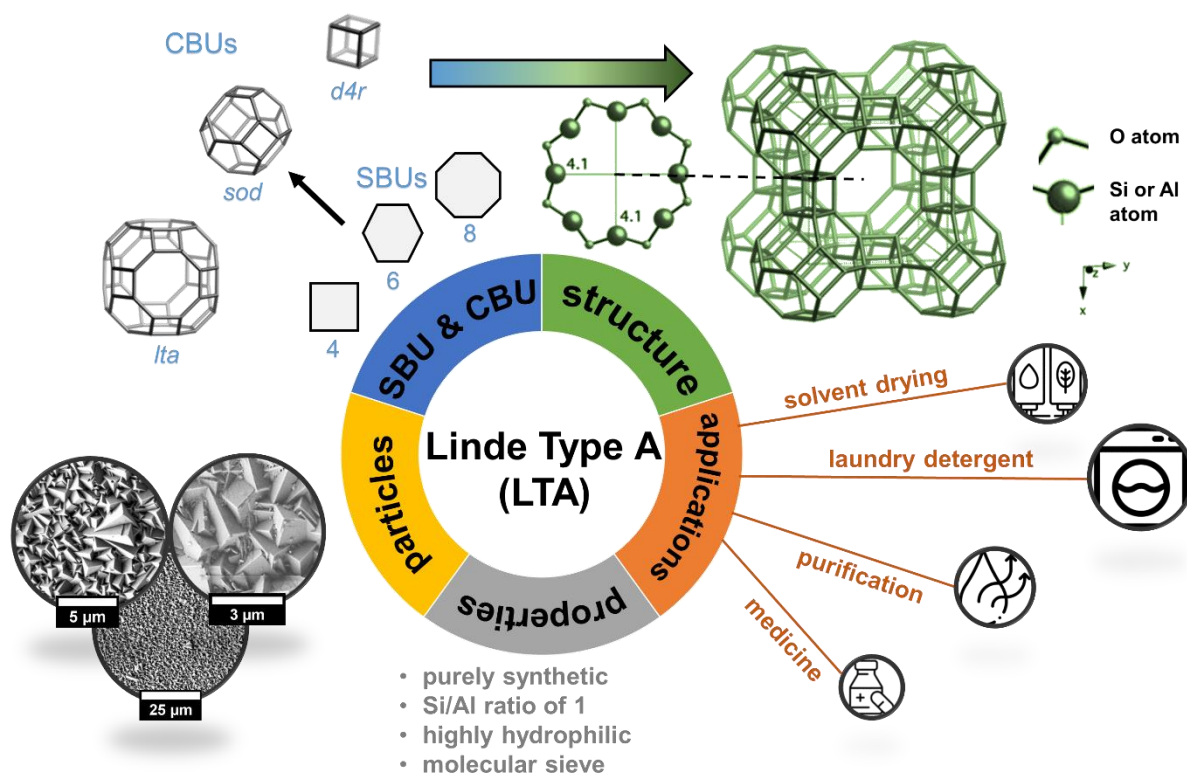
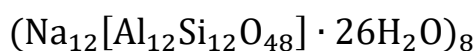


Figure 4. Overview of Linde Type A structure, properties and possible applications.

Linde Type A (IZA code: LTA) is a zeolitic framework type, which does not occur in the nature as a mineral and has to be synthesized. It was first discovered by DONALD W. BRECK and ROBERT M. MILTON in 1956 at LINDE AIR PRODUCTS (where its name originated from), a sub division of UNION CARBIDE CORPORATION, with the successful synthesis of Zeolite A, the most important representative of the LTA type.<sup>161</sup> Zeolite A was the first synthesized zeolite to find its way into commercialized industrial application as an adsorbent to remove oxygen impurities from argon.<sup>162</sup> The same group already found the FAU types with Zeolite X and Zeolite Y a few years earlier.<sup>163</sup> They also initiated the use of Latin alphabet, like Zeolite A, X, Y, L or P, while later discoveries received Greek letters like alpha, beta and omega.<sup>39</sup> The commonly used Zeolite A has a couple of synonyms and is often also labelled to as LTA, Zeolite NaA, Zeolite 4A or MS (molecular sieve) A / 4A, which all referred to the Na variant. LTA has the following optimal composition:



The LTA framework is a cubic structure with three different possible SBUs (4,6 and 8) and three CBUs: the cubic *d4r*, *sod* cages (structurally equivalent to those in the mineral sodalite) and the eponymous *lta* cages, see Figure 4. However, differently to the sodalite (SOD) structure, where the *sod* cages are directly connected, the *sod* CBUs (here also called  $\beta$ -cages) are located at the corners of the unit cell and are linked via the *d4r* unit, creating the characteristic *lta* cage ( $\alpha$ -supercage) in the middle.<sup>164</sup> The zeolite is accessible from all three dimensions through an eight-membered ring window (8mR) with a diameter of 4.1 Å, while the spherical *lta* cage possesses a diameter of ~ 11.4 Å.<sup>165</sup> The six-membered (6mR) oxygen apertures of the *sod* cage with a diameter of 2.7 Å are only penetrable for very small molecules like water or helium.<sup>166</sup>

LTA can only be synthesized in its Na<sup>+</sup>-form, which the abovementioned crystal parameters refer to. In one LTA unit cell, 12 Na atoms can be found, thereby, they can occupy three different positions in the structure<sup>164,167,168</sup>:

- (i) Slightly shifted from the centre of the 6mR windows of the *sod* cages. They make up a total of 8 Na atoms per unit cell with an occupancy of 0.97, meaning nearly all possible sites for this extra framework cation are filled.
- (ii) Slightly shifted from the centre of the 8mR windows of the *lta* ( $\alpha$ -)cages. They contribute to 3 Na atoms per cell and are the cations responsible for the accessible window diameter of 4.1 Å. Because Na is too small to fill the 8mR in a centred position, it is slightly distorted from the centre to form energetically more favoured distances to the O atoms. So, every 8mR possesses 4 different possible positions leading to an occupancy of 0.24.
- (iii) Opposite a four-ringed (4mR) ringed window of the *d4r* unit inside the  $\alpha$ -cage. With positions (i) and (ii) already counting for 11 of the Na atoms, as in average every 6mR and every 8mR possesses one Na atom, only one is left, which can take one of 8 possible isostructural position per cell (occupancy only 0.07).

On average every 6mR and every 8mR has almost one Na. Every Na atom in position (ii) only accounts for 0.5 Na per cell because it is shared with the adjacent unit cell. The exact position of the Na atoms in the publications above are all given for the idealized dehydrated

version of Na-LTA. Meanwhile, in the hydrated zeolite the extra framework cation positions shift a bit due to the presence of adsorbed water molecules.

LTA has the unique property, that the pore windows size can effortlessly be adjusted to three different size: in the common Na-LTA each 8mR window to the  $\alpha$ -cage is occupied by one Na atom, which results in the window diameter of 4.1 Å, given it the synonym Zeolite 4A. A post-synthesis ion exchange can be performed, usually by just submerging the zeolite in K<sup>+</sup>-containing aqueous solution, which replaces all Na<sup>+</sup> cations with K<sup>+</sup> cations. The K<sup>+</sup> occupies the same three position as Na<sup>+</sup>. As the K<sup>+</sup> cation is larger than the Na<sup>+</sup> cation, see Table 2., it takes up more empty space in the 8mR compared to the sodium, effectively decreasing the accessibly pore diameter to 2.9 Å and therefore, K-LTA is also called Zeolite 3A. On the other hand, a pore window widening can be achieved by exchanging the extra framework cation to Ca<sup>2+</sup>. Since the radii of Na<sup>+</sup> and Ca<sup>2+</sup> are virtually the same, the effect does not stem from the cation blocking in the 8mR. The Ca<sup>2+</sup> possesses two positive charges, consequently, the amount of needed cations is halved (6 per unit cell). These 6 occupy places in 6mR of the *sod* cages, equivalent to position (i), meaning the positions in the 8mR are vacant and the pore window is not influenced by the cation position, leaving the empty 8mR with a diameter of 5 Å.<sup>169</sup>

Table 2. Overview of the three common forms of LTA: K-LTA, Na-LTA and Ca-LTA with its pore parameters, capable adsorbed gases and possible molecular sieve applications.

type	window diameter <sup>170</sup>	form	cation radius [Å] <sup>168</sup>	adsorbed gases	applications
3A	2.9 Å	Na	0.95	H <sub>2</sub> O, NH <sub>3</sub>	drying of MeOH, EtOH and gases
4A	4.1 Å	K	1.33	+ CO <sub>2</sub> , H <sub>2</sub> S, ethene, ethane	drying of polar and nonpolar solvents
5A	5.0 Å	Ca	0.99	+ <i>n</i> -alkane, <i>n</i> -propanol, <i>n</i> -butanol	separation of <i>n</i> -alkanes from <i>iso</i> -alkanes

The LTA pore engineering is especially useful in its applications as a molecular sieve. Zeolite 3A can remove rest water from otherwise azeotrope mixtures with MeOH and EtOH, 4A is commonly used to dry a variety of organic solvents, while 5A is able to separate *n*-alkane from its *iso*-counterpart. However, post-synthesis ion exchange of already grown Na-LTA membranes is connected with increased or decreased cell parameters, the resulting distortion



can lead to micro cracks and leakages, so the exchange has to be performed carefully. A stable form of protonated H-LTA is not known to exist.

LTA combines the structure to perform shape-selective molecular sieve procedures, while also providing a highly hydrophilic pore, due to its large Al share. This makes LTA an ideal candidate for the continuous removal of water from reactions or solvents. LTA membranes have been exceedingly useful in pervaporation experiments. A leading role in the development of LTA membranes is the commercialization for sustainable chemicals by the BUSSAN NANOTECH RESEARCH INC. (BNRI) in Japan to produce fuel grade bio-ethanol through LTA membrane-assisted dehydration in 2008.<sup>88</sup>

Apart from drying solvents, the esterification reaction is a promising field for LTA water removal membranes, as the extraction of the product water leads to an increased conversion based on the equilibrium shift.<sup>171</sup> The pervaporation-assisted esterification was performed with success on a variety of reactants: ethanol + acetic acid<sup>172</sup>, *n*-propanol + acetic acid<sup>173</sup>, *iso*-propanol + propionic acid<sup>174</sup> and ethanol + lactic acid<sup>175</sup>, just to name a few.

Increasingly important is the purification of water as world population is consistently increasing and the access to fresh water is limited. LTA showed promising results for desalination of salt water, while additionally removing low level radioactive wastes, dyes, heavy metals and drug residues with high rejection rates. The water purification is either performed via pervaporation or reverse osmosis. With a good long-term stability, high water fluxes and a non-toxic material, LTA membranes may be the way of drinking water production moving forward.<sup>114,176</sup>

The application, which made LTA and zeolites in general known, is as an additive to laundry detergents. Developed by SCHWUGER and SMOLKA at HENKEL & CIE GMBH in the early 1970s, LTA was already replacing the before used, environmental polluting phosphate containing detergents, by 1977.<sup>177,178</sup> In this system Na-LTA works as a water softener by changing their extra framework sodium with calcium or magnesium in the water. While both earth alkaline elements can form insoluble salts, sodium is not able to. Based on the Si/Al ratio of 1 for LTA, it has the highest possible cation exchange capacity with decent exchange rates ( $\text{Ca}^{2+}$  exchange is significantly faster than  $\text{Mg}^{2+}$ ) and is the low-cost, non-toxic alternative that was

searched for. In general, it can be stated that the Na-LTA is preferably exchanging to the cation that has the<sup>177</sup>:

- (i) higher valence
- (ii) higher atom weight
- (iii) smaller tendency for hydration
- (iv) higher polarizability
- (v) in solution forms the stronger dissociated complex,

also making the uptake of a variety of metal ions from waste water possible.

Together with the concentration gradient of hard water compared to the zeolite, Na-LTA does the job as a detergent exceedingly well and is still the most produced zeolite as of today.<sup>38</sup> In recent years, continuous research is performed to improve the  $Mg^{2+}$  uptake, while the competition of Zeolite P is increasing because of its enhanced exchange rate.<sup>45,46</sup>

A niche application is the use of Ag-, Ca- and Zn-exchanged LTA for wound healing as the system combines wound dehydration, electrolyte supply and sterilization. With consistently over 100 publications per year related to LTA, it remains one of the most influential and well researched zeolites.<sup>46</sup>

### 5.3. Chabazite (CHA)

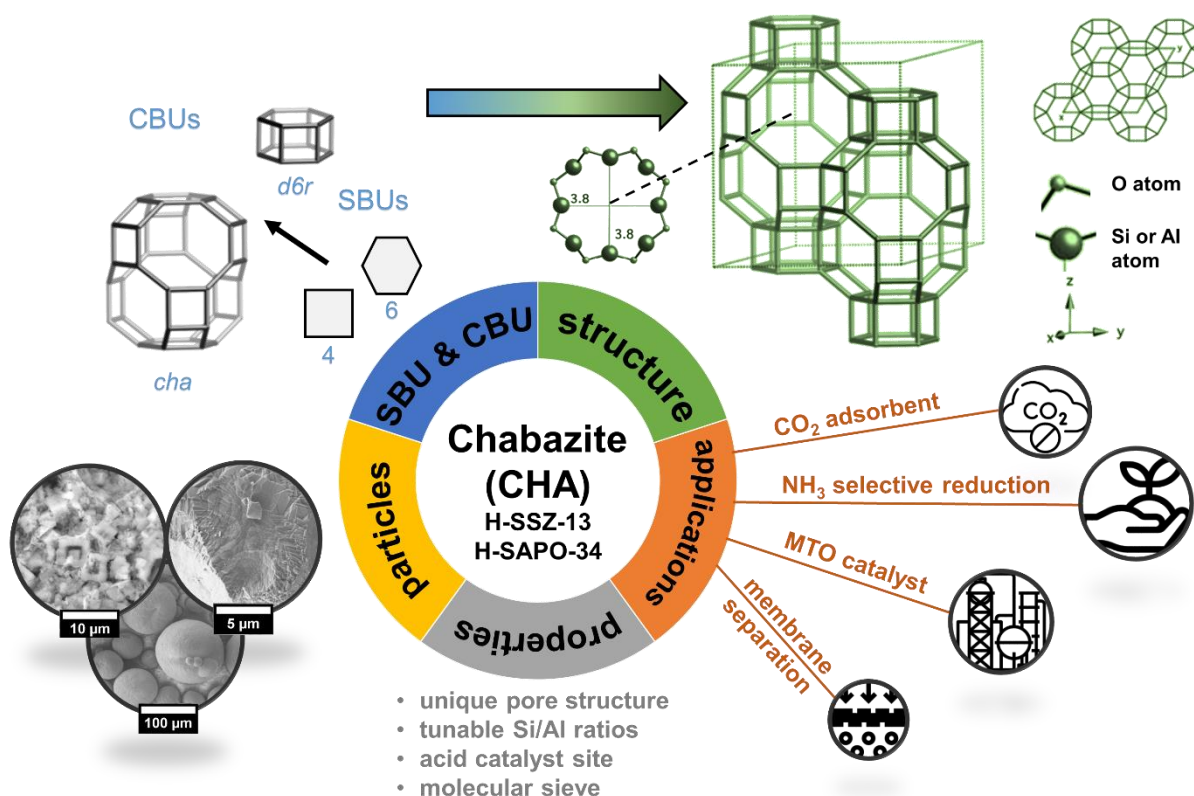


Figure 5. Overview of chabazite (CHA) structure, properties and possible applications for the SSZ-13 zeolite and SAPO-34 aluminosilicophosphate.

Chabazite is a mineral first discovered by IGNAZ VON BORN in 1772 in Iceland, which he named “Zeolithus crystallisatus cubicus Islandiae” just 16 years after the term zeolite was first introduced. Because of its cubic crystallites LOUIS BOSC D’ANTIC called the mineral “chabazie”, after the ancient Greek word for hailstone, from which today’s title “chabazite” derives.<sup>179</sup> Natural chabazite holds a special place in history, as pioneering work on zeolite research was performed on this mineral: in 1909 GRANDJEAN showed that dehydrated chabazite adsorbed small molecules like ammonia, air components and hydrogen<sup>180</sup>, while WEIGEL and STEINHOFF demonstrated the molecular sieve properties of zeolites for the first time in 1925 as chabazite absorbed water, methanol and ethanol, but practically no acetone or benzenes<sup>181</sup>. Chabazite often incorporates Na, K and Ca, and occasionally Mg and Sr, at the same time, thus the given chemical formula is based as an example on the sodium-rich Chabazite-Na<sup>182</sup>:



The first report of a synthetic chabazite zeolite was achieved by RICHARD M. BARRER in 1956 in form of the potassium variant.<sup>183</sup>

In this work two aluminosilicates with the chabazite structure type are being discussed in detail: H-SSZ-13 and H-SAPO-34.

### 5.3.1. H-SSZ-13

Zeolite SSZ-13 was first synthesized by STACEY I. ZONES in 1985 for the CHEVRON RESEARCH COMPANY, formerly known as the STANDARD OIL COMPANY<sup>184</sup> and has become the commonly used zeolite with the CHA structure. The acronym SSZ stands for “Standard Oil Synthetic Zeolite” and has given its abbreviation to a large number of synthetic zeolites with different structure types. SSZ-13 shares the same framework topology with the chabazite mineral, but is a high-silica variant with a Si/Al ratio above 5. The synthesis is usually performed with the expensive structure-directing agent (SDA) *N,N,N*-trimethyladamantylammonium hydroxide<sup>185</sup>, thus, efforts for synthesis without organic SDAs were carried out.<sup>186</sup>

The chabazite structure has a trigonal system with the IZA code: CHA<sup>187</sup>. It has two different SBUs (4 and 6), which are used to build the two CBUs: the hexagonal *d6r* and the characteristic ellipsoidal *cha* cage, see Figure 5. One *cha* unit is connected to four other *cha* cages by *d6r* channels. The *cha* CBUs are connected via three different rings<sup>188-190</sup>, see Figure 5:

- (i) through the *d6r* CBU, where each 4mR window is connected to one *cha* CBU on the *xy*-plane. These windows are too small for any molecules to fit through.
- (ii) through the 6mrR windows of the *d6r* CBU along the *z*-axis.
- (iii) directly by the 8mR windows of the *cha* unit. Each *cha* cage is therefore directly linked to 6 other *cha* cages. The 8mR windows possess a diameter of 3.8 Å (and are the reason that CHA is classified as a small-pore zeolite), while the *cha* cages have dimensions of 6.5 Å × 11 Å with a diameter of 7.4 Å.

The combination of the *d6r* and *cha* CBUs leads to a three-dimensional pore system. Another way to describe the CHA crystal structure is the stacking of double 6mRs in an AABBCCAA order, which are connected through tilted 4mRs, showing that only 4 and 6 SBUs are necessary to form the structure, even though the *cha* CBUs possesses 8mR windows. For extra framework cations protons and copper have the highest relevance in research because of

their catalytic properties. Subsequently, the position of only protons in H-SSZ-13 are discussed in detail, because they are relevant in this work. Protons, unlike Na or K, only need to coordinate to one oxygen atom. H-SSZ-13 has four structurally different O positions<sup>191</sup>:

- (i) at the O atom connecting the two 6mR in the *d6r* CBU. The proton itself is not located in the *d6r* CBU, but is accessible inside the *cha* cage, because it is the same O atom incorporated in the 8mR. (16 possible isostructural positions)
- (ii) at the O atom, which is shared by the 6mR of the *d6r* unit and the 8mR at the top and bottom of the *cha* cage. (6 possible isostructural positions)
- (iii) at the O atom, which is shared by the 6mR of the *d6r* unit and the 4mR of the *cha* unit. (6 possible isostructural positions)
- (iv) at the O atom linking two *d6r* cages. It is also part of two 8mR of two different *cha* units and one 4mR of *cha*. (24 possible isostructural positions)

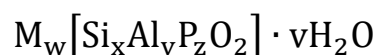
Protons prefer to occupy either position (i) or (ii) in dehydrated chabazites and tend to slightly shift into the *cha* cage to coordinate to adsorbed water in the hydrated samples.<sup>43</sup> In this projection a characteristic can be applied for position (iii), as it's the only site that has no direct connection to the 8mR windows, therefore, is not accessible in the windows but rather only from inside the pore, making it unique from the others. The number of protons per cage is heavily depending on the Si/Al ratio, which theoretically can adopt any value between 1 and infinity. With increasing Si/Al ratio, however, the number of acidic sites per pore and the hydrophilicity of the pore itself decreases, while the strength of the individual acid site increases.<sup>192,193</sup> Extra framework cations outside of protons, occupy slightly different position because they can coordinate to multiple O atoms<sup>194,195</sup>:

- (i) inside the *d6r* cage
- (ii) in front of the 6mR of the *d6r* cage inside the *cha* unit
- (iii) in front of the 8mR of the *cha* cage

### 5.3.2. SAPO-34

SAPOs (abbr. for silicoaluminophosphate) are a group of molecular sieves first discussed in the early 1980s. They are strongly connected to the AlPOs (aluminophosphate). The first

ALPO structure was discovered by BRENT M. LOK and EDITH M. FLANIGEN in 1982 at the UNION CARBIDE CORPORATION.<sup>196</sup> With their defined structure, applications for catalysis, molecular sieving and adsorption were taken into consideration, even though the ALPO framework itself is neutral. By introducing silicon into the structure negative charges are created, which can be balanced out by protons, creating the ever so valuable acid sites for catalysis. This new class of materials was called SAPO and was first described in 1984 by the same group that performed the research on AIPOs.<sup>197</sup> Both AIPOs and SAPOs sometimes adopt structure types analogous to zeolites, like CHA (SAPO-34), LEV (SAPO-35), FAU (SAPO-37), LTA (SAPO-42) and AEI (AIPO-18), AWW (AIPO-22), AFT (AIPO-52). However, they are occasionally SAPO and AIPO structure types, that are exclusive to the phosphates.<sup>197,198</sup> The structural similarities between SAPOs/AIPOs and zeolite derive from the fact, that phosphorous forms PO<sub>4</sub> tetrahedra, analogous to the SiO<sub>4</sub> and AlO<sub>4</sub> tetrahedra found in the typical zeolite structure. The LOEWENSTEIN rule is not applied here, as the structures stem from the aluminophosphate, conclusively Al-O-Al bondings can be found frequently. Unlike the Al-O-Si connections, which tend to hydrolyse irreversibly in the presence of water and high temperatures, the Al-O-Al only hydrolyse reversibly.<sup>199</sup> In the following only SAPO-34 with its CHA structure will be discussed. The elemental composition of SAPO-34 can be described like this:



with  $x = 0.01-0.98$ ,  $y = 0.01-0.60$ ,  $z = 0.01-0.52$  and  $x + y + z = 1$ . With the high variety of possible chemical composition of SAPO-34 the number of extra framework cations (including protons) and adsorbed water in the hydrated form heavily depends on the amount of silicon implemented.<sup>200</sup> Due to their identical structure type, H-SSZ-13 and H-SAPO-34 are often compared with each other. The pore dimensions are essentially the same, with the SAPO-34 exhibiting a slightly larger unit cell volume of 2.1%<sup>201</sup>, while the accessible pore volume of SAPO-34 is reduced by about 15% compared to SSZ-13<sup>191</sup>. With the same number of acid sites, SAPO-34 possesses overall weaker acidic properties as IR measurements showed that the proton is bonded stronger in the SAPO reducing its acid strength. The proton (and the possible non-proton cation) positions are the same for both the H-SSZ-13 and the H-SAPO-34.<sup>202</sup>

Since the chabazite structure type is considered unique, a few specific applications are considered for SSZ-13 and SAPO-34. As both the zeolite and the silicoaluminophosphate resemble

one another in many of their properties, they frequently competing about the same applications, while in the end the demand on a slightly higher acidity or a better hydrothermal stability can turn the scales on which type of chabazite to use.

The automobile branch is one of the most financially profitable industry. One of the largest problem is the emission control and the elimination of environmentally harmful  $\text{NO}_x$  exhaust gas components. The common three-way catalytic materials struggle to reduce  $\text{NO}_x$  in engines with high air/fuel ratios, like diesel engines.<sup>203</sup> A solution to completely eliminate nitrogen oxide is the selective catalytic reduction of  $\text{NO}_x$  with  $\text{NH}_3$  to form water and molecular nitrogen ( $\text{NH}_3$ -SCR). This reaction can be performed with metal oxide or noble-metal catalysts, though, high cost, toxicity and unwieldy handling shifted the attention to metal-exchanged zeolites, as they promised cost-reduction and better material distribution.<sup>204</sup> In this process Cu- and Fe-exchanged chabazite structures emerged as the frontrunner, due to their unique pore systems.<sup>205–207</sup> They both exhibit  $\text{NO}_x$  conversions of over 99%, with Cu/SAPO-34 producing less of the unwanted by-product  $\text{N}_2\text{O}$  compared to Cu/SSZ-13 at  $250^\circ\text{C}$ .<sup>203</sup> Adding that to the fact, that Cu/SAPO-34 showed better hydrothermal stability at  $900^\circ\text{C}$  compared to its SSZ-13 counterpart, its somewhat surprising that research on Cu/SAPO-34 for  $\text{NH}_3$ -SCR is gradually declining. The deactivation of Cu/SAPO 34 at low temperatures is its biggest drawback in the emerging cold-start exhaust gas conversion problems and the reason why Cu/SSZ-13 prevailed as the chabazite material of choice for the  $\text{NH}_3$ -SCR.<sup>208,209</sup> Long-term stability is still a hurdle to overcome, but the outlook for another large-scale application of zeolite in exhaust gas catalysis is promising.

As both SAPO-34 and SSZ-13 showed high affinities towards carbon dioxide due to their structure and extra framework cation positions, which differentiate them from other zeolite structures, adsorption and separation applications were taken into consideration.<sup>210</sup> SSZ-13 was determined as the preferred choice featuring  $\text{CO}_2$  adsorption and carbon capture<sup>211,212</sup>, with SAPO-34 being used as a membrane material to separate  $\text{CO}_2$  and  $\text{CH}_4$  and for hydrogen purification<sup>213,214</sup>.

Two emerging reactions that use CHA type catalysts are the methylamine synthesis from methanol and ammonia and the methanol-to-olefins (MTO) reaction. Both will be discussed in the next chapter in detail. To summarize, in both reactions the small CHA windows and the

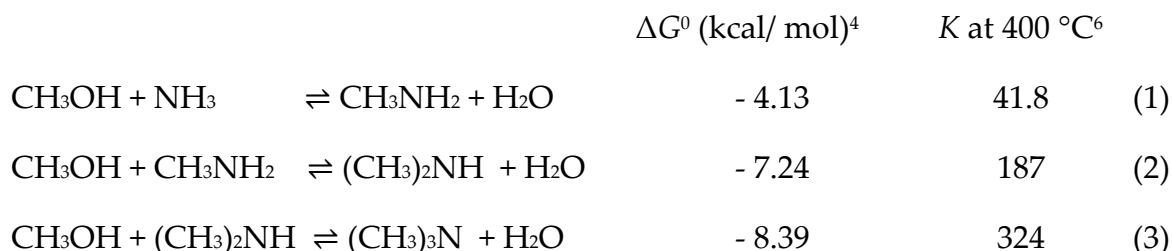
mild acidic sites of their protonated forms are the reason for improved selectivities of desired products. While in the methylamine synthesis H-SSZ-13 showed better results<sup>4,215</sup>, H-SAPO-34 is the material of choice in the MTO reaction<sup>199,216</sup>.

## 6. Methylamine synthesis

The methylamine synthesis is a vapour phase reaction that forms a variety of products from methanol and ammonia, including monomethylamine (MMA), dimethylamine (DMA), trimethylamine (TMA), water, dimethylether (DME) and more.



This form of the methylamine synthesis is a cascade reaction, meaning that methanol and ammonia first react to MMA, which gets methylated by another methanol molecule to form DMA and, subsequently, TMA. Various side reactions occur, like disproportionation, DME and coke formation, making the influence of certain reaction parameters difficult to predict. The reaction rate increases in the following order:  $\text{NH}_3 < \text{MMA} < \text{DMA}$ , in addition the thermodynamic parameters of each reaction step is given in the equations (1) - (3), showing that TMA is both the thermodynamically and kinetically favoured product.



The first documented methylamine synthesis from CHARLES WURTZ is dated back to 1849 through the hydrolysis of alkyl isocyanates<sup>217</sup>, while the first successful formation from methanol and ammonia was set to 1884 in a batch reactor. The reaction was performed in the vapour phase in 1909 with an alumina catalyst. In the 1920s DuPont and Commercial Solvents Corporation both filed patents for their approach on the methylamine synthesis. Almost simultaneously they commercialized the process and set up industrial sized reactor plants.<sup>4</sup> They used high pressures (10 to 50 bar) with dehydrating catalysts to increase the reactant contact times at temperatures between 350 and 500 °C. Today's conversion is still performed with a catalyst

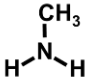
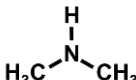
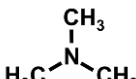
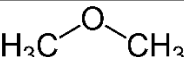
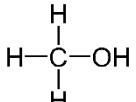
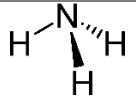
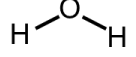


containing amorphous aluminium oxide or aluminosilicates but the pressures could be lowered to 2-3 MPa.<sup>218,219</sup> Each of the three main products MMA, DMA and TMA serves different purposes as an intermediate product:

- (i) MMA is used in the synthesis of the pharmaceuticals ephedrine and theophylline, pesticides, surfactants, explosives and solvents (like *N*-methyl-2-pyrrolidone and *N*-methyl formamide)<sup>5,8,220</sup>
- (ii) DMA is used in the synthesis of fungicides, vulcanization accelerators, solvents, catalysts, pharmaceuticals and rocket fuel<sup>4,5,220,221</sup>
- (iii) TMA is used in the synthesis of choline, ion exchange resins and dyes<sup>5,8,220</sup>

Their chemical properties are summarized in Table 3.

Table 3. Summary of the formula, physical and chemical properties of monomethylamine, dimethylamine and trimethylamine<sup>8,222,223</sup>, as well DMA, MeOH, H<sub>2</sub>O and NH<sub>3</sub>.<sup>224,225</sup>

name	formula	molecule size/ diameter [Å]	CHA fit*	MOR fit**	molecular mass [g/mol]	boiling point [°C]
MMA		3.7 x 3.9 x 4.4	✓	✓	31.06	-6.3
DMA		3.8 x 4.7 x 6.0	✓	✓	45.08	6.8
TMA		3.9 x 5.4 x 6.1	✗	✓	59.11	2.8
DME		2.9 x 4.7	✓	✓	46.06	-24.8
MeOH		3.6	✓	✓	32.04	65.0
NH <sub>3</sub>		2.9	✓	✓	17.03	-33.0
H <sub>2</sub> O		2.6	✓	✓	18.01	100.0

\* can the chemical compound fit through the 3.8 x 3.8 windows of the CHA structure

\*\* can the chemical compound fit through the 6.5 x 7.0 windows of the MOR structure

With an overall worldwide production of more than 1.3 million metric tons, the methylamines belong the most important chemical intermediates.<sup>8</sup> The present variant of the methylamine synthesis from methanol and ammonia yields between 35 – 75 wt% of TMA, depending on temperature, pressure, catalyst and nitrogen/carbon (N/C) ratio.<sup>226</sup> However, demand of TMA is only about 20 wt%, additionally TMA forms a complex azeotropic mixture with water. DMA has the highest demand of the methylamine, so subsequent research to enrich the product mixtures with DMA have been performed.<sup>6,8</sup> In the LEONARD process MMA and TMA gets reintroduced to the catalysts together with ammonia for dismutation and disproportionation.<sup>227</sup> Other works focused on developing shape-selective catalyst materials. In commercial plants two catalyst systems are used consisting of an amorphous solid acid catalyst and a shape-selective zeolite catalyst.<sup>8</sup> To further intensify the understanding of the process, the reaction mechanism will be discussed in detail.

For achieving high methanol conversion rates catalytic acid sites are needed. The catalysts have to withstand harsh reaction temperatures and pressures while providing long-term stability and the desired product composition. This descriptions fits zeolites well, therefore research on a wide variety of porous, zeolite based catalysts has been performed, including framework structures of MOR (H-Mordenite), CHA (H-SAPO-34, H-SSZ-13), LEV (H-Levyne), MTF (H-MCM-35), AFX (H-SSZ-16, H-SAPO-56) and RHO (H-Rho).<sup>222</sup> The reaction mechanism is thereby depending whether the reaction is performed in a small-pore catalyst or in a large-pore catalyst, see Figure 6.

- (i) For small-pore catalysts, like H-CHA, a LANGMUIR-HINSHELWOOD mechanism is proposed by ILAO et al.<sup>6,215</sup>, see Figure 6a). The CHA framework has a small window with a diameter of just 3.8 Å, while the pore diameter stands at 7.4 Å. They measured the simultaneous adsorption of methanol and ammonia via infrared spectroscopy. CHA type catalysts produce unusually low amounts of TMA. This can be related to the fact that the large TMA molecules are not fitting through the pore window, see Table 3. It is further stated that TMA is not formed at all, because the transition state of DMA together with methanol to produce TMA cannot be established, because it's too big to fit in the CHA cage. Subsequently, it is concluded that for the reaction in the CHA cage both reactants have to adsorb to the surface because every transition state for the formation of MMA and DMA if only one reactant is adsorbed

(ELEY-RIDEAL mechanism) is too large for the cages. When both reactants adsorb to acidic sites of the zeolite enough space is saved to perform the reaction and formation of the transition states necessary for the production of MMA and DMA (TMA transition state still does not fit inside the pores, essentially stopping methylation at the DMA). In this LANGMUIR-HINSHELWOOD mechanism the surface-bound methanol is attacked by the surface-bound ammonia in an intramolecular  $S_N2$  reaction. After splitting of water, the resulted MMA can either diffuse out of the pore or perform the same reaction path instead of ammonia to yield DMA.

However, carbon residues in other reactions with CHA-type catalysts show that even larger benzene derivatives fit inside the CHA cages.<sup>228</sup> Therefore, it can be stated that the absence of TMA in the CHA pores is not only due to space restrictions but influenced by other pore characteristics as well.

- (ii) For medium- and large-pore zeolite catalysts a ELEY-RIDEAL mechanism was first proposed by FETTING et al. for the ZK-5 zeolite<sup>229</sup>, see Figure 6b). The ELEY-RIDEAL is energetically favoured compared to the LANGMUIR-HINSHELWOOD mechanism (when there are no steric restrictions) as only one reactant has to bind to the surface and they do not have to rely on adjacent adsorption sites. Ammonia is preferably adsorbed over water or methanol.<sup>230</sup> The methanol has to be protonated to improve its dehydration properties, thus it is forming its oxonium ion by either attack the adsorbed ammonium cation or any acidic surface site. The adsorbed ammonia now can perform a  $S_N2$  attack to form the transition state and split off water to produce MMA. The reaction path is repeated not with ammonia but with either MMA or DMA to form DMA or TMA, respectively.

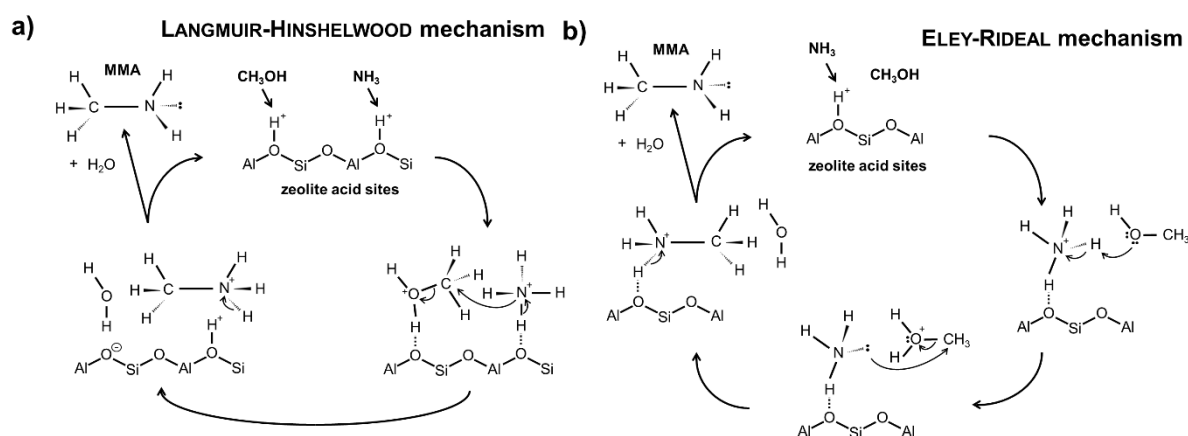


Figure 6. Visualized reaction mechanism of methylamine synthesis for a) small-pore zeolites after LANGMUIR-HINSHELWOOD and b) large-pore zeolite after ELEY-RIDEAL modelled after proposals of ILAO et al.<sup>6</sup> and FETTING et al.<sup>229</sup>.

An exemplary product composition of the methylamine synthesis with H-CHA and H-MOR catalyst can be found in Table 4. It shows that the CHA effectively excluded TMA from the product mixtures by its shape selective pore system, while the DME selectivity is low as well, resulting in an almost 1:1 mixture of MMA and DMA and a methanol conversion rate of 90%.

Table 4. Typical product composition of the methylamine synthesis from methanol and ammonia at 340 °C, 2.8 kPa, N/C ratio of 2 with an acidic small-pore catalyst (H-CHA) and an acidic large-pore catalyst (H-MOR) from<sup>6,222</sup>.

catalyst	pore size [Å]	methanol conversion [%]	selectivity [%]			
			MMA	DMA	TMA	DME
H-CHA	3.8 x 3.8	89	46	49	4	1
H-MOR	6.5 x 7.0	68	36	23	34	7

While the CHA type zeolite H-SSZ-13 performs excellently in the methylamine synthesis, its silicoaluminophosphate counterpart H-SAPO-34 showed poor results. H-SAPO-34 exhibits high DME selectivities, due to its lower acidity compared to H-SSZ-13 because the SAPO is not able to properly stabilize the methylammonium ions. Furthermore, a larger amount of H-SAPO-34 catalysts is needed due to the smaller acid site density, making H-SSZ-13 the superior CHA catalyst for the methylamine synthesis.<sup>222</sup>

H-MOR, on the other hand, has lower conversion rates and almost equal ratios of MMA, DMA and TMA, with the desired DMA exhibiting the lowest yield. However, H-MOR is usually the catalyst of choice for the commercialized methylamine synthesis. This development is based on the observation that H-MOR can withstand the harsh conditions and upheld a stable product composition longer than the H-CHA. Therefore, it was used in the NITTO process, the first commercial methylamine plant based on shape-selective zeolite catalyst at the NITTO CHEMICAL INDUSTRY COMPANY in Japan in 1990.<sup>231</sup> To improve the selectivity towards DMA and to tune the product composition of H-MOR, post synthesis treatment (like silylation) is applied to narrow the channel sizes of the mordenite, thus trying to suppress the formation of TMA.<sup>8</sup>

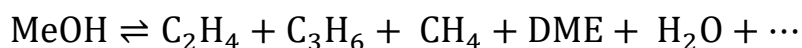
The methylamine synthesis catalysts are benefiting from the fact that there are many factors and reaction parameters to change that influence the product composition. Thus, the reaction can be tailored to achieve the desired product mixture. For future applications, CHA based catalysts have to improve its long-term stability, while MOR catalysts are required to narrow down their pore diameters to inhibit the TMA formation.

## 7. Methanol-to-olefins

The methanol-to-olefins (MTO) is regarded as one of the fundamental reactions in C1 chemistry, with the possibility for the widespread production of small olefins, like ethene and propene, from just methanol. Compared to the methylamine synthesis, which has its origin over 100 years ago, the methanol-to-olefins (MTO) reaction is a fairly new process.<sup>11</sup> It was first introduced by CLARENCE CHANG and ANTHONY SILVESTRI at MOBIL OIL COMPANY in 1977.<sup>232</sup> The MTO reaction is a subtype of a variety of reactions, which can be summarized under the term Methanol-to-Hydrocarbons (MTH). Based on the type of catalyst and the reaction parameters like pressure, temperature, gas flow and more, methanol can be converted to either small olefins (MTO), to aromatics (methanol-to-aromatics, MTA) or to fuel components with low octane numbers (methanol-to-gasoline, MTG). The MTH reaction type was discovered by accident at MOBIL OIL COMPANY in the early 1970s, as they originally tried to convert methanol to oxygen-based organic chemicals with an acidic zeolite catalyst, but received large quantities of hydrocarbons. In the following years the MTO reaction gathered the most interest as it promised an alternative way to the extraordinary valuable light olefins ethene (production per

annum: 150 million metric tons) and propene (production per annum: 80 million metric tons). However, the majority is still produced in a top-down reaction, via steam cracking. With depleting crude oil reserves, alternative formation reactions gained attention. In the MTO reaction the same olefins are getting produced via a bottom-up principle from synthesis gas (first a conversion to methanol is required, rivalling the FISCHER-TROPSCH synthesis) or from methanol of biomass. Today, many petrochemical companies operate MTH plants, ExxonMobil applied an H-ZSM-5 zeolite catalyst, while UOP/Hydro uses the silicoaluminophosphate H-SAPO-34. Especially in China, research and commercialization of the MTO process has been promoted, resulting in the first coal-to-olefin plant in 2010.<sup>9,11,233</sup>

The MTO reaction equation can be formulated as followed:



The reaction is usually performed at temperatures between 300 – 500 °C and moderate pressures, over an acidic zeolite-based catalyst. The reaction mechanism is complex, has attracted much research effort and certain parts, like the formation of the first C-C bond, are still subject of uncertainty.<sup>234</sup> It is generally accepted that methanol initially builds up an equilibrium mixture of methanol, dimethylether and water at the acidic sites of the catalyst. For the formation of the first C-C bond over 20 different mechanisms have been proposed, however, they are often implausible due to high energy requirements and lack experimental back up. Research showed that the importance of this first formation is negligible in steady-state conversion, so its solving is not needed in large-scale operation.<sup>235</sup> The MTO reaction is labelled as an autocatalytic reaction, indicating that the products itself catalyse the reaction. However, these products are not the small olefins, there are compounds summarized under the often deprecatingly used term, “coke”. In this case, coke can either describe carbonaceous residues inside the pores (inner coke) or on the outside of the catalyst particles (outer coke). For better understanding the hydrocarbon pool (HCP) mechanism was described by DAHL and KOLBOE in 1993 and was later extended, see Figure 7.<sup>236,237</sup>

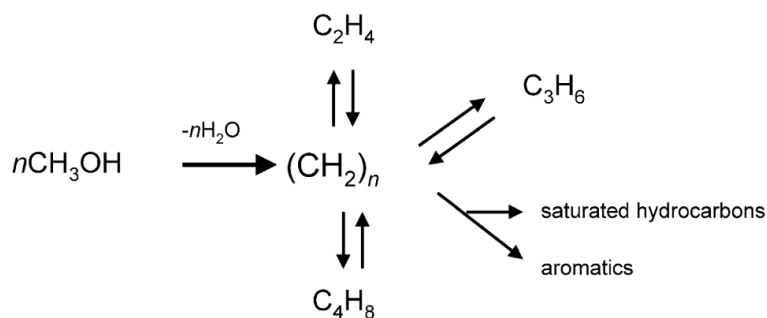


Figure 7. Original hydrocarbon pool (HCP) mechanism after DAHL and KOLBOE, recreated from<sup>238</sup>.

It was used to simplify that all of methanol, ethene, propene, butene, saturated hydrocarbons and aromatics contribute to a catalytic species not further specified as  $(\text{CH}_2)_n$ . From that point on, it was concluded that the first steps in the MTO reaction was the formation of (polymethyl-)benzenes.<sup>239</sup> Further studies of the coke residues from inside the catalyst pores confirmed the presence of methylated benzenes and HAW et al. later summarized the discoveries regarding the small olefin formation mechanism.<sup>240,241</sup> Today's understanding on the MTO reaction is that the most important step in the "initial phase" of the reaction is the formation of methylated benzenes from compounds in the HCP with help of the acidic sites of the catalyst. The higher methylated benzenes (penta- and hexamethyl benzenes) are able to split off small olefins (ethene and propene) to form lower methylated benzenes (mono-, di- and trimethyl benzenes). Through re-methylation via dimethylether or methanol, the benzenes are again converted to the higher methylated variant, repeating the process (working phase). In the mid-2000s a dual-cycle concept was proposed that added the possibility of a propene formation through consecutive cracking and disproportionation of higher alkenes.<sup>242</sup> Since then the possibility of splitting the propene cracking mechanism and the ethene mechanism and run them separately on certain zeolite catalysts has been an intruding option.

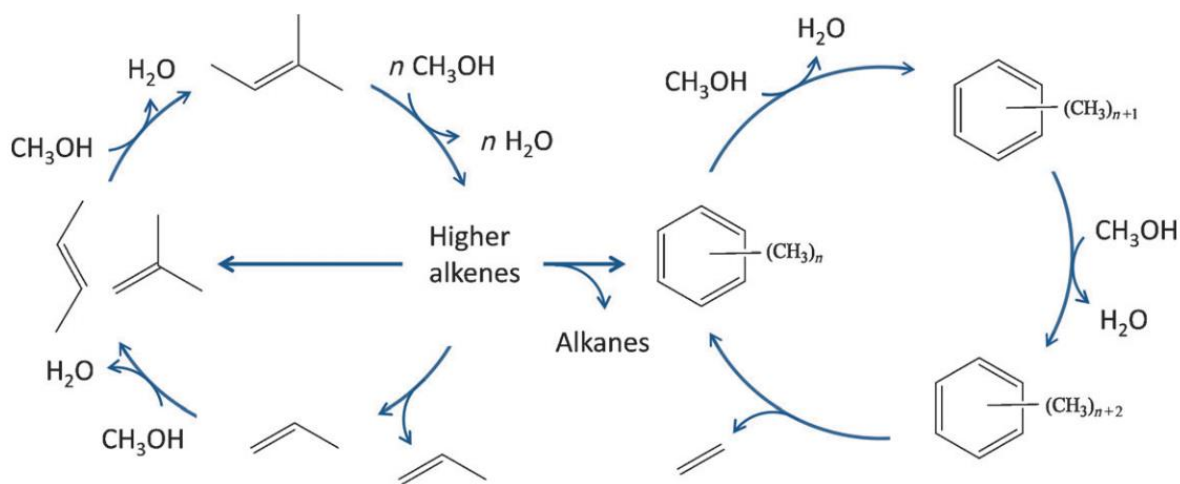


Figure 8. Dual-cycle mechanism of propene formation by higher alkene cracking (left) and ethene formation by re- and de-methylation of benzenes ring systems (right) by SVELLE et al., recreated from<sup>238</sup>.

A problem the MTO suffers heavily under is the deactivation due to extensive coke formation. With increasing time on stream and continuous re- and de-methylation of the benzene rings, possible side reactions can occur. This includes the formation of larger aromatics like methylated naphthalenes. Naphthalenes are still able to get methylated and to selectively produce the small olefins, however, their reactivity and conversion rate is severely reduced compared to the benzenes derivatives.<sup>243</sup> Furthermore, the naphthalene's increased space requirements hinders diffusion, blocks pore windows and acidic sites. The space restrictions due to the larger 2-ring aromatic are the reason propylene formation gets gradually suppressed, as they simply have not enough space inside the pore to form. A typical MTO product composition has its ethene selectivity increased over time due to the formation of larger carbonaceous residues inside the pore over time.<sup>244</sup> Eventually, the methylated naphthalenes turn to phenantrenes (3-ring aromatics) and, ultimately, pyrenes (4-ring aromatics). In the case of H-SAPO-34, the most prevalent MTO catalyst, pyrenes are the largest possible aromatics, which possibly fit inside the CHA cage and effectively blocking the whole pore, resulting in catalyst deactivation (deactivation phase).<sup>245</sup>

In conclusion, the aromatics (inner coke) formed inside the catalyst pores are both beneficial, as they work as catalysts and enhance selectivities over time, and destructive, as they massively hinder mass transport and methanol conversion when they grow too large. To prevent catalyst coking or the formation of larger aromatics, while improving the longevity of the



methylated benzene species the addition of hydrogen or steam to the methanol feed was successfully tested.<sup>246</sup>

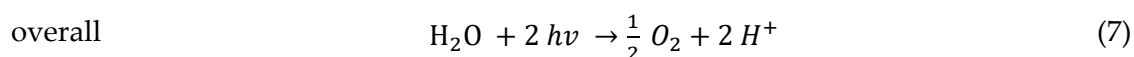
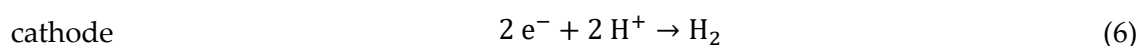
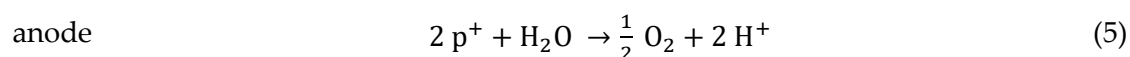
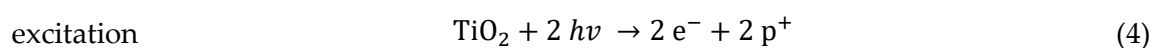
In commercialized MTO plants, fluidized bed reactors are partially used. Besides the aforementioned deactivation through coking, attrition becomes an additional concern.<sup>11</sup> In the other type of utilized reactor, the packed-bed reactor, an additional phenomena is occurring, known as the “Cigar Burn” mechanism, proposed by JAMES HAW and DAVID MARCUS in 2005.<sup>247</sup> The methanol conversion in packed-bed catalyst reactors is so high, that methanol immediately reacts when reaching to catalyst. Therefore, the reaction is performed in the first layer of SAPO particles in the catalyst bed until the first particles completely deactivate. The methanol then repeats the same procedure in the next layer of catalyst particles. This is in accordance with the formation of outer coke at the outside of the catalyst particles, which change their colour depending on the reaction phase: an H-SAPO-34 catalyst particles is white before the reaction. In the working phase the particle acquires a light yellow tone and turns brown in the transition to the deactivation phase. When the catalyst is deactivated, it has turned completely black. In-situ observations of this colour pattern in the MTO reaction, show similarities to a cigar burning down after ignition at the top.

Since the MTO reaction is a fairly new procedure, advancements are still made consistently. As the catalyst, H-SAPO-34 prevailed, as its CHA structure with a pore window diameter of 3.8 Å prevents diffusion from olefins larger than propylene and combines it with an acidity, that's lower than its zeolite variants, which is beneficial in the first reaction step with the formation of DME and H<sub>2</sub>O. The main focus on improving the process lays on postponing the point of deactivation through coking, catalyst reactivation, new synthesis methods, improved catalyst properties and post-synthesis functionalizations.<sup>11,199,248,249</sup> Since in nearly every reaction step water is produced as a side product, in situ water removal is an intruding possibility.

## 8. Photocatalytic water splitting

The demand for hydrogen will be rising for the foreseeable future, as the replacement of fossil fuel is inevitable due to their depleting available deposits. Even today the majority of the energy demand is covered with fossil fuels, but the urge for alternative energy carriers is intensifying. Hydrogen is an intruding option as it offers high energy conversion efficiencies,

abundance, green production and conversion reactions and a variety of storage and transport possibilities.<sup>250</sup> However, especially the hydrogen formation reactions often times lack efficiency, hence, almost 90% of hydrogen production is still based on fossil fuel conversion. The most environmentally friendly method is the water splitting to hydrogen and oxygen, which only makes up around 5% of the total worldwide hydrogen production. Water splitting can either be performed via electrolysis or skipping the step of electricity production and directly using (visible) light in photocatalysis.<sup>251</sup> The first demonstration of electrochemical photolysis of water was performed by AKIRA FUJISHIMA and KENICHI HONDA in their ground-breaking experiments in 1972 on a semiconducting TiO<sub>2</sub> electrode.<sup>252</sup> The reaction equations with a cell consisting of a TiO<sub>2</sub> (anode) and a platinum black electrode (cathode) are as follows:



The first step is the excitation of electrons in the n-type semiconductor TiO<sub>2</sub> through the bandgap of 3.2 eV which equals a wavelength of around 380 nm and the subsequent formation of holes in the valence band. Usually, the electron-hole pair immediately recombines, by using sacrificial agents and noble metals as cocatalysts, though, electron-hole formation can be partially trapped and the electrons are carried to the cathode generating an electric current. At the anode water is decomposed into oxygen and protons, with the protons generate gaseous hydrogen at the cathode.<sup>14</sup> The actual mechanism is much more complex and includes radical involvement.

To perform the water splitting, a potential lower than the H<sup>+</sup> reduction potential of 0 V vs NHE at pH = 0, at the bottom of the conduction band (where the electrons are located) and a potential higher than the H<sub>2</sub>O to O<sub>2</sub> oxidation (1.23 V vs NHE at pH = 0) at the top of the valence band (where the holes are located) are required. The ideal water splitting photocatalyst should possess a band gap larger than the needed 1.23 eV to include the whole redox potential of water. Unfortunately, at the same time the band gap should be kept as small as possible, as basic TiO<sub>2</sub> catalysts need ultraviolet light, to improve the absorption of as much visible light instead as possible. To adjust the performance of semiconductors, the delay of the recombination and efficiency of charge carrier transport to the surface, as well as the reaction rate of the

charges with surface adsorbed molecules are the most important research topics. Crystal structure and size, crystallinity, surface structure and area, as well as the type of cocatalysts all have influence on the photocatalytic performance of  $\text{TiO}_2$ .<sup>15</sup>

The choice of the cocatalyst is prioritised in recent research as it provides a straightforward option to influence to omnipresent  $\text{TiO}_2$  catalyst. The most promising results were shown with noble metals such as silver and gold. However, based on their high cost, alternative materials like copper are moved into focus. Copper offers similar benefits as gold and silver, as it is able to trap the electron and therefore providing an improved electron-hole separation, but the most active species  $\text{Cu}^0$  tend to oxidise to the less active  $\text{Cu}^{2+}$ , thus, stabilizing capping agents (e.g. carbon-based materials) where tested to improve the longevity of  $\text{Cu}^0$ .<sup>253</sup>

While only the hydrogen production is really necessary, with the abundance of oxygen, ideas shifted to use the holes in the  $\text{TiO}_2$  after excitation not for the formation of oxygen but for the degradation of organic molecules. Based on this, dual-functional hydrogen producing and organic chemical removing reactors from waste water are in the realm of possibility.<sup>254</sup> While those organic molecules sometimes possess strong carbon-halogen bonds, which makes them not only environmentally worrisome but also stable, aggressive methods for their decomposition are required. In the case of the photocatalysis, these are the highly reactive holes in the valence band or radicals, which are formed at otherwise mild reaction conditions. In this specific application zeolites have again found their way into usage in form of hybrid composite materials with  $\text{TiO}_2$ . They offer additional acidic catalyst sites and unique pore structures to improve the adsorption capacity of organic molecules and separation of electric carriers to improve the photocatalytic performance. However, the zeolite-based photocatalysts are still in the early stages of development with only a basic understanding of the degradation mechanisms at the aluminosilicates.<sup>255</sup>

## 9. Measurement setup and membrane separation principle

Figure 9 describes the for this work used membrane reactor and permeation setups.

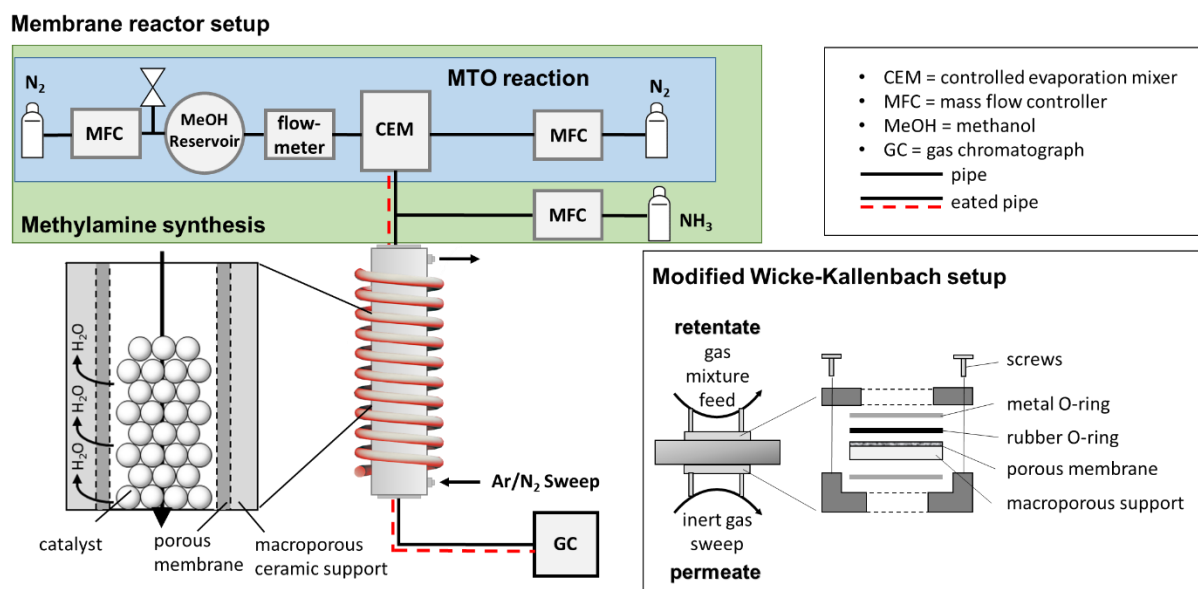


Figure 9. Scheme of the (left) used tubular membrane reactor for the membrane supported MTO and methylamine syntheses and (right) the used modified Wicke-Kallenbach setup.

### 9.1. Membrane separation

The performance of membranes in separation experiments can be determined via a few presentations, the ROBESON plot is one of them. First introduced by LLOYD M. ROBESON in 1991, it originally described the correlation between the selectivity  $\alpha$  and the permeance  $P$  or the permeability  $PE$  of polymer membranes for He/N<sub>2</sub> separation, but can be created for every membrane material and gas mixture. In separation experiments, a mixture of compounds (feed) is led to the membrane, where it partially diffuses through the membrane. The components, which get withhold are called the retentate, while everything diffusing through the membrane is labelled permeate. On the permeate side often times a sweep gas is applied to guide the gas mixture away from the membrane to the respective measurement system. However, the sweep gas can influence the permeation through the membrane in two ways:

- A beneficial way: by carrying away the permeated gas it prevents accumulation on the permeate side and maintains a steep gradient-driven diffusion, either induced

by the concentration gradient after the FICK model or by the chemical potential gradient after the MAXWELL-STEFAN model.<sup>256</sup>

- (ii) An adverse way: by promoting counter-diffusion effects from the permeate back to the original retentate side and, thus, affect the sensitive permeation results.

To calculate the most important factors in gas separation, the permeance, the flux  $J$  (amount of permeated gas  $n$  divided by the membrane area  $A$  and the time  $t$ ) is divided by the pressure differences between retentate and permeate side. For the permeability, the thickness of the membrane  $d$  is taken into account, see equations (8)-(10).

$$J = \frac{n}{t \cdot A} \quad (8) \quad P = \frac{n}{t \cdot A \cdot \Delta p} \quad (9) \quad PE = \frac{n \cdot d}{t \cdot A \cdot \Delta p} \quad (10)$$

The selectivity or separation factor  $\alpha$  is an indicator of how well the membrane separates gases of a binary mixture with the components a and b, as it shows the molar ratios of the respective gas of the permeate and of the retentate, see equation (11).

$$\alpha = \frac{n_{a,\text{permeate}}/n_{b,\text{permeate}}}{n_{a,\text{retentate}}/n_{b,\text{retentate}}} \quad (11)$$

In the aforementioned ROBESON plot the permeability of one component from a binary mixture is shown against the separation factor. From the plot, the observation is derived that the higher the permeability is, the lower the separation factor gets. The plot gets constantly revised and offers a benchmark for state-of-the-art membrane technologies.<sup>257</sup>

To measure the ideal surface diffusion values of CO<sub>2</sub> at activated carbon, WICKE and KALLENBACH created the eponymous setup in 1941. It required isobaric conditions while applying a binary gas mixture of N<sub>2</sub>/CO<sub>2</sub> as the feed and a N<sub>2</sub> stream on the permeate side to transport permeated CO<sub>2</sub> away.<sup>258</sup> The general setup is still used today for permeation measurements, but is usually labelled a modified WICKE-KALLENBACH setup by applying pressure on the feed side to create another gradient that further promotes permeation besides the concentration/chemical potential.<sup>259</sup>

The diffusion mechanism is heavily depending on the membrane material and the feed gas components. Generally, it can be stated that the permeation follows an adsorption-diffusion-desorption mechanism<sup>260</sup>:

- (i) adsorption to the membrane surface on the retentate side
- (ii) surface diffusion on the membrane to the pore
- (iii) diffusion through the pore system
- (iv) diffusion to the membrane surface on the permeate side
- (v) desorption from the membrane surface

Only in pure molecular sieving no adsorption occurs and influences the permeation, however, these systems are rarely relevant. The interaction between adsorption and diffusion determines the separation quality of the membrane material, but already in binary mixtures calculations to predict the permeation behaviour get exceedingly difficult due to the increasing numbers of interactions between the components itself and the membrane. Calculating live reaction composition in our examined catalytic membrane reactors is nearly impossible because of the large number of intermediates and components.

The diffusion itself is determined by the membrane material and its interactions with the gaseous components. There are five main mechanisms:

- (i) **KNUDSEN diffusion.** In most mesoporous materials **KNUDSEN** diffusion is the main mechanism, as it occurs when the mean free path in **BROWNIAN** motion is larger than the pore diameter. Conclusively, the molecules rather collide with the pore walls than with each other. The shape of the porous system plays a significant role in **KNUDSEN** diffusion, the **KNUDSEN** diffusion factor is thereby in inverse proportion to the square root of the components molecular weight.<sup>261</sup>
- (ii) **Surface diffusion.** If one component is strongly adsorbed to the pore surface, surface diffusion can improve the permeance of the respective molecule. It is depending mostly on the potential gradient and especially relevant at lower temperatures as adsorption strength is at its highest.<sup>262</sup>

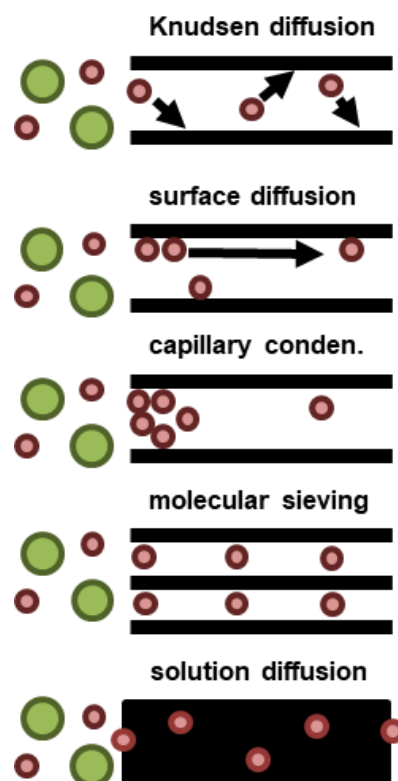


Figure 10. Schematic overview of diffusion mechanism through membranes.

- (iii) Capillary condensation. Specific occurrence when monolayer adsorption is surpassed in the membrane pores and the molecules are separated from the gas phase to dissolve as the condensate, which impedes diffusion.<sup>263</sup>
- (iv) Molecular sieving. Excluding molecules purely based on their size rarely occurs, since adsorption effects and molecule interactions almost always are observed in addition.<sup>264</sup>
- (v) Solution diffusion. Is important solely in dense membranes without real pore systems, where the compounds have to dissolve in the membrane.<sup>265</sup> Examples are the selective diffusion of hydrogen through dense Pd membranes and the diffusion through polymers.<sup>98,266</sup>

The real diffusion in specific membrane systems is presumably a combination of several diffusion mechanisms.

## 9.2. Quantities in catalysis

In catalysis, there are three terms to describe the quality of the reaction:

- (i) Conversion ( $X$ ) is the ratio of the converted reactant  $r$  to the originally provided reactant (equation (12)).

$$X_r = \frac{n_{r,0} - n_r}{n_{r,0}} \quad (12)$$

- (ii) Selectivity ( $S$ ) is the ratio of a specific formed product  $p$  in relation to all of the converted reactant under consideration of the stoichiometric coefficients  $\nu$  (equation (13)).

$$S_p = \frac{n_p}{n_{r,0} - n_r} \cdot \frac{-\nu_r}{\nu_p} \quad (13)$$

- (iii) Yield ( $Y$ ) is the ratio of a specific formed product in relation to the amount of originally provided reactant under consideration stoichiometric coefficients  $\nu$  (equation (14)).

$$Y_p = \frac{n_p}{n_{e,0}} \cdot \frac{-\nu_r}{\nu_p} \quad (14)$$

To describe the correlation in heterogeneous catalysis between amount of catalyst needed for a specific reactant flow, the weight hourly space velocity (WHSV), which is defined as the weight of a specific feed component per catalyst weight per hour. It gives a value for how much catalyst is needed to give similar results. An example in this work is that certain reactions require a large amount of acidic sites. The H-SAPO-34 has less acidic sites than its

isostructural counterpart H-SSZ-13. Therefore, in some reactions, more H-SAPO-34 is needed to provide the same number of catalytic sites, resulting in a lower WHSV value. The inverse of the WHSV is the contact time, which evaluates how much time the reactant spends in contact with the catalyst. Controlling the contact times can provide changes in the reaction outcome.<sup>267</sup>

In heterogeneous catalysis, there are two main reaction/adsorption mechanisms: LANGMUIR-HINSHELWOOD and ELEY-RIDEAL.<sup>268</sup>



This reaction mechanism requires two adsorption sites for both reactants to adsorb to the catalyst surface. Through surface diffusion they are brought into contact, as they occupy two adjacent sites.



In this mechanism only one of the reactants needs to adsorb to the surface, the other reactant is able to react with the bonded component from the gas phase. However, ELEY-RIDEAL transition states are generally bulkier than their LANGMUIR-HINSHELWOOD counterparts.

It is generally accepted that most heterogeneous catalytic reactions are performed after the LANGMUIR-HINSHELWOOD mechanism. Only a few reactions in specific circumstances use the ELEY-RIDEAL mechanism, for example when catalysts lack a high number of adjacent catalytic sites.<sup>229</sup> Interestingly enough, even though the LANGMUIR-HINSHELWOOD mechanism is the usually preferred one, it has a higher energy barrier to overcome. As two reactants are adsorbed, the reactant-catalyst bond strength is initially higher for the LANGMUIR-HINSHELWOOD mechanism compared for the same system in the ELEY-RIDEAL mechanism. In the oxidation of CO on a Pt catalyst, it was shown that CO preferred the adsorption on the catalyst surface over entering the ELEY-RIDEAL transition state. Therefore, after the CO adsorption, there is no further opportunity for attempting the ELEY-RIDEAL mechanism, as the desorption energy is higher than the energy barrier for the LANGMUIR-HINSHELWOOD reaction.<sup>269</sup> This principle can be applied on various heterogeneous catalytic reactions.



## 10. Published results

### 10.1. Methanol-to-Olefins in a Membrane Reactor with in Situ Steam Removal – The Decisive Role of Coking

The original idea of this publication was to apply the idea of a water removing zeolite membrane in a heterogeneous catalytic reaction besides the already established FISCHER-TROPSCH synthesis. However, vastly different reaction parameters and problems of the MTO reaction made the outcome difficult to predict. It was originally predicted that the water removal may improve the stability of the used catalyst H-SAPO-34, as it is vulnerable to hydrothermal damaging. On the other hand, it was feared that the addition of the zeolite membrane led to a further aggravation of the coking problems the MTO reaction possesses, as normally water is even added to the feed, because it slows down the coking of the catalyst bed. The experiments were performed based on an idea of Prof. Dr. Jürgen Caro and were part of the later mentioned DFG project.

In this study, my part was conducting the MTO catalysis experiments, as well as performing XRD and SEM measurements. Furthermore, I carried out most of the measurement analysis of GC, GC-MS, XRD, SEM and TG/DTA and wrote the majority of the manuscript. The necessary zeolite, in this study zeolite A or LTA, membranes were provided by the Fraunhofer Institute for Ceramic Technologies and Systems led by Dr. Hannes Richter.

## Methanol-to-Olefins in a Membrane Reactor with in situ Steam Removal – The Decisive Role of Coking

Felix Rieck genannt Best,<sup>\*,[a]</sup> Alexander Mundstock,<sup>[a]</sup> Gerald Dräger,<sup>[b]</sup> Pascal Rusch,<sup>[a]</sup> Nadja C. Bigall,<sup>[a]</sup> Hannes Richter,<sup>[c]</sup> and Jürgen Caro<sup>\*,[a]</sup>

The reaction of methanol to light olefins and water (MTO) was studied in a fixed bed tubular membrane reactor using commercial SAPO-34 catalyst. In the fixed bed reactor without membrane support, the MTO reaction collapsed after 3 h time on stream. However, if the reaction by-product steam is in situ extracted from the reactor through a hydrophilic tubular LTA membrane, the reactor produces long-term stable about 60% ethene and 10% propene. It is shown that the reason for the

superior performance of the membrane-assisted reactor is not the prevention of catalyst damage caused by steam but the influence of the water removal on the formation of different carbonaceous residues inside the SAPO-34 cages. Catalytically beneficial methylated 1 or 2 ring aromatics have been found in a higher percentage in the MTO reaction with a water removal membrane compared to the MTO reaction without membrane support.

### Introduction

The majority of light olefins as the basic of our today's chemical industry is produced via steam cracking. Increasingly, alternative ways of light olefin formation are studied.<sup>[1–3]</sup> The methanol-to-olefins (MTO) process, which is based on the catalytic conversion of methanol to light olefins and water, offers a new and eco-friendly synthesis route. Methanol as the feedstock can be easily produced by catalytic conversion of synthesis gas, which is usually provided by methane (natural or biogas) steam reforming and/or partial oxidation as well as directly from coal. Different acidic molecular sieve catalysts like zeolites or aluminum phosphates such as SAPO-34,<sup>[4]</sup> ZSM-5<sup>[5]</sup> or ZSM-22<sup>[6]</sup> have been evaluated in the MTO process and show decent selectivities towards the light olefins ethene and propene. Alkenes with higher molecular weights, methane and other paraffins are the main by-products of the MTO reaction. However, the product composition heavily depends on the

reaction parameters like particle sizes, temperature, time on stream (TOS) and catalyst cage dimensions.<sup>[7–11]</sup> The exact mechanism, in particular the forming of the first C–C bond from methanol, is still subject of uncertainty. Dahl et al. first introduced the mechanism of the hydrocarbon pool (HCP) in 1993,<sup>[12]</sup> which is researched extensively and extended since.<sup>[13–17]</sup> Several studies led to the conclusion that aromatic species in the HCP take part in the formation of light olefins due to de- and re-alkylation of the aromatic rings rather than by direct dimerization of methanol. MTO as an autocatalytic reaction is fueled by the formation of those beneficial aromatics in the HCP, which leads to an increased methanol conversion.<sup>[18]</sup> However, these aromatics which are necessary for the MTO, transform with increasing TOS into more complex carbon residues called coke, resulting in a varying product selectivity over time and ultimately leads to a breakdown of the MTO due to pore blocking.<sup>[14,19]</sup>

The application of ceramic membranes for in-situ water removal was already considered for different reactions like the hydrogenation of CO<sub>2</sub><sup>[20]</sup> or pervaporation-assisted esterification,<sup>[21]</sup> mainly due to the increased conversion and changing product distribution caused by the water removal induced reaction equilibrium shift. However, in the case of the MTO reaction, the by-product water could damage the catalyst hydrothermally as well.

As mentioned above, coking of the catalyst is a severe problem of the MTO process since it leads to pore blocking of the catalyst and severe diffusion problems.<sup>[22–27]</sup> Literature reports that the presence of steam in the feed should reduce catalyst coking, thus extending its lifetime.<sup>[28–31]</sup>

The industrial application of the MTO reaction, a fluidized bed reactor, suffers heavily from attrition and requires the permanent exchange of the catalyst. In the used membrane reactor with fixed catalyst bed, the attrition problems are not existent, but the catalyst regeneration is more complex compared to the fluidized bed reactor.

[a] F. Rieck genannt Best, A. Mundstock, P. Rusch, Prof. N. C. Bigall, Prof. J. Caro  
Institute for Physical Chemistry and Electrochemistry  
Leibniz University Hannover  
Callinstr. 3 A  
Hannover 30167 (Germany)  
E-mail: felix.best@pci.uni-hannover.de  
juergen.caro@pci.uni-hannover.de

[b] Dr. G. Dräger  
Institute for Organic Chemistry  
Leibniz University Hannover  
Schneiderberg 1B  
Hannover 30167 (Germany)

[c] Dr. H. Richter  
Institute for Ceramic Technologies and Systems  
Fraunhofer IKTS  
Michael-Faraday-Straße 1  
Hermsdorf 07629 (Germany)

Supporting information for this article is available on the WWW under <https://doi.org/10.1002/cctc.201901222>

© 2019 The Authors. Published by Wiley-VCH Verlag GmbH & Co. KGaA. This is an open access article under the terms of the Creative Commons Attribution License, which permits use, distribution and reproduction in any medium, provided the original work is properly cited.

## Results and Discussion

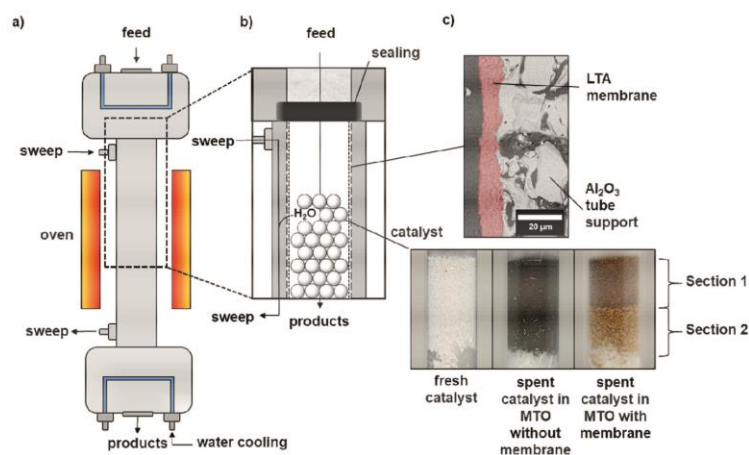
To further influence yield, selectivity and longevity of the catalyst and compare it with state of the art processes, we performed the MTO reaction in a membrane reactor with a SAPO-34 packed bed catalyst, as shown in Figure 1. We have used the commercial SAPO-34 catalyst developed for the MTO process by the Dalian Institute of Chemical Physics (DICP), which is described in detail elsewhere.<sup>[32–34]</sup> In this paper, we have studied the influence of an in situ water removal through a hydrophilic membrane on the MTO reaction. The reaction is supported by a semi-commercial hydrophilic Linde Type A (LTA) zeolite membrane, produced by the Fraunhofer IKTS Hermsdorf.<sup>[35]</sup> The LTA membrane layer was grown on a tubular  $\alpha$ -Al<sub>2</sub>O<sub>3</sub> support, to remove water in situ from the reaction environment.

Figure 1 a and b show the used membrane reactor setup. The MTO reaction was performed at 450 °C for 250 minutes (i) without a membrane and (ii) with in situ water removal through a tubular LTA membrane. The SAPO-34 catalyst was piled on glass wool in the vertically oriented reactor. The SAPO-34 catalyst changes its color from white in the beginning to black and brown as a result of the formation of high molecular weight hydrocarbon species inside the SAPO-34 pores, often referred to as coke (Figure 1 c). However, while the catalyst without membrane support turns completely black, the SAPO-34 catalyst bed, under in situ water removal through the LTA membrane, shows two sharply separated sections of different colors: A dark brown zone towards the reactor inlet, called Section 1, and a light brown zone in the direction of the reactor outlet, called Section 2. Later in this paper, we will analyze the carbonaceous depositions of these sections in detail. The main products (ethene, propene and methane) of the MTO reaction

as well as non-converted methanol, as determined by gas chromatography, are shown in Figure 2.

The MTO reaction on SAPO-34 without membrane support exhibits changing product selectivity during the reaction and a significant deactivation of the catalyst after 180 minutes. The desired main products ethene (after 120 min) and propene (100 min) reach maxima in their selectivity at different points during the active period. Simultaneously, the conversion of methanol decreases and the concentration of methane strongly increases. On the other hand, the MTO reaction under continuous water removal through a LTA membrane shows a constant productivity of ethene, propene and methane over 250 minutes, without major fluctuations of the product concentrations. This is surprising, since we expected a decrease in the catalyst longevity due to the water removal. The reaction rate remains high, shown by the consistent low amount of unreacted methanol. The yield of light olefins does not exhibit any significant differences between the two measurement setups with and without membrane support. Compared to literature<sup>[32]</sup> we received similar results for an almost 100% methanol conversion. Our DICP-SAPO-34 catalyst shows an exceptional high selectivity towards ethene, while the selectivity for propene and higher molecular alkenes is low. However, the product composition also depends, as mentioned above, on such experimental parameters like particle size and shape, reaction temperature, type of reactor and more. The LTA membrane itself without the SAPO-34 catalyst showed almost no catalytic activity towards the MTO reaction.

A possible reason for the breakdown of the MTO reaction in the packed bed reactor without membrane support could be the hydrothermal damage of the SAPO-34 catalyst due to steam. However, in our case the chabazite (CHA) crystal structure of SAPO-34 stayed intact during the MTO reaction, as



**Figure 1.** a) Membrane reactor setup for the MTO reaction at 450 °C. b) Magnification of the reactor inlet with the fixed bed of the SAPO-34 catalyst (particle size 10 to 100  $\mu\text{m}$ ) inside the tubular LTA membrane. c) Cross section SEM image of LTA membrane on tubular  $\alpha$ -Al<sub>2</sub>O<sub>3</sub> support and photos of the fresh SAPO-34 catalyst, the spent catalyst after 250 min MTO reaction without membrane and the catalyst in the membrane reactor with water removal through the LTA tube membrane. Note that in case of the membrane supported MTO reaction, there is a sharp step in the color of the SAPO-34 catalyst bed.

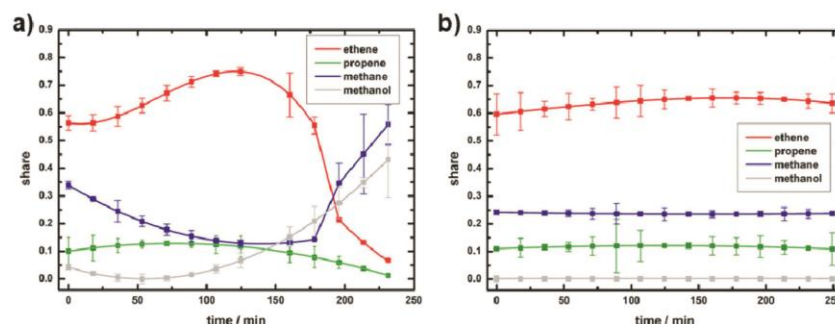


**Figure 2.** Development of the products (ethene, propene and methane) and non-converted methanol in the MTO reaction at 450 °C over 250 minutes: a) without and b) supported by a LTA membrane.

well as after regeneration by coke combustion in synthetic air at 500 °C, as the X-ray diffraction patterns show (see SI Figure S1). The coked catalysts show a slight shift to lower diffraction angles compared to the fresh SAPO-34 catalyst, indicating an expansion of the lattice due to the formation of larger hydrocarbon species inside the pores of the SAPO-34. Therefore, the reason for the collapse of the MTO reaction after 3 h in the packed bed without membrane support seems to be solely the coking. The used SAPO-34 is a silicoaluminophosphate of the CHA structure with  $6.5 \times 11$  Å cages, connected through narrow  $3.8 \times 3.8$  Å windows, consisting of 8-membered oxygen rings, resulting in a 3D pore system.<sup>[36,37]</sup> The used catalyst has a reported acid density of 0.81 mmol/g.<sup>[34]</sup> The different methanol reactions at the acidic sites will not only form light olefins but also a variety of high molecular weight hydrocarbon species in the pore system. Their formation and influence inside the pores of different acidic catalysts and their participation in the MTO reaction is a widely researched topic.<sup>[8,15,17,22,24,36,38]</sup>

The induction period, starting with empty SAPO cages, is characterized by the sluggish kinetics of the formation of the first C–C bonds from methanol.<sup>[39,40]</sup> Eventually, they will transform into polymethylbenzenes inside the zeolite cages. The ongoing reaction of methanol ensures a high share of

polymethylbenzenes with a high number of methyl groups (initiation phase). Studies with  $^{13}\text{C}$ -labeled methanol showed the direct participation of the polymethylbenzenes in the formation of light olefins.<sup>[41]</sup> The selective conversion of methanol to light olefins is set to take place in the so-called working phase. It is assumed that in the working phase the penta- and hexamethylated arenes split off small alkenes, and turn into di- and trimethylated arenes. The re-methylation and de-alkylation of arenes is the essential mechanism of the light olefins formation.<sup>[14,42]</sup> The beneficial effects of the, in the MTO reaction participating, hydrocarbons recently led to the intentional and controlled formation prior to the reaction by “precoking”, which results in an enhanced ethene selectivity.<sup>[43]</sup> However, with increasing TOS, the carbon species in the zeolite cages will build up and transform into naphthalenes, then phenanthrenes and ultimately pyrenes, the largest hydrocarbon species which will fit into the SAPO-34 CHA cages. The space requirements of the most common hydrocarbons in the CHA cages of SAPO-34 are schematically shown in Figure 3. The larger ones block the pores and acidic sites, resulting in a severely hindered mass transport (deactivated phase).<sup>[22,44]</sup> The medium sized aromatics in the cages lead to an improved light olefins formation in the initial TOS. Furthermore, the inherent structure of SAPO-34 with its small windows prevents the

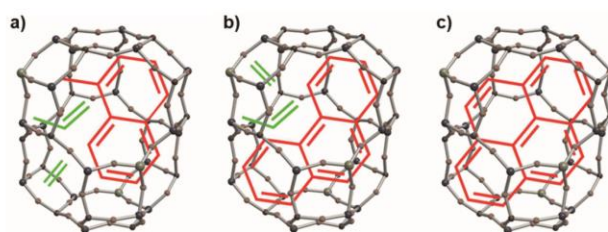


**Figure 3.** Schematic representation of the space requirements of the most common hydrocarbon species (see Figure 7) in a SAPO-34 CHA cage, which build up in the course of the MTO reaction (red): a) methyl naphthalene, b) phenanthrene and c) pyrene. For the sake of comparison, the space requirements of the main products ethene and propene are shown (green), where they still fit additionally into the cage.

diffusion of the arenes, as well as larger alkenes, enhancing the selectivity towards the light olefins even further.

Surprisingly, the different thermogravimetric (TG) profiles (Figure 4) show similar contents of carbonaceous residues in the spent SAPO-34 catalysts without and with membrane support (Sections 1 and 2, see Figure 1) of around 9% (Table 1). However, the peaks in the differential thermal analysis (DTA) curves reflect different types of high molecular hydrocarbon species formed during the MTO reaction inside the SAPO-34 CHA cages, indicating different stages of coking. The first type of hydrocarbon species formed is attributed to methylated benzene or naphthalene. Their decomposition temperature ranges between 400 °C and 500 °C. The DTA profile of Section 2 of the SAPO-34 catalyst with the LTA membrane indicates a large presence of these types of hydrocarbons. Higher condensed and bulkier polyaromatics, combust at temperatures higher than 500 °C, peaking above 550 °C.<sup>[24,38]</sup> All types of catalyst (without and with LTA membrane Sections 1 and 2) have local maxima in the DTA curves at 600 °C (see dotted line, Figure 4) suggesting the existence of polyaromatics in all cases. Due to the observation that the catalyst without membrane support has a lower heat flow in the range between 400 and

500 °C, the percentage of larger polyaromatics is therefore higher compared to the catalysts + membrane.

The coking of the catalysts can additionally be seen by the decrease of the surface area, which was measured via BET nitrogen adsorption at 77.4 K. The results are summarized in Table 1. Due to the coke deposition, the surface area of SAPO-34 without membrane was reduced by an order of magnitude compared to the fresh catalyst. However, in the case of membrane support, the reduction of the BET surface for similar coke contents is less severe. Though the BET surface areas of the coked SAPO-34 from Sections 1 and 2 are very similar, they are still a third larger compared to the catalyst without membrane. By coke combustion, the surface area can be regenerated almost entirely, showing furthermore that there is no structural damage of the CHA structure due to the steam during the MTO reaction. Figure 5 displays the carbon balances of the two MTO reaction, indicating to which carbonaceous compound the carbon from the methanol source reacted. It summarizes the accumulated product over the whole 250 minutes of reaction time and gives similar results for the reaction with and without a LTA membrane. The course of the reaction, though, is more linear for the reaction with a LTA membrane, while the product composition of the MTO reaction without membrane fluctuates more (compare Figure 2).

For the most important points of the characteristic reaction course of the MTO reaction without membrane, we provide a similar study in the SI (Figure S4). The addition of an LTA membrane to the MTO reaction has no significant influence on the product composition after our defined reaction time of 250 minutes, as in both cases around 70% of the carbon from the methanol reacts to ethene. However, the MTO reaction with the LTA membrane still works with the same efficiency, while the MTO reaction without membrane support collapsed. While the ethene yield of the membrane supported reaction should stay on the same level for even longer reaction times, the share of ethene without membrane support decreases due to the increasing amount of unreacted methanol. Moreover, the amount of carbon which reacts to the aforementioned carbon residues is slightly higher for the MTO reaction without

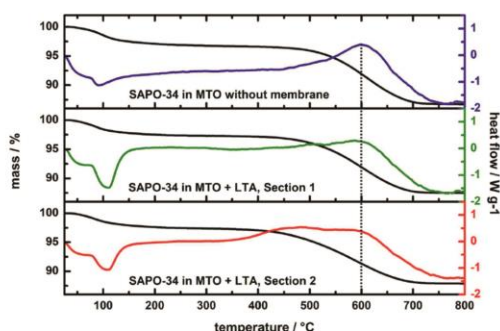


**Figure 4.** Thermogravimetry (black) and differential thermal analysis (colored) profiles of spent SAPO-34 catalysts in a temperature range of 25 °C to 800 °C.

**Table 1.** Mass loss due to carbon combustion in TG, decomposition temperatures of the high molecular hydrocarbon deposits (coke) in SAPO-34 catalysts and BET surface area of fresh, coked and regenerated SAPO-34, measured by nitrogen adsorption at 77 K. Coked samples after 250 minutes time on stream.

sample name	mass loss in carbon combustion step [%]	carbon combustion temp. [°C]	BET surface area [m <sup>2</sup> g <sup>-1</sup> ]
SAPO-34	–	–	314.8
SAPO-34 in MTO without membrane	9.3	539.8	31.1
SAPO-34 in MTO + LTA, Section 1	9.1	529.1	45.2
SAPO-34 in MTO + LTA, Section 2	9.0	488.5	46.4
SAPO-34 in MTO after coke combustion	–	–	301.6

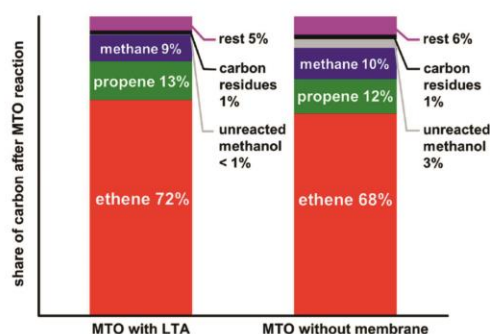


**Figure 5.** C-balance: Share of carbon after performing the MTO reaction over the whole 250 minutes of reaction time with and without a water removal membrane.

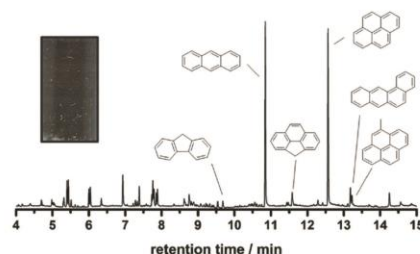
membrane, but is located at around 1% in both cases, see Figure 4 as well.

Figure 6 a) shows a SEM image of a spherical SAPO-34 grain after the MTO reaction. The carbon content of a broken SAPO-34 particle was determined via line scan EDXS (Figure 6 b) along the particle cross section. The results show that the amount of residual carbon inside the grain is dispersed relatively even over the whole particle. Subsequently, this shows again that the hydrocarbon species mainly form inside the catalyst and their desorption is heavily restricted by the small windows of the SAPO-34 structure.

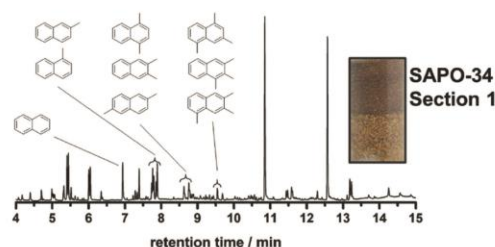
For the detailed characterization of the carbonaceous deposits (coke), gas chromatography-mass spectrometry coupling (GC-MS) has been applied. Therefore, a slightly modified extraction method, first introduced by Guisnet et al. was used to recover the confined hydrocarbon species from the SAPO-34 cages.<sup>[45]</sup> 15 mg of the spent catalyst were dissolved in 1.5 mL of 15% HF. The organic compounds have been extracted with *n*-hexane from the acidic solution. Subsequently, the analysis of the organic phase was carried out by GC-MS, detailed information can be found in the supporting information. The analysis of the three types of spent catalysts (without membrane and with LTA membrane support Sections 1 and 2) are shown in Figure 7, the relative shares of the most common hydrocarbon species are summarized in Table 2. It becomes apparent that the three spent catalysts represent different stages of the MTO reaction. After 250 minutes of MTO reaction, the hydrocarbon species in the SAPO-34 catalyst without membrane consists of over 55% of bulky polyaromatics, like phenanthrene and pyrene. These large hydrocarbons block the pores and the catalytic active acidic sites, hinder diffusion and are responsible for the deactivation of the catalyst. These high molecular weight deposits explain the relative high combustion temperature in the TG profiles (Figure 4), as well as the low yield of light olefins after 250 minutes in the MTO reaction (Figure 2 a).

The GC-MS results of section 1 of the SAPO-34 catalyst with the membrane show a similar carbon composition like the catalyst without membrane support. However, the share of phenanthrene, anthracene and pyrene is only 43%, the share of the medium sized aromatics, like methylated benzenes and naphthalene is therefore higher, compared to the catalyst

### a) SAPO-34 MTO



### b) SAPO-34 MTO + LTA Section 1



### c) SAPO-34 MTO + LTA Section 2

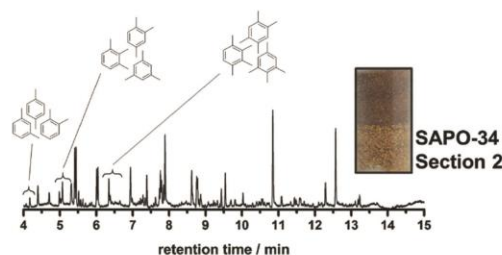


Figure 7. Gas chromatograms of retained hydrocarbon species in the CHA pores and/or deposited inside the catalyst grain of spent SAPO-34 catalyst after 250 min in the MTO reaction at 450 °C: a) from the catalyst without membrane, b) from Section 1 and c) Section 2 of the catalyst with membrane-support.

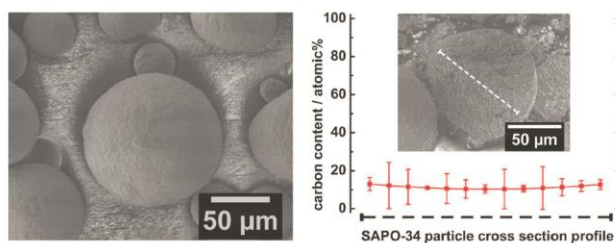


Figure 6. SEM pictures of coked SAPO-34 catalyst after 250 min in MTO reaction at 450 °C. The particle size ranges between 10 and 100 μm, the individual SAPO-34 crystal size is between 0.5 and 5 μm. Left: Outer surface of the spherical catalyst grain. Right: Coke content inside the broken SAPO-34 particle according to EDXS. Inset: SEM image of broken SAPO-34 particle, the direction of EDXS line scan path is shown (dotted line).

**Table 2.** Share of the most common retained high molecular hydrocarbon deposits in the CHA pores and/or inside the catalyst SAPO-34 grains after 250 minutes time on stream.

hydrocarbon species	SAPO-34 in MTO without membrane	SAPO-34 in MTO + LTA, Section 1	SAPO-34 in MTO + LTA, Section 2
methylated benzenes	6.6%	11.5%	20.7%
naphthalene	6.6%	7.5%	9.3%
methylated naphthalenes	16.2%	21.6%	36.9%
phenanthrene/anthracene	30.8%	24.4%	15.8%
pyrene	24.6%	18.9%	10.7%

without membrane. These medium sized aromatics do not hinder the diffusion of educts/products as much and can participate in the conversion of methanol to light olefins. While the SAPO-34 catalyst without membrane is deactivated after 250 minutes, the catalyst in the membrane reactor is still active. Due to the presence of a high concentration of methylated benzenes and naphthalenes in Section 1 of the SAPO-34 bed, we assume that this part of the bed membrane is still partially active. Section 2 of the bed has an even lower content of about 25% of the bulky polyaromatic coke, while most of the hydrocarbon species are present as methylated smaller aromatics. Section 2 is, due to the high share of catalytically active hydrocarbon species, mainly working in the MTO reaction. The color changes of the catalyst are not necessarily connected to the contained aromatics, since the residues are all either colorless or light yellow. The different colors are the reason, why we decided to split the catalyst with membrane support into two sections in the first place and most likely stem from external coke, which does not play a significant role in the deactivation of the MTO reaction compared to the internal coke (hydrocarbon residues inside the SAPO-34 pores).<sup>[11]</sup>

To further understand these findings, including the formation of the different Sections 1 and 2 of the catalyst bed inside the tubular LTA membrane, comparisons to existing models are required. Haw and Marcus proposed in 2005 a "cigar burn" mechanism to describe the development of the product selectivity of the MTO reaction in a SAPO-34 catalyst bed, which is comparable to our approach of a membrane reactor with a packed catalyst bed.<sup>[42]</sup> The reaction primarily takes place at the point where the methanol hits the catalyst first due to the high conversion rate of SAPO-34.<sup>[24]</sup> Consequently, the catalytically working zone (with methylated benzenes and naphthalenes) moves through the catalyst bed and leaves the deactivated catalyst (CHA cages completely occupied by pyrenes) behind. In our case, this working phase seems to be stabilized due to the water removal. We assume that this removal supports such reactions as the formation of the first C–C-bonds and the methylation of aromatics, as Le Chatelier's principle would predict.

The formation of the first C–C-bonds and, more importantly, the formation of the hydrocarbons from the HCP is more focused on the top of the moving working phase, whereas the

aromatics inside the cages in the experiment without a membrane are more spread across the whole catalyst bed. As the catalyst bed inside the tubular LTA membrane developed two distinctive different sections, with different species of the carbonaceous deposits, the working phase is possibly a much narrower layer. Moreover, the methanol conversion rate stays high as well, due to the high amount of still active catalyst. On the contrary, the olefin production of the SAPO-34 catalyst without membrane support changes during the reaction (Figure 2 a). First, it increases passing a maximum after 2 h and collapses after 3 h. Two mechanisms could cause this deactivation of the bed: (i) There is a homogeneous poisoning of the bed by coke, or (ii) an active zone like in the cigar burn mechanism moves faster, layer after layer, through the catalyst bed. The selectivity towards ethene increases with time caused by the formation of larger hydrocarbon species, due to steric limitations. The subsequent formation of even larger and bulkier hydrocarbons (coke) soon afterwards leads to the definite deactivation of the catalyst bed.

Improving selectivity and longevity of the MTO catalyst is a challenge to date. Control of the chemical composition of hydrocarbon deposits seems to be the key to fulfil this task, either by controlled preformation ("precoking")<sup>[93]</sup> or the influence of in-situ methods like the shown continuous water removal through the LTA membrane.

Literature reports the beneficial impact of adding water to the feed on the longevity of the catalyst.<sup>[28–31,34]</sup> These reports show a massive decrease in coke deposition due to the addition of water. In our experiment with similar reaction parameters, except for the addition of the LTA membrane, the removal of water also effects the longevity of the SAPO-34 catalyst positively since – with the same amount of high-molecular deposits as found by TG – in the case of the membrane reactor with steam removal these residues mainly consist of multi-methylated benzenes. These methylated benzenes are believed to be active in the MTO reaction since they act as the main reaction intermediate, which will form ethylene by de-alkylation as shown in.<sup>[11]</sup> While the addition of water to the feed decreases the overall amount of coke produced, the removal of water primarily influences the composition.

We found that all types of post-reaction catalyst (with and without membrane support) contain a similar amount of carbonaceous deposits, but their composition differs severely, even after they converted very similar amounts methanol to light olefins. Therefore, we conclude that the water removal seems to stabilize the catalytic active species (like methylated benzenes) longer, compared to the catalyst without membrane support. We believe the main reason is the assistance of the alkylation of the aromatics rings, where water is split off and can be immediately removed by the LTA membrane. Due to this equilibrium shift re-alkylation and de-alkylation may be favored compared to the condensation of the deposits to larger aromatic multi-ring systems. This would maintain the catalytic active phase longer and explain why this phase moved slower through the catalyst bed. Furthermore, water removal could benefit the re-alkylation of the larger aromatic rings (like naphthalene and phenanthrene) as well, leading to a possibly

increased participation of these larger aromatics in the formation of light olefins.

The product composition and development of the MTO reaction is influenced by a variety of reaction and material parameters, in particular the reactor type, the reaction temperature, the feed and sweep gas flow. Obviously, the catalyst type, the bulk density and its form and particle and crystal size distribution play the biggest role. We maintained these parameters for all of our experiments except for the addition of the LTA tube membrane, which conclusively led to the change of the carbonaceous deposits composition and the enhanced catalyst lifetime.

## Conclusions

We demonstrated the positive influence of removing water through an LTA zeolite membrane from a SAPO-34 catalyst bed during MTO reaction in a tube membrane reactor. While the SAPO 34 catalyst without membrane deactivates after 3 hours, the SAPO 34 catalyst in combination with a water removing membrane maintains a steady conversion rate and selectivity over more than 4 hours. Thermogravimetry and GC-MS confirmed that the reason for the collapse of the SAPO-34 catalyst without membrane support is the pore blocking due to high molecular weight polyaromatics such as phenanthrene/anthracene and pyrene, referred to as coke. In the membrane reactor, however, equal amounts of carbonaceous residues are found, but of less condensed rings such as methylated benzenes and naphthalenes. This type of residues is less likely to block acid sites and pore channels and even beneficial for the MTO reaction. Furthermore, the catalyst bed inside the tubular LTA membrane developed two distinctive different sections with different ratios of the various carbon residues species, called sections 1 and 2, which can additionally be distinguished by their colors. The catalyst bed near to the reactor inlet (section 1) contains a higher amount this high molecular weight polyaromatics and seems to be mostly deactivated. However, the lower section in the direction of the reactor outlet (section 2) contains mainly the catalytically active methylated benzenes and naphthalenes, which take part in the olefin production and give enough space for methanol conversion. We conclude that this zone, containing catalytically active hydrocarbons, moves through the catalyst bed, similar to the cigar burn mechanism. This motion of the coking zone is slower if water is removed since the re-methylation of the aromatic rings inside the CHA cages is facilitated by the removal of water. Therefore, the water removal through the membrane supports the re-methylation thus preventing the condensation of the aromatic rings to coke. In this study, we show that the fixed bed reactor setup in combination with a hydrophilic membrane could be an alternative to the existing fluidized bed reactor concept which suffers from an enormous attrition problem and requires, therefore, the permanent addition of new catalyst. Further research on this topic can be done by variation of several reaction parameters, such as temperature or

particle size, as well as LTA pore size engineering by ion exchange.

## Experimental Section

The MTO reaction was performed at 450 °C for 250 minutes in a vertically orientated tube membrane reactor (Figure 1). The Al<sub>2</sub>O<sub>3</sub> tube had a length of 300 mm and an outer diameter of 10 mm and was coated with a LTA zeolite membrane. The ceramic tube, respectively the reactor itself, were centrally filled with glass wool and 2 g of the SAPO-34 catalyst was loosely piled on top, the catalyst was not chemically bounded to the LTA membrane. 50 ml/min of N<sub>2</sub> were sent through a methanol reservoir, which was heated up to 50 °C and then directed into the tube reactor (WHSV = 4.6 g<sub>cat</sub><sup>-1</sup>h<sup>-1</sup>). To extract to retained hydrocarbon species from the spent catalyst, 15 mg of the respective spent SAPO-34 was completely dissolved into 1.5 mL of 15% HF for about 20 minutes. Afterwards, the HF solution was mixed with 1.5 mL of *n*-hexane and left until the two phases had separated completely. The organic phase was removed and washed with saturated CaCl<sub>2</sub> (in H<sub>2</sub>O) solution to remove possible HF remains. A detailed experimental section can be found in the supporting information.

## Acknowledgements

Jürgen Caro and Felix Rieck genannt Best thank the Deutsche Forschungsgemeinschaft (DFG), grant CA147/21-1, project number 322911753, for supporting this work. Pascal Rusch and Nadja C. Bigall thank the European Research Council (ERC) for financial support (grant agreement no. 714429). We further thank Frank Steinbach for the help during the preparation and measurement of the SEM samples and Zhogmin Liu from the Dalian Institute of Chemical Physics for providing the catalyst.

## Conflict of Interest

The authors declare no conflict of interest.

- [1] I. Amghizar, L. A. Vandewalle, K. M. Van Geem, G. B. Marin, *Engineering* **2017**, *3*, 171–178.
- [2] H. M. Torres Galvis, K. P. De Jong, *ACS Catal.* **2013**, *3*, 2130–2149.
- [3] S. M. Sadrameli, *Fuel* **2016**, *173*, 285–297.
- [4] J. Liang, H. Li, S. Zhao, W. Guo, R. Wang, M. Ying, *Appl. Catal.* **1990**, *64*, 31–40.
- [5] M. Kaarsholm, F. Joensen, J. Nerlov, R. Cenni, J. Chaouki, G. S. Patience, *Chem. Eng. Sci.* **2007**, *62*, 5527–5532.
- [6] J. Li, Y. Wei, G. Liu, Y. Qi, P. Tian, B. Li, Y. He, Z. Liu, *Catal. Today* **2011**, *171*, 221–228.
- [7] W. Song, H. Fu, J. F. Haw, *J. Am. Chem. Soc.* **2001**, *123*, 4749–4754.
- [8] D. Chen, K. Moljord, A. Holmen, *Microporous Mesoporous Mater.* **2012**, *164*, 239–250.
- [9] X. Wu, M. G. Abraha, R. G. Anthony, *Appl. Catal. A* **2004**, *260*, 63–69.
- [10] J. W. Park, J. Y. Lee, K. S. Kim, S. B. Hong, G. Seo, *Appl. Catal. A* **2008**, *339*, 36–44.
- [11] U. Olsbye, S. Svelle, M. Bjrgen, P. Beato, T. V. W. Janssens, F. Joensen, S. Bordiga, K. P. Lillerud, *Angew. Chem. Int. Ed.* **2012**, *51*, 5810–5831; *Angew. Chem.* **2012**, *124*, 5910–5933.
- [12] I. M. Dahl, S. Kolboe, *Catal. Lett.* **1993**, *20*, 329–336.
- [13] I. M. Dahl, S. Kolboe, *J. Catal.* **1994**, *149*, 458,464.
- [14] B. Arstad, S. Kolboe, *Catal. Lett.* **2001**, *71*, 209–212.
- [15] B. Arstad, S. Kolboe, *J. Am. Chem. Soc.* **2001**, *123*, 8137–8138.



- [16] J. Li, Z. Wei, Y. Chen, B. Jing, Y. He, M. Dong, H. Jiao, X. Li, Z. Qin, J. Wang, *J. Catal.* **2014**, *317*, 277–283.
- [17] J. F. Haw, W. Song, D. M. Marcus, J. B. Nicholas, *Acc. Chem. Res.* **2003**, *36*, 317–326.
- [18] C. D. Chang, *Catal. Rev.* **1983**, *25*, 1–118.
- [19] W. Song, D. M. Marcus, H. Fu, J. O. Ehresmann, J. F. Haw, *J. Am. Chem. Soc.* **2002**, *124*, 3844–3845.
- [20] G. Barbieri, G. Marigliano, G. Golemme, E. Drioli, *Chem. Eng. J.* **2002**, *85*, 53–59.
- [21] M. Pilar Bernal, J. Coronas, M. Menéndez, J. Santamaría, *Chem. Eng. Sci.* **2002**, *57*, 1557–1562.
- [22] A. T. Aguayo, A. E. Sánchez Del Campo, A. G. Gayubo, A. Tarrío, J. Bilbao, *J. Chem. Technol. Biotechnol.* **1999**, *74*, 315–321.
- [23] R. B. Rostami, M. Ghavipour, Z. Di, Y. Wang, R. M. Behbahani, *RSC Adv.* **2015**, *5*, 81965–81980.
- [24] M. Luo, H. Zang, B. Hu, B. Wang, G. Mao, *RSC Adv.* **2016**, *6*, 17651–17658.
- [25] S. V. Konnov, V. S. Pavlov, P. A. Kots, V. B. Zaytsev, I. I. Ivanova, *Catal. Sci. Technol.* **2018**, *8*, 1564–1577.
- [26] X. Yuan, H. Li, M. Ye, Z. Liu, *Chem. Eng. J.* **2017**, *329*, 35–44.
- [27] B. Hu, G. Mao, D. Wang, Y. Fu, B. Wang, M. Luo, *Catal. Sci. Technol.* **2017**, *7*, 5785–5794.
- [28] A. G. Gayubo, A. T. Aguayo, A. E. Sánchez Del Campo, A. M. Tarrío, J. Bilbao, *Ind. Eng. Chem. Res.* **2000**, *39*, 292–300.
- [29] Y. Kumita, J. Gascon, E. Stavitski, J. A. Moulijn, F. Kapteijn, *Appl. Catal. A* **2011**, *391*, 234–243.
- [30] X. Wu, R. G. Anthony, *Appl. Catal. A* **2001**, *218*, 241–250.
- [31] A. J. Marchi, G. F. Froment, *Appl. Catal.* **1991**, *71*, 139–152.
- [32] P. Tian, Y. Wei, M. Ye, Z. Liu, *ACS Catal.* **2015**, *5*, 1922–1938.
- [33] G. Liu, P. Tian, Q. Xia, Z. Liu, *J. Nat. Gas Chem.* **2012**, *21*, 431–434.
- [34] X. Zhao, J. Li, P. Tian, L. Wang, X. Li, S. Lin, X. Guo, Z. Liu, *ACS Catal.* **2019**, *9*, 3017–3025.
- [35] Fraunhofer-Institut für Keramische Technologien und Systeme IKTS, “Kompetenz in Keramik - Fraunhofer IKTS,” can be found under <https://www.ikts.fraunhofer.de/>, **2019**.
- [36] M. Guisnet, *J. Mol. Catal. A* **2002**, *183*, 367–382.
- [37] L. Leardini, S. Quartieri, G. Vezzolini, *Microporous Mesoporous Mater.* **2010**, *127*, 219–227.
- [38] E. Epelde, M. Ibañez, A. T. Aguayo, A. G. Gayubo, J. Bilbao, P. Castaño, *Microporous Mesoporous Mater.* **2014**, *195*, 284–293.
- [39] S. Kolboe, *Stud. Surf. Sci. Catal.* **1988**, *36*, 189–193.
- [40] W. Wang, A. Buchholz, M. Seiler, M. Hunger, *J. Am. Chem. Soc.* **2003**, *125*, 15260–15267.
- [41] T. Mole, *J. Catal.* **1983**, *84*, 423–434.
- [42] J. F. Haw, D. M. Marcus, *Top. Catal.* **2005**, *34*, 41–48.
- [43] J. Zhou, Y. Zhi, J. Zhang, Z. Liu, T. Zhang, Y. He, A. Zheng, M. Ye, Y. Wei, Z. Liu, *J. Catal.* **2019**, *377*, 153–162.
- [44] M. Guisnet, P. Magnoux, *Appl. Catal.* **1989**, *54*, 1–27.
- [45] P. Magnoux, P. Roger, C. Canaff, V. Fouche, N. S. Gnep, M. Guisnet, *Stud. Surf. Sci. Catal.* **1987**, *34*, 317–330.

Manuscript received: July 9, 2019  
 Revised manuscript received: October 16, 2019  
 Accepted manuscript online: October 16, 2019  
 Version of record online: November 25, 2019

# CHEM**CAT**CHEM

## Supporting Information

© Copyright Wiley-VCH Verlag GmbH & Co. KGaA, 69451 Weinheim, 2019

### **Methanol-to-Olefins in a Membrane Reactor with in situ Steam Removal – The Decisive Role of Coking**

Felix Rieck genannt Best,\* Alexander Mundstock, Gerald Dräger, Pascal Rusch, Nadja C. Bigall, Hannes Richter, and Jürgen Caro\*©2019 The Authors. Published by Wiley-VCH Verlag GmbH & Co. KGaA.

This is an open access article under the terms of the Creative Commons Attribution License, which permits use, distribution and reproduction in any medium, provided the original work is properly cited.

## SUPPORTING INFORMATION

### **Methanol-to-Olefins in a Membrane Reactor with in situ Steam Removal – The Decisive Role of Coking**

Felix Rieck genannt Best\*<sup>[a]</sup>, Alexander Mundstock<sup>[a]</sup>, Gerald Dräger<sup>[b]</sup>, Pascal Rusch<sup>[a]</sup>,  
Nadja C. Bigall<sup>[a]</sup>, Hannes Richter<sup>[c]</sup>, Jürgen Caro\*<sup>[a]</sup>

<sup>[a]</sup> Institute for Physical Chemistry and Electrochemistry, Leibniz University Hannover, 30167 Hannover, Germany

<sup>[b]</sup> Institute for Organic Chemistry, Leibniz University Hannover, 30167 Hannover, Germany

<sup>[c]</sup> Fraunhofer IKTS - Institute for Ceramic Technologies and Systems, 07629 Hermsdorf, Germany

## Experimental Section

The MTO reaction was performed at 450°C for 250 minutes in a vertically orientated tube membrane reactor (**Fehler! Verweisquelle konnte nicht gefunden werden.**). The Al<sub>2</sub>O<sub>3</sub> tube had a length of 300 mm and an outer diameter of 10 mm and was coated with a LTA zeolite membrane. The ceramic tube, respectively the reactor itself, were centrally filled with glass wool and 2 g of the SAPO-34 catalyst was suspended on top. 50 ml/min of N<sub>2</sub> were sent through a methanol reservoir, which was heated up to 50°C and then directed into the tube reactor (WHSV = 4.6 g<sub>cat</sub><sup>-1</sup> h<sup>-1</sup>). The analysis of the MTO product composition was carried by gas chromatography on an Agilent GC 6890A, which was equipped with an Agilent 19095P-QO4, a Restek 19742 Q-Bond column and a thermal conductivity detector (TCD).

To extract to retained hydrocarbon species from the spent catalyst, 15 mg of the respective spent SAPO-34 was completely dissolved into 1.5 mL of 15% HF for about 20 minutes. Afterwards, the HF solution was mixed with 1.5 mL of *n*-hexane and left until the two phases had separated completely. The organic phase was removed and washed with saturated CaCl<sub>2</sub> (in H<sub>2</sub>O) solution to remove possible HF remains. GC-MS analysis was performed on an Agilent 6890Plus GC with 5973N MSD using a Machery&Nagel Optima 5-MS capillary column (30 m\*320 µm, 0.25 µm film; constant flow of 1.5 mL/min helium 5.0; 50 °C initial oven temperature with 1 min hold time, 20 °C/min gradient and 300 °C final temperature). EI mass spectra were recorded at 70 eV and analyzed based on the NIST spectral database.

X-Ray diffraction patterns, in the 2θ range of 5° to 40°, were acquired on a Bruker D8 Advance diffractometer operating at 40 kV and 40 mA with Cu-Kα-radiation (λ = 0.154 nm).

The SEM images and EDXS measurements were acquired on a JEOL JSM 6700F operating at 10 kV and 10 µA with a LEI detector.

Thermogravimetric profiles were measured in air at a TGA/DSC 3+ from Mettler-Toledo in a temperature range between 20°C and 800°C with a heating rate of 15°C/min.

## Results

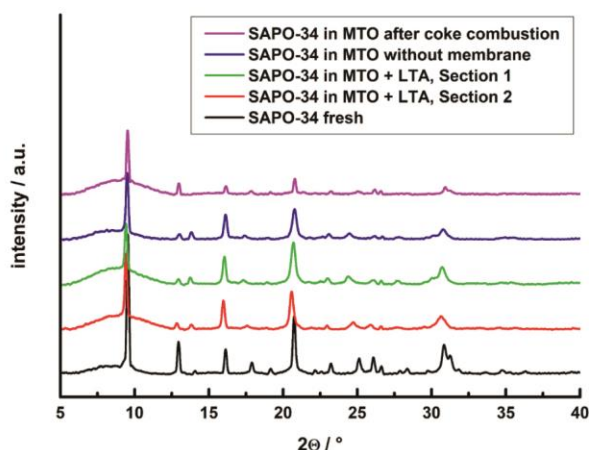


**Figure S1.** X-ray diffraction patterns of the fresh, spent and regenerated (via coke combustion at 500 °C in 40% oxygen/nitrogen stream for 4 h) SAPO-34 catalyst.

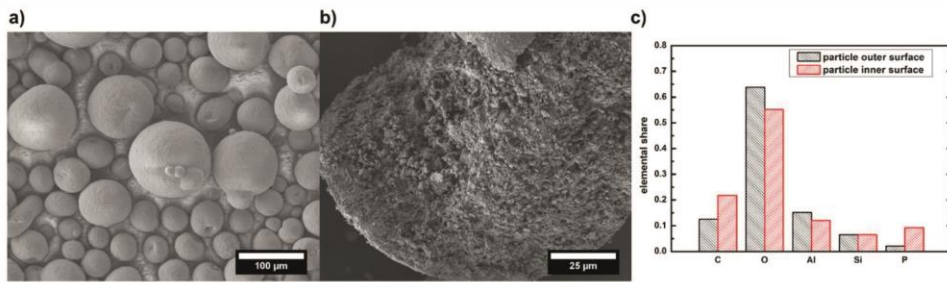


Figure S2. a) SEM image of the particle size distribution of the SAPO-34 catalyst, b) cross-section image and c) elemental distribution on the (i) inner and (ii) outer surface of SAPO-34 particle.

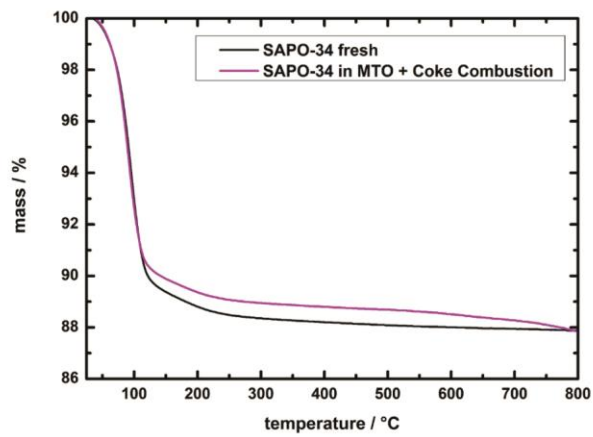


Figure S3. Thermogravimetry profiles of fresh and regenerated SAPO-34 catalysts in a temperature range of 20°C to 800°C.

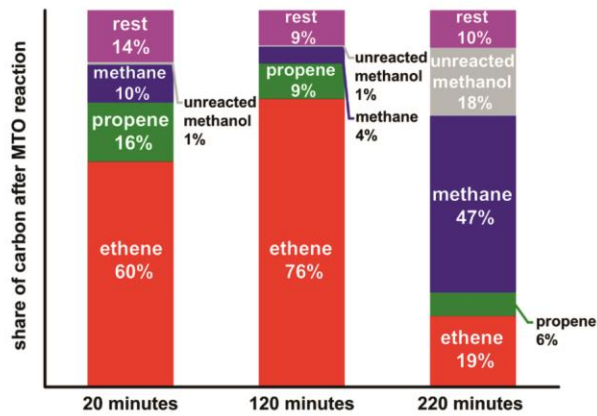


Figure S4. Share of carbon at selected points during the MTO reaction without membrane support.

**Table 1.** Extended analysis of retained hydrocarbons, extracted from the spent catalyst, via GC-MS.

hydrocarbon species	SAPO-34 in MTO without membrane	SAPO-34 in MTO + LTA, Section 1	SAPO-34 in MTO + LTA, Section 2
<i>p-m-o</i> -xylene	1.1%	4.5%	6.7%
1,2,4-/ 1,3,5-trimethylbenzene	3.8%	5.8%	8.6%
1,2,3,5-tetramethylbenzene	1.7%	1.3%	5.4%
naphthalene	6.6%	7.5%	9.3%
1,3-di- <i>tert</i> -butylbenzene	3.8%	5.0%	6.6%
1-/ 2-methylnaphthalene	9.8%	11.9%	21.3%
cyclopentane	2.4%	2.6%	0.0%
1,3-/ 2,3-/ 2,7-... dimethylnaphthalene	5.2%	6.8%	10.2%
1,6,7-/ 1,4,6-... trimethylnaphthalene	1.3%	1.8%	5.4%
fluorene	1.4%	1.7%	0.0%
phenantrene/ anthracene	30.8%	24.4%	15.8%
4H-cyclopenta[ <i>def</i> ]phenanthrene	2.3%	3.2%	0.0%
11H-benzo[ <i>b</i> ]fluorene	2.3%	0.8%	0.0%
pyrene	24.6%	18.9%	10.65%
benzanthracene	1.9%	1.6%	0.0%
1-/ 4- methylpyrene	1.15	1.4%	0.0%

## 10.2. Boosting Dimethylamine Formation Selectivity in a Membrane Reactor by In Situ Water Removal

Based on the success and the surprising results of the application of the LTA membrane on the MTO reaction, the next step was to expand the concept to another reaction, in which water removal may play a beneficial role. Based on the input by Prof. Dr. Jürgen Caro and Dr. Alexander Mundstock, the water removing membrane reactors with an Na-LTA membrane were tested in the methylamine synthesis. Compared to the MTO reaction, which is a fairly new reaction, the methylamine synthesis is an established procedure to provide the base chemicals MMA, DMA and TMA. However, much work has been done on optimizing the catalysts, but influencing the equilibrium by in situ water removal was not successfully conducted until now. Since coking problems are not as severe, the expectation of the reactions was that the water extraction will influence the product composition of the methylamine synthesis. This was first tested on two different pore-sized catalysts: H-SAPO-34 and H-MOR. It was shown that the water removal increased the share of higher methylated amines, but this trend was stopped in H-SAPO-34 due to size exclusion of the TMA. However, larger amount of the by-product DME were observed. To optimize the choice of the catalyst, the experiments were repeated with H-SSZ-13, which is isostructural to H-SAPO-34. In this work, my part was again conducting the synthesis experiments and interpreting all the results to form and write a cohesive study.

Reprinted with permission from **Rieck genannt Best, F.; Mundstock, A.; Kißling, P. A.; Richter, H.; Hindricks, K. D. J.; Huang, A.; Behrens, P.; Caro, J.** Boosting Dimethylamine Formation Selectivity in a Membrane Reactor by In Situ Water Removal. *Ind. Eng. Chem. Res.* **2021**. <https://doi.org/10.1021/acs.iecr.1c04149>. Copyright 2021 American Chemical Society.

## Boosting Dimethylamine Formation Selectivity in a Membrane Reactor by In Situ Water Removal

Felix Rieck genannt Best,\* Alexander Mundstock, Patrick A. Kißling, Hannes Richter, Karen D. J. Hindricks, Aisheng Huang, Peter Behrens, and Jürgen Caro

Cite This: *Ind. Eng. Chem. Res.* 2022, 61, 307–316

Read Online

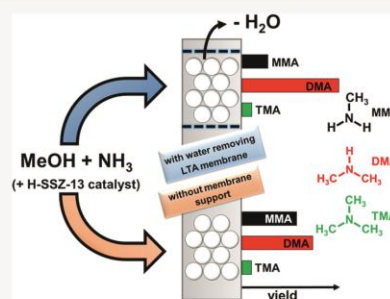
ACCESS |

Metrics & More

Article Recommendations

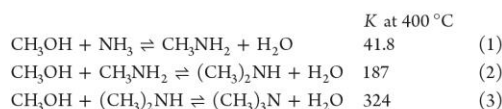
Supporting Information

**ABSTRACT:** Mono-, di-, and trimethylamine are the products of the successive methylation of ammonia. Using narrow-pore acidic catalysts of the CHA family like H-SAPO-34 or H-SSZ-13, the formation of the thermodynamically but bulky trimethylamine can be suppressed due to steric effects; thus, methylation is stopped at dimethylamine. In this work, the continuous in situ removal of the byproduct water through the 4 Å wide pores in an LINDE Type A (LTA) (grown on an  $\alpha$ -Al<sub>2</sub>O<sub>3</sub> support) membrane reactor further increased the selectivity toward the economically desired product dimethylamine by 50%. This experimental finding can be explained by the release of adsorbed water blocking the catalytic site. Water removal through the hydrophilic LTA zeolite membrane allows methanol to adsorb at the acidic catalyst sites, which in turn accelerates the methylation rate of monomethylamine to the desired product dimethylamine. Further methylation to trimethylamine as the thermodynamically most favored product is not possible in narrow-pore catalysts because of space restrictions, but it takes place in the 12-membered-ring H-Mordenite (H-MOR) catalyst.



### INTRODUCTION

Methylamines are important basic chemicals and are often used as intermediates in the synthesis of nitrogen-based pharmaceuticals, pesticides, and organic solvents.<sup>1</sup> The synthesis of the methylamines is usually performed with ammonia and methanol over acidic aluminosilicate catalysts at temperatures between 300 and 500 °C. However, the reaction can result in three different methylated amines since the monomethylamine (MMA) as a primary product reacts with another methanol molecule to form dimethylamine (DMA) and, subsequently, trimethylamine (TMA) as shown in eqs 1–3, with dimethyl ether (DME) as the most common byproduct.<sup>2</sup> The equilibrium constants *K* for each reaction step are given with a NH<sub>3</sub>/MeOH ratio of 1.9 at 400 °C.<sup>3</sup>



The composition of the product mixture heavily depends on various parameters, such as the catalyst (acidity, pore size), temperature, pressure, as well as the N/C ratio in the feed. DMA is the industrially preferred methylamine followed by MMA. Therefore, the TMA formation is generally tried to be suppressed, as it forms an azeotropic mixture with NH<sub>3</sub>, which requires an expensive product separation. The desired product

selectivity toward DMA is usually achieved by space restrictions inside the catalyst pores. Large-pore zeolites like H-Mordenite (H-MOR) are modified by pore-narrowing to prevent TMA formation.<sup>4</sup> Different zeolites and zeolite-like structures of the CHA family (like the aluminosilicate H-SSZ-13 and the silico-aluminophosphate H-SAPO-34<sup>5</sup>) naturally suppress TMA formation due to restricted transition states and product shape selectivity based on their narrow pores and/or small cages. These acidic catalysts exhibit high methanol conversion rates and have been, therefore, subject of methylamine synthesis research. The molecule sizes of the different methylamines and the pore dimension of the catalysts under study can be found in Table 1.

In this work, we examine the influence of the in situ removal of the byproduct water on the methylamine product distribution. It is removed through a hydrophilic LINDE Type A (LTA) membrane, which was grown inside of a tubular  $\alpha$ -Al<sub>2</sub>O<sub>3</sub> support and forms the outer wall of our catalytic membrane reactor. The established methylamine catalysts H-SAPO-34, H-MOR, and H-SSZ-13 are placed inside the tubular reactor as a packed bed (Figure 1).

Received: October 19, 2021  
Revised: December 8, 2021  
Accepted: December 10, 2021  
Published: December 22, 2021





**Table 1.** Molecule Sizes of MMA, DMA, and TMA<sup>6</sup> and Pore Channel/Cage Sizes of H-MOR,<sup>7</sup> H-SAPO-34,<sup>8</sup> and H-SSZ-13<sup>9</sup>

methylamine	molecule size [Å]	zeolite	pore channel size [Å]	pore cage size [Å]
MMA	3.7 × 3.9 × 4.4	H-MOR	6.5 × 7.0	no cages
DMA	3.9 × 4.7 × 6.0	H-SAPO-34	3.8 × 3.8	6.5 × 11
TMA	3.9 × 5.4 × 6.1	H-SSZ-13	3.8 × 3.8	6.5 × 11

General benefits of membrane reactors toward conversion, selectivity, and yield of a catalytic reaction have been described in some recent reviews.<sup>10–14</sup> Prominent examples for reactions with in situ water removal through a hydrophilic membrane are the increase of the yield in esterifications,<sup>15</sup> DME synthesis from methanol,<sup>16</sup> methanol-to-olefin reaction,<sup>17</sup> FISCHER-TROPSCH synthesis,<sup>18</sup> and CO<sub>2</sub> hydrogenation.<sup>19</sup>

## RESULTS AND DISCUSSION

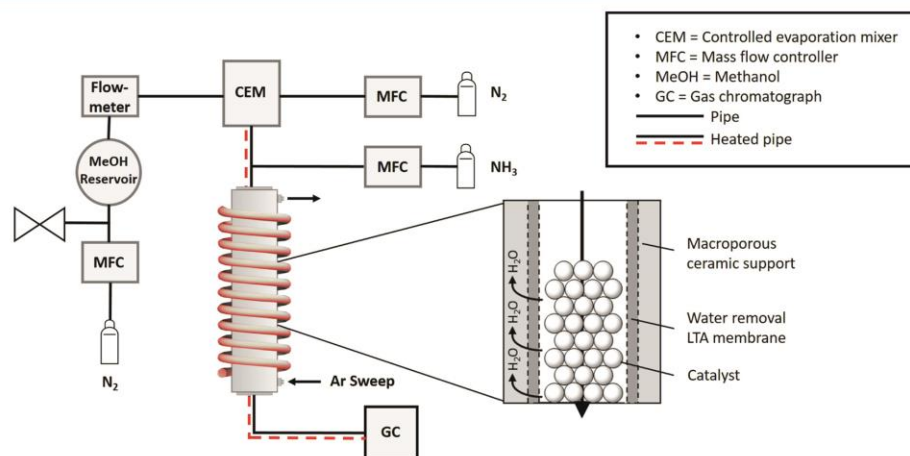
Figure 2 displays scanning electron microscopy (SEM) micrographs and the corresponding energy-dispersive X-ray spectroscopy (EDXS) mappings of the H-SAPO-34, H-SSZ-13, and H-MOR catalysts. Further details of the three catalysts under study can be found in the SEM images in Figures S1–S3. Their Si/Al ratios, specific surface areas, as well as acid site density and strength can be found in Table 2. SEM and EDXS cross-sectional images of the tubular LTA membrane are shown in Figure 3 and exhibit a uniformly grown layer of the water-selective LTA zeolite of up to 10 μm on tubular ceramic.

Table 3 shows the product distribution of the ammonia methylation by methanol which consists of monomethylamine (MMA), dimethylamine (DMA), trimethylamine (TMA), and the most common byproduct dimethyl ether (DME). Water could not be detected, i.e., it was nearly completely removed from the product stream through the hydrophilic LTA

membrane. As expected, the pure LTA membrane reactor without catalyst filling showed no catalytic activity toward the amine methylation due to the lack of acidic catalytic sites. On the other hand, there exists a report that somewhat conflicts our findings and claimed a pure LTA without any acidity as a catalyst for the ammonia methylation by methanol.<sup>21</sup>

H-SAPO-34 without any membrane support shows a high methanol conversion rate of 89% and the typical product distribution for narrow-pore catalysts with nearly equal shares of MMA and DMA of each about 39%. The TMA formation through further DMA methylation is sterically suppressed by the narrow pore diameter of the H-SAPO-34. This experimental finding is in good agreement with previous papers.<sup>3,6,21</sup> The low amount of the observed TMA (4%) was certainly formed on the outside of the H-SAPO-34 catalyst, additionally relatively high quantities of DME (18%) were found.

As a reaction mechanism of methylamine formation from methanol and ammonia in narrow-pore catalysts like H-SAPO-34 and H-SSZ-13, a Langmuir–Hinshelwood mechanism was proposed by Ilaó et al.<sup>3</sup> They attributed the TMA formation was suppressed to a transition state selectivity. The intermediates of the reaction from DMA and MeOH are too big to fit in the CHA cages, concluding that TMA is not formed at all. Furthermore, this transition state selectivity is an indication that the ELEY-RIDEAL mechanism cannot be applied since the transition states for even the smaller amines in this mechanism are too large for the cages. Conclusively, they proposed a Langmuir–Hinshelwood mechanism for the CHA-type small-pore zeolites because infrared (IR) measurements showed that both MeOH and NH<sub>3</sub> were simultaneously adsorbed, even if high-silica zeolite are lacking higher numbers of adjacent acidic sites.<sup>22</sup> The transition states for MMA and DMA can fit the inside space of the pores; here, both MeOH and ammonia adsorb at the acidic sites of the catalyst. In a surface reaction, the bound reactants form MMA and water in



**Figure 1.** Schematic image of the reaction setup. The mass flow controller (MFC) on the left side provides a slight overpressure in the MeOH reservoir and presses it to the controlled evaporation mixer (CEM), where it is mixed with nitrogen, forming an aerosol. In the heated pipe after the outlet, the aerosol is mixed with ammonia, and this reaction mixture is sent into the heated tube membrane reactor ( $T = 350\text{ }^{\circ}\text{C}$ ). The reactor wall consists of an LTA tube membrane on a tubular Al<sub>2</sub>O<sub>3</sub> support, filled with the granular mild acid catalysts (H-SAPO-34, H-SSZ-13, or H-MOR). In the case of the membrane-supported reactions, the permeate—mainly water—is removed from the reactor with an Ar sweep in counter direction to the reaction gas flow.

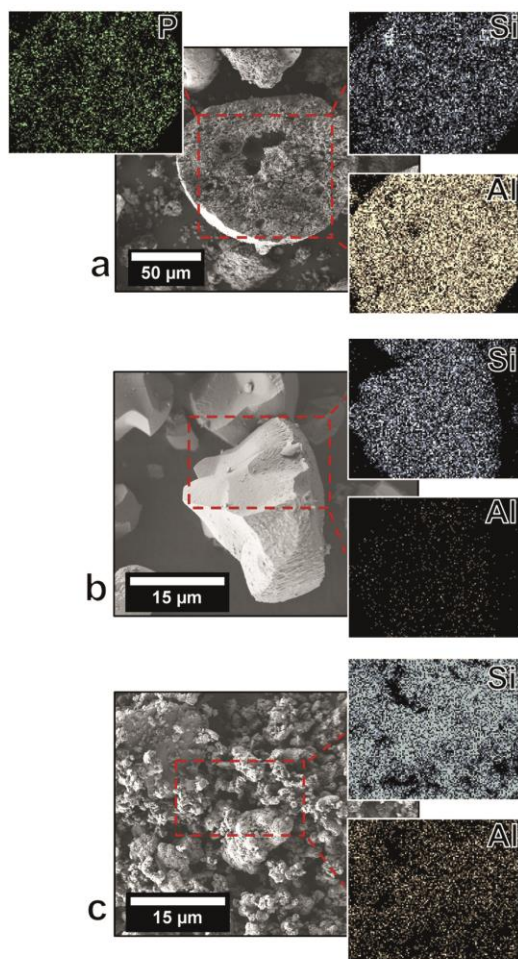


**Figure 2.** SEM images of: (a) Crushed spherical H-SAPO-34 catalyst particle as used commercially in the Dalian methanol-to-olefin (MTO) process developed by the Dalian Institute for Chemical Physics of the Chinese Academy of Sciences. The spheres are sized between 10 and 100  $\mu\text{m}$  and composed of primary H-SAPO-34 particles of about 1  $\mu\text{m}$ . A detailed description of this catalyst can be found elsewhere.<sup>5</sup> Enlarged EDXS sections show the homogeneous distributions of the elements Si, Al, and P. (b) Self-prepared H-SSZ-13 catalyst particle with a size of up to 30  $\mu\text{m}$ . EDXS mappings show homogeneous elemental distribution and characterize it as high-silica chabazite with a Si/Al ratio of 15 (see Table 2). (c) Commercially available H-MOR (Süd-Chemie) catalyst consisting of primary crystallites <0.1  $\mu\text{m}$  (see Figure S3). EDXS measurements point to a higher Al content (Si/Al = 5) compared to H-SSZ-13, which corresponds to higher acidity, see Table 3, as the acidity increases with decreasing Si/Al ratio.<sup>20</sup>

an “intramolecular”  $S_N2$  reaction. Analogous to this, the formation of DMA is accomplished by bound MMA and MeOH. However, recent studies showed that large molecules like polybenzenes in the MTO reaction can fit inside the CHA cages.<sup>23</sup> With the absence of proof that TMA intermediates were located inside the CHA pores, it can be stated that the

**Table 2.** Element Ratios of Si/Al and Si/P, Total BET Surface Area, Acid Site Density, and Acid Site Strength for H-SAPO-34, H-SSZ-13, and H-MOR Catalysts

	element ratio <sup>a</sup>		BET surface area [ $\text{m}^2 \text{g}^{-1}$ ]	acid site properties		
	Si/Al	Si/P		density <sup>b</sup> [ $\text{mmol g}^{-1}$ ]	$\text{NH}_3$ desorption temp. <sup>c</sup> [ $^\circ\text{C}$ ]	weak
H-SAPO-34	0.4	1.4	287	0.74	196	426
H-SSZ-13	15		855	1.43	220	541
H-MOR	5		390	1.74	227	648

<sup>a</sup>Determined via EDXS SEM measurements (see Figure 2). <sup>b</sup>via ammonia temperature-programmed desorption (TPD) and. <sup>c</sup>desorption peak maximum temperature of weak and strong sites in TPD profiles. BET pore size distribution, isotherms, and  $\text{NH}_3$  TPD curves can be found in Figures S4 and S5, respectively.

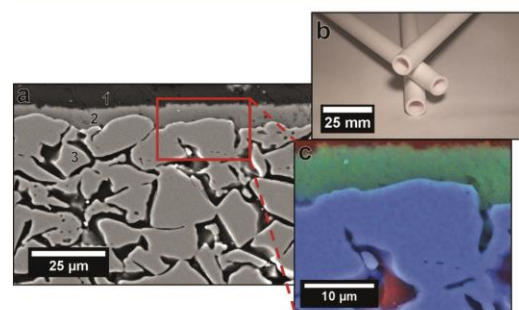


**Figure 3.** (a) SEM cross-sectional image of the used LTA membrane fixed in epoxy resin in 1000 $\times$  magnification: 1 epoxy resin, 2 LTA membrane, 3 tubular  $\alpha\text{-Al}_2\text{O}_3$  support. (b) Picture of used tubular support with LTA membrane grown inside. (c) EDXS mapping of LTA membrane (red = epoxy resin/ $C_{k\alpha}$  transition, green = LTA membrane/ $S_{i_{k\alpha}}$  transition, and blue =  $\alpha\text{-Al}_2\text{O}_3$  support/ $Al_{k\alpha}$  transition) in 2500 $\times$  magnification. The hydrophilic membrane is defect-free ( $\text{N}_2$  test) and uniformly grown with an average thickness of 10  $\mu\text{m}$ .

lack of TMA formation is not only limited to space restrictions but also influenced by several pore properties.

Surprisingly, the combination of the H-SAPO-34 catalyst with a water-removing LTA membrane in the form of a membrane reactor resulted in a remarkable increase in the yield of the industrially desired product DMA by over 50%, while the MMA production decreased. As expected, the amount of TMA in the product distribution stayed as low as in the case without membrane since narrow-pore CHA catalysts cannot produce TMA. The DME production slightly increased from 18 to 23%.

In a second run of experiments, H-SSZ-13 was used as the mild acidic zeolite, which has a CHA structure like H-SAPO-34, but a higher acidity; see Table 2. However, H-SSZ-13 is a pure aluminosilicate with the same channel and pore size like the Si-doped aluminophosphate H-SAPO-34. An H-SSZ-13 catalyst achieves a better DMA selectivity on its own and also largely suppresses the formation of the byproduct DME compared to H-SAPO-34, as previously reported.<sup>3</sup> For the ammonia methylation without membrane support, we achieved an MMA selectivity of 41% and a DMA selectivity of 50% on H-SSZ-13. Similar to H-SAPO-34, the use of a water-removing

**Table 3.** Product Distribution in Methylamine Synthesis of Narrow-Pore Catalysts H-SAPO-34 and H-SSZ-13 (Both CHA Structure Type) and Large-Pore Catalyst H-MOR<sup>a</sup>

	H-SAPO-34		H-SSZ-13		H-MOR	
	without membrane (%)	with membrane (%)	without membrane (%)	with membrane (%)	without membrane (%)	with membrane (%)
X(MeOH)	89	86	91	90	70	71
S(MMA)	39	15	40	19	36	29
S(DMA)	39	56	51	71	24	25
S(TMA)	4	5	7	7	35	39
S(DME)	18	23	2	3	5	7

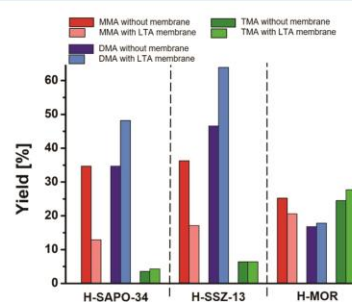
<sup>a</sup>The catalysts were activated by heating in a N<sub>2</sub> stream at 400 °C for 90 min. The reaction was performed at 350 °C with MeOH/NH<sub>3</sub> = 2.5 and WHSV<sub>MeOH</sub> = 2.39 g g<sub>cat</sub><sup>-1</sup> h<sup>-1</sup> at 1 bar. The overall methanol conversion was calculated based on the original feed composition.

LTA membrane increased the share of the desired product DMA drastically from 50 to 71% and decreased the share of MMA (from 40 to 19%). TMA and DME production stayed roughly the same.

Finally, the same experiments of methylamine formation without and with membrane support were performed with H-MOR as a catalyst. In contrast to the CHA structure, the 12-membered ring MOR geometry allows the formation of TMA. H-MOR is suited well as the test object as it already found usage in industrial appliances, exhibits a 70% MeOH conversion rate, and was observed with almost equal amounts of the three methylamines, which can be useful to examine the product composition shift and the influence of the LTA membrane on the methanol conversion rate. Compared with H-SAPO-34 as a catalyst, for H-MOR, the concentration of the thermodynamically favored product TMA is much higher at the expense of the DMA concentration. The formation of DME, however, is mostly inhibited. It is surprising that the distribution of the different methylamines in H-MOR does not change significantly (as for H-SAPO-34 and H-SSZ-13) when the byproduct water is removed from the reactor through the LTA membrane. This experimental finding is most probably led by the reaction route of MMA from methanol and ammonia in large-pore catalysts like unmodified H-MOR. The ELEY-RIDEAL-based mechanism was proposed by Fetting et al. for ZK-5 zeolite.<sup>24</sup> First, the ammonia is preferably adsorbed on the BRØNSTED acidic adsorption site of the catalyst. MeOH is protonated by the adsorbed ammonium molecule (or by the protons of the aluminosilicate). The adsorbed ammonia now can perform an S<sub>N</sub>2 attack on the protonated methanol to form MMA and water. The partial subsequent reaction to DMA or TMA occurs in a similar reaction path, only that the lesser methylated compound is adsorbed instead of the ammonia.<sup>21</sup> Therefore, in the case of the MOR catalyst, the application of the LTA membrane has only a low influence on the product distribution. The MMA share decreased by 7%, while the TMA share in the products increased by 4%, with DMA staying at the same. The DME production marginally increased to 7%.

The yields of MMA, DMA, and TMA for all three catalysts with and without membrane support can be seen in Figure 4. For both the narrow-pore CHA structures (H-SAPO-34 and H-SSZ-13), the yield of DMA greatly benefits from applying the LTA membrane, while the formation of TMA is suppressed. Furthermore, the almost extinction of the DME formation for H-SSZ-13 led to a major yield increase of DMA by 15% compared to H-SAPO-34.

In general, for both the narrow- and large-pore-sized catalysts H-SAPO-34/H-SSZ-13 and H-MOR, it can be stated that the in situ water removal through the LTA membrane led

**Figure 4.** Yield of MMA, DMA, and TMA with and without LTA membrane support for H-SAPO-34, H-SSZ-13, and H-MOR.

to a decrease of the MMA yield and a consequential increase of the higher methylated amines. This trend of consecutive methylation is stopped for the narrow pores of CHA-type zeolites (H-SAPO-34 and H-SSZ-13) due to steric effects on the DMA formation step since TMA cannot be formed, while H-MOR showed an increase in the TMA yield. Furthermore, this effect is much more relevant for two catalysts: H-SAPO-34 with an MMA decrease of nearly 25% and a DMA increase of 17%, and H-SSZ-13 with an MMA decrease of 21% and a DMA increase of 20%. Only H-MOR seems to be less impacted by the membrane support, changing the product distribution by just a few percent.

This experimental finding can be explained through the mechanism of the methylamine formation by the consecutive methylation of ammonia by methanol at the acidic sites. In the SAPO framework, a Si atom replaces a P atom, and for charge balance, a proton is bound to one of the neighboring O atoms. The byproduct water is strongly adsorbed at the protonated Al–O–Si, thus blocking this site through “product poisoning”. At low water loadings, water adsorption is exclusively due to hydrogen bonding, whereas at higher loadings, deprotonation takes place.<sup>25</sup>

Figure 5 shows the X-ray diffraction (XRD) patterns of the activated and spent methylamine catalysts H-SAPO-34, H-SSZ-13, and H-MOR with and without LTA membrane support.

The results exhibit for both spent CHA-type catalysts (after the methylamine reaction) a 2θ shift to smaller values compared to the fresh catalyst, suggesting a lattice expansion. This XRD finding can be explained through the deposition of a few macromolecular residues (coke). Furthermore, both spent CHA-type catalysts H-SAPO-34 and H-SSZ-13 show a slightly larger lattice expansion whenever the LTA membrane is in place to withdraw the water—compared to the corresponding

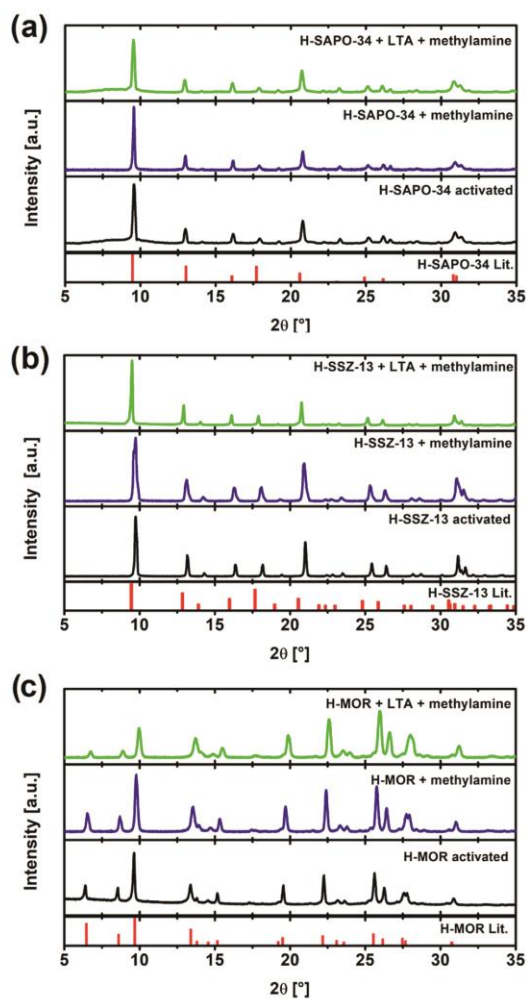


Figure 5. XRD patterns of fresh and spent catalysts (with and without LTA membrane support): (a) H-SAPO-34, (b) H-SSZ-13, and (c) H-MOR in a  $2\theta$  range of  $5\text{--}35^\circ$  in comparison with literature data, which is obtained from refs 7, 26, 27.

spent catalysts without membrane support. This is expected since the presence of steam usually reduces the formation of carbonaceous residues.<sup>28</sup> Surprisingly, the H-MOR catalyst showed the opposite behavior: The lattice of the spent catalyst shrunk compared to the fresh H-MOR. We assume either that the adsorption of  $\text{NH}_3$  and the amines at the strong acidic sites led to a contraction of the lattice similar to ion exchange experiments in H-MOR<sup>29,30</sup> or that dealumination through steaming, which is more significant for the H-MOR due to its high alumina content, is responsible for the decreased lattice spacing.

The increase of higher methylated amines by the in situ water removal with the LTA membrane is supported through GC-based mixed gas adsorption experiments and the IR spectra of MeOH/water and  $\text{NH}_3$ /water adsorbed on the different catalysts, as described in the following.

Since water is competing with methanol and ammonia for the same acidic adsorption sites, the removal of water from the active sites creates space for the adsorption of the reactants. It is likely that the adsorption of methanol and ammonia (as well as MMA and DMA for the formation of DMA and TMA, respectively) is increased in the absence of water. Furthermore, the water removal frees up space for the bulky transition states.

To investigate the competitive adsorption of the reactants MeOH and  $\text{NH}_3$  with water at the catalytic sites, we measured the IR spectra of the loaded H-SAPO-34 and H-MOR (Figure 6). The catalysts were evacuated at  $100^\circ\text{C}$  and then loaded at  $150^\circ\text{C}$  with gaseous pure MeOH and  $\text{H}_2\text{O}$  or a 1:1 mixture of MeOH/ $\text{H}_2\text{O}$  at 1 bar.

By comparing the distinctive methanol signals of the three  $\text{-CH}$  stretching modes ( $\nu(\text{CH})$  at  $2831\text{--}2949\text{ cm}^{-1}$ ), clear differences in the IR spectra of the adsorbed MeOH/water mixture in H-SAPO-34 and H-MOR can be found (see Tables S1 and S2). For the adsorbed MeOH/ $\text{H}_2\text{O}$  mixture in H-SAPO-34, the IR signal is much lower in comparison with that of the adsorption of pure methanol. This indicates that the MeOH adsorption is hindered by the presence and concurrent adsorption of water.

On the other hand, if the MeOH/ $\text{H}_2\text{O}$  mixture is adsorbed in H-MOR, large IR signals of both components are found, which leads to the conclusion that the MeOH adsorption in H-MOR is only influenced to a smaller extent by the presence of water. An extended analysis of the IR results can be found in the Supporting Information.

Solely based on the proton affinity, methanol ( $\text{PA} = 773.6\text{ kJ mol}^{-1}$ ) should be adsorbed slightly preferred over water ( $\text{PA} = 723.8\text{ kJ/mol}$ ) at the acidic sites of H-MOR.<sup>31</sup> Though both, water and methanol, compete for the same acidic sites, the general hydrophilicity of the catalysts favors water adsorption from water/methanol mixtures. Mixed gas adsorption isotherms on different hydrophilic porous materials, including zeolites or certain modified zeolitic metal–organic frameworks (ZIFs), show the preferred adsorption of water over alcohol.<sup>32–34</sup> These findings of mixed adsorption from literature fit our results well since all three of our catalysts are hydrophilic materials. However, the influence of water adsorption on the catalytic methylamine synthesis can be reduced if catalysts with lower hydrophilicity and decreased polarity are used.<sup>35</sup> H-SSZ-13 with its relatively high Si/Al ratio of 15 (see Table 2) shows an increased hydrophobicity, which benefits ammonia methylation in two ways: The alcohol adsorption is supported<sup>36,37</sup> and water is less strongly adsorbed by the catalyst, easing its removal through the water-selective LTA membrane. Additionally, the higher acidity of the H-SSZ-13 sites compared to H-SAPO-34 (see Table 2) further favors the MeOH adsorption. This decreased water adsorption is in complete accordance with the finding that H-SSZ-13 has the highest yield of DMA<sup>3</sup>—even without the membrane support—and benefits both CHA-type catalysts from the water removal through the LTA membrane in terms of an increased DMA yield (Table 3).

Considering the results of IR and mixed gas adsorption, it becomes more apparent that the presence of water hinders the adsorption of methanol only in CHA-type catalysts significantly. Most probably, adsorbed water is blocking the diffusion paths and adsorption sites for methanol inside the hydrophilic catalyst pores. In 12-membered-ring MOR catalysts, methanol can still diffuse in the presence of adsorbed water and adsorb on free sites. The effect of catalyst poisoning by water becomes

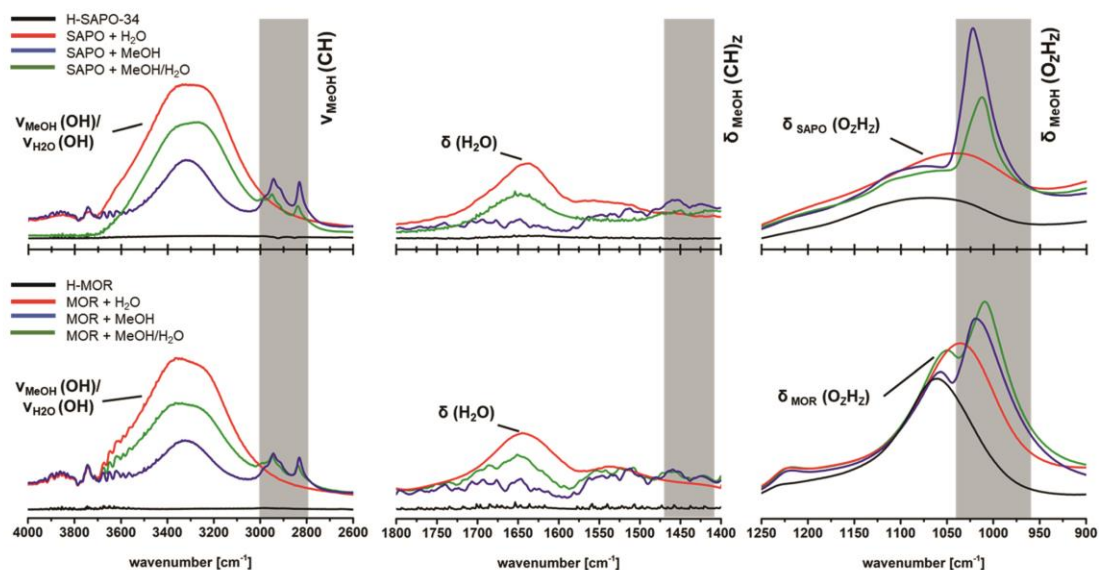


**Figure 6.** IR spectra of H-SAPO-34 and H-MOR at 100 °C and loaded with either pure MeOH or pure water, respectively, or a 1:1 mixture of both. Each gray area shows a distinct MeOH signal that does not overlap with water signals. Left: Overall three signals of  $\nu_{\text{MeOH}}(\text{CH})$ ; middle: two signals of  $\delta_{\text{MeOH}}(\text{CH})_3$  and  $\delta_{\text{MeOH}}(\text{CH})_2$ ; and right: one signal of  $\delta_{\text{MeOH}}(\text{O}_2\text{H}_2)$ .

more relevant in a catalytic reaction environment when water is formed in situ inside the pores and weighs even more heavily with H-SAPO-34 and H-SSZ-13. In narrow-pore catalysts, the space restrictions influence the amine methylation to a higher extent: The reaction requires two nearby adsorption sites (Langmuir–Hinshelwood mechanism), and a critical space is needed for the transition states. Further, blocking effects on diffusion due to strongly adsorbed molecules are more severe. In the methylamine synthesis with H-MOR, methanol does not directly adsorb at the acidic sites since it attacks the already adsorbed ammonia, or MMA/DMA (ELEY-RIDEAL mechanism). The methanol protonation can thereby occur with ammonia or acidic protons of the H-MOR. In this case, methanol does not depend on a nearby proton, which can be blocked or the site can be deprotonated by water, but depends on the water content<sup>25</sup> and can get protonated anywhere in the H-MOR pore channel. The methanol in the Langmuir–Hinshelwood mechanism of the CHA catalyst requires a free adsorption site adjacent to already adsorbed  $\text{NH}_3$ . Hence, catalytic site blocking by water is much more severe in the case of narrow-pore catalysts like H-SAPO-34 and H-SSZ-13.

A previous study already showed that a dry mordenite catalyst possessed higher MMA conversion and DMA selectivity compared to a catalyst exposed to moisture.<sup>38</sup> An important variable is the contact time of MeOH inside the catalyst pore. As the amination of methanol is highly sensitive toward the contact time, a higher contact time leads to an increased MMA conversion to DMA or DMA to TMA, respectively.<sup>3</sup> In this work, the MeOH contact time could be increased by in situ water removal with the LTA membrane, amplifying the methylation and conclusively resulting in an increased share of DMA and TMA. Furthermore, previous studies on the reactivity of methanol in the methanol-to-olefin (MTO) reaction and the influence of water present were conducted. It was shown that the presence of water lowered

the methanol reactivity and inhibited the formation of the highly reactive methoxide species as well.<sup>39,40</sup> While water can work beneficial in the MTO reaction as it influences the coke formation, these deactivation problems do not play an important role in the methylamine synthesis, indicating that the removal of water enhances the overall methanol reactivity and consequently the methylation rate. This adds another layer to the explanation on why a larger share of the higher methylated amines was found in the experiments with the addition of the water extraction membrane.

Another explanation for the formation of higher methylated amines is the thermodynamic approach. Removing water leads to an equilibrium shift of the reaction toward the product side, as Le Chatelier's principle predicts. As every methylation step produces water as a byproduct, the water removal would shift each consecutive methylation toward TMA as the highest methylated amine or DMA, respectively.

With the equilibrium shift due to the water removal, we can expect an overall increase in the methanol conversion. However, we observed an almost stable methanol conversion with and without LTA membrane support for H-SSZ-13 and H-MOR and even a slight decrease from 89% without membrane to 86% with membrane for H-SAPO-34. A possible reason for this experimental finding could be the limited  $\text{H}_2\text{O}/\text{MeOH}$  selectivity of the LTA membrane.

To understand this unexpected result, we measured single and mixed gas permeation data at 200 °C on a self-constructed permeation device working after a modified Wicke–Kallenbach principle.<sup>41</sup> For the study of the water, ammonia, and methanol permeation, we used mixtures with  $\text{N}_2$  as a carrier gas to simulate the catalytic methylamine synthesis conditions in the membrane reactor. Detailed information can be found in the Experimental Section. For the mixed permeation of  $\text{H}_2\text{O}/\text{NH}_3$  and  $\text{H}_2\text{O}/\text{MeOH}$ , we combined equimolar amounts of

the gas streams (mixed with N<sub>2</sub> as carrier gas). The results of the permeation measurements are shown in Table 4.

**Table 4. Single Gas Permeances for H<sub>2</sub>O, MeOH, and NH<sub>3</sub>, as well as Permeances for MeOH and NH<sub>3</sub> Mixed with Water through an LTA Membrane at 200 °C<sup>a</sup>**

component	permeance [mol s <sup>-1</sup> m <sup>-2</sup> Pa <sup>-1</sup> ]	separation factor
Permeation with N <sub>2</sub> Carrier Gas		
H <sub>2</sub> O	1.1 × 10 <sup>-7</sup>	
MeOH	4.4 × 10 <sup>-10</sup>	H <sub>2</sub> O/MeOH ≈ 250
NH <sub>3</sub>	1.0 × 10 <sup>-9</sup>	H <sub>2</sub> O/NH <sub>3</sub> ≈ 110
Permeation with N <sub>2</sub> Carrier Gas Mixed Feed with H <sub>2</sub> O		
MeOH	9.4 × 10 <sup>-9</sup>	H <sub>2</sub> O/MeOH ≈ 14
H <sub>2</sub> O	1.3 × 10 <sup>-7</sup>	
NH <sub>3</sub>	7.6 × 10 <sup>-9</sup>	H <sub>2</sub> O/NH <sub>3</sub> ≈ 18
H <sub>2</sub> O	1.4 × 10 <sup>-7</sup>	

<sup>a</sup>Ideal separation factors are given for single gas permeation and for mixed gas permeation of MeOH and NH<sub>3</sub> with water.

As expected, the hydrophilic LTA membrane shows a high permeance for the small water (2.6 Å). Since the kinetic molecule size of methanol (3.6 Å) is smaller than the pore size of the rigid zeolite (4 Å), a measurable MeOH permeation through the LTA membrane is observed. The single gas permeation measurements predict a H<sub>2</sub>O/MeOH separation factor of 250, which is higher than previously reported for LTA.<sup>42</sup> LTA membranes exhibit water/alcohol separation factors of up to 10 000 for alcohols larger than MeOH.<sup>35,43</sup> However, the separation factor is drastically lowered if MeOH permeates in the presence of steam. The MeOH permeance was found to be increased by a factor of 21, when MeOH together with water is sent through an LTA membrane; see Table 4. In mixed gas permeation, the interaction between the two components can affect their diffusion as well as their adsorption behavior. Regarding methanol, this results in an increase of the permeance due to hydrogen bonding and cluster building.<sup>36</sup> This behavior was studied in a variety of pervaporation experiments, where the effect of the coupled diffusion and intermolecular interaction is higher due to the lower temperature.<sup>44–46</sup> We expect similar reasons for the increased permeance of MeOH in the presence of water but to a lesser extent at a high temperature of 200 °C. Since our methanol conversion rate is calculated based on the original feed composition, the amount of MeOH which slipped through the membrane is considered nonreacted. Therefore, due to this undesired MeOH extraction, the apparent calculated MeOH conversions in the membrane reactor are not higher than in the reactor without a membrane.

Comparable permeation measurements were repeated with NH<sub>3</sub> in a N<sub>2</sub> stream. Since ammonia's kinetic diameter (2.9 Å) is smaller than the 4 Å pores of the LTA zeolite and lower compared to MeOH (3.6 Å),<sup>47</sup> a relatively high permeance of 1.0 × 10<sup>-9</sup> mol s<sup>-1</sup> m<sup>-2</sup> Pa<sup>-1</sup> can be observed, resulting in a single gas separation factor of 110 for H<sub>2</sub>O/NH<sub>3</sub>. Due to the coupled diffusion, an increased NH<sub>3</sub> permeance can be seen in the presence of water. The increase is not as distinct as with MeOH, while both gases exhibit similar separation factors on a saturated membrane (H<sub>2</sub>O/NH<sub>3</sub> ≈ 18).

The permeation results show a possible reason for the stagnant instead of the expected increased MeOH conversion. Parts of MeOH and NH<sub>3</sub> are also withdrawn from the reactor together with water due to the limited H<sub>2</sub>O/MeOH and H<sub>2</sub>O/

NH<sub>3</sub> selectivity of the LTA membrane. This problem could be solved by cation exchange. Replacing the Na<sup>+</sup> by K<sup>+</sup> ions, the windows of LTA are narrowed to 3 Å, thus preventing MeOH diffusion through the LTA membrane while maintaining its water selectivity. The use of a K<sup>+</sup>-LTA membrane doubled the mixture separation factor H<sub>2</sub>O/MeOH in pervaporation experiments at room temperature.<sup>42</sup>

## CONCLUSIONS

We studied ammonia methylation by methanol in a membrane reactor at 350 °C with the narrow-pore CHA-type catalysts H-SAPO-34 and H-SSZ-13. By removing the byproduct water through a hydrophilic LTA membrane, the selectivity to the desired product dimethylamine (DMA) can be boosted. This experimental finding is explained by a Langmuir–Hinshelwood mechanism: The removal of water supports the adsorption of methanol and ammonia, thus favoring the formation of higher methylated amines. Furthermore, water removal creates a crucial space for bulky transition states. In the case of the narrow-pore CHA-type catalysts, the methylation is stopped at DMA for steric reasons. Using the large-pore catalyst H-MOR, the major product is trimethylamine (TMA). Since the LTA membrane in its Na<sup>+</sup> form allows also some loss of methanol and ammonia, the methanol conversion rate in the membrane reactor was steady or slightly lower than in the packed-bed reactor without membrane.

## EXPERIMENTAL SECTION

The methylamine synthesis was performed at 350 °C for 180 min in a vertically orientated tube membrane reactor (Figure 1). The Al<sub>2</sub>O<sub>3</sub> tube had a length of 300 mm and an outer diameter of 10 mm and was coated on the inside with an LTA zeolite membrane (Figure 3). The ceramic tube, or the reactor itself in experiments without membrane support, where centrally filled with glass wool and 2 g of the respective catalyst (H-SAPO-34, H-SSZ-13, or H-MOR) was loosely piled on top. Methanol (Roth, ≥99.9%), was introduced at 4.78 g h<sup>-1</sup> into the reactor system by combining with N<sub>2</sub> (Q<sub>N<sub>2</sub></sub> = 23.5 mL min<sup>-1</sup>) to create an aerosol using a Bronkhorst Controlled Evaporator Mixer (CEM) W-102A. The aerosol was mixed with NH<sub>3</sub> (Q<sub>NH<sub>3</sub></sub> = 23.5 mL min<sup>-1</sup>) before being directed into the tube reactor. In experiments with the LTA membrane, Ar (Q<sub>Ar</sub> = 2 mL min<sup>-1</sup>) was applied on the permeate side. The gases N<sub>2</sub> (≥99.999%, Linde), NH<sub>3</sub> (≥99.999%, Linde), and Ar (≥99.999%, Linde) were dosed by Bronkhorst mass flow controllers EL-FLOW Prestige.

The membrane was manufactured by the Fraunhofer Institute of Ceramic Technologies and Systems (IKTS) in Hermsdorf/Germany.

H-MOR was acquired from Süd-Chemie AG, and H-SAPO-34 was kindly provided by Zhongmin Liu from the Dalian Institute of Chemical Physics (DICP).

H-SSZ-13 was synthesized using a modified method from Fahami et al.<sup>48</sup> A mixture of 0.39 g of sodium hydroxide, 23.6 g of Millipore water, 8.51 g of *N,N,N*-trimethyladamantylammonium hydroxide (TMAdOH, 25 wt % in water, TCI), and 0.25 g of aluminum hydroxide (Sigma-Aldrich) were stirred for 30 min and subsequently mixed with 7.48 g of LUDOX AS-40 (Sigma-Aldrich). The formed gel aged 2 h in a 115 mL Teflon autoclave, which was then heated to 160 °C for 4 days. The resulting powder was filtered and thoroughly washed with Millipore water and dried at 80 °C overnight, before being

calcinated at 550 °C for 2 h. The ion exchange was performed with 1 M  $\text{NH}_4\text{NO}_3$  ( $\text{NH}_4\text{NO}_3$  from Sigma-Aldrich,  $\geq 99.0\%$ ) solution with 20 mL  $\text{g}^{-1}$  Na-SSZ-13 for 3 h at 80 °C. The gel was subsequently filtered, washed, dried at 80 °C overnight, and calcinated at 550 °C for 2 h. The ion exchange steps were repeated three times overall.

The product analysis was performed by gas chromatography on an Agilent 7890A GC System, equipped with a Restek RTX Volatile Amine column and a thermal conductivity detector (TCD).

X-ray diffraction patterns were acquired via a Bruker D8 Advance diffractometer operating at 30 kV and 40 mA with Cu  $K\alpha$ -radiation ( $\lambda = 0.154$  nm) in a  $2\theta$  range of 5–35°. SEM images and EDXS mapping were performed on a JEOL JSM 6700F operating at 2 kV (10 kV for EDXS) and 10  $\mu\text{A}$  with an LEI detector. The total catalyst specific surface areas were acquired by  $\text{N}_2$  physisorption measurements: The  $\text{N}_2$  isotherms were measured at 87 K on a Micromeritics 3Flex instrument. Prior to the measurements, the samples were degassed under vacuum at 120–200 °C for 24 h. Surface areas were determined by applying the Brunauer–Emmett–Teller (BET) equation.<sup>49</sup> The total pore volume was estimated using the single-point method at  $p/p_0 = 0.95$ . All evaluations were performed via 3Flex software version 5.02. The quantity and strength of the acidic catalyst sites were calculated from  $\text{NH}_3$  temperature-programmed desorption on an AMI-300 at 3P Instruments GmbH & Co., KG. IR measurements were carried out on an Agilent Carry 630 FTIR equipped with a ZnSe attenuated total reflectance sampler with a thermoelectrically cooled deuterated triglycine sulfate (dTGS) detector. The spectra were acquired with a spectral resolution of 2  $\text{cm}^{-1}$  and 128 scans in a range of 4000–650  $\text{cm}^{-1}$ .

Permeation experiments were performed in a modified Wicke–Kallenbach setup at 200 °C. Gases and mass flow controllers are the same as mentioned above. The aerosols of water and methanol were directed into the permeation cell with 20 mL  $\text{min}^{-1}$ .  $\text{N}_2$  ( $Q_{\text{N}_2} = 2$  mL  $\text{min}^{-1}$ ) was applied on the permeation site. Analysis was carried out with the same GC setup as mentioned above.

## ■ ASSOCIATED CONTENT

### Supporting Information

The Supporting Information is available free of charge at <https://pubs.acs.org/doi/10.1021/acs.iecr.1c04149>.

SEM images of H-SAPO-34, H-SSZ-13, and H-MOR catalysts, temperature-programmed desorption curves, physisorption curves for the aforementioned catalysts, and peak positions of H-SAPO-34 and H-MOR loaded with  $\text{H}_2\text{O}/\text{MeOH}$  with extended discussion (PDF)

## ■ AUTHOR INFORMATION

### Corresponding Author

Felix Rieck genannt Best – Institute of Physical Chemistry and Electrochemistry, Leibniz University Hannover, Hannover 30167, Germany; [orcid.org/0000-0003-1058-9034](https://orcid.org/0000-0003-1058-9034); Email: felix.best@pci.uni-hannover.de

### Authors

Alexander Mundstock – Institute of Physical Chemistry and Electrochemistry, Leibniz University Hannover, Hannover 30167, Germany

Patrick A. Kißling – Institute of Physical Chemistry and Electrochemistry, Leibniz University Hannover, Hannover 30167, Germany

Hannes Richter – Institute for Ceramic Technologies and Systems, Fraunhofer IKTS, Hermsdorf 07629, Germany

Karen D. J. Hindricks – Institute of Inorganic Chemistry, Leibniz University Hannover, Hannover 30167, Germany; Cluster of Excellence PhoenixD (Photonics, Optics, and Engineering – Innovation Across Disciplines), 30167 Hannover, Germany

Aisheng Huang – Shanghai Key Laboratory of Green Chemistry and Chemical Processes, Department of Chemistry, East China Normal University, Shanghai 200241, China; [orcid.org/0000-0002-9727-4379](https://orcid.org/0000-0002-9727-4379)

Peter Behrens – Institute of Inorganic Chemistry, Leibniz University Hannover, Hannover 30167, Germany; Cluster of Excellence PhoenixD (Photonics, Optics, and Engineering – Innovation Across Disciplines), 30167 Hannover, Germany; Laboratory of Nano and Quantum Engineering, Leibniz University Hannover, 30167 Hannover, Germany

Jürgen Caro – Institute of Physical Chemistry and Electrochemistry, Leibniz University Hannover, Hannover 30167, Germany; Laboratory of Nano and Quantum Engineering, Leibniz University Hannover, 30167 Hannover, Germany; School of Chemistry and Chemical Engineering, South China University of Technology, Guangzhou 510640, China; [orcid.org/0000-0003-0931-085X](https://orcid.org/0000-0003-0931-085X)

Complete contact information is available at: <https://pubs.acs.org/10.1021/acs.iecr.1c04149>

## Author Contributions

The manuscript was written through contributions of all authors. All authors have given approval to the final version of the manuscript.

## Funding

The Deutsche Forschungsgemeinschaft (DFG, German Research Foundation) is thanked for financing the project (CA147/21-1) by F.R.g.B. and J.C., P.A.K. thanks the DFG (Project B11708/S-1).<sup>50</sup> Additionally, the project has in part been funded by the German Science Foundation (DFG, German Research Foundation) under Germany's Excellence Strategy within the Cluster of Excellence PhoenixD (EXC 2122, Project ID 390833453).

## Notes

The authors declare no competing financial interest.

## ■ ACKNOWLEDGMENTS

The H-SAPO-34 catalyst was kindly provided by Zhongmin Liu of the Dalian Institute for Chemical Physics of the Chinese Academy of Sciences. The LTA membranes on tubular alumina supports have been prepared at Fraunhofer IKTS Dresden/Hermsdorf. Further thanks to Frank Steinbach for preparing and taking the SEM cross-sectional images.

## ■ REFERENCES

- (1) Dusselier, M.; Davis, M. E. Small-Pore Zeolites: Synthesis and Catalysis. *Chem. Rev.* **2018**, *118*, 5265–5329.
- (2) Keane, M., Jr.; Sonnichsen, G. C.; Abrams, L.; Corbin, D. R.; Gier, T. E.; Shannon, R. D. Selective Synthesis of Dimethylamine over Small Pore Zeolites. *Appl. Catal.* **1987**, *32*, 361–366.
- (3) Ila, M. C.; Yamamoto, H.; Segawa, K. Shape-Selective Methylamine Synthesis over Small-Pore Zeolite Catalysts. *J. Catal.* **1996**, *161*, 20–30.

- (4) Segawa, K.; Hiroyasu, T. Highly Selective Methylamine Synthesis over Modified Mordenite Catalysts. *J. Catal.* **1991**, *131*, 482–490.
- (5) Tian, P.; Wei, Y.; Ye, M.; Liu, Z. Methanol to Olefins (MTO): From Fundamentals to Commercialization. *ACS Catal.* **2015**, *5*, 1922–1938.
- (6) Jeon, H. Y.; Shin, C. H.; Jung, H. J.; Hong, S. B. Catalytic Evaluation of Small-Pore Molecular Sieves with Different Framework Topologies for the Synthesis of Methylamines. *Appl. Catal., A* **2006**, *305*, 70–78.
- (7) Structure Commission of the International Zeolite Association. Framework Type MOR. <https://europe.iza-structure.org/IZA-SC/framework.php?STC=MOR> (accessed Feb 15, 2021).
- (8) Guisnet, M. “Coke” Molecules Trapped in the Micropores of Zeolites as Active Species in Hydrocarbon Transformations. *J. Mol. Catal. A: Chem.* **2002**, *182–183*, 367–382.
- (9) Hudson, M. R.; Queen, W. L.; Mason, J. A.; Fickel, D. W.; Lobo, R. F.; Brown, C. M. Unconventional, Highly Selective CO<sub>2</sub> Adsorption in Zeolite SSZ-13. *J. Am. Chem. Soc.* **2012**, *134*, 1970–1973.
- (10) Diban, N.; Aguayo, A. T.; Bilbao, J.; Urtiaga, A.; Ortiz, I. Membrane Reactors for in Situ Water Removal: A Review of Applications. *Ind. Eng. Chem. Res.* **2013**, *52*, 10342–10354.
- (11) Lu, N.; Xie, D. Novel Membrane Reactor Concepts for Hydrogen Production from Hydrocarbons: A Review. *Int. J. Chem. React. Eng.* **2016**, *14*, 1–31.
- (12) Gallucci, F.; Basile, A.; Hai, F. I. Introduction - A Review of Membrane Reactors. *Membr. Membr. React.* **2011**, *85*, 1–61.
- (13) Sunarso, J.; Hashim, S. S.; Zhu, N.; Zhou, W. Perovskite Oxides Applications in High Temperature Oxygen Separation, Solid Oxide Fuel Cell and Membrane Reactor: A Review. *Prog. Energy Combust. Sci.* **2017**, *61*, 57–77.
- (14) Shuit, S. H.; Ong, Y. T.; Lee, K. T.; Subhash, B.; Tan, S. H. Membrane Technology as a Promising Alternative in Biodiesel Production: A Review. *Biotechnol. Adv.* **2012**, *30*, 1364–1380.
- (15) Khajavi, S.; Jansen, J. C.; Kapteijn, F. Application of a Sodalite Membrane Reactor in Esterification - Coupling Reaction and Separation. *Catal. Today* **2010**, *156*, 132–139.
- (16) Caro, J.; Noack, M. Zeolite Membranes - Recent Developments and Progress. *Microporous Mesoporous Mater.* **2008**, *115*, 215–233.
- (17) Rieck genannt Best, F.; Mundstock, A.; Dräger, G.; Rusch, P.; Bigall, N. C.; Richter, H.; Caro, J. Methanol-to-Olefins in a Membrane Reactor with in Situ Steam Removal - The Decisive Role of Coking. *ChemCatChem* **2020**, *12*, 273–280.
- (18) Rohde, M. P.; Schaub, G.; Khajavi, S.; Jansen, J. C.; Kapteijn, F. Fischer-Tropsch Synthesis with in Situ H<sub>2</sub>O Removal - Directions of Membrane Development. *Microporous Mesoporous Mater.* **2008**, *115*, 123–136.
- (19) Zhou, C.; Wang, N.; Qian, Y.; Liu, X.; Caro, J.; Huang, A. Efficient Synthesis of Dimethyl Ether from Methanol in a Bifunctional Zeolite Membrane Reactor. *Angew. Chem., Int. Ed.* **2016**, *55*, 12678–12682.
- (20) Bordiga, S.; Regli, L.; Cocina, D.; Lamberti, C.; Bjørgen, M.; Lillerud, K. P. Assessing the Acidity of High Silica Chabazite H-SSZ-13 by FTIR Using CO as Molecular Probe: Comparison with H-SAPO-34. *J. Phys. Chem. B* **2005**, *109*, 2779–2784.
- (21) Corbin, D. R.; Schwarz, S.; Sonnichsen, G. C. Methylamines Synthesis: A Review. *Catal. Today* **1997**, *37*, 71–102.
- (22) Wang, L.; Zhu, D.; Wang, J.; Cui, W.; Han, J.; Li, B.; Fan, D.; Tian, P.; Liu, Z. Embryonic Zeolite-Assisted Synthesis of SSZ-13 with Superior Efficiency and Their Excellent Catalytic Performance. *J. Mater. Chem. A* **2021**, *9*, 15238–15245.
- (23) Yang, M.; Fan, D.; Wei, Y.; Tian, P.; Liu, Z. Recent Progress in Methanol-to-Olefins (MTO) Catalysts. *Adv. Mater.* **2019**, *31*, No. 1902181.
- (24) Fetting, F.; Dingerissen, U. Production of Methylamines over ZK-5 Zeolite Treated with Tetramethoxysilane. *Chem. Eng. Technol.* **1992**, *15*, 202–212.
- (25) Fischer, M. Water Adsorption in SAPO-34: Elucidating the Role of Local Heterogeneities and Defects Using Dispersion-Corrected DFT Calculations. *Phys. Chem. Chem. Phys.* **2015**, *17*, 25260–25271.
- (26) Fjermestad, T.; Svelle, S.; Swang, O. Mechanistic Comparison of the Dealumination in SSZ-13 and the Desilication in SAPO-34. *J. Phys. Chem. C* **2013**, *117*, 13442–13451.
- (27) Structure Commission of the International Zeolite Association. Framework Type CHA. <http://www.iza-structure.org/IZA-SC/references.php?STC=CHA> (accessed May 14, 2021).
- (28) Rostami, R. B.; Ghavipour, M.; Di, Z.; Wang, Y.; Behbahani, R. M. Study of Coke Deposition Phenomena on the SAPO<sub>34</sub> Catalyst and Its Effects on Light Olefin Selectivity during the Methanol to Olefin Reaction. *RSC Adv.* **2015**, *5*, 81965–81980.
- (29) Shelyapina; Krylova; Zhukov; Zvereva; Rodriguez-Iznaga; Petranovskii; Fuentes-Moyado. Comprehensive Analysis of the Copper Exchange Implemented in Ammonia and Protonated Forms of Mordenite Using Microwave and Conventional Methods. *Molecules* **2019**, *24*, 4216–4231.
- (30) Demuth, T.; Hafner, J.; Benco, L.; Toulhoat, H. Structural and Acidic Properties of Mordenite. An Ab Initio Density-Functional Study. *J. Phys. Chem. B* **2000**, *104*, 4593–4607.
- (31) Chen, D. T.; Zhang, L.; Yi, C.; Dumesic, J. A. Methylamine Synthesis over Solid Acid Catalysts: Microcalorimetric and Infrared Spectroscopic Studies of Adsorbed Species. *J. Catal.* **1994**, *146*, 257–267.
- (32) Nalaparaju, A.; Zhao, X. S.; Jiang, J. W. Molecular Understanding for the Adsorption of Water and Alcohols in Hydrophilic and Hydrophobic Zeolitic Metal-Organic Frameworks. *J. Phys. Chem. C* **2010**, *114*, 11542–11550.
- (33) Rutkai, G.; Csányi, É.; Kristóf, T. Prediction of Adsorption and Separation of Water-Alcohol Mixtures with Zeolite NaA. *Microporous Mesoporous Mater.* **2008**, *114*, 455–464.
- (34) Kosinov, N.; Auffret, C.; Borghuis, G. J.; Sripathi, V. G. P.; Hensen, E. J. M. Influence of the Si/Al Ratio on the Separation Properties of SSZ-13 Zeolite Membranes. *J. Membr. Sci.* **2015**, *484*, 140–145.
- (35) Bowen, T. C.; Noble, R. D.; Falconer, J. L. Fundamentals and Applications of Pervaporation through Zeolite Membranes. *J. Membr. Sci.* **2004**, *245*, 1–33.
- (36) Krishna, R.; Van Baten, J. M. Water/Alcohol Mixture Adsorption in Hydrophobic Materials: Enhanced Water Ingress Caused by Hydrogen Bonding. *ACS Omega* **2020**, *5*, 28393–28402.
- (37) Zhang, K.; Lively, R. P.; Noel, J. D.; Dose, M. E.; McCool, B. A.; Chance, R. R.; Koros, W. J. Adsorption of Water and Ethanol in MFI-Type Zeolites. *Langmuir* **2012**, *28*, 8664–8673.
- (38) Weigert, F. J. Selective Synthesis and Equilibration of Methylamines on Sodium Mordenite. *J. Catal.* **1987**, *103*, 20–29.
- (39) De Wispelaere, K.; Wondergem, C. S.; Ensing, B.; Hemelsoet, K.; Meijer, E. J.; Weckhuysen, B. M.; Van Speybroeck, V.; Ruiz-Martínez, J. Insight into the Effect of Water on the Methanol-to-Olefins Conversion in H-SAPO-34 from Molecular Simulations and in Situ Microspectroscopy. *ACS Catal.* **2016**, *6*, 1991–2002.
- (40) Moors, S. L. C.; De Wispelaere, K.; Van Der Mynsbrugge, J.; Waroquier, M.; Van Speybroeck, V. Molecular Dynamics Kinetic Study on the Zeolite-Catalyzed Benzene Methylation in ZSM-5. *ACS Catal.* **2013**, *3*, 2556–2567.
- (41) Wicke, E.; Kallenbach, R. Die Oberflächendiffusion von Kohlendioxid in Aktiven Kohlen. *Kolloid-Z.* **1941**, *97*, 135–151.
- (42) Wang, N.; Liu, Y.; Huang, A.; Caro, J. Hydrophilic SOD and LTA Membranes for Membrane-Supported Methanol, Dimethylether and Dimethylcarbonate Synthesis. *Microporous Mesoporous Mater.* **2015**, *207*, 33–38.
- (43) Wenten, I. G.; Dharmawijaya, P. T.; Aryanti, P. T. P.; Mukti, R. R.; Khoiruddin, K. LTA Zeolite Membranes: Current Progress and Challenges in Pervaporation. *RSC Adv.* **2017**, *7*, 29520–29539.
- (44) Paschek, D.; Krishna, R. Diffusion of Binary Mixtures in Zeolites: Kinetic Monte Carlo versus Molecular Dynamics Simulations. *Langmuir* **2001**, *17*, 247–254.



(45) Van Baelen, D.; Van Der Bruggen, B.; Van Den Dungen, K.; Degreve, J.; Vandecasteele, C. Pervaporation of Water-Alcohol Mixtures and Acetic Acid-Water Mixtures. *Chem. Eng. Sci.* **2005**, *60*, 1583–1590.

(46) Liu, B.; Kita, H.; Yogo, K. Preparation of Si-Rich LTA Zeolite Membrane Using Organic Template-Free Solution for Methanol Dehydration. *Sep. Purif. Technol.* **2020**, *239*, No. 116533.

(47) Li, J. R.; Kuppler, R. J.; Zhou, H. C. Selective Gas Adsorption and Separation in Metal-Organic Frameworks. *Chem. Soc. Rev.* **2009**, *38*, 1477–1504.

(48) Fahami, A. R.; Günter, T.; Doronkin, D. E.; Casapu, M.; Zengel, D.; Vuong, T. H.; Simon, M.; Breher, F.; Kucherov, A. V.; Brückner, A.; Grunwaldt, J. D. The Dynamic Nature of Cu Sites in Cu-SSZ-13 and the Origin of the Seagull NOX Conversion Profile during NH<sub>3</sub>-SCR. *React. Chem. Eng.* **2019**, *4*, 1000–1018.

(49) Naderi, M. Surface Area: Brunauer-Emmett-Teller (BET). *Prog. Filtr. Sep.* **2015**, *180*, 585–608.

(50) DFG SPP 2005—Priority Programm Opus Fluidum Futurum—Rheology of Reactive, Multiscale, Multiphase Construction Materials. [https://www.dfg.de/en/funded\\_projects/current\\_projects\\_programmes/list/projectdetails/index.jsp?id=313773090&sort=nr\\_asc&prg=SPP](https://www.dfg.de/en/funded_projects/current_projects_programmes/list/projectdetails/index.jsp?id=313773090&sort=nr_asc&prg=SPP)(accessed Sep 9, 2021).

## Supporting Information

# Boosting Dimethylamine Formation Selectivity in a Membrane Reactor by in situ Water Removal

*Felix Rieck genannt Best,<sup>\*,a</sup> Alexander Mundstock,<sup>a</sup> Patrick A. Kießling,<sup>a</sup> Hannes Richter,<sup>b</sup>*

*Karen D. J. Hindricks,<sup>c,d</sup> Aisheng Huang,<sup>e</sup> Peter Behrens,<sup>c,d,f</sup> Jürgen Caro<sup>a,f,g</sup>*

<sup>a</sup> Institute of Physical Chemistry and Electrochemistry, Leibniz University Hannover,

Callinstrasse 3A, Hannover 30167, Germany

<sup>b</sup> Fraunhofer IKTS, Institute for Ceramic Technologies and Systems, Fraunhofer IKTS,

Michael-Faraday-Straße 1, Hermsdorf 07629, Germany

<sup>c</sup> Institute of Inorganic Chemistry, Leibniz University Hannover, Callinstrasse 9, Hannover

30167, Germany

<sup>d</sup> Cluster of Excellence PhoenixD (Photonics, Optics, and Engineering – Innovation Across

Disciplines), Welfengarten 1A, 30167 Hannover, Germany

<sup>e</sup> Shanghai Key Laboratory of Green Chemistry and Chemical Processes, Department of Chemistry, East China Normal University, Dongchuan Road 500, Shanghai 200241, China

<sup>f</sup> Laboratory of Nano and Quantum Engineering, Leibniz University Hannover,  
Schneiderberg 39, 30167 Hannover, Germany

<sup>g</sup> School of Chemistry and Chemical Engineering, South China University of Technology,  
Wushan Road 381, Guangzhou 510640, China

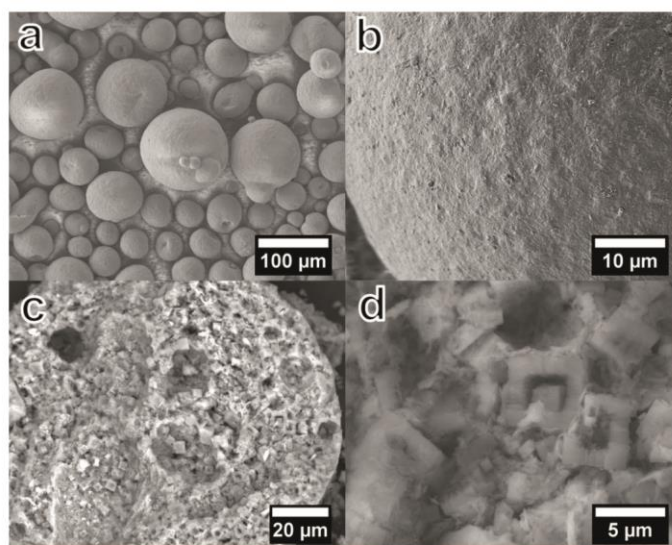


**Figure S1.** SEM micrographs of H-SAPO-34 particles at a magnification of (a) 250x, (b) 2500x, (c) 1000x and (d) 5000x. The particles in (c) and (d) have been crushed to investigate the inside of the spherical particles showing cubic H-SAPO-34 crystals.

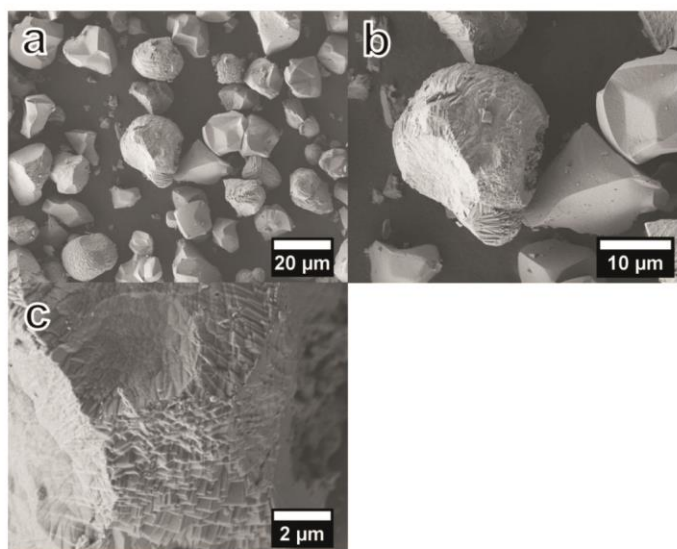


**Figure S2.** SEM micrographs of H-SSZ-13 particles at a magnification of (a) 1000x, (b) 2500x and (c) 10000x.

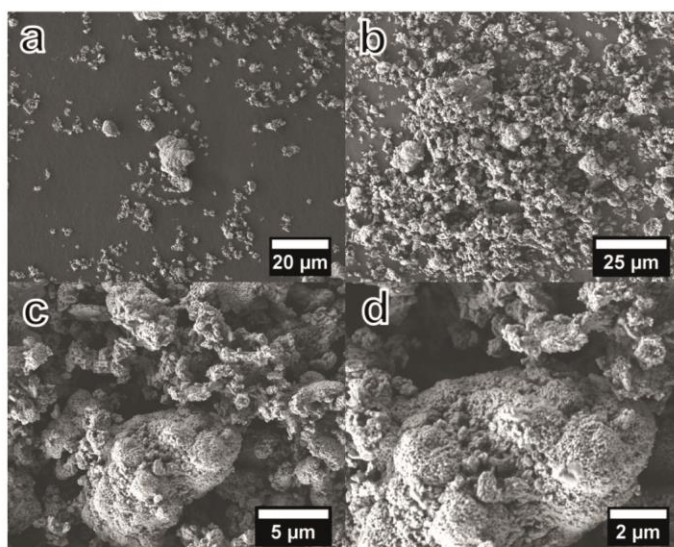


**Figure S3.** SEM micrographs of H-MOR particles at a magnification of (a), (b) 1000x, (c) 5000x and (d) 10000x.

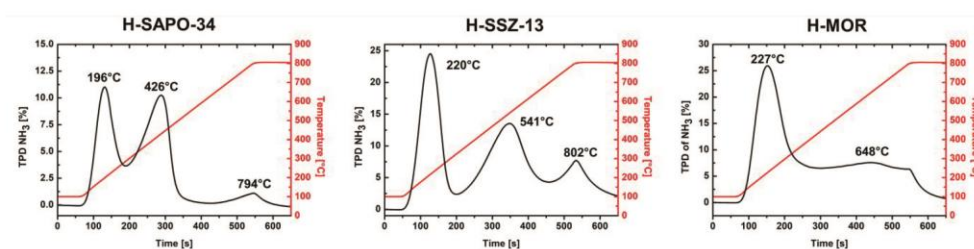


**Figure S4.** Temperature programmed desorption (TPD) curves of NH<sub>3</sub> of H-SAPO-34, H-SSZ-13 and H-MOR in a temperature range of 100-800 °C. Acquisition time = 650 s.

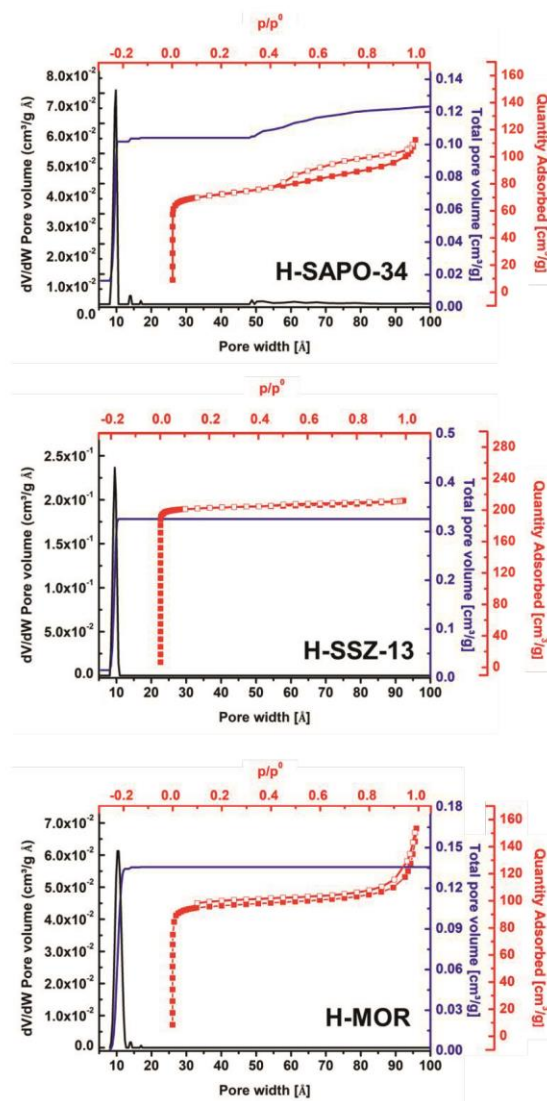


**Figure S5.** Pore size distribution curves of H-SAPO-34, H-SSZ-13 and H-MOR with  $dV/dW$  pore volume (black) and total pore volume (blue) shown in relation to the pore width, as well as sorption isotherms (red).

**Table S1.** Main peak positions of the IR spectra of H<sub>2</sub>O, MeOH and the 1:1 mixture of H<sub>2</sub>O/MeOH adsorbed on H-SAPO-34 based on **Figure 6**. All modes are given as wavenumbers [cm<sup>-1</sup>].

	H-SAPO-34	H-SAPO-34 + H <sub>2</sub> O	H-SAPO-34 + MeOH	H-SAPO-34 + MeOH/H <sub>2</sub> O
<b>H-SAPO-34</b>	$\delta_t(\text{O}_z\text{H}_z)$ )	1066		
<b>H<sub>2</sub>O</b>	$\nu(\text{H}_2\text{O})$	3368-3256		3374-3270
	$\delta(\text{H}_2\text{O})$	1636		1653
<b>MeOH</b>	$\nu(\text{OH})$		3319	
	$\nu(\text{CH})$		2943/ 2924/ 2831	2949/ 2929/ 2837
	$\delta(\text{CH})$		1458	1448
	$\delta(\text{CH}_3)$		1437	1419
	$\delta(\text{O}_z\text{H}_z)$		1022	1012



**Table S2.** Main peak positions of the IR spectra of H<sub>2</sub>O, MeOH and the 1:1 mixture of H<sub>2</sub>O/MeOH adsorbed on H-MOR based on the data shown in **Figure 6**. All modes are given as wavenumbers [cm<sup>-1</sup>].

		H-MOR	H-MOR + H <sub>2</sub> O	H-MOR + MeOH	H-MOR + MeOH/H <sub>2</sub> O
<b>H-MOR</b>	$\delta_t(\text{O}_z\text{H}_z)$	1071			
<b>H<sub>2</sub>O</b>	$\nu(\text{H}_2\text{O})$		3364-3246		3365-3255
	$\delta(\text{H}_2\text{O})$		1645		1650
<b>MeOH</b>	$\nu(\text{OH})$			3324	
	$\nu(\text{CH})$			2943/ 2925/ 2832	2947/ 2932/ 2838
	$\delta(\text{CH})$			1458	1457
	$\delta(\text{CH}_3)$			1437	1422
	$\delta(\text{O}_z\text{H}_z)$			1019	1009

HEMELSOET et al. previously calculated the IR band positions of methanol adsorbed on SAPO-34.<sup>1</sup> Our spectra match these results well with a slight red shift, in particular for the OH-stretching mode of methanol. The exact peak positions of the most prominent vibrational modes of guest molecules in H-SAPO-34 can be found in **Table S1** and for H-MOR in

**Table S2.**

The methanol signals of the three -CH stretching modes ( $\nu(\text{CH})$  at 2831-2949  $\text{cm}^{-1}$ ), the two bending modes of -CH and -CH<sub>3</sub> ( $\delta(\text{CH})$ ,  $\delta(\text{CH}_3)$  at 1419-1458  $\text{cm}^{-1}$ ) and the out-of-plane bending mode ( $\delta(\text{O}_z\text{H}_z)$  at 1009-1022  $\text{cm}^{-1}$ ) show clear differences in the IR spectra of the adsorbed MeOH/water mixture in H-SAPO-34 and H-MOR, see **Figure 6**. Overall, the distinctive signals for adsorption at H-SAPO-34 all show the same tendency: The MeOH/water mixture results in MeOH signals with a decreased intensity compared to the adsorption of pure MeOH. Thereof, it can be concluded that the adsorption of MeOH is hindered due to the competitive adsorption of water.

On the other hand, if the MeOH/H<sub>2</sub>O mixture is adsorbed in H-MOR, large IR signals of both components can be found, which leads to the conclusion that the MeOH adsorption in H-MOR is barely influenced by the water content.

(1) Hemelsoet, K.; Ghysels, A.; Mores, D.; Wispelaere, K. De; Speybroeck, V. Van;

Weckhuysen, B. M.; Waroquier, M. Experimental and Theoretical IR Study of Methanol and Ethanol Conversion over H-SAPO-34. *Catal. Today* **2011**, *177* (1), 12–24.  
<https://doi.org/10.1016/j.cattod.2011.05.040>.

### **10.3. Controlled methylamine synthesis in a membrane reactor featuring a highly steam selective K<sup>+</sup>-LTA membrane**

While the results of the previous study were promising, as the DMA and TMA selectivities could be influenced by the water extraction through the LTA membrane, one finding was still bothersome. The water removal did not enhance the methanol conversion rate, as LE CHATELIER'S principle would have predicted. This was presumably based on the observation that the Na-LTA membrane lacked a sufficient separation selectivities of water with the reactant methanol and ammonia, respectively. To bypass this upcoming problem, we decided based on my idea and previous work done on the topic in Prof. Dr. Jürgen Caro research group, to perform a post synthesis ion exchange with the Na-LTA membrane to receive a dense K-LTA membrane. The ion exchange should narrow down the pore windows of the zeolite membrane, resulting in enhanced water/methanol and water/ammonia selectivities and improving the methanol conversion rate, while further optimizing the concept of water removal through zeolite membrane support in the methylamine synthesis.

In this study, my part was performing the ion exchange experiments to receive the K-LTA membrane and testing this membrane in the methylamine synthesis. I, furthermore, conducted the difficult high temperature single- and mixed-gas permeation experiments to evaluate the membranes' performances.



Contents lists available at ScienceDirect

## Microporous and Mesoporous Materials

journal homepage: [www.elsevier.com/locate/micromeso](http://www.elsevier.com/locate/micromeso)Controlled methylamine synthesis in a membrane reactor featuring a highly steam selective K<sup>+</sup>-LTA membraneFelix Rieck genannt Best<sup>a,\*</sup>, Alexander Mundstock<sup>a</sup>, Hannes Richter<sup>b</sup>, Patrick A. Kißling<sup>a</sup>, Karen D.J. Hindricks<sup>c,d</sup>, Aisheng Huang<sup>e</sup>, Peter Behrens<sup>c,d,f</sup>, Jürgen Caro<sup>a,f,g</sup><sup>a</sup> Institute of Physical Chemistry and Electrochemistry, Leibniz University Hannover, Callinstraße 3A, Hannover, 30167, Germany<sup>b</sup> Fraunhofer IKTS, Institute for Ceramic Technologies and Systems, Michael-Faraday-Straße 1, Hemsdorf, 07629, Germany<sup>c</sup> Institute of Inorganic Chemistry, Leibniz University Hannover, Callinstraße 9, Hannover, 30167, Germany<sup>d</sup> Cluster of Excellence PhoenixD (Photonics, Optics, and Engineering – Innovation Across Disciplines), Welfengarten 1A, 30167, Hannover, Germany<sup>e</sup> Shanghai Key Laboratory of Green Chemistry and Chemical Processes, Department of Chemistry, East China Normal University, Dongchuan Road 500, Shanghai, 200241, China<sup>f</sup> Laboratory of Nano and Quantum Engineering, Leibniz University Hannover, Schneiderberg 39, 30167, Hannover, Germany<sup>g</sup> School of Chemistry and Chemical Engineering, South China University of Technology, Wushan Road 381, Guangzhou, 510640, China

## ARTICLE INFO

## Keywords:

Zeolite membranes  
Cation exchange  
Hydrophilic LTA membrane  
In situ water removal  
Methylamines  
Membrane reactor

## ABSTRACT

Water permeation through a hydrophilic zeolite membrane can be used to promote reactions under equilibrium controlled conditions through the in situ removal of the by-product water. In the methylamine synthesis, mono- (MMA), di- (DMA) and trimethylamine (TMA) are formed by the successive methylation of ammonia with methanol (MeOH) over a mildly acidic catalyst. The methylamine yield can be increased through selective water extraction from the reactor through a membrane. Since both reactants and water have similar molecular kinetic diameters below 3.7 Å, because of the limited steam selectivity of the commonly used hydrophilic Na-LTA membrane (zeolite 4A), not only water has been removed. Therefore, in this work a K-LTA membrane, which was obtained by ion exchange with a reduced pore window diameter of 3 Å and thus with a higher water selectivity, was used in the membrane-supported methylamine synthesis. When replacing the Na-LTA with the K-LTA membrane, the H<sub>2</sub>O/MeOH mixed gas separation factor increases up to 1100 and the H<sub>2</sub>O/NH<sub>3</sub> separation could also be improved. This in turn leads to an overall boost of the higher methylated amines DMA and TMA in methylamine synthesis. When using the narrow-pore aluminosilicate catalyst H-SSZ-13 with CHA structure, the application of the K-LTA membrane increases the share of the industrially desired product DMA from 51% without membrane to 74% with slightly increased conversion. When using the large-pore catalyst H-MOR, the thermodynamically most stable product TMA can be formed and the selectivity was increased from 35% without membrane to 41% with the K-LTA membrane.

## 1. Introduction

Hydrophilic zeolite membranes for dehydration of alcohols and other solvents via pervaporation and steam permeation processes have already been subject of research [1,2], though only occasionally Linde Type A (LTA) membranes have been scaled-up successfully [3,4].

Additionally, water vapor removing zeolite membranes have also been successfully applied in catalytic membrane reactors on a lab scale to boost yield or steer selectivity. Examples for the yield increase are the DME synthesis [5], methanol-to-olefins (MTO) reaction [6], Fischer-Tropsch synthesis [7] and CO<sub>2</sub> hydrogenation [8]. In this work,

we will improve the methylamine synthesis in a membrane reactor through altering the pore size of a hydrophilic LTA membrane grown on an α-Al<sub>2</sub>O<sub>3</sub> tube. Methylamine is formed from methanol and ammonia over mildly acidic catalysts at temperatures of around 400 °C. The reaction results in three different amines: First monomethylamine (MMA), which can react with another methanol molecule to form dimethylamine (DMA) and, subsequently, trimethylamine (TMA), with water in each methylation step as a by-product [9,10]. Further, the formation of dimethyl ether (DME) can occur via the reaction of two MeOH molecules. We previously reported the effect of the Na-variant of the LTA membrane on the selectivity towards these different amines [11]. We

\* Corresponding author.

E-mail address: [felix.best@pci.uni-hannover.de](mailto:felix.best@pci.uni-hannover.de) (F. Rieck genannt Best).<https://doi.org/10.1016/j.micromeso.2022.111920>

Received 18 February 2022; Received in revised form 11 April 2022; Accepted 13 April 2022

Available online 16 April 2022

1387-1811/© 2022 Elsevier Inc. All rights reserved.

found that the removal of water leads to an increased methylation rate, which results in a higher selectivity towards DMA and TMA. DMA is the industrially preferred product, as it is used as the starting compound for dimethylformamide synthesis [12] and is commonly used as an additive. On the other hand, the formation of TMA is tried to be suppressed as its demand is considerably lower compared to DMA, while it forms an azeotropic mixture with water, which requires an expensive product separation [13]. Depending on the used methylamine catalyst, the methylation reaction can be effectively stopped at the DMA step. H-SSZ-13, a CHA type aluminosilicate, has a narrow pore diameter, which prevents the development of the transition state required to form TMA [14]. The use of the water removing Na-LTA membrane massively increases the DMA selectivity. When using the catalyst H-MOR, a zeolite with large pores, the thermodynamically favored TMA formation can occur and the water removal increases the TMA selectivity.

However, the application of the hydrophilic Na-LTA membrane did not result in the expected overall yield increase, presumably due to an unexpected loss of the reactants MeOH and NH<sub>3</sub> through the membrane alongside with water. To minimize this unintended and non-selective extraction, we decided to narrow the pore windows of the LTA membrane from 4 Å (Na-LTA) to 3 Å through a post-synthesis K<sup>+</sup> ion exchange. Ion exchanged zeolites have been studied in numerous works to modify the pore size with a control over other certain properties (hydrophilicity, adsorption sites) to improve separation [15–17]. In our study the Na-LTA membrane was submerged in 0.5 M KNO<sub>3</sub> solution for 24 h, thoroughly washed with Millipore water and afterwards dried up to 120 °C in 10 °C steps for 2 h each.

All relevant pore properties and reactant molecule dimensions are given in Table 1.

Hydrophilic membranes show a high selectivity towards water, which is mainly due to adsorption instead diffusion control and they tend to struggle with releasing the water until the membrane is saturated, so external factors are needed to the diffusion, like higher temperatures or pressure gradients with overpressure on the retentate side. In this study, both Na-LTA and K-LTA are hydrophilic membranes with an Si/Al ratio of 1. By introducing Al into the silicate framework, negative charges are generated, which get balanced by the corresponding cations Na<sup>+</sup> or K<sup>+</sup> and thereby increase the framework polarity. Conclusively, the high Al contents directly lead to the hydrophilic pore surface. The benefits of K<sup>+</sup> ion exchange, as the improved selectivities have been described in previous publications [18–21].

## 2. Experimental section

The methylamine synthesis was performed at 350 °C for 180 min in a vertically orientated tube membrane reactor. The Al<sub>2</sub>O<sub>3</sub> tube had a length of 300 mm, an outer diameter of 10 mm and was coated on the inside with a K-LTA zeolite membrane. The ceramic tube, or the reactor itself in experiments without membrane support, where centrally filled with glass wool and 1 g of the respective catalyst (H-SSZ-13 or H-MOR) was loosely piled on top. Methanol (Roth, ≥ 99.9%) was introduced at 4.78 g/h into the reactor system by combining with N<sub>2</sub> (Q<sub>N<sub>2</sub></sub> = 23.5 mL/min) to create an aerosol using a Bronkhorst Controlled Evaporator Mixer (CEM) W-102A. The aerosol was mixed with NH<sub>3</sub> (Q<sub>NH<sub>3</sub></sub> = 23.5

mL/min) before being directed into the tube reactor. In experiments with the LTA membrane, Ar (Q<sub>Ar</sub> = 2 mL/min) was applied on the permeate side. The gases N<sub>2</sub> (≥99.999%, Linde), NH<sub>3</sub> (≥99.999%, Linde) and Ar (≥99.999%, Linde) were dosed by Bronkhorst mass flow controllers EL-FLOW® Prestige.

The tubular Na-LTA membranes were manufactured by the Fraunhofer Institute of Ceramic Technologies and Systems (IKTS) in Hermsdorf/Germany, for further information on the synthesis process please contact them directly.

Ion exchange to get K-LTA was performed with a 0.5 M KNO<sub>3</sub> solution, in which the respective membrane was submerged for 24 h. The membrane was washed thoroughly with Millipore water and then dried up to 120 °C in 10 °C steps for 2 h each.

H-MOR was acquired from Süd-Chemie AG and H-SSZ-13 was synthesized following a modified method from Fahami et al. [22] A mixture of 0.39 g sodium hydroxide, 23.6 g Millipore water, 8.51 g *N,N,N*-trimethyladamantylammonium hydroxide (TMAdOH, 25 wt% in water, TCI) and 0.25 g aluminium hydroxide (Sigma-Aldrich) were stirred for 30 min and subsequently mixed with 7.48 g LUDOX® AS-40 (Sigma-Aldrich). The formed gel aged 2 h in a 115 mL Teflon autoclave which was then heated to 160 °C for 4 days. The resulting powder was filtered and thoroughly washed with Millipore water and dried at 80 °C over-night, before being calcined at 550 °C for 2 h. The ion exchange was performed with 1 M NH<sub>4</sub>NO<sub>3</sub> (Sigma Aldrich, ≥ 99.0%) solution with 20 mL/g Na-SSZ-13 for 3 h at 80 °C. The gel was subsequently filtered, washed, dried at 80 °C over-night and calcined at 550 °C for 2 h. The ion exchange steps were repeated three times overall.

The methylamine synthesis product analysis was performed by gas chromatography on an Agilent 7890A GC System, equipped with a Restek RTX® Volatile Amine column and a thermal conductivity detector (TCD).

X-ray diffraction patterns were acquired via a Bruker D8 Advance diffractometer operating at 30 kV and 40 mA with Cu-K<sub>α</sub> radiation (λ = 0.154 nm) in a 2θ range of 5°–45°. SEM images and EDXS mapping were performed on a JEOL JSM 6700F operating at 2 kV (10 kV for EDXS) and 10 μA with a LEI detector.

Permeation experiments were performed in a modified Wicke-Kallenbach setup between 100 °C and 250 °C. Gases and mass flow controllers are the same as mentioned above. The aerosols of water and methanol were directed into the permeation cell with 20 mL/min. N<sub>2</sub> (Q<sub>N<sub>2</sub></sub> = 2 mL/min) was applied on the permeation side. Analysis was carried out with the same GC setup as mentioned above.

Prior to all sorption measurements, the samples were degassed under vacuum at 200 °C for 20 h. Nitrogen physisorption isotherms were measured at 77 K on a Micromeritics 3Flex instrument. Surface areas were determined by applying the Brunauer-Emmet-Teller (BET) equation. The total pore volume was estimated using the single-point method at p/p<sub>0</sub> = 0.95. Barrett-Joyner-Halenda (BJH) method was applied to determine the pore size distribution. CO<sub>2</sub> physisorption measurements were carried out at 273.15 K on a Micromeritics ASAP 2020. The static H<sub>2</sub>O and MeOH sorption measurements were performed on a vapor 100C from 3P instruments at 298 K. The H<sub>2</sub>O and MeOH vapor source were freeze dried three times using liquid nitrogen to assure a pure vapor and heated during the measurements at 40 °C and 25 °C

**Table 1**

Pore window sizes and Na/K atomic% for Na-LTA [18] and K-LTA [36], kinetic diameters for H<sub>2</sub>O [27], NH<sub>3</sub> [27], MeOH [27], DME [37] and molecule dimensions for MMA, DMA, TMA [9].

	Na LTA	K LTA	Compound	Kinetic diameter [Å]	Methylamine	Molecule size [Å]
Pore window size [Å]	4.1	3.0	H <sub>2</sub> O	2.6	MMA	3.7 × 3.9 × 4.4
Na atomic% <sup>a</sup>	11.3 ± 0.48	0.22 ± 0.05	NH <sub>3</sub>	2.9	DMA	3.9 × 4.7 × 6.0
K atomic% <sup>a</sup>	0	11.4 ± 0.35	MeOH	3.6	TMA	3.9 × 5.4 × 6.1
			DME	4.7		

<sup>a</sup> Measured via EDXS, see Fig. 1.

respectively.

### 3. Results and discussion

Scanning electron microscopy (SEM) micrographs and energy dispersive X-ray spectroscopy (EDXS) mappings of the Na- and K-LTA membranes are displayed in Fig. 1.

The SEM images in Fig. 1 in combination with a successful  $N_2$  leak test show that the membrane after the  $K^+$ -ion exchange is free of microscopic cracks. The membranes are uniformly grown and possess an average thickness of around  $4\ \mu\text{m}$ , while the EDXS mappings of the Na-LTA and K-LTA membranes exhibit the expected distribution for Si and Al, as Si can only be found in the LTA membrane, while Al is spread across both the  $\alpha\text{-Al}_2\text{O}_3$  support and the supported LTA zeolite membrane. The corresponding cations  $Na^+$  or  $K^+$  are mainly located in the LTA layer and the elemental ratios from EDXS show that the  $Na^+$  was exchanged with  $K^+$  almost completely with over 98%, see Table 1.

X-ray diffraction (XRD) measurements (Fig. 2) and  $CO_2$  physisorption and vapor sorption measurements (Fig. S2) were performed to evaluate the influence of the  $K^+$ -ion exchange on the LTA zeolite crystal structure, its pore dimensions and adsorption capacities.

The XRD patterns show that the crystal structure is preserved after the  $K^+$  ion exchange. Interestingly, the signals in the lower  $2\theta$  area, are much more distinct for the K-LTA. No impurities or signals from leftover  $KNO_3$  can be observed in the K-LTA pattern. The zoom-in highlights the expected expansion of the LTA framework through the incorporation of the large  $K^+$ -ions. As the  $K^+$  ion is larger than  $Na^+$ , the crystal lattice expands while the free passage through the windows becomes subsequently smaller due to the 3 large K-cations found for LTA near the center of the eight-rings and close to the eight-ring planes, resulting in an angle shift to smaller values for K-LTA [23].

The Na-LTA membrane was grown inside a tubular  $\alpha\text{-Al}_2\text{O}_3$  support by the Fraunhofer IKTS and afterwards ion exchanged with 0.5 M  $KNO_3$  solution to receive a K-LTA membrane. The tube was filled with glass wool and 1 g of the respective catalyst was piled on top. Two acidic zeolites with different pore sizes, H-SSZ-13 (Si/Al ratio based on EDXS measurements  $\sim 15$ ) and H-MOR (Si/Al  $\sim 5$ ), were tested as methylamine catalysts. They possess different crystal structures and pore systems, leading to different reaction paths in the methylamine synthesis by ammonia methylation. For the small-pore zeolite H-SSZ-13 (pore diameter  $3.8\ \text{\AA}$  [24]) a Langmuir-Hinshelwood mechanism was proposed, as space restrictions inside the pore system require both reactants

to adsorb to the surface [13]. The steric effects lead to a transition state selectivity with a high DMA selectivity and are the reason for the largely suppressed formation of TMA, since the required transition state cannot be formed. For H-MOR, a zeolite with large-sized pore channels (channel size  $6.5\ \text{\AA} \times 7.0\ \text{\AA}$ ), an Eley-Rideal mechanism is likely the predominant reaction path [25]. The results of the methylamine formation with and without Na-LTA and K-LTA membranes can be found in Fig. 3.

The performance differences of the catalysts H-SSZ-13 and H-MOR with and without Na-LTA membrane support have been discussed in detail in our previous work [11]. The key discovery was that removing water through the LTA membrane led to an increase of higher-methylated amines. While H-MOR can produce the thermodynamically favored product TMA, this trend of consecutive methylation was stopped at DMA for H-SSZ-13 since the narrow CHA pores do not allow the TMA formation for steric reasons. Furthermore, we observed that the application of the Na-LTA membrane had a more significant influence in the case of the small-pore zeolite catalyst, as space restrictions and active site blocking by water play a bigger role in the narrow pore system. Surprisingly, we could not observe the expected increase of MeOH conversion, as *s*-LeChatelier's principle would have predicted. Instead the methanol conversion remained steady for both H-SSZ-13 and H-MOR with and without Na-LTA membrane support. We concluded that the insufficient  $H_2O/MeOH$  and  $H_2O/NH_3$  selectivity of the Na-LTA membrane was responsible for an unintentional loss of the reactants MeOH and  $NH_3$  through the membrane, leading to a higher share of unreacted MeOH.

The higher water selectivity of the K-LTA membrane compared to Na-LTA membrane results in an MeOH conversion rate increased from 91% (without membrane) to 94% (with membrane) for H-SSZ-13, and in an improvement from 70% (without membrane) to 80% in the case of the H-MOR catalyst. The K-LTA membrane causes an even larger shift to the higher methylated amines, as the share of DMA (for H-SSZ-13) increases by 23% and of TMA (for H-MOR) by 6%, an even higher share of DMA or TMA than obtained using the Na-LTA membrane. Since the pore narrowing of the K-LTA membrane slightly reduces water permeance, as Table 2 shows, this shift is probably not induced by a higher water removal. Even if the water permeance is reduced to 2/3 for the K-LTA membrane, it is still sufficient to extract all water in situ from the membrane reactor. The K-LTA membrane massively reduces the MeOH permeance compared to Na-LTA, while  $NH_3$  with its kinetic diameter of  $2.9\ \text{\AA}$  nearly fits the pore window of the K-LTA. The increased share of DMA and TMA when using the K-LTA membrane is due to the fact that

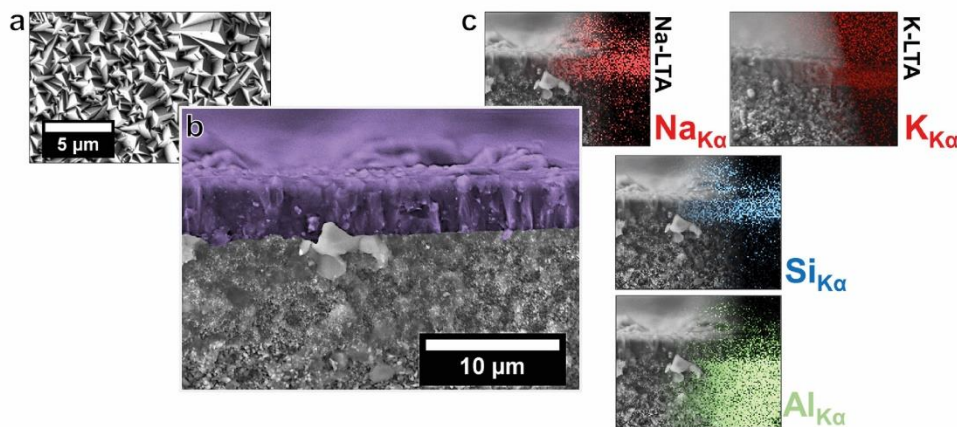


Fig. 1. SEM micrographs of an LTA membrane: a top-down image, b cross sectioned images with the K-LTA membrane in purple on the  $Al_2O_3$  support, and c SEM cross section with superimposed EDXS mapping of  $Na_{Ka}$  for Na-LTA (before  $K^+$ -ion exchange),  $K_{Ka}$  for K-LTA,  $Si_{Ka}$  and  $Al_{Ka}$ . (For interpretation of the references to colour in this figure legend, the reader is referred to the Web version of this article.)

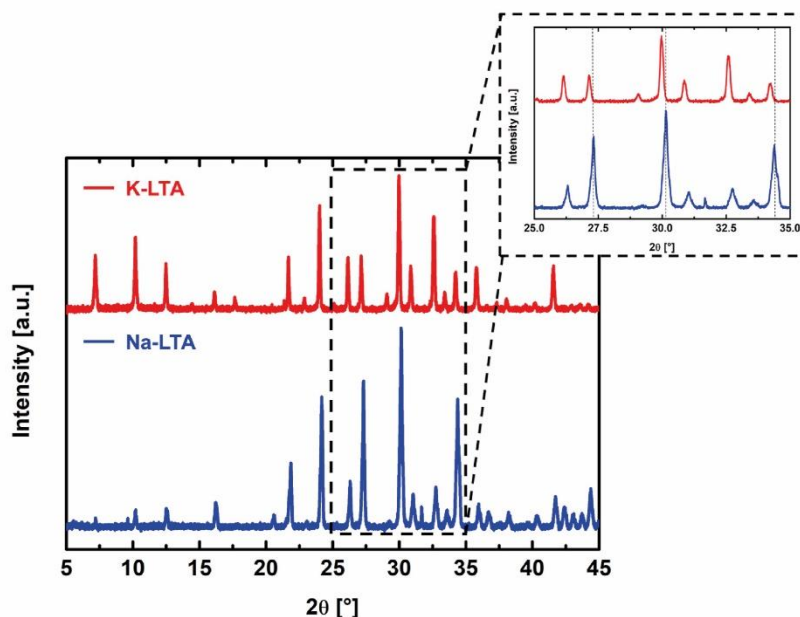


Fig. 2. X-ray diffraction (XRD) patterns of Na-LTA (black) and K-LTA (red) in angle ranges of  $5^\circ \leq 2\theta \leq 45^\circ$ , including a zoom-in in a range of  $25^\circ \leq 2\theta \leq 35^\circ$ . (For interpretation of the references to colour in this figure legend, the reader is referred to the Web version of this article.)

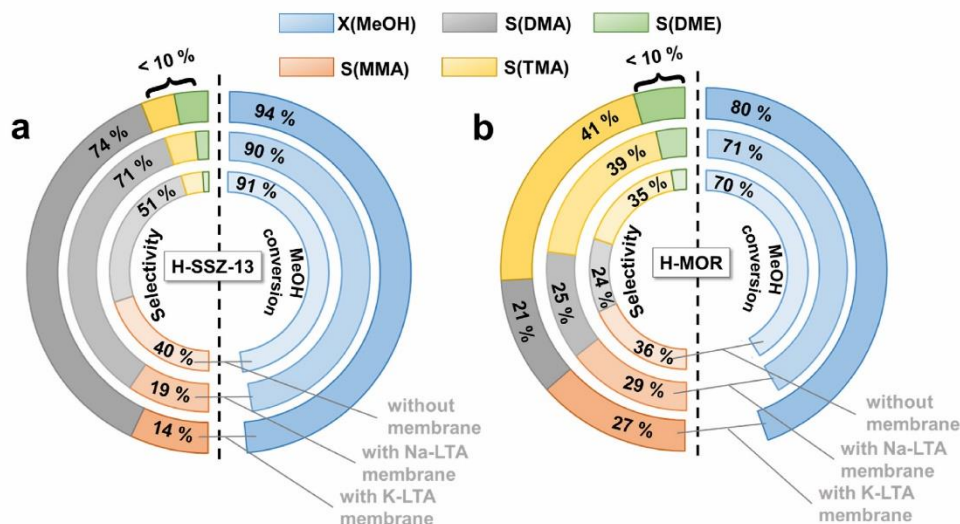


Fig. 3. Methylamine synthesis performance scheme for a H-SSZ-13 and b H-MOR. Shown are the methanol conversion (blue); MMA (red), DMA (grey), TMA (yellow) and DME selectivities (green) without membrane support (inner circle), with Na-LTA membrane (middle circle) and K-LTA membrane (outer circle). The catalysts were activated by heating in a  $N_2$  stream at  $400^\circ C$  for 90 min. The reaction was performed at  $350^\circ C$  with  $MeOH/NH_3 = 2.5$  and  $WHSV_{MeOH} = 2.4 \text{ g cat}^{-1} \text{ h}^{-1}$  at 1 bar. The overall methanol conversion was calculated based on the original feed composition. Detailed information can be found in Table S1. (For interpretation of the references to colour in this figure legend, the reader is referred to the Web version of this article.)

ammonia still gets removed in small parts by the K-LTA membrane, while MeOH is kept inside the tube reactor, see Table 2, which leads to a slightly altered reactant composition of the original MeOH/ $NH_3$  ratio of 2.5. An increased contact time of MeOH with ammonia or the

methylated amine is a further reason for the improved  $H_2O/MeOH$  selectivity, which benefits methylation and, conclusively, leads to a higher share of DMA and TMA [26]. An indication towards the higher MeOH contact time can be found in the increasing yield of DME, as it is



**Table 2**

Gas permeances of H<sub>2</sub>O, NH<sub>3</sub> and MeOH through Na-LTA and K-LTA membranes at 100 °C, 150 °C, 200 °C and 250 °C in **a** H<sub>2</sub>O/NH<sub>3</sub> mixed gas permeation, **b** H<sub>2</sub>O/MeOH mixed gas permeation, **c** H<sub>2</sub>O and NH<sub>3</sub> single gas permeation and **d** H<sub>2</sub>O and MeOH single gas permeation.

a H <sub>2</sub> O/NH <sub>3</sub> mixed gas permeation					
	Temperature [°C]	100	150	200	250
<b>Na-LTA</b>	H <sub>2</sub> O permeance [mol s <sup>-1</sup> m <sup>-2</sup> Pa <sup>-1</sup> ]	3.5 × 10 <sup>-8</sup>	9.0 × 10 <sup>-8</sup>	1.4 × 10 <sup>-7</sup>	1.2 × 10 <sup>-7</sup>
	NH <sub>3</sub> permeance [mol s <sup>-1</sup> m <sup>-2</sup> Pa <sup>-1</sup> ]	3.2 × 10 <sup>-8</sup>	8.0 × 10 <sup>-9</sup>	7.6 × 10 <sup>-9</sup>	6.8 × 10 <sup>-9</sup>
	Selectivity H <sub>2</sub> O/ NH <sub>3</sub>	1	11	18	17
<b>K-LTA</b>	H <sub>2</sub> O permeance [mol s <sup>-1</sup> m <sup>-2</sup> Pa <sup>-1</sup> ]	3.6 × 10 <sup>-8</sup>	7.5 × 10 <sup>-8</sup>	8.3 × 10 <sup>-8</sup>	8.5 × 10 <sup>-8</sup>
	NH <sub>3</sub> permeance [mol s <sup>-1</sup> m <sup>-2</sup> Pa <sup>-1</sup> ]	3.0 × 10 <sup>-9</sup>	2.8 × 10 <sup>-9</sup>	2.0 × 10 <sup>-9</sup>	1.4 × 10 <sup>-9</sup>
	Selectivity H <sub>2</sub> O/ NH <sub>3</sub>	12	27	41	61
b H <sub>2</sub> O/MeOH mixed gas permeation					
	Temperature [°C]	100	150	200	250
<b>Na-LTA</b>	H <sub>2</sub> O permeance [mol s <sup>-1</sup> m <sup>-2</sup> Pa <sup>-1</sup> ]	5.9 × 10 <sup>-8</sup>	9.2 × 10 <sup>-8</sup>	1.3 × 10 <sup>-7</sup>	1.3 × 10 <sup>-7</sup>
	MeOH permeance [mol s <sup>-1</sup> m <sup>-2</sup> Pa <sup>-1</sup> ]	1.2 × 10 <sup>-8</sup>	1.0 × 10 <sup>-8</sup>	9.4 × 10 <sup>-9</sup>	9.0 × 10 <sup>-9</sup>
	Selectivity H <sub>2</sub> O/ MeOH	5	10	14	15
<b>K-LTA</b>	H <sub>2</sub> O permeance [mol s <sup>-1</sup> m <sup>-2</sup> Pa <sup>-1</sup> ]	4.8 × 10 <sup>-8</sup>	6.6 × 10 <sup>-8</sup>	8.4 × 10 <sup>-8</sup>	9.0 × 10 <sup>-8</sup>
	MeOH permeance [mol s <sup>-1</sup> m <sup>-2</sup> Pa <sup>-1</sup> ]	3.0 × 10 <sup>-10</sup>	1.0 × 10 <sup>-10</sup>	8.7 × 10 <sup>-11</sup>	8.3 × 10 <sup>-11</sup>
	Selectivity H <sub>2</sub> O/ MeOH	160	630	966	1081
c H <sub>2</sub> O and NH <sub>3</sub> single gas permeation					
	Temperature [°C]	100	150	200	250
<b>Na-LTA</b>	H <sub>2</sub> O permeance [mol s <sup>-1</sup> m <sup>-2</sup> Pa <sup>-1</sup> ]	6.5 × 10 <sup>-8</sup>	9.7 × 10 <sup>-8</sup>	1.1 × 10 <sup>-7</sup>	1.3 × 10 <sup>-7</sup>
	NH <sub>3</sub> permeance [mol s <sup>-1</sup> m <sup>-2</sup> Pa <sup>-1</sup> ]	1.3 × 10 <sup>-9</sup>	1.2 × 10 <sup>-9</sup>	1.0 × 10 <sup>-9</sup>	1.0 × 10 <sup>-9</sup>
	Ideal selectivity H <sub>2</sub> O/NH <sub>3</sub>	51.6	82	108	125
<b>K-LTA</b>	H <sub>2</sub> O permeance [mol s <sup>-1</sup> m <sup>-2</sup> Pa <sup>-1</sup> ]	5.4 × 10 <sup>-8</sup>	7.8 × 10 <sup>-8</sup>	8.6 × 10 <sup>-8</sup>	8.8 × 10 <sup>-8</sup>
	NH <sub>3</sub> permeance [mol s <sup>-1</sup> m <sup>-2</sup> Pa <sup>-1</sup> ]	8.8 × 10 <sup>-10</sup>	9.0 × 10 <sup>-10</sup>	5.7 × 10 <sup>-10</sup>	4.6 × 10 <sup>-10</sup>
	Ideal selectivity H <sub>2</sub> O/NH <sub>3</sub>	62	87	151	193
d H <sub>2</sub> O and MeOH single gas permeation					
	Temperature [°C]	100	150	200	250
<b>Na-LTA</b>	H <sub>2</sub> O permeance [mol s <sup>-1</sup> m <sup>-2</sup> Pa <sup>-1</sup> ]	6.5 × 10 <sup>-8</sup>	9.7 × 10 <sup>-8</sup>	1.1 × 10 <sup>-7</sup>	1.3 × 10 <sup>-7</sup>
	MeOH permeance [mol s <sup>-1</sup> m <sup>-2</sup> Pa <sup>-1</sup> ]	4.5 × 10 <sup>-10</sup>	4.6 × 10 <sup>-10</sup>	4.4 × 10 <sup>-10</sup>	4.4 × 10 <sup>-10</sup>
	Ideal selectivity H <sub>2</sub> O/MeOH	143	212	252	302
<b>K-LTA</b>	H <sub>2</sub> O permeance [mol s <sup>-1</sup> m <sup>-2</sup> Pa <sup>-1</sup> ]	5.5 × 10 <sup>-8</sup>	7.8 × 10 <sup>-8</sup>	8.6 × 10 <sup>-8</sup>	8.8 × 10 <sup>-8</sup>
	MeOH permeance [mol s <sup>-1</sup> m <sup>-2</sup> Pa <sup>-1</sup> ]	5.5 × 10 <sup>-8</sup>	7.8 × 10 <sup>-8</sup>	8.6 × 10 <sup>-8</sup>	8.8 × 10 <sup>-8</sup>

**Table 2 (continued)**

a H <sub>2</sub> O/NH <sub>3</sub> mixed gas permeation					
	Temperature [°C]	100	150	200	250
MeOH permeance [mol s <sup>-1</sup> m <sup>-2</sup> Pa <sup>-1</sup> ]		1.0 × 10 <sup>-10</sup>	9.1 × 10 <sup>-11</sup>	8.2 × 10 <sup>-11</sup>	7.4 × 10 <sup>-11</sup>
Ideal selectivity H <sub>2</sub> O/MeOH		528	852	1045	1189

also a common by-product in methanol-to-olefins reactions, which occur in a pure MeOH reaction environment.

The observation that the conversion rate increases more for the H-MOR catalyst compared to H-SSZ-13, is based on the fact that the methylamine synthesis is already at 91% MeOH conversion for H-SSZ-13 (Fig. 3), which does not leave much space for improvement. Both catalysts benefit from the fact that the reactant MeOH is kept inside the tube reactor, while the by-product water is removed, which leads to an equilibrium shift towards the product side. To compensate the NH<sub>3</sub> loss and to maintain a steady MeOH/NH<sub>3</sub> ratio, a different reaction mixture with a higher NH<sub>3</sub> share could be applied.

The K-LTA membrane improves both (i) the methanol conversion rate, with the catalyst H-MOR to a higher extent compared to H-SSZ-13, and (ii) the selectivity towards the higher methylated amines. To understand the improved performance of K-LTA membranes in methylamine synthesis compared to Na-LTA membranes and to describe the precise influence of the pore-narrowing due to the Na<sup>+</sup>-K<sup>+</sup> cation exchange on the relevant compounds in methylamine synthesis, we carried out physisorption and vapor sorption measurements on Na-LTA and K-LTA, see Fig. S2. To evaluate the influence of the K<sup>+</sup> cation exchange on the pore dimensions of the LTA, CO<sub>2</sub> and N<sub>2</sub> physisorption was carried out. Since the 3 Å pore windows of the K-LTA are neither accessible for CO<sub>2</sub> (d ~ 3.3 Å) nor for N<sub>2</sub> (d ~ 3.7 Å) [27], the measured gas adsorption is most likely limited to the external surface of the zeolite [28]. While this indicates a successful ion exchange leading to pore window narrowing, it makes a comparison between the pore properties of Na-LTA and K-LTA based on these data senseless. Additionally, vapor sorption of MeOH and H<sub>2</sub>O on the membrane materials were conducted. It is shown that the ion exchange massively decreased the capacity of K-LTA to adsorb MeOH, diffusion paths are getting impeded with the uptake being 75% to 90% less than in Na-LTA at corresponding partial pressures. This decrease can be ascribed to the size exclusion of MeOH (d ~ 3.6 Å) by the narrowed pore entrances in K-LTA. The adsorption of water is also influenced by the ion exchange. At small partial pressures, the sorption curves are very similar for Na-LTA and K-LTA, indicating that similar places on the inner surface of the zeolites are occupied. At higher partial pressures, when the adsorbent fills the cages, the uptake is higher for Na-LTA than for K-LTA. This can be traced back to the increased space requirement of the larger K<sup>+</sup> ions as compared to the Na<sup>+</sup> ions.

Both the Na-LTA and K-LTA membranes showed no signs of crystal structure damages in XRD measurements after the methylamine synthesis, indicating that they are stable in the reaction environment at relative mild temperatures of 350 °C. Previous studies showed that both Na-LTA and K-LTA are stable up to 800 °C in ambient air [29]. Additionally, computational studies indicated that the type of cation in the zeolite structure does not significantly change the energy barriers of the hydrolysis reaction, which is the main path of zeolite decomposition through water vapor [30]. Therefore, it is concluded that the ion exchange from Na<sup>+</sup> to K<sup>+</sup> does not influence the hydrothermal stability of LTA to an extended degree.

The impact of the decreased MeOH adsorption capacity of K-LTA compared to Na-LTA was further tested in mixed gas as well as single gas permeation studies between 100 and 250 °C with H<sub>2</sub>O/MeOH, as well as H<sub>2</sub>O/NH<sub>3</sub>. The results can be found in Fig. 4, the corresponding values in Table 2.

As expected, the permeance of the K-LTA membrane is smaller for all

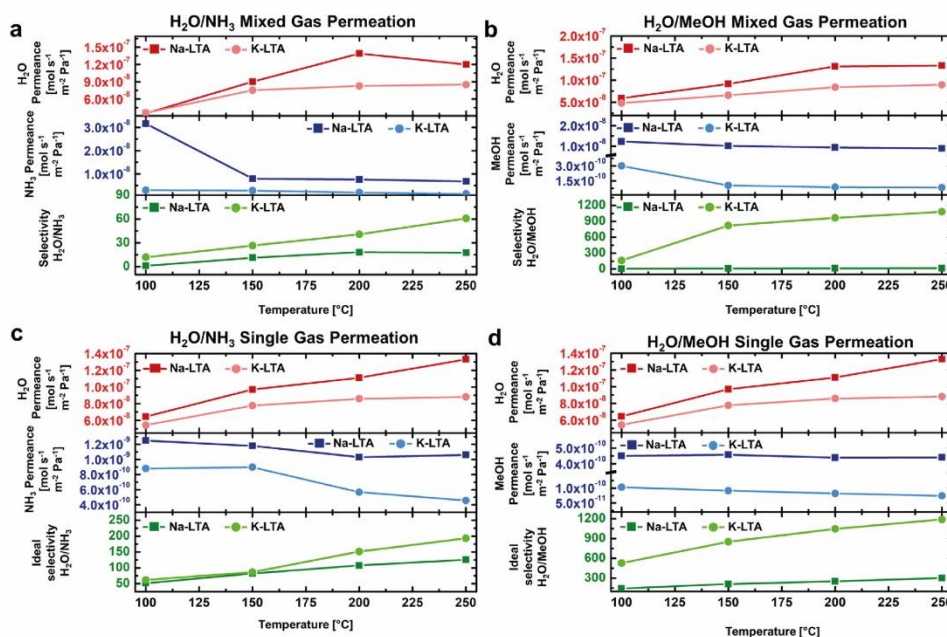


Fig. 4. Mixed gas permeances and selectivity of a  $\text{H}_2\text{O}/\text{NH}_3$ , b  $\text{H}_2\text{O}/\text{MeOH}$  on Na-LTA and K-LTA membranes and single gas permeances and ideal single gas selectivities of c  $\text{H}_2\text{O}$  and  $\text{NH}_3$ , d  $\text{H}_2\text{O}$  and  $\text{MeOH}$  with Na-LTA and K-LTA membranes. The permeation studies were carried out in a modified Wicke-Kallenbach setup, for details see experimental section.

three compounds under study compared to the Na-LTA membrane, induced by the pore window narrowing from 4 Å to 3 Å (Fig. 4a–d). Most relevant regarding our methylamine experiments are the mixed gas permeation measurements of  $\text{H}_2\text{O}/\text{NH}_3$  in Fig. 4a and  $\text{H}_2\text{O}/\text{MeOH}$  in Fig. 4b through the Na-LTA and K-LTA membranes, which demonstrate that in mixed gas permeation, the water permeance initially increases with higher temperatures for both membranes and remains relatively steady at 200 °C and above, which is in accordance with previous work [18]. The corresponding gaseous partner of water, either  $\text{NH}_3$  or  $\text{MeOH}$ , follows the opposite trend, their permeance slightly decreases or remains mostly steady with higher temperatures. Consequently, the mixed gas  $\text{H}_2\text{O}/\text{NH}_3$  and  $\text{H}_2\text{O}/\text{MeOH}$  selectivity increase with rising temperatures. Comparing the different zeolite membranes Na-LTA and K-LTA, water always has a higher permeance in Na-LTA. The same observation can be found for  $\text{NH}_3$  and  $\text{MeOH}$  between Na-LTA and K-LTA membranes. However, the fluxes become reduced more severely by K-LTA, see Fig. 4a and b. While the water permeance through the K-LTA membrane still exhibits about 2/3 of the flow through Na-LTA,  $\text{MeOH}$  is getting reduced by three orders of magnitude. This finding results in an enhanced  $\text{H}_2\text{O}/\text{MeOH}$  selectivity of 1189 for K-LTA, which is 80 times higher compared to Na-LTA separation of 15 at 250 °C.  $\text{NH}_3$  shows the same tendency as  $\text{MeOH}$  in mixed gas permeation with  $\text{H}_2\text{O}$ . However, the selectivity could only be improved from 17 with Na-LTA to 61 with K-LTA, as the ammonia flux is only reduced by 50% through K-LTA membrane.

The kinetic diameter of  $\text{NH}_3$  (2.9 Å) nearly matches the window size of the K-LTA, partially inhibiting the permeation flow. Comparisons between Na-LTA and K-LTA for  $\text{H}_2\text{O}/\text{NH}_3$  and  $\text{H}_2\text{O}/\text{MeOH}$ , Fig. 4a and b, show that the ion exchange from  $\text{Na}^+$  to  $\text{K}^+$ , vastly improves the separation for both systems but decreases the overall permeance. The pore window narrowing to 3 Å for the K-LTA membrane effectively excludes methanol ( $d = 3.6$  Å) from entering the pore, thus drastically increasing the separation properties of the K-LTA membrane. However,

there is some permeation through non-zeolitic defect pores, resulting in a measurable gas flow of methanol.  $\text{NH}_3/\text{H}_2\text{O}$  separation also benefits from the  $\text{K}^+$  ion exchange, but to a lesser extent (Fig. 4a) as notable differences only occur at 200 °C and above.

To further comprehend the mixed gas results, we additionally performed mixed gas permeation measurements of  $\text{H}_2\text{O}$ ,  $\text{NH}_3$  and  $\text{MeOH}$  through the Na-LTA and K-LTA membranes.

The first thing to notice is that the  $\text{H}_2\text{O}/\text{NH}_3$  selectivity and  $\text{H}_2\text{O}/\text{MeOH}$  mixed gas permeation are remarkably lower than the ideal selectivities calculated from  $\text{H}_2\text{O}$ ,  $\text{NH}_3$  and  $\text{MeOH}$  single gas permeation (Fig. 4c and d). While the water permeance is higher in single gas permeation compared to mixed gas separation, the  $\text{NH}_3$  and  $\text{MeOH}$  fluxes are lower in single gas experiments. With increasing temperatures, the  $\text{H}_2\text{O}$ ,  $\text{NH}_3$  and  $\text{MeOH}$  fluxes approach the mixed gas results. The finding that  $\text{H}_2\text{O}$  permeance is lower through K-LTA compared to Na-LTA still applies for the single gas permeation. On the other hand, the absolute selectivities increase for single gas permeation by a factor of 8 for  $\text{H}_2\text{O}/\text{NH}_3$  separation at 150 °C and of 20 for  $\text{H}_2\text{O}/\text{MeOH}$  through the Na-LTA membrane compared to the mixed gas results. The differences become smaller with increasing temperature. For  $\text{MeOH}/\text{H}_2\text{O}$ , both in single and mixed gas permeation, a jump of the separation factor can be found between 100 and 150 °C (Fig. 4b and d).

The different findings from single and mixed gas permeation are due to intramolecular interactions between two or more of the permeating molecules. Coupled diffusion has been thoroughly researched for pervaporation through zeolite membranes [31]. There are two different effects in diffusional coupling: (i) The slow-down effect, where one component occupies adsorption sites in the membrane thus hindering the other component from passing through, or by increasing the size and influence properties of the diffusants by molecular cluster formation or by hydrogen bonding; (ii) An increased permeance, when the presence of one compound enhances the permeation behavior of the other to let it pass the membrane more easily [32]. Both effects can be commonly

found in water/alcohol pervaporation, resulting in an overall decreased water selectivity. We suggest similar reasons in our gas permeation, as water exhibits a slightly lower permeance and the LTA membranes show a vastly reduced water selectivity in mixed gas permeation compared to single gas experiments (Fig. 4). In comparison,  $\text{NH}_3$  and MeOH undergo a significant increase in permeance in the presence of water. However, this tendency decreases at higher temperatures, indicating that intermolecular effects are getting diminished. The  $\text{H}_2\text{O}/\text{MeOH}$  mixture selectivity on Na-LTA is only 5 at 100 °C compared to the ideal selectivity of 143 as calculated from the single gas permeances. With increasing permeation temperature, both the mixed gas and the ideal selectivities increase, while the differences between them becomes smaller with rising temperatures, see Table 2b,d and Fig. 4b,d.

Previous reports suggested that  $\text{H}_2\text{O}/\text{H}_2$  and  $\text{H}_2\text{O}/\text{CH}_4$  systems are only weakly temperature dependent, and correspondingly their experimental selectivities only slightly decrease with higher temperatures [33]. However, in the work of Zhu et al. [33], the mixtures do not develop intermolecular interactions, as water does in our case with MeOH or  $\text{NH}_3$ . Especially in narrow zeolite pores, intermolecular forces are highly relevant for mixed gas permeation [34].

#### 4. Conclusions

We studied the effect of the selective in situ steam removal through Na-LTA and K-LTA membranes on the methylamine synthesis in a membrane reactor at 350 °C. To optimize the extractor type membrane reactor, highly steam selective membranes in the presence of ammonia and methanol are required. Using an Na-LTA membrane, the selectivity towards DMA could be enhanced due to steam extraction but the conversion in the membrane reactor did not increase since there was an unintended loss of ammonia and methanol.  $\text{K}^+$ -ion exchange of the Na-LTA membrane resulted in a pore window narrowing from 4 Å to 3 Å with increased steam selectivity. Mixed gas permeation resulted in a higher separation selectivity of the K-LTA membrane for  $\text{H}_2\text{O}/\text{NH}_3$  and  $\text{H}_2\text{O}/\text{MeOH}$ , compared to Na-LTA. The use of the K-LTA membrane in the methylamine synthesis led to an increased methylation rate, which resulted in an altered product composition. For the narrow pore zeolite catalyst H-SSZ-13, the methanol conversion rate could be enhanced, as the in situ steam removal through the K-LTA membrane decreased the share of MMA from 40% to 14% in the product, while the share of DMA increased due to steam removal from 51% to 75%. The thermodynamically most favored TMA cannot be formed in the narrow pore zeolite catalyst H-SSZ-13 for steric reasons. With the large pore zeolite catalyst H-MOR, the use of the K-LTA membrane reduced MMA from 36% to 27% and increased TMA from 35% to 41%, while the share of DMA was almost constant, and improved the overall conversion rate by 10%. These results recommend the application of a K-LTA membrane instead of an Na-LTA membrane for the methylamine synthesis in an extractor type membrane reactor, because of its improved  $\text{H}_2\text{O}/\text{NH}_3$  and  $\text{H}_2\text{O}/\text{MeOH}$  selectivity.

#### Funding sources

The Deutsche Forschungsgemeinschaft (DFG, German Research Foundation) is thanked for financing the project (CA147/21-1). Patrick A. Kießling thanks the DFG (Project BI1708/5-1) [35]. Additionally, the project has in parts been funded by the DFG under Germany's Excellence Strategy within the Cluster of Excellence PhoenixD (EXC 2122, Project ID 390833453). Karen Hindricks is thankful for a grant from the Deutsche Studienstiftung.

#### CRedit authorship contribution statement

**Felix Rieck genannt Best:** Writing – original draft, Visualization, Investigation, Formal analysis, Data curation, Conceptualization. **Alexander Mundstock:** Writing – review & editing, Conceptualization.

**Hannes Richter:** Writing – review & editing, Methodology. **Patrick A. Kießling:** Writing – review & editing, Formal analysis, Data curation. **Karen D.J. Hindricks:** Writing – review & editing, Methodology, Data curation. **Aisheng Huang:** Writing – review & editing, Methodology. **Peter Behrens:** Writing – review & editing, Supervision. **Jürgen Caro:** Writing – review & editing, Supervision.

#### Declaration of competing interest

The authors declare the following financial interests/personal relationships which may be considered as potential competing interests: Felix Rieck genannt Best reports financial support was provided by German Research Foundation. Patrick A. Kießling reports financial support was provided by German Research Foundation. Karen Hindricks reports financial support was provided by German Research Foundation, Cluster PhoenixD. Karen Hindricks reports financial support was provided by German Academic Scholarship Foundation.

#### Acknowledgement

We are thanking Adrian Hannebauer for conduction of the vapor sorption measurements.

#### Appendix A. Supplementary data

Supplementary data to this article can be found online at <https://doi.org/10.1016/j.micromeso.2022.111920>.

#### References

- [1] S. Khajavi, J.C. Jansen, F. Kapteijn, Application of a sodalite membrane reactor in esterification – coupling reaction and separation, *Catal. Today* 156 (2010) 132–139, <https://doi.org/10.1016/j.cattod.2010.02.042>.
- [2] N. Schmitz, C.F. Breitkreuz, E. Ströfer, J. Bürger, H. Hasse, Separation of water from mixtures containing formaldehyde, water, methanol, methylal, and poly (oxymethylene) dimethyl ethers by pervaporation, *J. Membr. Sci.* 564 (2018) 806–812, <https://doi.org/10.1016/j.memsci.2018.07.053>.
- [3] N. Rangnekar, N. Mittal, B. Elyassi, J. Caro, M. Tsapatsis, Zeolite membranes – a review and comparison with MOFs, *Chem. Soc. Rev.* 44 (2015) 7128–7154, <https://doi.org/10.1039/c5cs00292c>.
- [4] J. Jeong, H. Jeon, K. Ko, B. Chung, G.-W. Choi, Production of anhydrous ethanol using various PSA (Pressure Swing Adsorption) processes in pilot plant, *Renew. Energy* 42 (2012) 41–45, <https://doi.org/10.1016/j.renene.2011.09.027>.
- [5] J. Caro, M. Noack, Zeolite membranes – recent developments and progress, *Microporous Mesoporous Mater.* 115 (2008) 215–233, <https://doi.org/10.1016/j.micromeso.2008.03.008>.
- [6] F. Rieck genannt Best, A. Mundstock, G. Dräger, P. Rusch, N.C. Bigall, H. Richter, J. Caro, Methanol-to-Olefins in a membrane reactor with in situ steam removal – the decisive role of coking, *ChemCatChem* 12 (2020) 273–280, <https://doi.org/10.1002/cctc.201901222>.
- [7] M.P. Rohde, G. Schaub, S. Khajavi, J.C. Jansen, F. Kapteijn, Fischer-Tropsch synthesis with in situ  $\text{H}_2\text{O}$  removal – directions of membrane development, *Microporous Mesoporous Mater.* 115 (2008) 123–136, <https://doi.org/10.1016/j.micromeso.2007.10.052>.
- [8] N. Wang, Y. Liu, Z. Qiao, L. Diestel, J. Zhou, A. Huang, J. Caro, Polydopamine based synthesis of a zeolite imidazolate framework ZIF-100 membrane with high  $\text{H}_2/\text{CO}_2$  selectivity, *J. Mater. Chem. A* 3 (2015) 4722–4728, <https://doi.org/10.1039/C4TA06763K>.
- [9] H.Y. Jeon, C.H. Shin, H.L. Jung, S.B. Hong, Catalytic evaluation of small-pore molecular sieves with different framework topologies for the synthesis of methylamines, *Appl. Catal. Gen.* 305 (2006) 70–78, <https://doi.org/10.1016/j.apcata.2006.02.044>.
- [10] D.R. Corbin, S. Schwarz, G.C. Sonnichsen, Methylamines synthesis: a review, *Catal. Today* 37 (1997) 71–102, [https://doi.org/10.1016/S0920-5861\(97\)00003-5](https://doi.org/10.1016/S0920-5861(97)00003-5).
- [11] F. Rieck genannt Best, A. Mundstock, P.A. Kießling, H. Richter, K.D.J. Hindricks, A. Huang, P. Behrens, J. Caro, Boosting dimethylamine formation selectivity in a membrane reactor by in situ water removal, *Ind. Eng. Chem. Res.* (2021), <https://doi.org/10.1021/acs.iecr.1c04149>.
- [12] J. Liu, C. Guo, Z. Zhang, T. Jiang, H. Liu, J. Song, H. Fan, B. Han, Synthesis of dimethylformamide from  $\text{CO}_2$ ,  $\text{H}_2$  and dimethylamine over Cu/ZnO, *Chem. Commun.* 46 (2010) 5770–5772, <https://doi.org/10.1039/c0cc00751j>.
- [13] M.C. Ilaio, H. Yamamoto, K. Segawa, Shape-selective methylamine synthesis over small pore zeolite catalysts, *J. Catal.* 161 (1996) 20–30, <https://doi.org/10.1006/jcat.1996.0158>.
- [14] M. Dusselier, M.E. Davis, Small-pore zeolites: synthesis and catalysis, *Chem. Rev.* 118 (2018) 5265–5329, <https://doi.org/10.1021/acs.chemrev.7b00738>.

- [15] C. Xu, C. Zhou, S. Wang, A. Huang, Copper-exchanged LTA zeolite membranes with enhanced water flux for ethanol dehydration, *Chin. Chem. Lett.* 30 (2019) 1204–1206, <https://doi.org/10.1016/j.ccl.2019.01.016>.
- [16] R. Ektejari Salmas, B. Demir, E. Yildirim, A. Sirkecioglu, M. Yurtsever, M. G. Ahunbay, Silver-sodium ion exchange dynamics in LTA zeolite membranes, *J. Phys. Chem. C* 117 (2013) 1663–1671, <https://doi.org/10.1021/jp311534e>.
- [17] G. Guan, K. Kusakabe, S. Morooka, Gas permeation properties of ion-exchanged LTA type zeolite membranes, *Separ. Sci. Technol.* 36 (2001) 2233–2245, <https://doi.org/10.1081/SS-100105915>.
- [18] N. Wang, Y. Liu, A. Huang, J. Caro, Hydrophilic SOD and LTA membranes for membrane-supported methanol, dimethylether and dimethylcarbonate synthesis, *Microporous Mesoporous Mater.* 207 (2015) 33–38, <https://doi.org/10.1016/j.micromeso.2014.12.028>.
- [19] E. Okumuş, T. Gürkan, L. Yılmaz, Effect of fabrication and process parameters on the morphology and performance of a PAN based zeolite filled pervaporation membrane, *J. Membr. Sci.* 223 (2003) 23–38, [https://doi.org/10.1016/S0376-7388\(03\)00287-4](https://doi.org/10.1016/S0376-7388(03)00287-4).
- [20] N.A. Artsiusheuski, A.L. Grachev, B.A. Kolozhviri, D.A. Fedosov, Pervaporation of water–alcohol mixtures on cation exchanged LTA zeolite membranes, *Petrol. Chem.* 59 (2019) 880–886, <https://doi.org/10.1134/S0965544119080024>.
- [21] S. Shirazian, S.N. Ashrafzadeh, LTA and ion exchanged LTA zeolite membranes for dehydration of natural gas, *J. Ind. Eng. Chem.* 22 (2015) 132–137, <https://doi.org/10.1016/j.jiec.2014.06.034>.
- [22] A.R. Fahami, T. Günter, D.E. Doronkin, M. Casapu, D. Zengel, T.H. Vuong, M. Simon, F. Breher, A.V. Kucherov, A. Brückner, J.D. Grunwaldt, The dynamic nature of Cu sites in Cu-SSZ-13 and the origin of the seagull NO<sub>x</sub> conversion profile during NH<sub>3</sub> SCR, *React. Chem. Eng.* 4 (2019) 1000–1018, <https://doi.org/10.1039/c8re00290h>.
- [23] H. Lähms, J. Derr, R.X. Fischer, K and Ca exchange behavior of zeolite A, *Microporous Mesoporous Mater.* 151 (2012) 457–465, <https://doi.org/10.1016/j.micromeso.2011.09.025>.
- [24] H. Kalipcilar, T.C. Bowen, R.D. Noble, J.L. Falconer, Synthesis and separation performance of SSZ-13 zeolite membranes on tubular supports, *Chem. Mater.* 12 (2002) 3458–3464, [https://doi.org/10.1016/S0376-7388\(02\)00380-0](https://doi.org/10.1016/S0376-7388(02)00380-0).
- [25] F. Fetting, U. Dingerdissen, Production of methylamines over ZK-5 zeolite treated with tetramethoxysilane, *Chem. Eng. Technol.* 15 (1992) 202–212, <https://doi.org/10.1002/cent.270150309>.
- [26] F.J. Weigert, Selective synthesis and equilibration of methylamines on sodium mordenite, *J. Catal.* 103 (1987) 20–29, [https://doi.org/10.1016/0021-9517\(87\)90088-1](https://doi.org/10.1016/0021-9517(87)90088-1).
- [27] J.R. Li, R.J. Kuppler, H.C. Zhou, Selective gas adsorption and separation in metal-organic frameworks, *Chem. Soc. Rev.* 38 (2009) 1477–1504, <https://doi.org/10.1039/b802426j>.
- [28] T. Montanari, G. Busca, On the mechanism of adsorption and separation of CO<sub>2</sub> on LTA zeolites: an IR investigation, *Vib. Spectrosc.* 46 (2008) 45–51, <https://doi.org/10.1016/j.vibspec.2007.09.001>.
- [29] E. Gabruš, J. Nastaj, P. Tabero, T. Aleksandrak, Experimental studies on 3A and 4A zeolite molecular sieves regeneration in TSA process: aliphatic alcohols dewatering–water desorption, *Chem. Eng. J.* 259 (2015) 232–242, <https://doi.org/10.1016/j.cej.2014.07.108>.
- [30] J. Sun, H. Fang, P.I. Ravikovitch, D.S. Sholl, Understanding dealumination mechanisms in protonic and cationic zeolites, *J. Phys. Chem. C* 124 (2020) 668–676, <https://doi.org/10.1021/acs.jpcc.9b09693>.
- [31] W. Li, P. Luis, Understanding coupling effects in pervaporation of multi-component mixtures, *Separ. Purif. Technol.* 197 (2018) 95–106, <https://doi.org/10.1016/j.seppur.2017.12.041>.
- [32] D. Paschek, R. Krishna, Diffusion of binary mixtures in zeolites: kinetic Monte Carlo versus molecular dynamics simulations, *Langmuir* 17 (2001) 247–254, <https://doi.org/10.1021/la000695h>.
- [33] W. Zhu, L. Gora, A.W.C. Van Den Berg, F. Kapteijn, J.C. Jansen, J.A. Moulijn, Water vapour separation from permanent gases by a zeolite-4A membrane, *J. Membr. Sci.* 253 (2005) 57–66, <https://doi.org/10.1016/j.memsci.2004.12.039>.
- [34] K.I. Okamoto, H. Kita, K. Horii, K. Tanaka, M. Kondo, Zeolite NaA membrane: preparation, single gas permeation, and pervaporation and vapor permeation of water/organic liquid mixtures, *Ind. Eng. Chem. Res.* 40 (2001) 163–175, <https://doi.org/10.1021/ie0006007>.
- [35] DFG SPP 2005—Priority Programm Opus Fluidum Futurum—Rheology of Reactive, Multiscale, Multiphase Construction Materials., (n.d.), [https://www.dfg.de/en/funded\\_projects/current\\_projects\\_programmes/list/projectdetails/index.jsp?id=313773090&sort=nr\\_asc&prg=SPP](https://www.dfg.de/en/funded_projects/current_projects_programmes/list/projectdetails/index.jsp?id=313773090&sort=nr_asc&prg=SPP) (accessed September 9, 2021).
- [36] C.E. Goumaris, C.A. Floudas, J. Wei, Rational design of shape selective separation and catalysis I: concepts and analysis, *Chem. Eng. Sci.* 61 (2006) 7933–7948, <https://doi.org/10.1016/j.ces.2006.09.012>.
- [37] E. Schulman, W. Wu, D. Liu, Two dimensional zeolite materials: structural and acidity properties, *Materials* 13 (2020), <https://doi.org/10.3390/MA13081822>.

## Supporting Information

# Controlled methylamine synthesis in a membrane reactor featuring a highly steam selective $K^+$ -LTA membrane

*Felix Rieck genannt Best,<sup>\*a</sup> Alexander Mundstock,<sup>a</sup> Hannes Richter,<sup>b</sup> Patrick A. Kießling,<sup>a</sup>  
Karen D. J. Hindricks,<sup>c,d</sup> Aisheng Huang,<sup>e</sup> Peter Behrens,<sup>c,d,f</sup> Jürgen Caro<sup>a,f,g</sup>*

<sup>a</sup> Institute of Physical Chemistry and Electrochemistry, Leibniz University Hannover,  
Callinstraße 3A, Hannover 30167, Germany

<sup>b</sup> Fraunhofer IKTS, Institute for Ceramic Technologies and Systems,  
Michael-Faraday-Straße 1, Hermsdorf 07629, Germany

<sup>c</sup> Institute of Inorganic Chemistry, Leibniz University Hannover, Callinstraße 9, Hannover  
30167, Germany

<sup>d</sup> Cluster of Excellence PhoenixD (Photonics, Optics, and Engineering – Innovation Across  
Disciplines), Welfengarten 1A, 30167 Hannover, Germany

<sup>e</sup> Shanghai Key Laboratory of Green Chemistry and Chemical Processes, Department of  
Chemistry, East China Normal University, Dongchuan Road 500, Shanghai 200241, China

<sup>f</sup> Laboratory of Nano and Quantum Engineering, Leibniz University Hannover,  
Schneiderberg 39, 30167 Hannover, Germany

<sup>g</sup> School of Chemistry and Chemical Engineering, South China University of Technology,  
Wushan Road 381, Guangzhou 510640, China

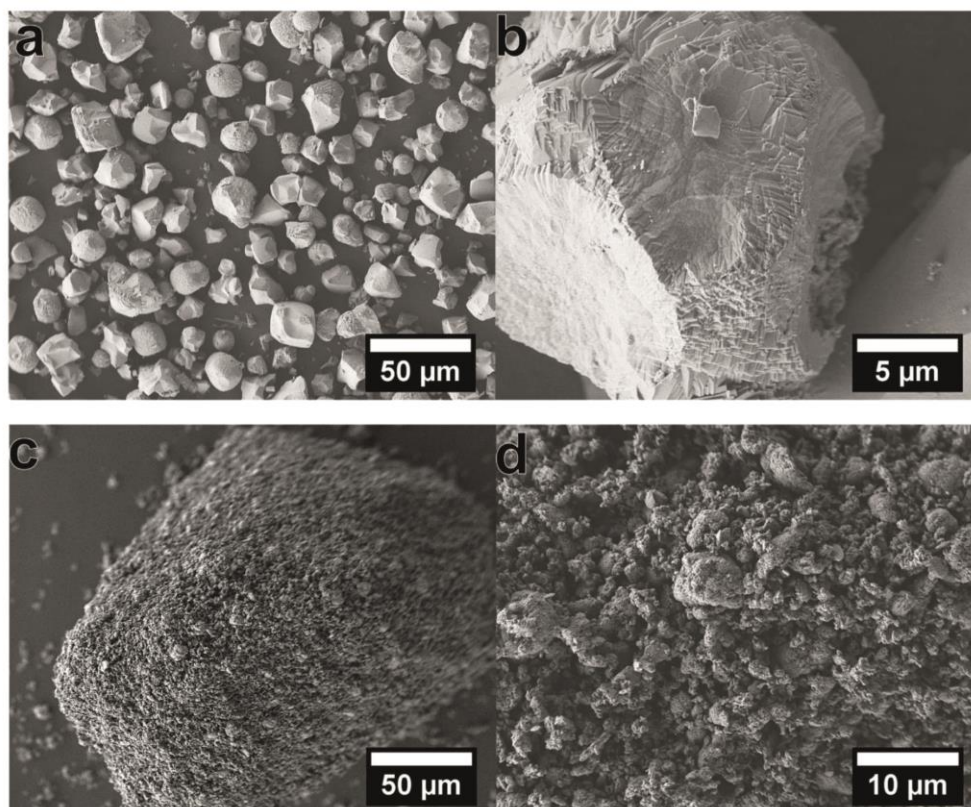


**Figure S1.** SEM micrographs of H-SSZ-13 particles at a magnification of **a** 500x, **b** 5000x and H-MOR particles **c** 500x and **d** 2500x.

**Table S1.** Performance of H-SSZ-13 and H-MOR in methylamine synthesis without membrane support and with the addition of an Na-LTA or K-LTA membrane.

	H-SSZ-13			H-MOR		
	Without membrane	With Na-LTA membrane	With K-LTA membrane	Without membrane	With Na-LTA membrane	With K-LTA membrane
X(MeOH)	91%	90%	94%	70%	71%	80%
S(MMA)	40%	19%	14%	36%	29%	27%
S(DMA)	51%	71%	74%	24%	25%	21%
S(TMA)	7%	7%	6%	25%	39%	43%
S(DME)	2%	3%	6%	5%	7%	9%

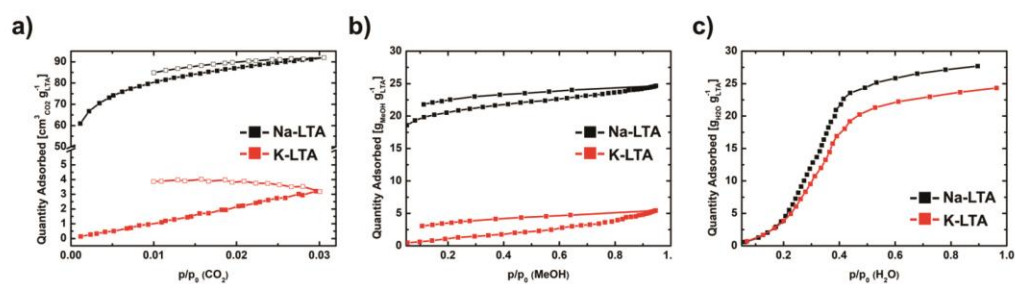


**Figure S2.** a) CO<sub>2</sub> physisorption measurements on Na-LTA and K-LTA. The pores of K-LTA are accessible for CO<sub>2</sub>, as seen in the low amounts of absorbed gas. Therefore, calculations to evaluate and compare the pore properties of Na-LTA and K-LTA were not carried out. Vapor sorption curves of b) MeOH and c) H<sub>2</sub>O on Na-LTA and K-LTA.

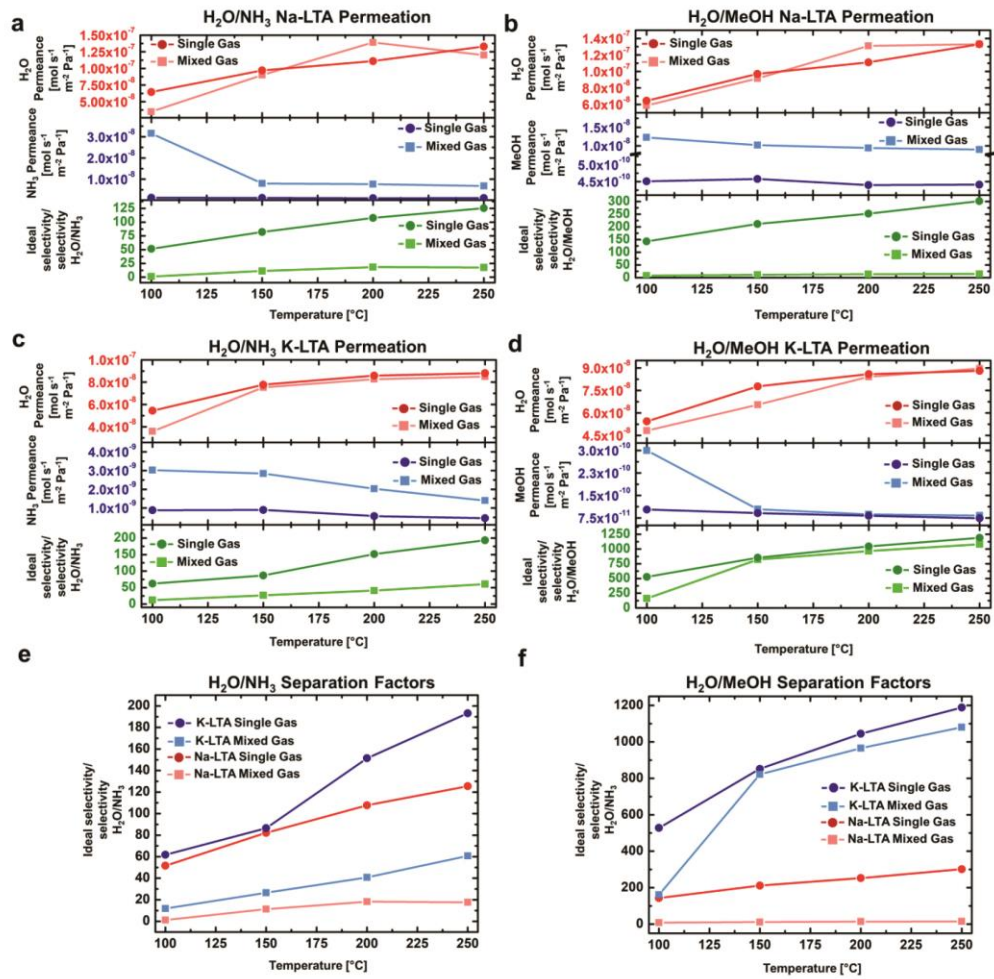


**Figure S3.** Visualized permeation results based on **Table 2**: Comparisons of **a)** single and mixed gas permeation of H<sub>2</sub>O/NH<sub>3</sub> with Na-LTA, **b)** single and mixed gas permeation of H<sub>2</sub>O/MeOH with Na-LTA, **c)** single and mixed gas permeation of H<sub>2</sub>O/MeOH with K-LTA, **d)** single and mixed gas permeation of H<sub>2</sub>O/MeOH with K-LTA, **e)** ideal selectivity and selectivity of single and mixed gas permeation of H<sub>2</sub>O/NH<sub>3</sub> with Na- and K-LTA and **f)** ideal selectivity and selectivity of single and mixed gas permeation of H<sub>2</sub>O/MeOH with Na- and K-LTA.



## **10.4. Bridging the interface between Metallic Copper and TiO<sub>2</sub> via B/N-graphene for enhanced Photocatalytic H<sub>2</sub> Production and 2-Chlorophenol Degradation: A DFT, experimental and mechanistic investigation**

Since the discovery of its photochemical properties, TiO<sub>2</sub> has drawn considerable attention due to the wide variety of possible applications it might offer. One thoroughly researched topic is the photocatalytic water splitting to produce hydrogen and cover its ever increasing demand. However, a wide spread application was not achieved until now, mostly due to the catalyst's poor efficiency and lacking stability. Similar to the previous studies, where dual-functional production/separation reactors were investigated, we decided to apply a similar concept in the photocatalytic research area. Here the production part was taken by the hydrogen production, while the resulting highly reactive surface species could be used to simultaneously reduce the otherwise stable pollutant 2-chlorophenol, resulting in a dual-functional production/degradation system. The addition of copper and doped graphene to the TiO<sub>2</sub> particles were considered to enhance stabilities and conversion rates, while the dual-functional system should add a novelty to further improve the chances of TiO<sub>2</sub>-based photochemical reaction to find application outside of pilot plants. The idea to this study and large parts of its realization was from Dr. Lucy Ombaka, while my part was to provide aid to develop a sustainable and repeatable synthesis route towards the B/N-doped graphene/Cu/TiO<sub>2</sub> composite particles and in the end to revise the manuscript for a successful publication.



Contents lists available at ScienceDirect

Journal of Environmental Management

journal homepage: [www.elsevier.com/locate/jenvman](http://www.elsevier.com/locate/jenvman)

## Photocatalytic H<sub>2</sub> production and degradation of aqueous 2-chlorophenol over B/N-graphene-coated Cu<sup>0</sup>/TiO<sub>2</sub>: A DFT, experimental and mechanistic investigation

Lucy M. Ombaka<sup>a,b,\*</sup>, James D. McGettrick<sup>c</sup>, Ekemena O. Oseghe<sup>d</sup>, Osama Al-Madanat<sup>a</sup>, Felix Rieck genannt Best<sup>e</sup>, Titus A.M. Msagati<sup>d</sup>, Matthew L. Davies<sup>c,f</sup>, Thomas Bredow<sup>g</sup>, Detlef W. Bahnemann<sup>a,h,i</sup>

<sup>a</sup> Institut für Technische Chemie, Gottfried Wilhelm Leibniz Universität Hannover, Callinstrasse 3, Hannover, 30167, Germany

<sup>b</sup> School of Chemistry and Material Science, Technical University of Kenya, P.O Box 52428-00200, Nairobi, Kenya

<sup>c</sup> SPECIFIC IKC, Materials Research Centre, College of Engineering, Swansea University, Bay Campus, Fabian Way, Swansea, SA1 8EN, UK

<sup>d</sup> Institute for Nanotechnology and Water Sustainability, College of Science, Engineering and Technology, University of South Africa, Florida Campus, 1709, Johannesburg, South Africa

<sup>e</sup> Institute for Physical Chemistry and Electrochemistry, Leibniz University Hannover, 30167, Hannover, Germany

<sup>f</sup> School of Chemistry and Physics, University of KwaZulu-Natal, Westville Campus, Private Bag X54001, Durban, 4000, South Africa

<sup>g</sup> Mulliken Center for Theoretical Chemistry, Institute for Physical and Theoretical Chemistry, University of Bonn, Beringstr. 4, Bonn, Germany

<sup>h</sup> Laboratorium für Nano- und Quantenengineering, Gottfried Wilhelm Leibniz Universität Hannover, Schneiderberg 39, Hannover, 30167, Germany

<sup>i</sup> Laboratory for Photoactive Nanocomposite Materials, Department of Photonics, Faculty of Physics, Saint-Petersburg State University, Ulianovskaia Str. 3, Peterhof, Saint-Petersburg, 198504, Russia

### ARTICLE INFO

#### Keywords:

Green energy  
Hydrogen production  
Metallic copper  
Photocatalysis  
2-Chlorophenol degradation

### ABSTRACT

Energy and environmental challenges are global concerns that scientists are interested in alleviating. It is on this premise that we prepared boron/nitrogen graphene-coated Cu<sup>0</sup>/TiO<sub>2</sub> (B/N-graphene-coated Cu<sup>0</sup>/TiO<sub>2</sub>) photocatalyst of varying B:N ratios with dual functionality of H<sub>2</sub> production and 2-Chlorophenol (2-CP) degradation. *In situ* coating of Cu<sup>0</sup> with B/N-graphene is achieved *via* solvothermal synthesis and calcination under an inert atmosphere. All B/N-graphene-coated Cu<sup>0</sup>/TiO<sub>2</sub> exhibit higher photonic efficiencies (5.68%–7.06% at 300 < λ < 400 nm) towards H<sub>2</sub> production than bare TiO<sub>2</sub> (0.25% at 300 < λ < 400 nm). Varying the B:N ratio in graphene influences the efficiency of H<sub>2</sub> generation. A B:N ratio of 0.08 yields the most active composite exhibiting a photonic efficiency of 7.06% towards H<sub>2</sub> evolution and a degradation rate of 4.07 × 10<sup>-2</sup> min<sup>-1</sup> towards 2-chlorophenol (2-CP). Density functional theory (DFT) investigations determine that B-doping (p-type) enhances graphene stability on Cu<sup>0</sup> while N-doping (n-type) increases the reduction potential of Cu<sup>0</sup> relative to H<sup>+</sup> reduction potential. X-ray photoelectron spectroscopy reveals that increasing the B:N ratio increases p-type BC<sub>2</sub>O while decreasing n-type pyridinic-N in graphene thus altering the interlayer electron density. Isotopic labelling experiments determine water reduction as the main mechanism by which H<sub>2</sub> is produced over B/N-graphene-coated Cu<sup>0</sup>/TiO<sub>2</sub>. The reactive species involved in the degradation of 2-CP are holes (h<sup>+</sup>), hydroxyl radical (OH<sup>•</sup>), and O<sub>2</sub><sup>•-</sup>, of which superoxide (O<sub>2</sub><sup>•-</sup>) plays the major role. This work displays B/N-graphene-coated Cu<sup>0</sup>/TiO<sub>2</sub> as a potential photocatalyst for large-scale H<sub>2</sub> production and 2-CP degradation.

### 1. Introduction

In recent years, heterogeneous photocatalysts that exhibit dual-functionality towards environmentally important processes such as the simultaneous production of green fuels (e. g. hydrogen) and degradation

of problematic pollutants (e. g. 2-chlorophenol) in wastewaters are increasingly gaining attention (van Renssen, 2020). Hydrogen that combusts in oxygen to form water as the only by-product is increasingly being utilized as a green fuel in fuel cells availing an alternative to fossil fuel as an energy source (van Renssen, 2020). On the other hand,

\* Corresponding author. Institut für Technische Chemie, Gottfried Wilhelm Leibniz Universität Hannover, Callinstrasse 3, Hannover, 30167, Germany.  
E-mail addresses: [lucyombaka@tukenya.ac.ke](mailto:lucyombaka@tukenya.ac.ke), [ombaka@iftc.uni-hannover.de](mailto:ombaka@iftc.uni-hannover.de) (L.M. Ombaka).

<https://doi.org/10.1016/j.jenvman.2022.114822>

Received 18 November 2021; Received in revised form 17 February 2022; Accepted 27 February 2022

Available online 4 March 2022

0301-4797/© 2022 Elsevier Ltd. All rights reserved.

2-chlorophenol (2-CP) is a well-known organic pollutant of concern in the aquatic systems with stable C–Cl bond which makes it toxic and persistent in the environment (Mohanty et al., 2003). To date, the industrial photocatalytic production of hydrogen fuel and degradation of 2-CP is hampered by the scarcity of naturally abundant, cost-effective and efficient photocatalysts (Wang et al., 2019; Kahng et al., 2020). To this end, titanium dioxide (TiO<sub>2</sub>) is extensively studied as one of the most prominent photocatalyst for hydrogen production and pollutant degradation due to its affordability and sustainable supply (Martins et al., 2017; Jeon et al., 2020). However, owing to its wide band gap (ca. 3.2 eV) and fast electron-hole recombination rate, its photocatalytic efficiency is low (~0.1–5%) (Jeon et al., 2020; Wang et al., 2017). Conventionally, the efficiency of TiO<sub>2</sub> photocatalysis can be increased by using sacrificial agents and noble metals (e.g. Pt or Au) as cocatalyst (Wang et al., 2019). Due to the high cost and precious nature of noble metals, earth abundant and affordable metals (e.g. Cu and Co) are increasingly investigated as cocatalysts of TiO<sub>2</sub> (Zhu et al., 2019). Metallic Cu, a group 11 element, is an excellent conductor exhibiting similar electronic properties to those of Au and Ag making it a promising cocatalyst. The major setback of using metallic copper/TiO<sub>2</sub> (Cu/TiO<sub>2</sub>) composites in photocatalytic reactions is the ease of Cu<sup>0</sup> oxidation to less active Cu<sup>2+</sup> species.

To overcome this, capping agents and surfactants are commonly used to stabilize Cu<sup>0</sup> and retard its oxidation (Gawande et al., 2016). However, such moieties can also be unstable undergoing photodegradation and exposing Cu<sup>0</sup> to oxidation during reactions. More recently, coating of Cu<sup>0</sup> co-catalyst with graphene layers is reported to increase the stability of Cu<sup>0</sup> during photocatalysis by retarding its photooxidation (Chen et al., 2019; Ombaka et al., 2020a). To the best of our knowledge, the strategic coating of Cu<sup>0</sup> with B/N co-doped graphene for enhanced stability and activity of Cu/TiO<sub>2</sub> has not been reported. Additionally, the effect of graphene, N-graphene and B/N-graphene coatings on Cu<sup>0</sup> electrocatalytic properties and interfacial charge transfer in Cu/TiO<sub>2</sub> has not yet been investigated. Herein, Cu<sup>0</sup> particles are coated with B/N-graphene of varying B:N ratios and used as cocatalysts for TiO<sub>2</sub> (B/N-graphene-coated Cu/TiO<sub>2</sub>) in photocatalytic H<sub>2</sub> generation and 2-CP degradation. The B:N ratio in graphene influences the H<sub>2</sub> generation and 2-CP degradation rate, and photonic efficiency by strategically tuning the stability of graphene coatings and Fermi energy of Cu<sup>0</sup>.

Therefore, this account presents B/N-graphene-coated Cu/TiO<sub>2</sub> as efficient dual-functional photocatalysts for H<sub>2</sub> production and 2-CP degradation (Zhu et al., 2019). A thorough investigation of the enhanced photocatalytic activity of the composites is conducted via mechanistic investigations and DFT simulations. Additionally, the structure-activity correlations between graphene-coated Cu<sup>0</sup>/TiO<sub>2</sub> and its photocatalytic activity is reported. Overall, the study provides a systematic and strategic approach towards tuning the photocatalytic properties of Cu<sup>0</sup>/TiO<sub>2</sub>.

## 2. Experimental section

### 2.1. Materials and reagents

Copper (II) acetylacetonate (Cu(acac)<sub>2</sub>, 99.9%), copper(I) oxide (99.99%), branched polyethylenimine (PEI), boric anhydride (B<sub>2</sub>O<sub>3</sub>, 99.98%), 2-chlorophenol (2-CP ≥ 99%) and deuterium oxide (D<sub>2</sub>O, 99.9 at. % D) were purchased from Merck, Germany. Methanol (99.8%) was purchased from Carl Roth, Germany. Titanium dioxide (aeroxide TiO<sub>2</sub> P25) was purchased from Evonik Industries, Germany. All reagents and solvents purchased were of analytical grade and therefore used without further purification (Ombaka et al., 2020b).

### 2.2. Preparation of photocatalysts

Particles of Cu<sup>0</sup> were synthesized using a solvothermal approach while coating of Cu<sup>0</sup> with N- or B/N-graphene layers was achieved by

calcination under nitrogen (Scheme S1) (Ombaka et al., 2020a). To synthesize N-graphene-coated Cu<sup>0</sup>, 500 mg of Cu(acac)<sub>2</sub> and 14 g of PEI were weighed into a 50 mL Pyrex test tube, mixed together then sealed with a Schott GL25 threaded cap containing a rubber septum (Ombaka et al., 2020b). The reactor tube was then heated at 200 °C for a period of 2 h to obtain a brown-orange semisolid, which was cooled to room temperature. The semisolid was then apportioned into four crucibles which were calcined for a period of 2 h at 600, 700, 750 and 800 °C (ramp rate of 5 °C min<sup>-1</sup>) under a flow of nitrogen gas (100 mL min<sup>-1</sup>) to obtain four samples as black solids. Upon cooling, each sample was separately pulverized using a pestle and mortar, then washed using three aliquots of 40 mL of a 1:1 mixture of Millipore water and ethanol. For each wash, the solid was agitated by hand shaking then reclaimed as a fine black powder by centrifugation at 2000 rpm for a period of 5 min. The obtained four samples of graphene-coated Cu were then oven-dried at 70 °C for a period of 12 h. Afterwards, a 60:40 mass ratio mixture of TiO<sub>2</sub> and coated Cu was mechanically ground for 5 min using a pestle and mortar to form a homogeneous grey powder of N-graphene-coated Cu/TiO<sub>2</sub> composite. N-graphene-coated Cu/TiO<sub>2</sub> composites containing Cu samples calcined at 600, 700, 750 and 800 °C were labelled C–N 600, C–N 700, C–N 750 and C–N 800 respectively.

To synthesize B/N-graphene-coated Cu<sup>0</sup> containing varying N:B ratios; 25, 50, 75 and 125 mg of B<sub>2</sub>O<sub>3</sub> was weighed into four different 50 mL Pyrex test tubes. Subsequently, 500 mg of Cu(acac)<sub>2</sub> and 14 g of PEI were weighed and added into each tube. The contents in each reactor tube were mixed together and the tubes sealed as previously described then heated at 200 °C for a period of 2 h to obtain a brown-orange semisolid (Ombaka et al., 2020a). Upon cooling to room temperature, the contents of each tube were transferred into a separate crucible and calcined for a period of 2 h at 600 °C (ramp rate of 5 °C min<sup>-1</sup>) under a flow of nitrogen gas (100 mL min<sup>-1</sup>) to obtain a black solid (Ombaka et al., 2020a). The obtained solid (B/N-graphene-coated Cu<sup>0</sup>) was pulverized, washed, dried and mixed with TiO<sub>2</sub> as previously outlined. B/N-graphene-coated Cu/TiO<sub>2</sub> composites containing Cu particles synthesized using 25, 50, 75 and 125 mg of B<sub>2</sub>O<sub>3</sub> were labelled C–NB-25, C–NB-50, C–NB-75 and C–NB-125 respectively.

### 2.3. Characterization

Micrographs of all photocatalysts were acquired using transmission electron microscopy (TEM) and scanning electron microscopy (SEM). TEM images were captured using a FEI Tecnai G2 F20 TMP fitted with a 200 kV field emission gun, while SEM images acquired using a JEOL JSM-6700 F equipped with a lower secondary electron image detector. A Bruker D8 Advance diffractometer (Bruker AXS GmbH) with a Cu K $\alpha$  radiation ( $\lambda = 1.54060 \text{ \AA}$ ) Bragg-Brentano geometry was used to collect the samples' X-ray diffractograms within the diffraction angle of (2 $\theta$ ) 10–80 at steps of 0.01054. The obtained diffraction patterns were compared with reference patterns from the JCPDS database. To evaluate the effect of calcination temperature and B/N co-doping on the average crystallite sizes of Cu, the Scherrer equation (1) was employed.<sup>11</sup>

$$D = \frac{k\lambda}{\beta\cos\theta} \quad (1)$$

Where D represents the crystallite size (nm), k is Scherrer constant (= 0.89),  $\lambda$  is the X-ray's wavelength (0.154 nm),  $\beta$  is the full width at half maximum while,  $\theta$  is the diffraction angle of Cu<sup>0</sup> (111) reflection plane. Functional groups present in the samples were probed using Attenuated total reflection Fourier-transform infrared (ATR-FTIR) spectroscopy on a Bruker IFS66v spectrometer of spectral range 50–10 000 cm<sup>-1</sup>. The optical properties of photocatalysts were evaluated using UV–visible spectroscopy on an Agilent Cary 5000 connected to an external DRA-2500 diffuse reflectance accessory. X-ray Photoelectron Spectroscopy (XPS) was performed on a Kratos Axis Supra. Wide scans were collected in triplicate for each sample with a pass energy of 160 eV. Due to XPS having a relatively low sensitivity for boron, two

complementary sets of high-resolution data were collected. Firstly, the stoichiometry of the samples was calculated from a set of spectra collected at pass energy 80 eV (with 50 x sweeps of a 1 s dwell time and step size of 0.25 eV for boron) to ensure a good boron signal. Unfortunately, a higher pass energy will improve signal: noise, but simultaneously broaden peaks – which can make deconvolution more difficult. Thus, a more traditional set of spectra were collected at a pass energy of 40 eV, step of 0.1 eV in order to examine any changes in binding energy for elements such as Cu, O, Ti, C, N. In all cases the x-ray source was a monochromated AlK $\alpha$  at 15 mA and 225 W. The quantification and peak fitting performed with CasaXPS (Version 2.3.23rev1.1 K) using the default GL (mixed Gaussian-Lorentzian) lineshape (Naumkin et al., 2012; Biesinger et al., 2010).

#### 2.4. Computational analysis

The interaction of a graphene monolayer with the Cu surface and the effect of N and B doping of graphene on the electronic structure was theoretically investigated at density-functional theory DFT level. The calculations were performed with the plane-wave program package VASP version 6.1.2.<sup>[VASP]</sup> A kinetic energy cutoff of 600 eV was used for the plane-wave basis. Core electrons were described with the projector-augmented wave method as implemented in VASP.<sup>[PAW]</sup> The meta-GGA functional SCAN [SCAN, BENCHMARK], was applied due to its accuracy for solid-state structures, energetics and electronic properties. This is different from a previous theoretical investigation [CRIS] by Di Valentin et al. which applied dispersion-corrected PBE and vdW-D2 functionals (Ferrighi et al., 2015). Here we focus on the absolute position of the Fermi level which was not investigated in the previous study. It was assumed that the surfaces of crystalline nano- and microparticles of Cu that are synthesized in this study can be represented by the most stable (111) surface. The Cu(111) surface was modeled in a similar way as done by Di Valentin et al. by a four-layer slab of a 4 × 4 surface supercell. Convergence of the calculated Fermi energy with respect to the number of atomic layers was checked and it was found the four layers are sufficient to ensure convergence below 0.1 eV. The Cu lattice constant optimized with SCAN is 3.566 Å, 0.8% smaller than the low-temperature reference value 3.595 Å.<sup>[KRESEBULK]</sup> For the bulk calculations, a dense 24 × 24 × 24 Monkhorst-Pack k-point grid was used. The surface supercell calculations were performed with 6 × 6 × 1 k-point grids. For the bare Cu(111) surface a Fermi energy with respect to vacuum level ( $E_F$ ) of -4.94 eV is obtained with SCAN. This matches the experimental work function  $\phi = 4.94$  eV.<sup>[EXP]</sup> The graphene monolayer adsorbed on Cu (111) consisted of 32 atoms which were placed on-top of surface Cu atoms. In the surface optimizations all atoms were allowed to relax. The surface cell lattice parameters were fixed to the values obtained from the bulk optimization. In this way stress is introduced on the graphene layer as pointed out by Di Valentin et al. But in our models, it is assumed that this is a real effect when the graphene monolayers are adsorbed on Cu.

#### 2.5. Photocatalytic hydrogen evolution test

Batch reactions were conducted in a 10 mL glass vial fitted with a foldable cap having a centrally placed silicon septum. For each experiment, 6 mg of the catalyst was weighed into the vial and suspended in 6 mL of either 10% v/v MeOH solution or pure Millipore water then sealed and purged with argon (99.9%) for a period of 20 min (Ombaka et al., 2020a). The vial and its contents were then fixed in an aluminum-coated container (visible light irradiation was obtained using a cut-off filter  $\lambda \leq 550$  nm) connected to a shaker and placed at a distance of 13.5 cm below a 1000 W xenon lamp (Hönle UV Technology, Sol 1200) or a Philips CLEO 15 W lamp emitting UV(A) light. The reaction progress was monitored over a 3-h period by hourly drawing 50  $\mu$ L of gas sample from the vial and injecting this into a gas chromatography-thermal conductivity detector (GC-TCD) (Shimadzu GC-8A) fitted with a stainless-steel molecular sieve 5 Å GC column (Sigma-Aldrich). For analysis the column

temperature was set at 80 °C, the injection temperature at 120 °C, and the TCD detector temperature at 120 °C. Analysis of formaldehyde in the liquid phase was conducted by mixing 300  $\mu$ L aliquots of the solution with 300  $\mu$ L Nash reagent (a solution of 15 g ammonium acetate, 0.2 mL acetylacetonate, and 0.3 mL acetic acid in 100 mL of Millipore water) and leaving the mixture to react overnight (Kleeberg and Klinger, 1982). Afterwards, formaldehyde concentrations were analyzed using a UV-visible spectrometry (Agilent).

For continuous analysis, a HIDDEN HPR-20 QIC gas analyzer equipped with a quadrupole mass spectrometer (QMS) was used to monitor the evolved H<sub>2</sub>, HD, and D<sub>2</sub> gases during the photocatalytic reforming of methanol or deuterated methanol. In all the experiment, 25 mg of different photocatalysts was suspended in 50 mL of a 10% (v/v) aqueous methanol or deuterated methanol dissolved in water or deuterated water inside a 65 mL cylindrical air-tight reactor with a quartz window (Ombaka et al., 2020a). A continuous flow of 5 mL min<sup>-1</sup> of argon carried the headspace into the QMS system. The temperature was kept constant at 25 ± 1 °C. Blank experiments showed no detectable gas evolution in the absence of light, the photocatalyst, or methanol. The quantitative determination of the evolved H<sub>2</sub> was done by calibrating the QMS with standard argon-diluted H<sub>2</sub> (Linde Gas, Germany).

#### 2.6. Photocatalytic 2-CP degradation test

Photocatalytic studies of the materials on 2-CP degradation were carried out under a HAL-320 Solar Simulator with compact Xenon as light source. Prior to irradiation, 250 mg L<sup>-1</sup> of the catalyst was dispersed in a 20 mL 2-CP (5 mg L<sup>-1</sup>) and stirred in the dark for 45 min to attain adsorption-desorption equilibrium before starting the photocatalytic experiment (Mohanty et al., 2003). At certain time intervals, aliquot (400  $\mu$ L) was sampled, immediately centrifuged at a speed of 12,000 RPM for 10 min using an Eppendorf Centrifuge 5415 R. After centrifuging, absorbance of the supernatant was measured on a ThermoFisher NanoDrop One spectrophotometer at 274 nm.

### 3. Results and discussions

#### 3.1. Morphological analysis

The surface features of C-N 600 and C-NB 50 (chosen as representative samples) were analyzed using TEM and SEM (Fig. 1). Crystalline facets of Cu are evidenced in both the lower and higher magnification TEM and SEM micrographs of both samples. Lower magnification images display Cu microparticles while higher magnification images show nanoparticles of Cu. Thus, the utilized synthesis approach yields a mixture of crystalline nano- and microparticles of Cu (Ombaka et al., 2020a, 2020b). The interface between Cu and TiO<sub>2</sub> is clearly observed from the higher magnification TEM images and lower magnification SEM micrographs of both samples (Fig. 1). In all cases, a constellation in which TiO<sub>2</sub> nanoparticles are anchored on the facets of Cu microparticles is observed. The presence of TiO<sub>2</sub> agglomerates on the surface Cu is indicative of heteroatom attraction forces (Bulushev et al., 2017). Thus, implying a possible coordination of Cu to TiO<sub>2</sub> via a simple grinding approach. Interestingly, Fig. 1(d) and (h) depicts TiO<sub>2</sub> nanoparticles anchored onto the edges and pores of Cu. According to other reports, such defects sites reinforce the interactions between TiO<sub>2</sub> and Cu and act as reactants' active sites thus increasing the stability and photocatalytic performance of the composites [17-18].

#### 3.2. XRD analysis

The crystalline phase and crystallite size of selected samples of pure Cu (Fig. S1) and all Cu composites (Fig. 2) were evaluated using powder XRD. Diffractograms of selected pure Cu samples and all Cu composites exhibit peaks at ca. 43.3°, 50.4° and 74.1° corresponding to the (111),

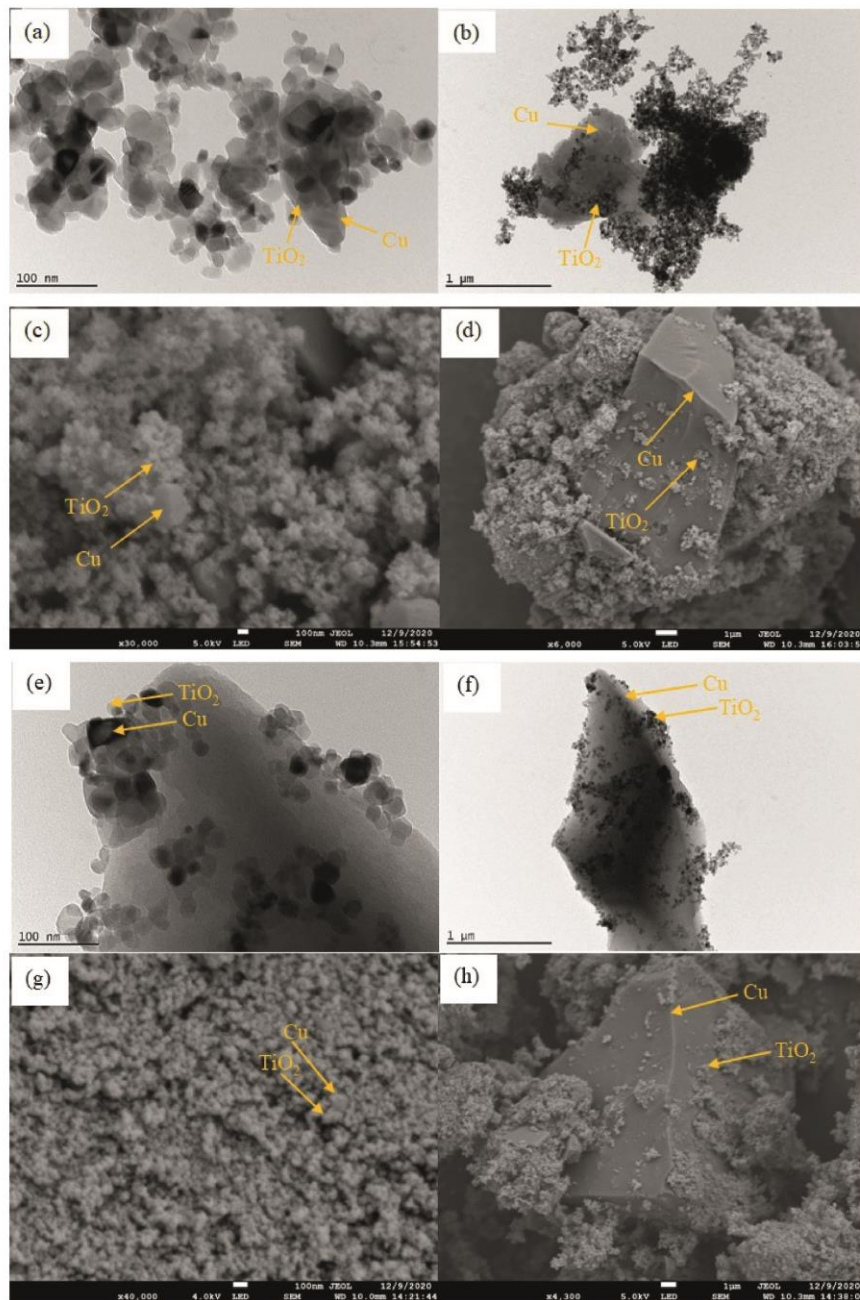


**Fig. 1.** High magnification (a) and low magnification (b) TEM images and high magnification (c) and low magnification (d) SEM images of C-N 600. High magnification (e) and low magnification (f) TEM images, and high magnification (g) and low magnification (h) SEM images of C-NB 50.

(200) and (220) reflection planes of metallic Cu (space group:  $Fm\bar{3}m$ ) as per the JCPDS 00-004-0836 data base (Kirfel and Eichhorn, 1990). Additional reflections at ca. 25.3°, 27.5°, 36.2°, 37.8°, 48.1°, 54.0°, 55.1°, 62.7°, 68.9°, 70.3° and 75.2° present only in the composites'

diffractograms are assigned to the reflection planes of anatase (JCPDS # 01-075-2545) and rutile (JCPDS # 01-073-1782) TiO<sub>2</sub>. Similar reflections are also evidenced in the diffractogram of pure TiO<sub>2</sub> (Nie et al., 2018). Thus, pure Cu samples consist of Cu<sup>0</sup> while all composites contain

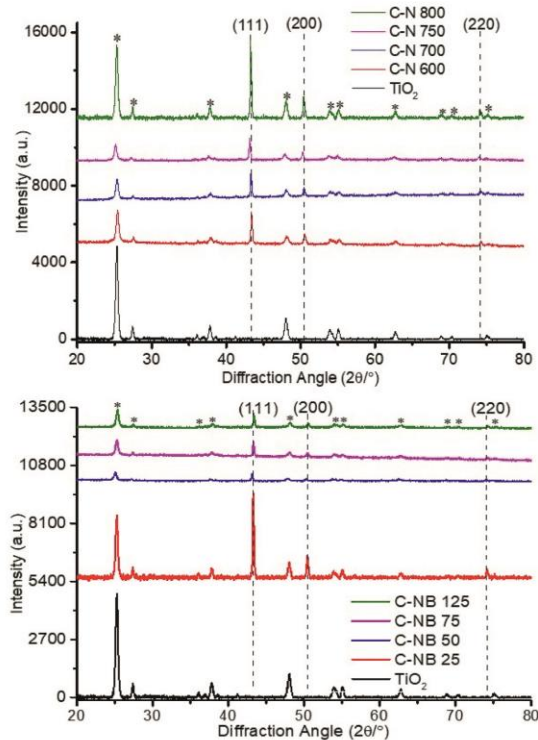


Fig. 2. XRD diffractograms of TiO<sub>2</sub>, C-N 600–800 (a) and C-NB 25–125 (b).

a mixture of TiO<sub>2</sub> and Cu<sup>0</sup> with no detectable Cu<sub>2</sub>O or CuO in the bulk material. This implies that synthesis of copper nanoparticles using PEI as a surfactant at different calcination temperatures (600–800 °C) or in the presence of B<sub>2</sub>O<sub>3</sub> as a boron source yields primarily metallic Cu (Ombaka et al., 2020a).

The average crystallite size of Cu particles calcined at 600, 700, 750 and 800 °C was 39.9, 39.2, 42.3 and 43.1 nm respectively. This implies that increasing the calcination temperature, gradual increases crystallite size of Cu particles (Granone et al., 2018). On average, the crystallite size of Cu nanoparticles synthesized in the presence of 25, 50, 75 and 125 mg of B<sub>2</sub>O<sub>3</sub> was 43.9, 44.3, 46.7 and 42.4 nm respectively. The crystallite sizes of B/N-containing samples (42.4–43.9 nm) were

generally higher than those of the corresponding Cu sample synthesized at 600 °C in the absence of B<sub>2</sub>O<sub>3</sub> (39.9 nm). Thus, the usage of B<sub>2</sub>O<sub>3</sub> during synthesis increased the crystallite size of Cu particles (Gawande et al., 2016).

### 3.3. FTIR analysis

ATR-FTIR is a powerful technique for probing interfacial surface interactions between organic moieties and TiO<sub>2</sub> (Atitar et al., 2015). The possible coordination of TiO<sub>2</sub> to functional groups present on the surface of the Cu particles is investigated using ATR-FTIR (Fig. 3a). The spectrum of pure TiO<sub>2</sub> has a broad absorption peak ranging from 2800 to 3650 cm<sup>-1</sup> and a narrower absorption with a peak maximum at 1638 cm<sup>-1</sup>. The former peak is attributed to Ti–OH stretching vibrations of δH<sub>2</sub>O while, the latter arises from the Fermi resonance overtone absorptions of Ti–OH bending modes (Deiana et al., 2010). Compared to pure TiO<sub>2</sub>, the spectra of all Cu composites depict a loss of intensity in the broad absorption band (2800–3650 cm<sup>-1</sup>) and a blue shifting of the narrower absorption peak (1638 cm<sup>-1</sup>) by ca. 74 cm<sup>-1</sup>. The observed decrease in absorption intensities indicates a reduction in the density of Ti–OH stretching modes upon coordinating TiO<sub>2</sub> to surface moieties on Cu (Deiana et al., 2010). Equally, the significant blue-shifting of absorptions associated with Ti–OH bending modes implies a change of electron distribution around Ti–OH (Atitar et al., 2015). This is indicative of the coordination of Cu surface functional groups to Ti–OH (Ombaka et al., 2020b). Such coordination occurring either by electrostatic or chemical interactions influence the electronic structure, redox properties and photocatalytic reaction pathway of TiO<sub>2</sub> (Atitar et al., 2015). Therefore, the formed coordinative linkages potentially influence the photocatalytic pathway of methanol oxidation over the composite (Ombaka et al., 2020a).

Co-doping of Cu coatings with B/N was confirmed by absorption bands associated with B–O stretching vibrations at 1388 and 1312 cm<sup>-1</sup>, and B–C stretching vibrations at 1039 cm<sup>-1</sup> (Yu et al., 2018; Mokhtar Mohamed et al., 2018). Similar peaks are absent in the spectra of pristine TiO<sub>2</sub> and C-N 600, verifying the successful co-doping of Cu carbon coatings with B/N. The absorption intensity of B–O band is weak in C-NB 25 and 50 but stronger in C-NB 75 and 125 (Fig. 3b), with C-NB 125 showing the highest peak intensity. Intense absorptions around 2000 cm<sup>-1</sup> present in all composites but absent in TiO<sub>2</sub> are attributed to C–N moieties.

### 3.4. Optical properties

A critical parameter influencing the photocatalytic performance of a photocatalyst is its optical characteristics. A desirable photocatalyst should efficiently absorb incident light photons and convert these into charge carriers (Janczarek and Kowalska, 2017; Zhang et al., 2015a).

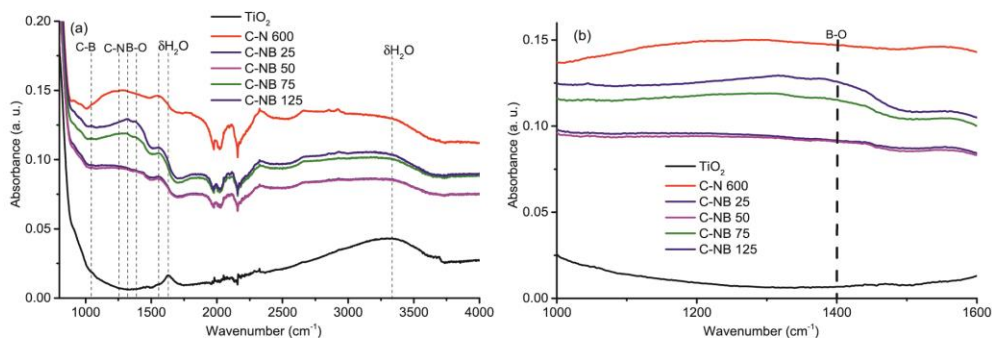


Fig. 3. FTIR spectra of TiO<sub>2</sub>, C-N 600 and C-NB 25–125 at full-range (a) and short-range (b) wavenumbers.

The optical properties of TiO<sub>2</sub> and its Cu composites were studied using UV-Vis-NIR diffuse reflectance spectroscopy (Fig. 4). Typical of pristine TiO<sub>2</sub>, its spectra shows a single UV-absorption band with a maximum at ca. 310 nm (Günneemann et al., 2019). All Cu/TiO<sub>2</sub> composites exhibit a similar strong UV absorption (ca. 310 nm), consequently, this absorption corresponds to TiO<sub>2</sub>-based absorptions. A red-shift of the TiO<sub>2</sub> absorption peak shoulder towards the visible range is noted in the spectra of all composites (Fig. 4). This is indicative of electron transfer processes between TiO<sub>2</sub> and Cu particles facilitated by coordination of Cu to TiO<sub>2</sub> as observed from ATR-FTIR analysis (Yao et al., 2018).

Pure Cu particles used to synthesize C-NB 50 were analyzed as a representative sample and their spectrum presented in Fig. S2. The Cu samples exhibit a continuous absorption in the entire UV-Vis range with no distinct absorption peaks. On the other hand, composites of Cu and TiO<sub>2</sub> exhibit broad absorptions in the entire visible region with the strongest absorption observed between 600 and 790 nm. Similar absorptions are absent in the spectra of pristine TiO<sub>2</sub> therefore, these absorptions are attributed to localized surface Plasmon resonance (LSPR) bands of metallic copper nanoparticles (Yang et al., 2017). For all composites, the LSPR absorptions are broad and weak. Such broad and weak LSPR absorptions are attributable to the inhomogeneous particle size of copper particles, intrinsic energy loss due to electron collision and interband transitions in spherical nanoparticles (Zhang et al., 2015a; Chan et al., 2007).

Compared to pristine TiO<sub>2</sub>, all composites exhibit a stronger visible and NIR light absorbance arising from LSPR and copper surface chromophore absorptions. Thus, conjugating coated Cu particles to TiO<sub>2</sub> significantly increases the composites' visible and NIR light harvesting efficiency towards enhanced photocatalytic activities. Generally, the intensity of the LSPR absorption of B/N-containing samples follows the order C-NB 25 < C-NB 50 ≈ C-NB 75 < C-NB 125. Since B% in these composites increase in a similar order (*vide infra*), it is deduced that the composites' LSPR absorption increases with increase in B%. The presence of Cu<sub>2</sub>O species on the surface of Cu<sup>0</sup> is reported to dampen LSPR absorbance of Cu<sup>0</sup> (Chan et al., 2007). Therefore, the observed increase in LSPR absorbance with increase in B% is attributable to increased resilience of Cu<sup>0</sup> towards oxidation. No absorption edge corresponding to CuO or Cu<sub>2</sub>O is present in the spectra of all composites indicating that the composites primarily consist of Cu<sup>0</sup> as observed from XRD analysis.

### 3.5. XPS analysis

The chemical states of B/N species present on the surface of coated Cu and the oxidation states of Cu were analyzed using XPS (Table 1, Figs. 5 and 6). N-containing samples calcined at 600, 700, 750 and

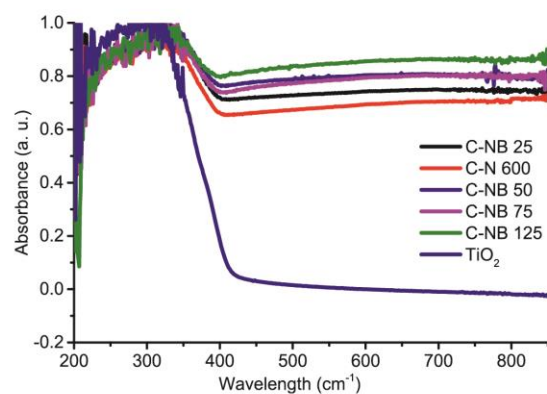


Fig. 4. UV-Vis-NIR diffuse absorbance spectra of TiO<sub>2</sub>, C-N 600 and C-NB 25–125.

850 °C contained 1.5%, 2.1%, 1.5% and 1.5% N respectively. Such an insignificant variation of N% in these samples implies that N-doping of graphene coatings occurs during the solvothermal process and is independent of the calcination temperature (Ombaka et al., 2015a). Contrary to N%, the C% increases with increasing calcination temperature. Samples calcined at 600, 700, 750 and 850 °C contain 39.9%, 39.9%, 40.8% and 45.4% C respectively. This implies that raising the calcination temperature increases the layers of carbon coatings without necessarily incorporating nitrogen into the additional carbon coatings (Oosthuizen and Nyamori, 2012).

The carbon contents in C-NB 25, 50 and 125 (33.3%–34.2% C) are significantly lower than those in C-N 600, 700, 750 and 850 (39.4%–45.6% C) (Table 1). However, a high carbon content is detected in C-NB 75 (44.8% C), this is attributed to experimental anomalies. Nonetheless, addition of B<sub>2</sub>O<sub>3</sub> to the synthesis precursor reduces the C% on copper via the etching effect of oxygen (Ombaka et al., 2015a). The carbon moieties in co-doped samples are mainly graphitic C (284.7 eV) and C-N species (286.5 eV) as depicted in the deconvoluted high-resolution C 1s spectra of C-NB 50 chosen as a representative spectrum (Fig. 5a). This confirms the successful coating of Cu particles with graphitic carbon layers.

Different levels of B-doping are detected in B/N co-doped samples. B-doping levels are noted to linearly increase with increase in the amounts of B<sub>2</sub>O<sub>3</sub> incorporated into the synthesis precursor (Table 1). The spectra of all co-doped samples depict a broad B 1s peak at ~191.9–192.2 eV which even at a pass energy of 80 eV, shows a high binding energy asymmetry. This peak is deconvoluted to yield two components at 191.5 and 192.5 eV corresponding to BC<sub>2</sub>O (B1) and B<sub>2</sub>O<sub>3</sub> (B2) respectively (Table 1) (Kong et al., 2019; Zaleska et al., 2008). The peak area ratio corresponding to B1 increases while that of B2 decreases with increasing B:N ratio (Table 1). This indicates that higher B% favors incorporation of B into graphene edges or defect sites. No components or asymmetries are visible at lower binding energies, where B-N species are detectable, implying that doping of B and N occurred at different carbon sites (Zhang et al., 2015b).

N-doping levels of co-doped samples are summarized in Table 1. All B/N co-doped samples display higher N-doping levels (2.3%–2.8% N) compared with samples doped only with N (1.5%–2.1% N). Considering that no B-N species are detected, the additional N-doping possibly occurs by replacing a carbon atom in the graphene sheet (Zheng et al., 2013). An insignificant variation in N-doping levels is observed in C-NB 25, 50 and 75 with no clear correlation between B- and N- doping levels. The N 1s spectra of all B/N co-doped samples exhibit a broad peak between 396.0 and 403.0 eV that is deconvoluted to give pyridinic-N (N1), pyrrolic-N (N2) and graphitic N (N3) (Table 1 and Fig. 5b) (Ombaka et al., 2015b). As the B% in co-doped samples increases, the peak area ratio for N1 decreases, that of N2 shows no significant variation while that of N3 increases. Thus, for the applied solvothermal synthesis, the presence of B favors N-doping of graphene via graphitic-N at the expense of pyridinic-N.

The Cu 2p spectra of samples calcined at 600 °C exhibit two peaks at 931.9 and 951.6 eV assigned to Cu 2p<sub>3/2</sub> and Cu 2p<sub>1/2</sub> respectively (Fig. 6) (Biesinger, 2017). Deconvolution of these peaks gives intense peaks of Cu<sup>1+/0</sup> (932.0 and 951.6 eV). A weak shoulder at 933.7 eV & very weak satellite features in the 940–945 eV region are attributed to low level presence of Cu<sup>2+</sup> species (Biesinger et al., 2010). The Cu 2p spectra of samples calcined at 700, 750 and 850 °C displays two peaks at 931.7 and 951.4 eV again ascribed to Cu 2p<sub>3/2</sub> and Cu 2p<sub>1/2</sub> in Cu<sup>1+/0</sup> respectively. However, for these samples no Cu<sup>2+</sup> satellite peaks are detected. Thus, samples calcined at temperatures higher than 600 °C purely consist of Cu<sup>1+/0</sup> while those calcined at 600 °C comprise of a mixture of Cu<sup>1+/0</sup> and Cu<sup>2+</sup>. This indicates that the additional graphene layers coating Cu calcined at 750 and 850 °C deter surface oxidation of Cu<sup>1+/0</sup> to Cu<sup>2+</sup>, further validating the coating of Cu with graphene layers as an effective strategy towards stabilizing Cu<sup>0</sup> (Ombaka et al., 2020a).

High-resolution Cu 2p spectra of B/N-containing samples are pre-

**Table 1**  
 Composition of B, N and C in the materials.

Catalyst	B			N			C	B:N
	B at.%	B1 BE (eV)/Peak area ratio %	B2 BE (eV)/Peak area ratio %	N at.%	N1 BE (eV)/Peak area ratio %	N3 BE (eV)/Peak area ratio %		
TiO <sub>2</sub>	0.02	191.6/80.3	193.5/19.7	0.3	398.0/4.2	401.2/0.0	25.5	–
C-NB 25	0.10	191.8/49.0	193.7/51.0	2.5	398.3/15.0	401.5/40.3	33.3	0.04
C-NB 50	0.20	192.0/75.3	193.9/24.7	2.3	398.2/10.0	401.3/44.0	35.7	0.08
C-NB 75	0.15	191.9/72.9	193.8/27.1	2.3	398.1/7.6	401.3/50.3	44.8	0.07
C-NB 125	0.28	192.2/100.0	194.1/0.0	2.8	398.4/7.8	401.5/48.7	34.2	0.1
C-N 600	0.01	191.8/100.0	193.7/0.0	1.5	398.2/11.0	401.3/40.5	39.4	–

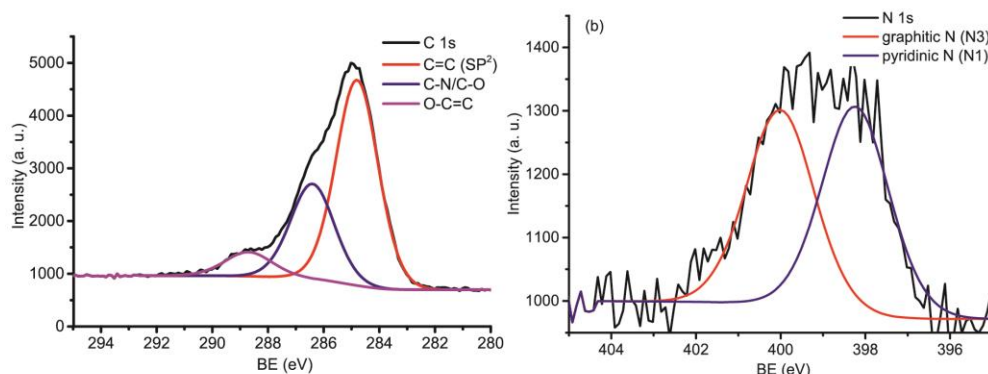


Fig. 5. High-resolution XPS C 1s spectra (a) and N 1s (b) of C-NB 50.

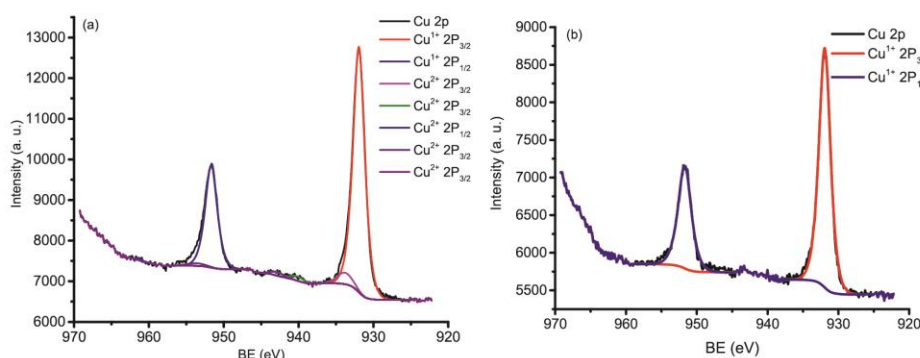


Fig. 6. High-resolution XPS Cu 2p spectra of C-N 600 (a) and C-NB 50 (b).

sented in Figs. 6 and S3. As in the case of C-N 600, the Cu 2p spectra of all B/N-modified samples exhibit a peak at 932.1 and 951.7 eV assigned to Cu 2p<sub>3/2</sub> and Cu 2p<sub>1/2</sub>, respectively. However, unlike C-N 600 these peaks are devoid of Cu<sup>2+</sup> shoulders and satellites, thus consist purely of Cu<sup>1+/0</sup>. It is worth noting that C-N 600 and all B/N-modified samples were calcined at 600 °C. Therefore, the remarkable stability of B/N-modified samples which consist purely of Cu<sup>1+/0</sup> is attributed to co-doping of Cu graphene coatings with N and B. It is postulated that the higher N-doping levels in B/N-modified samples coupled with the chelation of Cu atoms to B moieties results in stable Cu<sup>1+/0</sup> complexes that are resilient to atmospheric oxidation (Ombaka et al., 2020a; Pulkkinen et al., 2009).

### 3.6. DFT calculations

At the Cu-graphene (G) interface, minimal charge transfers and hybridization of graphene  $\pi$  orbitals and Cu d orbitals are reported to occur (Ferrighi et al., 2015). To gain further insight into the stability of the Cu-G (pristine and (co)doped) interface and the interfacial electronic interactions, DFT calculations were conducted using SCAN functional. For calculations, carbon was placed vertically above the Cu atom in accordance with previous studies that report such a constellation as the most stable (Fig. 7) (Xu and Buehler, 2010).

The stability of the G-Cu interface is inferred from the equilibrium distances between graphene and Cu and the calculated adsorption energy of graphene on Cu (Table 2). For undoped graphene monolayer, the vertical G-Cu distance is 3.36 Å. Doping the 32-atom graphene sheet



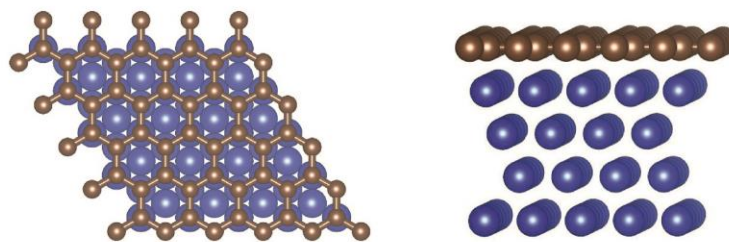


Fig. 7. Undoped graphene layer on Cu(111); left: top view, right: side view. Blue spheres denote Cu atoms, brown spheres denote C atoms. (For interpretation of the references to colour in this figure legend, the reader is referred to the Web version of this article.)

**Table 2**  
Equilibrium distances, adsorption energy, vacuum  $E_f$  and NHE potentials of Cu-G (pristine and (co)doped).

Sample	C-Cu (Å)	Adsorption energy (meV/atom) <sup>a</sup>	Fermi Energy (eV)	Normal Hydrogen Electrode (V)
Cu(111)	–	–	–4.94 eV	+0.09
G/Cu(111)	3.36	–26	–4.58	–0.27
N-G/ Cu(111)	3.47	–29	–4.41	–0.44
B-G/ Cu(111)	3.18	–48	–4.87	+0.02
BN-G/ Cu(111)	3.39	–39 (B–N = 1.45 Å)	–4.59	–0.26
Cu(111)	–	–29 (B–N = 2.52 Å)	–4.60	–0.25

<sup>a</sup> 32 C in G-Cu, 31 C + 1 N in N-G/Cu, 31 C + 1 B in B-G/Cu and 30 C + 1 B + 1 N in B/N-G/Cu.

with a single B atom reduces this distance while doping with a N atom or co-doping with B/N increases the distance giving the order B-G/Cu < G/Cu < B/N-G/Cu < N-G/Cu. N is electron-rich relative to C, consequently, N-G corresponds to n-type doping that reduces its tendency to accept electrons from Cu<sup>0</sup> thus increasing the N-G/Cu distance (Xu and Buehler, 2010). On the contrary, B is electron-deficient relative to C, thus B-G corresponds to p-type doping and readily accepts electrons from Cu<sup>0</sup> reducing the B-G/Cu distance. In addition, B is 0.06 Å closer to Cu than C and therefore exhibits stronger interactions with Cu. Undoped graphene monolayer binds to Cu with an interaction energy of –26 meV/atom (Table 2). This energy increases upon (co)doping with N, B or B/N of which B-doping shows the highest adsorption energy. Additionally, the B–N distance influences the adsorption energy of B/N-graphene with a shorter distance resulting in a higher interaction energy resulting in the general trend of increasing energy as G/Cu < N-G/Cu < BN-G/Cu (B–N = 1.45 Å, corresponding to nearest neighbors within G) < B-G/Cu.

Consequently, hetero-atom doping of graphene increases the adhesion of graphene to Cu and the stability of the G-Cu interface more than mono N-doping, with B-G/Cu interface being the most stable. Accordingly, increasing B% in B/N-G while keeping N% constant should increase the overall stability of the B/N-G/Cu interface and decrease its G-Cu equilibrium distance. Additionally, B/N-G coatings act both as electron acceptors via B and donors via N forming an internal redox system on the surface of Cu<sup>0</sup> that enhances the electronic communication between TiO<sub>2</sub> and Cu<sup>0</sup> that can result in enhanced activities.

The effect of (co)doping on G-Cu electronic interactions and the redox potential of Cu was evaluated by considering the DOS near the Cu Fermi energy ( $E_f$ ) (Filhol and Neurock, 2006). The bare Cu(111) surface has the most negative Fermi energy ( $E_f$ ) with respect to the vacuum reference, –4.94 eV. For all cases, layering Cu(111) with undoped or (co)doped graphene raises its  $E_f$  implying that electrons drift from Cu to graphene making the graphene n-type, and leaving Cu as a p-type (Table 2) (Xu and Buehler, 2010). Thus, graphene acts as an electron reservoir in which electrons circulate within its extensive  $\pi$ -electron system hence reducing the susceptibility of Cu<sup>0</sup> oxidation. Taking the  $E_f$

of undoped G-Cu (–4.58 eV) as a reference point, a downshift of –0.29 eV is achieved upon doping with B, an upshift of 0.17 eV is observed upon doping with N, while no significant variation is noted with B/N co-doping (Table 2). Thus, doping of graphene with N enhances the flow of electrons from Cu to graphene more than doping with B. For B/N-G/Cu, the n-type doping of N overcomes the p-type doping of B resulting in no net change in the chemical doping of graphene making its  $E_f$  similar to that of undoped G-Cu. The calculated  $E_f$  were compared to normal hydrogen electrode (NHE) potentials using the equation:

$$\varphi_{NHE} = -4.85 - \varphi_{vac}$$

Where  $\varphi_{NHE}$  is the normal hydrogen electrode (NHE) potential,  $\varphi_{vac}$  the vacuum  $E_f$  and –4.85 is the correction factor. (Filhol and Neurock, 2006)

The calculated reduction potential of free-standing Cu is more positive than the reduction potential of H<sup>+</sup>. Coating of Cu with pristine or (co)doped graphene raises the potential to more negative values with the reducing strength decreasing in the order N-G/Cu > G/Cu > B/N-G/Cu > B-G/Cu > Cu. Thus, these theoretical reduction potentials indicate that coating of Cu with graphene layers increases its H<sup>+</sup> reducing strength resulting in higher H<sub>2</sub> evolution rates. The highest activity is expected over N-G/Cu, which is in line with our previous findings that higher H<sub>2</sub> evolution rates are obtained over N-G/Cu compared with G/Cu (Ombaka et al., 2020a). In general, B-doping of graphene Cu coatings gives the most stable G-Cu interface while N-doping gives the highest reduction potential thus, co-doped graphene with tuned B:N ratios (Table 2) may exhibit high activity and stability.

### 3.7. Photocatalytic H<sub>2</sub> production

The effect of calcination temperature on the structure-activity relationship of N-containing Cu composites was evaluated based on the composites' H<sub>2</sub> evolution photonic efficiency at 300 <  $\lambda$  < 400 nm (Fig. 8a), determined using Equations S1-S2 (Melchionna and Fornasiero, 2020; Al-Madanat et al., 2020; Qureshi and Takane, 2017). Increasing the calcination temperature from 600 to 850 °C steadily decreases the photonic efficiency from 5.17% to 4.59% (Table S1). As inferred from XRD analysis, the crystallite size of Cu increases with calcination temperature, depicting an inverse correlation between size and photonic efficiency. Similarly, the carbon content in Cu increases with increase in calcination temperature, equally depicting an inverse correlation with photonic efficiency. Based on XPS analysis, all four composites contain almost equal N% (1.5%–2.1% N). Additionally, the less active Cu species (Cu<sup>2+</sup>) is detected only in the sample calcined at 600 °C (Ombaka et al., 2020a). Therefore, the decrease in H<sub>2</sub> production with increase in calcination temperature is ascribed increased crystallite sizes and carbon layers. Although carbon coatings and nitrogen moieties stabilize Cu<sup>0</sup> (Gawande et al., 2016) (Ombaka et al., 2020a), denser coatings tend to impede the substrate from reaching the Cu active sites, screen the composite from incident UV radiation and curtail electron transfer to Cu thus lowering the composites' overall efficiency

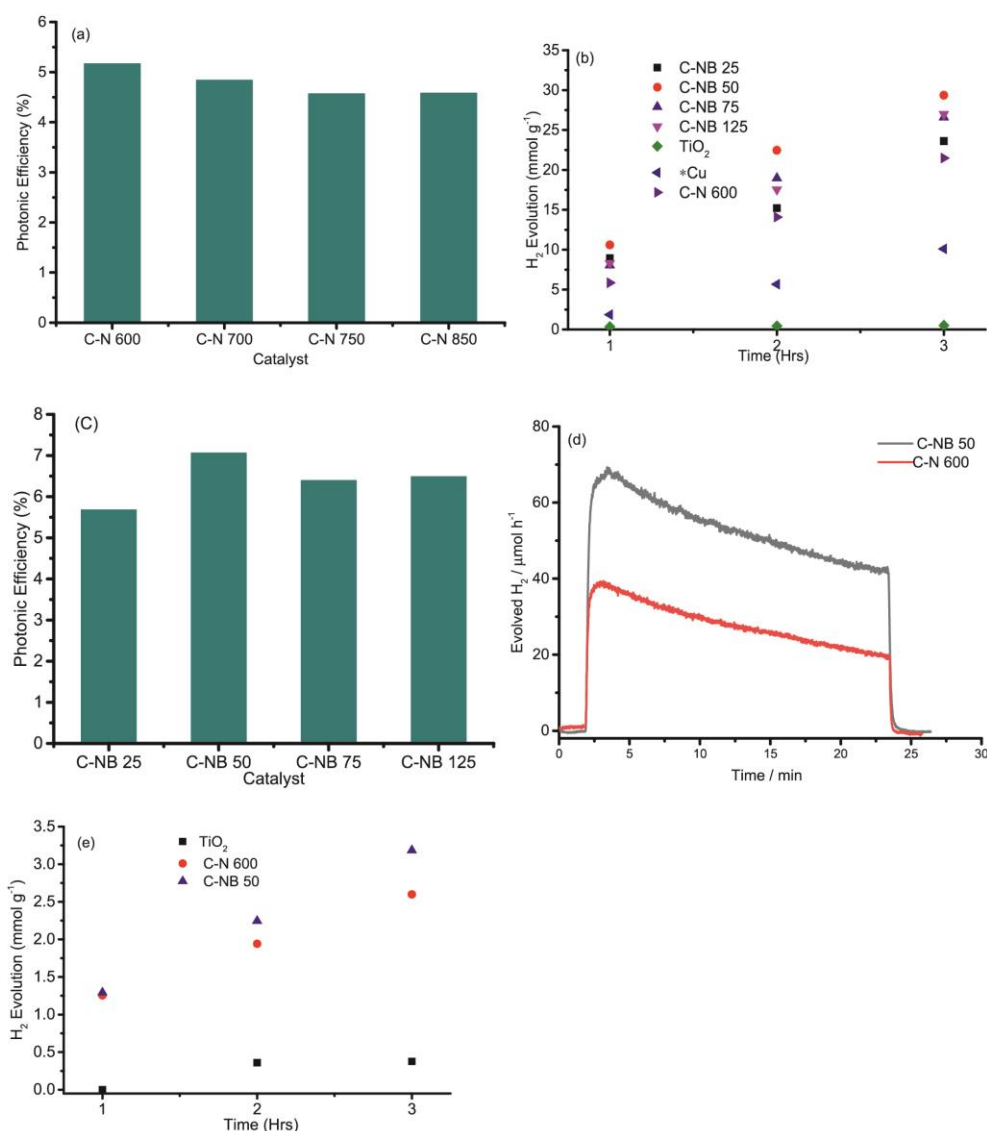


Fig. 8. Photocatalytic H<sub>2</sub> evolution photonic efficiency at  $300 < \lambda < 400$  nm of C-N 600–800 under solar irradiation (a), H<sub>2</sub> generation over TiO<sub>2</sub>, commercial \*Cu/TiO<sub>2</sub>, C-N 600 and C-NB 25–125 under solar irradiation (b), H<sub>2</sub> evolution photonic efficiency at  $300 < \lambda < 400$  nm of C-N 600 and C-NB 25–125 under solar irradiation (c), continuous flow of H<sub>2</sub> production over C-N 600 and C-NB 50 under solar irradiation (d) and H<sub>2</sub> production over TiO<sub>2</sub>, C-N 600 and C-NB 50 under UV irradiation (e).

(Kecsenovity et al., 2017).

B/N-co-doped samples were calcined at 600 °C as this temperature produces the most active N-containing Cu composites. Under solar irradiation, all co-doped composites exhibit higher H<sub>2</sub> evolution rates and photonic efficiencies compared with the mono N-doped composite labelled C-N 600 (Fig. 8b and c). XPS analysis showed that co-doped samples consist purely of Cu<sup>0/1+</sup> while C-N 600 contains Cu<sup>0/1+</sup> and low amounts of Cu<sup>2+</sup>. Since C-N 600 exhibits a higher activity and efficiency than C-N 700–850 that consist purely of Cu<sup>0/1+</sup>, the lower activity and efficiency of C-N 600 compared to all co-doped composites is

not primarily caused by the presence of Cu<sup>2+</sup> species. Instead, the higher activity and efficiency of co-doped composites points towards a synergistic enhancement of photoactivity facilitated by the composites' improved heterointerface stability and the formed redox systems via B/N co-doping as illustrated by DFT calculations (Ferrighi et al., 2015). Moreover, the photonic efficiencies increase from 5.68% to 7.06% (Table S1) upon doubling the B:N ratios from 0.04 to 0.08 (Table 1). A further increase of B:N ratios to 0.1 reduces the photonic efficiency to 6.49% which is still higher than that of C-N 600. Since all co-doped composites consist purely of Cu<sup>0/1+</sup> and exhibit a non-linear correlation

between activity and B:N ratios, the increase in efficiency from 5.68% to 7.06% is mainly attributed to increased B-doping levels to 0.2%. A further increase in B-doping levels to 0.28% slightly decreases the H<sub>2</sub> production rate.

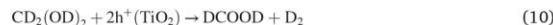
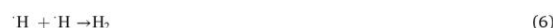
Based on XPS analysis, increasing B:N ratios increases the quantity of graphitic-N while decreasing the amount of pyridinic-N in co-doped samples. Thus, the decrease in efficiency from 7.06% to 6.49% is partially due to increase in graphitic-N that have no lone pairs of electrons at the expense of electron rich pyridinic-N as the B:N ratio increases. Additionally, at the interface between B/N-graphene and Cu, the p-type chemical doping via B (BC<sub>2</sub>O) accepts electrons from Cu creating a positively charged layer on the surface of Cu (Zhao et al., 2019). Increasing B% from 0.1% to 0.2% increases the p-type component of graphene (Table 1) as well as the stability of Cu coatings (Table 2) and further increasing the +ve charge on the surface of Cu. This creates a stronger driving force for electron migration to the surface of Cu resulting in increased H<sub>2</sub> evolution rates (Wu et al., 2021). At a lower B% (0.1%), the positive effect of the stronger driving force outweighs the negative effect of electron depletion by p-type B in BC<sub>2</sub>O. A further increase of B% to 0.28% not only increases the electron migration driving force but also increases the composition of BC<sub>2</sub>O which excessively consume the surface electrons. This competing process screens electrons from H<sup>+</sup> and shortens the lifetime of surface electrons thus reducing H<sub>2</sub> evolution rates and photonic efficiency (Samal et al., 2020). Consequently, the B:N ratio is crucial for tuning the photocatalytic activity of the composites with a ratio 0.08 giving the highest activity (Putri et al., 2018).

The stability of Cu/TiO<sub>2</sub> interfaces was evaluated by monitoring the continuous production of H<sub>2</sub> over C-NB 50 and C-N 600 within a period of 22 h (Fig. 8d). Higher H<sub>2</sub> evolution rates are recorded over C-NB 50 (68.9–42.18 μmol h<sup>-1</sup>) compared with C-N 600 (38.8–19.6 μmol h<sup>-1</sup>) as was also observed from batch reactions. After 22 h of solar irradiation, the H<sub>2</sub> evolution rate of C-NB 50 drops by 39% while that of C-N 600 drops by 49%. Therefore, both composites exhibit moderate stability with C-NB 50 being more stable than C-N 600. The higher stability of C-NB 50 is attributed to stronger adhesion of graphene coatings to Cu<sup>0</sup> as determined by DFT calculations. To further examine the stability of C-NB 50, used composites were reclaimed from the suspension and their photoactivity reanalyzed (Fig. S4). Recycled C-NB 50 does not exhibit lower H<sub>2</sub> production compared with freshly prepared C-NB 50. Thus, the overall stability of the recycled C-NB 50 showcases this catalyst as a potential candidate for large scale H<sub>2</sub> production.

All N- and B/N-containing copper composites produce higher quantities of H<sub>2</sub> compared to pristine TiO<sub>2</sub> and commercial Cu<sub>2</sub>O/TiO<sub>2</sub> composite (Fig. 8b). The most active composite was C-NB 50 that exhibited a photonic efficiency of 7.06% (Table S1) (Al-Madanat et al., 2020). Thus, C-NB 50 exhibited a 28-fold enhancement of the photonic efficiency of pristine TiO<sub>2</sub> (ξ = 0.25%). Evidently, the observed enhancement majorly originates from the redox systems in B/N-graphene and stronger electron migration driving forces in co-doped samples. However, the optical, physicochemical and elemental properties of copper must also be taken into consideration.

Conjugating coated copper to TiO<sub>2</sub> increased the visible light absorbance of the composites compared to pristine TiO<sub>2</sub> (Fig. 4). To evaluate the effect of visible light absorption on the composites' photocatalytic activity, H<sub>2</sub> production over TiO<sub>2</sub>, C-N 600 and C-NB 50 was monitored first under visible light, then under UV irradiation (Fig. 8e). No hydrogen was detected upon visible light irradiation of suspensions of all three catalysts. This nullifies the possibility of Plasmon resonance-initiated photocatalytic activity that has been reported to arise from visible light absorption of copper nanoparticles (Janczarek and Kowalska, 2017). UV irradiation of the suspensions of all three catalysts produces hydrogen in a trend similar to that observed under solar irradiation *vis* TiO<sub>2</sub> < C-N 600 < C-NB 50. Consequently, the water reduction process is initiated upon absorption of UV light by TiO<sub>2</sub> to generate electron-hole pairs (Ombaka et al., 2020a). The generated

electrons are then transferred from the conduction band of TiO<sub>2</sub> to Cu where the water reduction half reaction occurs. This indicates that the efficient transfer of generated electrons from TiO<sub>2</sub> to coated Cu and coppers' Fermi energy are the key parameters that influence the hydrogen production rate. The visible light absorbed by all composites may simply create thermal hot spots that accelerate H<sub>2</sub> production rates (Neelgund and Oki, 2018).



Insight into the nature of the interface and electronic communication between TiO<sub>2</sub> and coated Cu is inferable from morphological and FTIR studies (Atitar et al., 2015). TEM and SEM micrographs of Cu composites display TiO<sub>2</sub> nanoparticles anchored onto the facets, edges and other defect sites of Cu microparticles (Fig. 1). Such morphological arrangements depict an interparticle interface formed either electrostatically *via* weak van der Waals forces or through covalent bonding of TiO<sub>2</sub> to B/N functionalities on coated Cu (Deiana et al., 2010). The existence of coordinative forces at the composites' interface is inferred from FTIR analysis that depicts the perturbation of electron cloud around Ti-OH bonds. The thus formed coordinative bonds act as electron channels that facilitate efficient transfer of photogenerated electrons from TiO<sub>2</sub> to coated copper resulting in enhanced efficiencies (Sun et al., 2019).

### 3.7.1. H<sub>2</sub> formation mechanism

Photolysis of either methanol or water yields hydrogen. The former being termed methanol reformation while the latter a water reduction or water splitting process (Zhao et al., 2020). To identify the origin of the hydrogen evolved over the composites, isotopic reactions over C-NB 50 (probe catalyst) were monitored using quadrupole mass spectrometry (QMS). Four different solutions of water, methanol, deuterated water (D<sub>2</sub>O) and deuterated methanol (CD<sub>3</sub>OD) *vis* H<sub>2</sub>O/CH<sub>3</sub>OH, H<sub>2</sub>O/CD<sub>3</sub>OD, D<sub>2</sub>O/CH<sub>3</sub>OH and D<sub>2</sub>O/CD<sub>3</sub>OD were analyzed (Fig. 9). For all experiments the initial quantity of either CH<sub>3</sub>OH or CD<sub>3</sub>OD was 10% v/v. Irradiation of H<sub>2</sub>O/CH<sub>3</sub>OH yields H<sub>2</sub> as the major product (Fig. 9a). Similarly, irradiation of a H<sub>2</sub>O/CD<sub>3</sub>OD solution yields H<sub>2</sub> as the major product (Fig. 9b). This verifies that the H<sub>2</sub> produced over the composites (Fig. 8) primarily originates from the reduction of water-based H<sup>+</sup> ions. Although negligible quantities of HD and D<sub>2</sub> are evolved from H<sub>2</sub>O/CD<sub>3</sub>OD, the quantity of H<sub>2</sub> evolved using H<sub>2</sub>O/CD<sub>3</sub>OD is comparable to that obtained using H<sub>2</sub>O/CH<sub>3</sub>OH. Since both solutions statistically contain similar amounts of H<sub>2</sub>O, similar quantities of H<sub>2</sub> are expected from both solutions concurring with the observations (Kandiel et al., 2014).

The solution of D<sub>2</sub>O/CH<sub>3</sub>OH yields D<sub>2</sub> as the major product (Fig. 9c), with HD and H<sub>2</sub> being detected as minor products (D<sub>2</sub> > HD > H<sub>2</sub>). Considering the potential exchange between D<sup>+</sup> and H<sup>+</sup> ions, it is concluded that water is the main source of the H<sup>+</sup> ions reduced over copper to form H<sub>2</sub>. Given that statistically D<sub>2</sub>O comprises 90% v/v of the

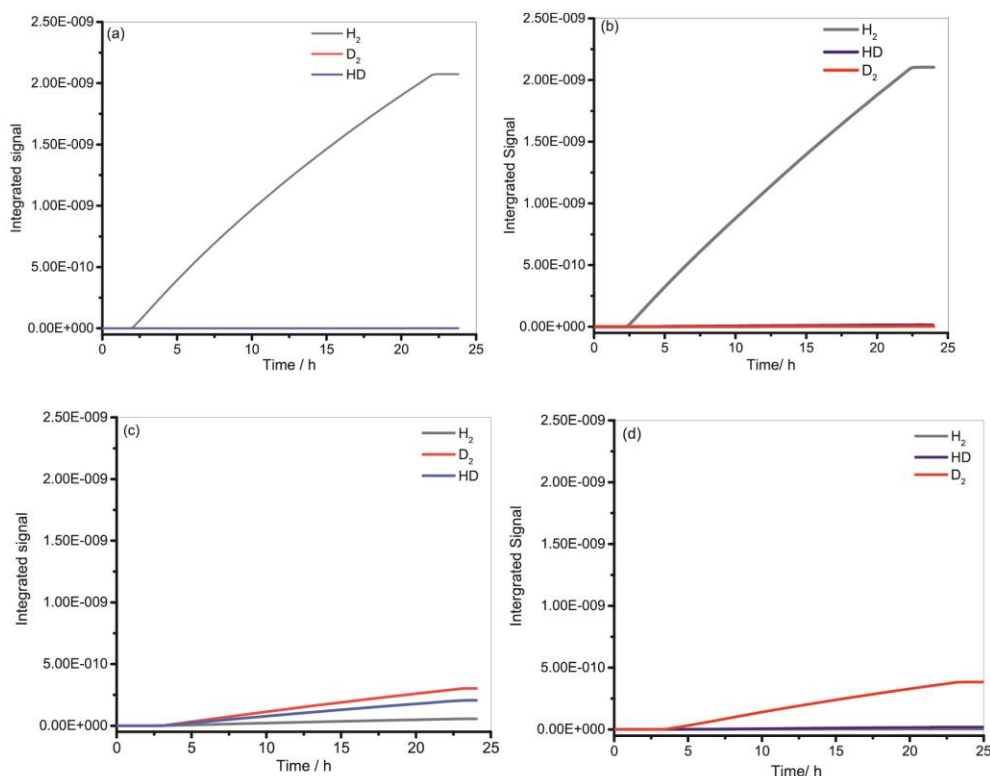


Fig. 9. QMS signals for H<sub>2</sub>, D<sub>2</sub> and HD formed under solar irradiation on C-NB 50 using H<sub>2</sub>O/CH<sub>3</sub>OH (a), H<sub>2</sub>O/CD<sub>3</sub>OD (b), D<sub>2</sub>O/CH<sub>3</sub>OH (c) and D<sub>2</sub>O/CD<sub>3</sub>OD (d) solutions.

D<sub>2</sub>O/CH<sub>3</sub>OH solution, it follows that the probability of D<sup>+</sup> ions being reduced to D<sub>2</sub> at the copper surface is higher than that of H<sup>+</sup> being reduced to H<sub>2</sub> (Belhadj et al., 2017). Therefore, although the reduction potential of D<sup>+</sup> is more negative than that of H<sup>+</sup>, the higher concentration of D<sup>+</sup> culminates in higher D<sub>2</sub> production. The quantity of D<sub>2</sub> detected from D<sub>2</sub>O/CH<sub>3</sub>OH is significantly lower than that of H<sub>2</sub> detected from H<sub>2</sub>O/CH<sub>3</sub>OH (Fig. 9a and c). Both solutions are of the same concentration (10% v/v CH<sub>3</sub>OH or CD<sub>3</sub>OD), therefore, the lower D<sub>2</sub> and higher H<sub>2</sub> evolution rate detected from D<sub>2</sub>O/CH<sub>3</sub>OH is attributed to the more negative reduction potential of D<sup>+</sup> ions compared to H<sup>+</sup> ions.

Substitution of both H<sub>2</sub>O and CH<sub>3</sub>OH with D<sub>2</sub>O and CD<sub>3</sub>OD respectively produces D<sub>2</sub> as the major product and negligible quantities of HD and H<sub>2</sub> originating from H<sub>2</sub>O adsorbed onto the surface of the catalyst and reaction apparatus (Fig. 9d). The amount of D<sub>2</sub> detected from D<sub>2</sub>O/CH<sub>3</sub>OH is slightly lower than that detected using D<sub>2</sub>O/CD<sub>3</sub>OD, thus implying that the amount of D<sub>2</sub> in the latter system originating from CD<sub>3</sub>OD is negligible. Consequently, affirming that H<sub>2</sub>O is the major source of the hydrogen produced over all catalysts. The major by-product detected in the solution of H<sub>2</sub>O/CH<sub>3</sub>OH after 3 h of solar irradiation was formaldehyde at a concentration of 1.23 mmol. Given that, low quantities of carbon dioxide (CO<sub>2</sub>) were detected, it is deduced that H<sub>2</sub> was mainly produced via a methanol-assisted water reduction process. In view of these and the observations that H<sub>2</sub> evolution occurred only in the presence of methanol and UV light, the mechanism for H<sub>2</sub>, D<sub>2</sub> and CO<sub>2</sub> formation is provided as depicted in Equations (2)–(11) (Belhadj et al., 2017). Based on the proposed mechanism a 1:1 mol ratio of H<sub>2</sub>: CH<sub>3</sub>OH is expected however, after 3 h of irradiation only 0.18 mmol

of H<sub>2</sub> is generated from a solution of H<sub>2</sub>O/CH<sub>3</sub>OH. This concentration gives a 15% yield of H<sub>2</sub> relative to that expected from the formed formaldehyde, indicating that other side reactions consume the generated protons before they recombine to form H<sub>2</sub>. It then follows that identification and reduction of these side reactions could significantly increase the quantities of H<sub>2</sub> formed via water reduction, thus boosting the composites' efficiency.

### 3.8. Photocatalytic degradation of 2-CP

Photocatalytic degradation of 2-CP under solar irradiation was conducted over pristine TiO<sub>2</sub> and C-NB 50 that gave the highest H<sub>2</sub> evolution photonic efficiency. Under solar irradiation, the tested catalysts were active towards the degradation of 2-CP (Fig. 10a). Within 80 min of irradiation, pristine TiO<sub>2</sub> degraded 91.67% of 2-CP. Upon modification with 40% of coated Cu (C-NB 50), there was a drastic decrease in the photocatalytic degradation of 2-CP. The decrease in performance was associated with the use of excess modifier on pristine TiO<sub>2</sub>, which in the presence of oxygen, facilitates oxidation of Cu<sup>0</sup> to Cu<sup>2+</sup> (Li et al., 2011; Oseghe et al., 2015). This was overcome by reducing the composition of coated Cu in the composite to 6% (C-NB 50<sub>6</sub>) resulting in 100% degradation of 2-CP within the experimental period. However, a further decrease in Cu composition to 3% (C-NB 50<sub>3</sub>) suppressed the activity by about 43%. The drop in performance may have resulted from limited electron trap site on coated Cu, thereby fostering electron-hole recombination in TiO<sub>2</sub>.

Linear pseudo-first order model (equation (12) and (13)) was used to investigate the reaction kinetics for 2-CP degradation.

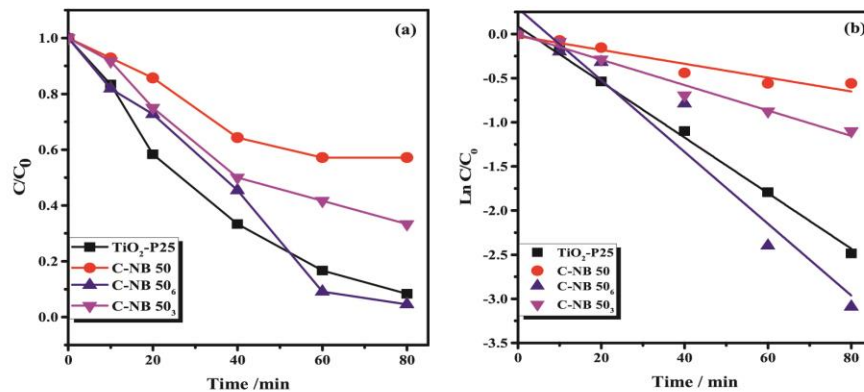


Fig. 10. Percentage degradation of 2-CP (a) and 2-CP degradation kinetics (b) over TiO<sub>2</sub>, C-NB 50, C-NB 50<sub>6</sub> and C-NB 50<sub>3</sub>.

$$\ln C/C_0 = k_{app}t \quad (12)$$

$$t_{1/2} = \frac{\ln 2}{k_{app}} \quad (13)$$

where  $C$  is the concentration of 2-CP after the photocatalytic experiment,  $C_0$  is the initial concentration before the experiment,  $k_{app}$  is the rate constant, and  $t$  is the reaction time (Li et al., 2014; Teng et al., 2014). The apparent rate constant,  $k_{app}$ , half-life,  $t_{1/2}$ , and coefficient of determination,  $R^2$  are presented in Table 3. Fig. 10b and the  $R^2$  shows that results obtained from the photocatalytic degradation experiment fits into the pseudo-first order kinetics.

$k_{app}$  and  $t_{1/2}$  are often compared to comparatively evaluate the performance of the photocatalysts. The catalysts having the highest  $k_{app}$  and lowest  $t_{1/2}$  is considered most active [58]. In this study C-NB 50<sub>6</sub> exhibits the best performance as it has the highest  $k_{app}$  ( $4.07 \times 10^{-2} \text{ min}^{-1}$ ) and the lowest  $t_{1/2}$  (17 min). This implies that it will take about 17 min for C-NB 50<sub>6</sub> to degrade 50% of aqueous 2-CP under the solar simulator.

### 3.8.1. Mechanism of 2-CP degradation

To understand the mechanism for the photodegradation 2-CP by C-NB 50<sub>6</sub>, photocatalytic experiments were conducted in the presence and absence of scavengers. The scavengers in this study were Ethylenediaminetetraacetic acid (EDTA), isopropanol (IPA), and benzoquinone (BQ) for scavenging  $h^+$ ,  $OH^\bullet$ , and  $O_2^\bullet$  respectively as have been reported in literature (Malefane et al., 2020; Moshoeu et al., 2020). Fig. 11a shows the effect of scavengers on the degradation of 2-CP in the presence of C-NB 50<sub>6</sub>. In 30 min of the photocatalytic reaction and in the absence of a scavenger, 100% degradation was achieved.

A drastic drop in percentage degradation was observed in the presence of scavengers most notably with BQ, indicating that all the reactive species played a role in the degradation of 2-CP. However,  $O_2^\bullet$  played the major role in the percentage degradation of 2-CP as no degradation was observed in the presence of BQ. Since  $O_2^\bullet$  are generated on the Cu<sup>0</sup> surface, the efficient transfer of electrons to coated Cu plays a major role in the enhancement of the degradation activity. Based on the outcome of

the scavenging experiment, the photocatalytic mechanism is proposed in Fig. 11b.

When C-NB 50<sub>6</sub> is illuminated with solar irradiations, electrons ( $e^-$ ) are excited from the valence band (VB) of TiO<sub>2</sub> into the conduction band (CB) thereby leaving a hole ( $h^+$ ) in the VB. Cu<sup>0</sup> in the composite act as  $e^-$  trap resulting in better separation of electron-hole pair. The separated charges react with surface hydroxyl, H<sub>2</sub>O, and O<sub>2</sub> in the solution to form superoxide anion radical ( $O_2^\bullet$ ) and hydroxyl radical ( $OH^\bullet$ ) which assists in the degradation. The  $h^+$  can also react directly with 2-CP to form products.

## 4. Conclusions

In the near future, hydrogen demands will exceedingly increase. Therefore, reaction routes that provide additional benefits may be brought to the fore. In the reported dual-functional reaction system, B/N-graphene-coated Cu/TiO<sub>2</sub> operates as a photocatalyst for the complete degradation of the pollutant 2-chlorophenol and simultaneous production of hydrogen via photocatalytic water splitting. The ratio of B:N in graphene coatings influence the H<sub>2</sub> production photonic efficiency with a ratio of 0.08 (C-NB 50) displaying the highest efficiency (7.06%). The overall trend of increasing catalytic photonic efficiency and stability follows the order TiO<sub>2</sub> < N-graphene-coated Cu/TiO<sub>2</sub> (C-N x) < B/N-graphene-coated Cu/TiO<sub>2</sub> (C-NB x). A lower composition of B/N-graphene-coated Cu<sup>0</sup> in TiO<sub>2</sub> (C-NB 50<sub>6</sub>) shows a faster rate towards 2-chlorophenol degradations compared to pristine TiO<sub>2</sub>. The higher activity and stability of B/N-graphene-coated Cu/TiO<sub>2</sub> is attributed to increased stability of carbon coatings on Cu<sup>0</sup> via B-doping, more negative reduction potential via N-doping, improved photoelectron transfer via the redox system at the Cu/TiO<sub>2</sub> interface and overall enhanced light harvesting capacity of the composites. However, the efficient transfer of photoelectrons from TiO<sub>2</sub> to Cu<sup>0</sup> and the Fermi energy of Cu<sup>0</sup> are key influences of Cu/TiO<sub>2</sub> photoactivity. B/N-graphene coatings are both p- and n-type doped via B- and N-doping respectively. Thus, increasing the B:N ratio increases p-type doping by increasing the BC<sub>2</sub>O in graphene while reducing n-type doping by decreasing pyridinic-N therefore stategically tuning the polarity of Cu<sup>0</sup>/TiO<sub>2</sub> interface and altering the composites photoactivity. Mechanistic investigations indicate that H<sub>2</sub> is majorly produced from water through a methanol-assisted water reduction reaction while  $O_2^\bullet$  is the main reactive species in the degradation of 2-chlorophenol. While the possibilities of the composite photocatalysts are intruding, regarding both the H<sub>2</sub> production and the 2-CP degradation, additional studies focusing on further optimizing the dual-functionalities of the best performing photocatalyst to improve its photocatalytic properties is a worthwhile venture.

Table 3  
Kinetics of 2-CP degradation by TiO<sub>2</sub> and C-NB 50<sub>3</sub>.

Materials	$k_{app}$ (min <sup>-1</sup> )	$t_{1/2}$ (min)	$R^2$
P25	$3.15 \times 10^{-2}$	22	0.9962
C-NB 50	$7.80 \times 10^{-3}$	89	0.9193
C-NB 50 <sub>6</sub>	$4.07 \times 10^{-2}$	17	0.9389
C-NB 50 <sub>3</sub>	$1.44 \times 10^{-2}$	48	0.9801

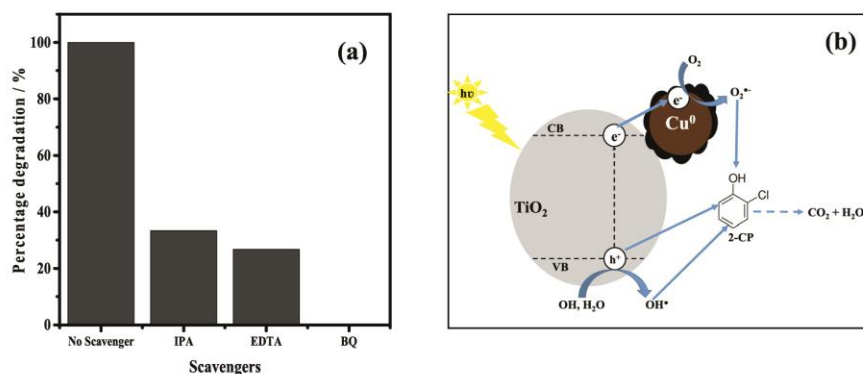


Fig. 11. Effect of scavengers on the degradation of 2-CP in the presence of C-NB 50<sub>6</sub> (a) and proposed mechanism for the degradation of 2-CP (b).

#### Credit author statement

**Lucy M. Ombaka** Conceptualization, Methodology, Investigation, writing, Project administration, Funding acquisition, Visualization, **James D. McGettrick** Investigation, Writing, **Ekemena O. Oseghe** Investigation, Writing, **Osama Al-Madanat** Investigation, Writing, **Felix Rieck** genannt-Best Investigation, Writing, **Titus A. M. Msagati** Visualization, Resources, **Matthew L. Davies** Visualization, editing, Resources, **Thomas Bredow** Software Validation, Formal analysis, Resources, **Detlef W. Bahneman** Supervision, Funding acquisition, Visualization, Resources

#### Notes

The authors declare no conflict of interest.

#### Declaration of competing interest

The authors declare that they have no known competing financial interests or personal relationships that could have appeared to influence the work reported in this paper.

#### Acknowledgments

This work was funded by the Alexander von Humboldt Foundation. Special thanks goes Patrick Bessel for the UV-Vis-NIR analysis. J.D.M. and M.L.D. are grateful for the support of the EPSRC, Welsh Government (Project 80708) and Innovate UK for the SPECIFIC Innovation and Knowledge Center (EP/N020863/1). M.L.D. is grateful for the financial support of the EPSRC (EP/R016666/1 and EP/S001336/1). F.R.g.B. thanks the Deutsche Forschungsgemeinschaft (DFG), grant CA147/21-1, projectnumber 322911753for the financial support. T.B. thanks the Paderborn Center for Parallel Computing for providing computational resources.

#### Appendix A. Supplementary data

Supplementary data to this article can be found online at <https://doi.org/10.1016/j.jenvman.2022.114822>.

#### References

- Al-Madanat, O., Alsalka, Y., Curti, M., Dillert, R., Bahnemann, D.W., 2020. Mechanistic insights into hydrogen evolution by photocatalytic reforming of naphthalene. *ACS Catal.* 10, 7398–7412.
- Atitar, M.F., Belhadj, H., Dillert, R., Bahnemann, D.W., 2015. The relevance of ATR-FTIR spectroscopy in semiconductor photocatalysis. *Emerg. Pollut. Environ. - Curr. Furth. Implic.* 201–227.

- Belhadj, H., Hamid, S., Robertson, P.K.J., Bahnemann, D.W., 2017. Mechanisms of simultaneous hydrogen production and formaldehyde oxidation in H<sub>2</sub>O and D<sub>2</sub>O over platinumized TiO<sub>2</sub>. *ACS Catal.* 7, 4753–4758.
- Biesinger, M.C., 2017. Advanced analysis of copper X-ray photoelectron spectra. *Surf. Interface Anal.* 49, 1325–1334.
- Biesinger, M.C., Lau, L.W.M., Gerson, A.R., Smart, R.S.C., 2010. Resolving surface chemical states in XPS analysis of first row transition metals, oxides and hydroxides: Sc, Ti, V, Cu and Zn. *Appl. Surf. Sci.* 257, 887–898.
- Bulusheva, D.A., Chuvilin, A.L., Sobolev, V.I., Stolyarova, S.G., Shubin, Y.V., Asanov, I.P., Ishchenko, A.V., Magnani, G., Ricco, M., Okotrub, A.V., Bulusheva, L.G., 2017. Copper on carbon materials: stabilization by nitrogen doping. *J. Mater. Chem. A* 5, 10574–10583.
- Chan, G.H., Zhao, J., Hicks, E.M., Schatz, G.C., Van Duyne, R.P., 2007. Plasmonic properties of copper nanoparticles fabricated by nanosphere lithography. *Nano Lett.* 7, 1947–1952.
- Chen, S., Li, X., Zhou, W., Zhang, S., Fang, Y., 2019. Carbon-coated Cu-TiO<sub>2</sub> nanocomposite with enhanced photostability and photocatalytic activity. *Appl. Surf. Sci.* 466, 254–261.
- Deiana, C., Fois, E., Coluccia, S., Martra, G., 2010. Surface structure of TiO<sub>2</sub> P25 nanoparticles: infrared study of hydroxy groups on coordinative defect sites. *J. Phys. Chem. C* 114, 21531–21538.
- Ferrighi, L., Trioni, M.L., Di Valentin, C., 2015. Boron-doped, nitrogen-doped, and codoped graphene on Cu(111): a DFT + vdW study. *J. Phys. Chem. C* 119, 6056–6064.
- Filhol, J.S., Neurock, M., 2006. Elucidation of the electrochemical activation of water over Pd by first principles. *Angew. Chem. Int. Ed.* 45, 402–406.
- Gawande, M.B., Goswami, A., Felpin, F.X., Asefa, T., Huang, X., Silva, R., Zou, X., Zboril, R., Varma, R.S., 2016. Cu and Cu-based nanoparticles: synthesis and applications in catalysis. *Chem. Rev.* 116, 3722–3811.
- Granone, L.L., Ulpe, A.C., Robben, L., Klinke, S., Jahns, M., Reuz, F., Gesing, T.M., Bredow, T., Dillert, R., Bahnemann, D.W., 2018. Effect of the degree of inversion on optical properties of spinel ZnFe<sub>2</sub>O<sub>4</sub>. *Phys. Chem. Chem. Phys.* 20, 28267–28278.
- Günemann, C., Curti, M., Gerrit Eckert, J., Schneider, J., Bahnemann, D.W., 2019. Tailoring the photoelectrochemical activity of TiO<sub>2</sub> electrodes by multilayer screen-printing. *ChemCatChem* 11, 6439–6450.
- Janczarek, M., Kowalska, E., 2017. On the origin of enhanced photocatalytic activity of copper modified titania in the oxidative reaction systems. *Catalysts* 7, 317–343.
- Jeon, J.P., Kweon, D.H., Jang, B.J., Ju, M.J., Baek, J.B., 2020. Enhancing the photocatalytic activity of TiO<sub>2</sub> catalysts. *Adv. Sustain. Syst.* 4, 1–19.
- Kalng, S., Yoo, H., Kim, J.H., 2020. Recent advances in earth-abundant photocatalyst materials for solar H<sub>2</sub> production. *Adv. Powder Technol.* 31, 11–28.
- Kandiel, T.A., Ivanova, I., Bahnemann, D.W., 2014. Long-term investigation of the photocatalytic hydrogen production on platinumized TiO<sub>2</sub>: an isotopic study. *Energy Environ. Sci.* 7, 1420–1425.
- Kecsenovity, E., Endrödi, B., Tóth, P.S., Zou, Y., Dryfe, R.A.W., Rajeshwar, K., Janáky, C., 2017. Enhanced photoelectrochemical performance of cuprous oxide/graphene nanohybrids. *J. Am. Chem. Soc.* 139, 6682–6692.
- Kirfel, A., Eichhorn, K., 1990. Accurate structure analysis with synchrotron radiation. The electron density in Al<sub>2</sub>O<sub>3</sub> and Cu<sub>2</sub>O. *Acta Crystallogr. A* 46, 271–284.
- Kleeberg, U., Klinger, W., 1982. Sensitive formaldehyde determination with NASH's reagent and a <sup>3</sup>tryptophan reaction. *J. Pharmacol. Methods* 8, 19–31.
- Kong, Y., Li, Y., Yang, B., Li, Z., Yao, Y., Lu, J., Lei, L., Wen, Z., Shao, M., Hou, Y., 2019. Boron and nitrogen co-doped porous carbon nanofibers as metal-free electrocatalysts for highly efficient ammonia electrosynthesis. *J. Mater. Chem. A* 7, 26272–26278.
- Li, H., Wang, D., Fan, H., Jiang, T., Li, X., Xie, T., 2011. Synthesis of ordered multivalent Mn-TiO<sub>2</sub> nanospheres with tunable size: a high performance visible-light photocatalyst. *Nano Res.* 4, 460–469.
- Li, S., Cai, J., Wu, X., Zheng, F., Lin, X., Liang, W., Chen, J., Zheng, J., Lai, Z., Chen, T., 2014. Fabrication of positively and negatively charged, double shelled, nanostructured hollow spheres for photodegradation of cationic and anionic

- aromatic pollutants under sunlight irradiation. *Appl. Catal. B Environ.* 160–161, 279–285.
- Malefane, M.E., Feleni, U., Mafa, P.J., Kuvarega, A.T., 2020. Fabrication of direct Z-scheme Co<sub>3</sub>O<sub>4</sub>/BiOI for ibuprofen and trimethoprim degradation under visible light irradiation. *Appl. Surf. Sci.* 514, 145940.
- Martins, A.C., Cazetta, A.L., Pezoti, O., Souza, J.R.B., Zhang, T., Pilau, E.J., Asefa, T., Almeida, V.C., 2017. Sol gel synthesis of new TiO<sub>2</sub>/activated carbon photocatalyst and its application for degradation of tetracycline. *Ceram. Int.* 43, 4411–4418.
- Melchionna, M., Fornasiero, P., 2020. Updates on the roadmap for photocatalysis. *ACS Catal.* 10, 5493–5501.
- Mohanty, S., Khare, P., Jain, R., Kaul, S.N., 2003. Photocatalytic degradation of 2-chlorophenol: a study of kinetics, intermediates and biodegradability. *J. Hazard Mater.* 101, 301–314.
- Mokhtar Mohamed, M., Mousa, M.A., Khairy, M., Amer, A.A., 2018. Nitrogen graphene: a new and exciting generation of visible light driven photocatalyst and energy storage application. *ACS Omega* 3, 1801–1814.
- Moshoeu, D.E., Sanni, S.O., Oseghe, E.O., Msagati, T.A.M., Mamba, B.B., Ofomaja, A.E., 2020. Morphological influence of TiO<sub>2</sub> nanostructures on charge transfer and tetracycline degradation under LED light. *ChemistrySelect* 5, 1037–1040.
- Naumkin, A.V., Kraut-Vass, A., Gaarenstroom, S.W., 2012. NIST X-ray photoelectron spectroscopy database. *Meas. Serv. Div. Natl. Inst. Stand. Technol.* 20899, 20899.
- Neelgund, G.M., Oki, A., 2018. Photothermal effect: an important aspect for the enhancement of photocatalytic activity under illumination by NIR radiation. *Mater. Chem. Front.* 2, 64–75.
- Nie, J., Patrocinio, A.O.T., Hamid, S., Sieland, F., Sann, J., Xia, S., Bahnemann, D.W., Schneider, J., 2018. New insights into the plasmonic enhancement for photocatalytic H<sub>2</sub> production by Cu-TiO<sub>2</sub> upon visible light illumination. *Phys. Chem. Chem. Phys.* 20, 5264–5273.
- Ombaka, L.M., Ndungu, P.G., Nyamori, V.O., 2015a. Tuning the nitrogen content and surface properties of nitrogen-doped carbon nanotubes synthesized using a nitrogen-containing ferrocenyl derivative and ethylbenzoate. *J. Mater. Sci.* 50, 1187–1200.
- Ombaka, L.M., Ndungu, P.G., Nyamori, V.O., 2015b. Pyrolytic nitrogen-doped carbon nanotubes: physicochemical properties, interactions with Pd and their role in the selective hydrogenation of nitrobenzophenone. *RSC Adv.* 5, 109–122.
- Ombaka, L.M., Curti, M., McGettrick, J.D., Davies, M.L., Bahnemann, D.W., 2020a. Nitrogen/carbon coated zero-valent copper as highly efficient Co-catalysts for TiO<sub>2</sub> applied in photocatalytic and photoelectrocatalytic hydrogen production. *ACS Appl. Mater. Interfaces* 12, 30365–30380.
- Ombaka, L.M., Dillert, R., Robben, L., Bahnemann, D.W., 2020b. Evaluating carbon dots as electron mediators in photochemical and photocatalytic processes of NiFe<sub>2</sub>O<sub>4</sub>. *Appl. Mater.* 8, 031105. –1.
- Oosthuizen, R.S., Nyamori, V.O., 2012. Heteroatom-containing ferrocene derivatives as catalysts for MWCNTs and other shaped carbon nanomaterials. *Appl. Organomet. Chem.* 26, 536–545.
- Oseghe, E.O., Ndungu, P.G., Jonnalagadda, S.B., 2015. Synthesis of mesoporous Mn/TiO<sub>2</sub> nanocomposites and investigating the photocatalytic properties in aqueous systems. *Environ. Sci. Pollut. Res.* 22, 211–222.
- Pulkkinen, P., Shan, J., Leppänen, K., Känkäkoski, A., Laiho, A., Järn, M., Tenhu, H., 2009. Poly(ethylene imine) and tetraethylenepentamine as protecting agents for metallic copper nanoparticles. *ACS Appl. Mater. Interfaces* 1, 519–525.
- Putri, L.K., Ng, B.J., Ong, W.J., Lee, H.W., Chang, W.S., Chai, S.P., 2018. Engineering nanoscale p-n junction: via the synergetic dual-doping of p-type boron-doped graphene hybridized with n-type oxygen-doped carbon nitride for enhanced photocatalytic hydrogen evolution. *J. Mater. Chem. A* 6, 3181–3194.
- Qureshi, M., Takanebe, K., 2017. Insights on measuring and reporting heterogeneous photocatalysis: efficiency definitions and setup examples. *Chem. Mater.* 29, 158–167.
- Samal, P.K., Sharma, L., Halder, A., 2020. Enhanced photoelectrochemical hydrogen evolution by 2D nanoleaf structured CuO. *J. Appl. Phys.* 127, 194902.
- Sun, L., Zhuang, Y., Yuan, Y., Zhan, W., Wang, X.J., Han, X., Zhao, Y., 2019. Nitrogen-doped carbon-coated CuO-In<sub>2</sub>O<sub>3</sub> p-n heterojunction for remarkable photocatalytic hydrogen evolution. *Adv. Energy Mater.* 9, 1902839.
- Teng, F., Zhang, G., Wang, Y., Gao, C., Chen, L., Zhang, P., Zhang, Z., Xie, E., 2014. The role of carbon in the photocatalytic reaction of carbon/TiO<sub>2</sub> photocatalysts. *Appl. Surf. Sci.* 320, 703–709.
- van Renssen, S., 2020. The hydrogen solution? *Nat. Clim. Change* 10, 799–801.
- Wang, M., Shen, S., Li, L., Tang, Z., Yang, J., 2017. Effects of sacrificial reagents on photocatalytic hydrogen evolution over different photocatalysts. *J. Mater. Sci.* 52, 5155–5164.
- Wang, Z., Li, C., Domen, K., 2019. Recent developments in heterogeneous photocatalysts for solar-driven overall water splitting. *Chem. Soc. Rev.* 48, 2109–2125 h.
- Wu, Y., Gao, Z., Li, H., Sun, X., Li, D., Zhou, G., Cai, H.-L., Wu, X., 2021. Promoting carrier separation efficiently by macroscopic polarization charges and interfacial modulation for photocatalysis. *Chem. Eng. J.* 410, 128393.
- Xu, Z., Buehler, M.J., 2010. Interface structure and mechanics between graphene and metal substrates: a first-principles study. *J. Phys. Condens. Matter* 22, 485301.
- Yang, L., Liu, B., Liu, T., Ma, X., Li, H., Yin, S., Sato, T., Wang, Y., 2017. A P25/(NH<sub>4</sub>)<sub>2</sub>WO<sub>6</sub> hybrid photocatalyst with broad spectrum photocatalytic properties under UV, visible, and near-infrared irradiation. *Sci. Rep.* 8, 1–11.
- Yao, G.-Y., Liu, Q.-L., Zhao, Z.-Y., 2018. Studied localized surface plasmon resonance effects of Au nanoparticles on TiO<sub>2</sub> by FDTD simulations. *Catalysts* 8, 236.
- Yu, X., Han, P., Wei, Z., Huang, L., Gu, Z., Peng, S., Ma, J., Zheng, G., 2018. Boron-doped graphene for electrocatalytic N<sub>2</sub> reduction.  *Joule* 2, 1610–1622.
- Zaleska, A., Sobczak, J.W., Grabowska, E., Hupka, J., 2008. Preparation and photocatalytic activity of boron-modified TiO<sub>2</sub> under UV and visible light. *Appl. Catal. B Environ.* 78, 92–100.
- Zhang, S., Peng, B., Yang, S., Wang, H., Yu, H., Fang, Y., Peng, F., 2015a. Non-noble metal copper nanoparticles-decorated TiO<sub>2</sub> nanotube arrays with plasmon-enhanced photocatalytic hydrogen evolution under visible light. *Int. J. Hydrogen Energy* 40, 303–310.
- Zhang, J., Nie, N., Liu, Y., Wang, J., Yu, F., Gu, J., Li, W., 2015b. Boron and nitrogen codoped carbon layers of LiFePO<sub>4</sub> improve the high-rate electrochemical performance for lithium ion batteries. *ACS Appl. Mater. Interfaces* 7, 20134–20143.
- Zhao, Z., Willard, E.J., Dominguez, J.R., Wu, Z., Osterloh, F.E., 2019. Depletion layer controls photocatalytic hydrogen evolution with p-type gallium phosphide particles. *J. Mater. Chem. A* 7, 18020–18029.
- Zhao, J., Shi, R., Li, Z., Zhou, C., Zhang, T., 2020. How to make use of methanol in green catalytic hydrogen production? *Nano Sel* 1, 12–29.
- Zheng, Y., Jiao, Y., Ge, L., Jaroniec, M., Qiao, S.Z., 2013. Two-step boron and nitrogen doping in graphene for enhanced synergistic catalysis. *Angew. Chem.* 125, 3192–3198.
- Zhu, J., Cheng, G., Xiong, J., Li, W., Dou, S., 2019. Recent advances in Cu-based cocatalysts toward solar-to-hydrogen evolution: categories and roles. *Sol. RRL* 3, 1–20.

## 11. Summary

The interdisciplinary work of chemistry and engineering go hand in hand in the design and realisation of complex chemical reactor systems. In the present work, the opportunities and different possibilities porous materials still are able to offer, even after decades of intense research, were highlighted. On the one hand, the application of an Na-LTA membrane was tested as an addition to the methylamine synthesis from methanol and ammonia. Na-LTA is known for their highly hydrophilic pores and was therefore already tested in a widespread number of reactions to in situ remove water from the reaction environment either in gas permeation or in pervaporation. With a rigid pore diameter of 4.1 Å it is able to selectively separate water from the other by-products of the methylamine synthesis. The methylamine synthesis itself is a cascade reaction, signifying that methanol can either react with ammonia to form monomethylamine (MMA) or with the MMA to produce dimethylamine (DMA) and consequently trimethylamine (TMA). TMA is thereby the kinetically and thermodynamically preferred product, but its demand is limited, as DMA is the most industrially desired product. The aim of the combination of the water extraction Na-LTA membrane and the methylamine synthesis in a tube reactor was to alter the product composition to achieve more concentrated mixtures. The water removal intensified the methylation rate, as each methylation step from MMA to DMA and to TMA produces water as the by-product. With the H-MOR zeolite catalysts used, the TMA selectivity was increased from 35% with membrane support to 39% with the Na-LTA membrane at 350 °C at the expense of less MMA in the product mixture. However, since the goal was to achieve higher quantities of DMA, other catalysts were tested. Aluminosilicates with the CHA structure type are destined for their application as a catalyst in the methylamine synthesis, as they provide pore windows with a diameter of 3.8 Å. This effectively traps any produced TMA inside the pores, which can disproportionate into the smaller amines. Previous research indicate that it is most likely, that TMA cannot be formed at all since the CHA pores do not allow the formation of the required transition states due to steric limitations. By excluding TMA from the product mixture, the increased methylation rate due to the in situ water removal essentially stopped at the DMA, in the case of a H-SAPO-34 catalyst the share of DMA could be massively increased from 39% without membrane support to 56% with membrane support, while the selectivity towards MMA decreased from 39% to 15% due to the addition of the Na-LTA membrane. However, the H-SAPO-34 catalyst in methylamine synthesis



suffers from large amounts of dimethylether (DME) production as an unwanted by-product, which increased even more with the water removing Na-LTA membrane. To solve this issue, the isostructural zeolite equivalent H-SSZ-13 was tested as the catalyst. It equally suppressed the TMA formation but also provided a higher acid site strength, which led to a negligible production of DME. H-SSZ-13 benefited from the water extraction similarly to H-SAPO-34 as the DMA share in the product mixture was improved from 51% to 71% with the addition of the steam removal Na-LTA membrane, while MMA went down from 40% to 19%. The methylamine synthesis with a H-SSZ-13 catalyst therefore provided an unmatched concentration of DMA in the product composition. To understand why the CHA type catalysts profited from the water extraction to a larger extent compared to H-MOR, IR experiments and comparisons with thermodynamic and adsorption isotherm data from literature were conducted.<sup>270</sup> It could be shown that water was preferably adsorbed at the acid site of the zeolite catalysts over methanol. In the small-pore catalysts of the CHA type, this results in blocking of important catalytic sites and diffusion paths. In the large-pore H-MOR catalyst the channels are so wide that methanol and the product still can move past adsorbed water. This led to the conclusion, that the in situ removal of water with the CHA catalysts not only influenced the equilibrium shift of the methylation steps, but also provided relief by removing it from blocked acid sites and pore channels, leading to the observation that the DMA selectivity could be massively improved. However, it was also expected that the methanol conversion rate would increase due to the water extraction, but the results showed a steady conversion for both the system with and without Na-LTA membrane supports. Additionally, performed H<sub>2</sub>O/NH<sub>3</sub> and H<sub>2</sub>O/MeOH gas separation experiments highlighted that the Na-LTA lacked the necessary selectivity to separate water from ammonia and methanol effectively. This resulted in an unintentional slip of ammonia and methanol through the membrane and therefore, higher amounts of unreacted methanol.

To solve this issue, an upgrade of the Na-LTA was approached in a variety of experiments. The post synthesis ion exchange from Na<sup>+</sup> to K<sup>+</sup> was researched and an optimal ion exchange route was found with an exchange rate of over 99% and the prevention of crack formation. The resulting K-LTA membranes were found to massively improve the H<sub>2</sub>O+MeOH separation factors, as the pore diameter was narrowed down to 2.9 Å and effectively excluded methanol due to its diameter of 3.6 Å, while the ideal separation factor was improved from 300

(Na LTA) to almost 1200 (K-LTA). The same tendency was shown for H<sub>2</sub>O+NH<sub>3</sub> separation with the separation factor going up from 17 for Na-LTA to 61 for K-LTA. In a novel set of measurements, mixed gas permeation of the, for the methylamine synthesis important, mixtures of H<sub>2</sub>O/NH<sub>3</sub> and H<sub>2</sub>O/MeOH were performed for the first time. It was shown, that the selectivity of the LTA membranes decreased when two gases are permeated at the same time compared to the ideal separation measured by single gas permeation. Conclusions led to similar reasons as in pervaporation experiments, as coupled diffusion leads to the improved diffusion of ammonia and methanol together with water because of intermolecular interactions. The overall improved separation of water with ammonia and methanol resulted in an improved conversion rate in the methylamine synthesis. The methanol conversion rate increased from 91% without membrane support to 94% due to the water removal by the K-LTA membrane. In the H-MOR catalyst the enhancement was even larger, as the methanol conversion rose from 70% to 80% with the K-LTA membrane. Therefore, K-LTA prevailed as the membrane material of choice for the methylamine synthesis with improved methanol conversion rates and high selectivities towards DMA with the CHA type catalysts.

The addition of the Na-LTA membrane was also tested for the methanol-to-olefins (MTO) reaction, in which methanol can form small olefins over a H-SAPO-34 catalyst. The reaction without membrane support exhibited a typical MTO route, where the selectivity towards ethene increased over time, at expense of the propene selectivity, before the reaction broke down after 3 hours due to extensive catalyst coking. This coking refers to the formation of methylated aromatics inside the CHA pores. The smallest coke residues, the (poly-)methylated derivatives of benzene function as an autocatalyst in the MTO reaction, as they split off small alkenes like ethene and propene, while afterwards getting re-methylated by methanol. When side-reactions occur, the aromatics can grow until they occupy the whole pore, effectively deactivating the catalyst particles. As each methylation step produces water, the application of the water removing LTA membrane was evident. It was observed, that the water extraction supported the reaction, as the fluctuating product composition over time without membrane support could be stabilized over the whole 3 hours of reaction time with the addition of the Na-LTA membrane. Furthermore, the SAPO catalyst with the membrane support was still functional after the set time of 3 hours while having produced similar amounts of olefins compared to

the bare catalyst. Conclusively, the coking process could be delayed due to the water extraction. This is a somewhat surprising results, as previous research showed that adding water to the methanol feed helped inhibiting the coking process.<sup>246</sup> Thermal gravimetric measurements showed that for both systems with and without membrane support similar amounts of coke were formed, but indicated that their nature differed. GC-MS analysis of the coke residue from inside the pores exhibited that the carbonaceous residues from the catalyst without water removal membrane support were primarily of high-molecular origin, like pyrenes, while in the catalyst with the LTA membrane support mainly smaller aromatics like the methylated benzenes were found. This showed that the reactions were at different phases and explained why the catalyst with membrane support was still functional. In further studies, based on our results, it has to be distinguished that water in the methanol feed and the water in situ formed in the catalyst pore may serve different purposes. We expect that the in situ water removal facilitated the re-methylation of the smaller aromatics in favour of the formation of larger aromatics.

The last experiment under study was the application of the porous doped graphene as a stabilizer for the  $\text{Cu}^0$  cocatalyst in the  $\text{TiO}_2$  photochemical simultaneous water splitting (or the hydrogen production from methanol reformation) and decomposition of 2-chlorophenol. In a systematic study different ratios of nitrogen (N-) and boron/nitrogen (B/N-) co-doped graphene were tested and a synthesis route for a variety of  $\text{Cu}/\text{TiO}_2/\text{B}/\text{N}$ -graphene composite materials was achieved. The co-doped B/N-graphene samples in the  $\text{Cu}/\text{TiO}_2$  photocatalyst thereby outperformed their N-graphene equivalents. In a systematic study the best boron/nitrogen ration was determined, which exhibited a photonic efficiency of around 7% towards the hydrogen production, while providing an improved long-term stability due to the p-type boron doping and more negative reduction potential via n-type nitrogen doping. However, this system was not able to split pure water into hydrogen and oxygen, it needed the addition of methanol to the reaction mixture. Further experiments were dedicated to revealing the mechanism of hydrogen formation from a methanol/water mixture at the B/N-graphene  $\text{Cu}/\text{TiO}_2$  photocatalysts. By using deuterated water and/or methanol it was shown that the hydrogen formation is based on hydrogen from water, resulting in a methanol-assisted water reduction process with an improved adsorption of molecules due to the graphene coating. Unfortunately, other side reactions can occur which significantly decrease the quantities of

hydrogen formed, hence, the improved photonic efficiency and enhanced visible light harvest capacity cannot be exploited to its fullest extent. Simultaneous degradation of 2-chlorophenol (2-CP) was tested with the best performing hydrogen producing photocatalyst. It was found out that the pristine TiO<sub>2</sub> performed better for the 2-CP degradation (around 90%) than the “best” B/N-graphene Cu/TiO<sub>2</sub> photocatalyst. Again the studying of the degradation mechanism showed that excessive amounts of oxygen radicals were the reason for the partial oxidation of Cu<sup>0</sup> to the less active Cu<sup>2+</sup>. By systematically reducing the Cu<sup>0</sup> share in the catalyst from 40% to 6%, a 100% degradation activity after 80 minutes could be achieved. Further lowering of the copper content reduced it under a critical composition, in which the copper was not able to trap all electrons from the TiO<sub>2</sub> anymore.

## 12. Conclusion & outlook

All three shown catalyst system are essentially dual-functional reactors:

- (i) In the methylamine synthesis the amines are formed, while the zeolite membrane in situ separates the products from the reactants methanol, ammonia and water. The water extraction additionally facilitates the methylation rate and provided a larger share of DMA.
- (ii) In the MTO synthesis small olefins are formed, while the zeolite membrane in situ separates the products from the reactants methanol and water. The water extraction additionally inhibits the harmful formation of larger carbonaceous aromatics inside the catalyst pores and enhanced the long-term stability.
- (iii) In the photochemical hydrogen production, the efficiency was improved with a co-doped graphene/Cu/TiO<sub>2</sub> composite, while also being able to degrade 2-chlorophenol. The graphene layers improved the stability of the Cu<sup>0</sup> cocatalyst and enhanced the adsorption properties.

Each reaction is providing promising results, which make them suitable for large scale applications. In the methylamine synthesis a novel option to influence the amine selectivity was achieved, with large quantities of the industrially desired DMA. In our tested time on stream no decline in the water extraction properties were observed. However, previous research

showed that Al-O-Si bondings, which are the only types of connections in LTA, tend to hydrolyse irreversibly at high temperatures in the presence of water.<sup>199</sup> Further studies are required to test the long-term stability of the LTA membranes, and the hydrolyse problem has to be addressed if necessary. The immense performance boost by the LTA membrane may be worth the effort in the long run.

In the MTO reaction the water extraction tackled of the biggest problems: coking. Further studies are needed to determine why exactly the coking process was delayed by the water removal through the LTA membrane. Furthermore, in the normally used fluidized-bed reactors, attrition due to constant particle collision is a growing issue. By using the presented packed-bed membrane reactors, attrition would be nullified and the coking issues were addressed at the same time. Problems arise again when approaching the long-term stability of the LTA membrane at high temperatures in the presence of water. In addition, in a fluidized-bed reactor the coked catalyst can be exchanged effortlessly, while the packed-bed membrane reactor catalyst requires a constant reactivation through carbon oxidation.

In the photochemical reaction the co-doping of graphene enhanced the Cu<sup>0</sup> stability. The issues, that restrain the large-scale application of photocatalysts the most, are the long-term stability and the photonic efficiency, which were both addressed. However, the best performing hydrogen production composite catalyst was not as effective in 2-CP degradation, while the best 2-CP catalysts had not fared as well in the hydrogen formation. Therefore, enhancements for the dual-functional application are required, but again the achieved advancements may justify the additional effort.

My wish is, that this work may promote the research on the porous material dual-functional reactor systems and further amplifying the connections in the fields of catalytic chemistry and chemical engineering.

## List of References

- (1) Haber, F. Nobel Lecture: The Synthesis of Ammonia from Its Elements <https://www.nobelprize.org/prizes/chemistry/1918/haber/lecture/>.
- (2) Kandemir, T.; Schuster, M. E.; Senyshyn, A.; Behrens, M.; Schlögl, R. The Haber-Bosch Process Revisited: On the Real Structure and Stability of “Ammonia Iron” under Working Conditions. *Angew. Chemie - Int. Ed.* **2013**, *52* (48), 12723–12726. <https://doi.org/10.1002/anie.201305812>.
- (3) Farrauto, R. J.; Deeba, M.; Alerasool, S. Gasoline Automobile Catalysis and Its Historical Journey to Cleaner Air. *Nat. Catal.* **2019**, *2* (7), 603–613. <https://doi.org/10.1038/s41929-019-0312-9>.
- (4) Corbin, D. R.; Schwarz, S.; Sonnichsen, G. C. Methylamines Synthesis: A Review. *Catal. Today* **1997**, *37* (2), 71–102. [https://doi.org/10.1016/S0920-5861\(97\)00003-5](https://doi.org/10.1016/S0920-5861(97)00003-5).
- (5) Roose, P.; Eller, K.; Henkes, E.; Rossbacher, R.; Höke, H. Amines, Aliphatic. In *Ullmann's Encyclopedia of Industrial Chemistry*; Wiley-VCH: Weinheim, 2015. [https://doi.org/10.1002/14356007.a02\\_001.pub2](https://doi.org/10.1002/14356007.a02_001.pub2).
- (6) Ilaó, M. C.; Yamamoto, H.; Segawa, K. Shape-Selective Methylamine Synthesis over Small-Pore Zeolite Catalysts. *J. Catal.* **1996**, *161*, 20–30. <https://doi.org/10.1006/jcat.1996.0158>.
- (7) Segawa, K.; Hiroyasu, T. Highly Selective Methylamine Synthesis over Modified Mordenite Catalysts. *J. Catal.* **1991**, *131* (2), 482–490. [https://doi.org/10.1016/0021-9517\(91\)90280-H](https://doi.org/10.1016/0021-9517(91)90280-H).
- (8) Roose, P. Methylamines. In *Ullmann's Encyclopedia of Industrial Chemistry*; Wiley-VCH Verlag GmbH & Co. KGaA: Weinheim, Germany, 2015; pp 1–10. [https://doi.org/10.1002/14356007.a16\\_535.pub4](https://doi.org/10.1002/14356007.a16_535.pub4).
- (9) Amghizar, I.; Vandewalle, L. A.; Geem, K. M. Van; Marin, G. B. New Trends in Olefin Production. *Engineering* **2017**, *3* (2), 171–178. <https://doi.org/10.1016/j.ENG.2017.02.006>.
- (10) Gogate, M. R. Methanol-to-Olefins Process Technology: Current Status and Future Prospects. *Pet. Sci. Technol.* **2019**, *37* (5), 559–565. <https://doi.org/10.1080/10916466.2018.1555589>.
- (11) Tian, P.; Wei, Y.; Ye, M.; Liu, Z. Methanol to Olefins (MTO): From Fundamentals to Commercialization. *ACS Catal.* **2015**, *5* (3), 1922–1938. <https://doi.org/10.1021/acscatal.5b00007>.
- (12) Global Hydrogen Market Insights, 2020-2024 by Production Process, End-User, Generation System and Region. *Focus Catal.* **2020**, *2020* (5), 2. <https://doi.org/10.1016/j.focat.2020.04.005>.
- (13) Naterer, G. F.; Fowler, M.; Cotton, J.; Gabriel, K. Synergistic Roles of Off-Peak Electrolysis and Thermochemical Production of Hydrogen from Nuclear Energy in Canada. *Int. J. Hydrogen Energy* **2008**, *33* (23), 6849–6857. <https://doi.org/10.1016/j.ijhydene.2008.09.011>.
- (14) Acar, C.; Dincer, I.; Naterer, G. F. Review of Photocatalytic Water-Splitting Methods for Sustainable Hydrogen Production. *Int. J. Energy Res.* **2016**, *40* (11), 1449–1473. <https://doi.org/10.1002/er.3549>.
- (15) Wang, Z.; Li, C.; Domen, K. Recent Developments in Heterogeneous Photocatalysts for Solar-Driven Overall Water Splitting. *Chem. Soc. Rev.* **2019**, *48* (7), 2109–2125. <https://doi.org/10.1039/c8cs00542g>.

## References

- (16) Day, G. S.; Drake, H. F.; Zhou, H. C.; Ryder, M. R. Evolution of Porous Materials from Ancient Remedies to Modern Frameworks. *Commun. Chem.* **2021**, *4* (1), 2–5. <https://doi.org/10.1038/s42004-021-00549-4>.
- (17) Holst, J. R.; Trewin, A.; Cooper, A. I. Porous Organic Molecules. *Nat. Chem.* **2010**, *2* (11), 915–920. <https://doi.org/10.1038/nchem.873>.
- (18) Cooper, A. I. Porous Molecular Solids and Liquids. *ACS Cent. Sci.* **2017**, *3* (6), 544–553. <https://doi.org/10.1021/acscentsci.7b00146>.
- (19) Thommes, M.; Kaneko, K.; Neimark, A. V.; Olivier, J. P.; Rodriguez-Reinoso, F.; Rouquerol, J.; Sing, K. S. W. Physisorption of Gases, with Special Reference to the Evaluation of Surface Area and Pore Size Distribution (IUPAC Technical Report). *Pure Appl. Chem.* **2015**, *87* (9–10), 1051–1069. <https://doi.org/10.1515/pac-2014-1117>.
- (20) Rouquerol, J.; Baron, G.; Denoyel, R.; Giesche, H.; Groen, J.; Klobes, P.; Levitz, P.; Neimark, A. V.; Rigby, S.; Skudas, R.; Sing, K.; Thommes, M.; Unger, K. Liquid Intrusion and Alternative Methods for the Characterization of Macroporous Materials (IUPAC Technical Report). *Pure Appl. Chem.* **2012**, *84* (1), 107–136. <https://doi.org/10.1351/PAC-REP-10-11-19>.
- (21) Liang, J.; Li, B.; Wu, L. Recent Advances on Porous Interfaces for Biomedical Applications. *Soft Matter* **2020**, *16* (31), 7231–7245. <https://doi.org/10.1039/d0sm00997k>.
- (22) Novoselov, K. S.; Geim, A. K.; Morozov, S. V.; Jiang, D.; Zhang, Y.; Dubonos, S. V.; Grigorieva, I. V.; Firsov, A. A. Electric Field Effect in Atomically Thin Carbon Films. *Science* (80-. ). **2004**, *306* (5696), 666–669. <https://doi.org/10.1126/science.1102896>.
- (23) Balandin, A. A.; Ghosh, S.; Bao, W.; Calizo, I.; Teweldebrhan, D.; Miao, F.; Lau, C. N. Superior Thermal Conductivity of Single-Layer Graphene. *Nano Lett.* **2008**, *8* (3), 902–907. <https://doi.org/10.1021/nl0731872>.
- (24) Wu, Z. S.; Ren, W.; Gao, L.; Zhao, J.; Chen, Z.; Liu, B.; Tang, D.; Yu, B.; Jiang, C.; Cheng, H. M. Synthesis of Graphene Sheets with High Electrical Conductivity and Good Thermal Stability by Hydrogen Arc Discharge Exfoliation. *ACS Nano* **2009**, *3* (2), 411–417. <https://doi.org/10.1021/nn900020u>.
- (25) Bolotin, K. I.; Sikes, K. J.; Jiang, Z.; Klima, M.; Fudenberg, G.; Hone, J.; Kim, P.; Stormer, H. L. Ultrahigh Electron Mobility in Suspended Graphene. *Solid State Commun.* **2008**, *146* (9–10), 351–355. <https://doi.org/10.1016/j.ssc.2008.02.024>.
- (26) Lee, C.; Wei, X.; Kysar, J. W.; Hone, J. Measurement of the Elastic Properties and Intrinsic Strength of Monolayer Graphene. *Science* (80-. ). **2008**, *321* (5887), 385–388. <https://doi.org/10.1126/science.1157996>.
- (27) Stoller, M. D.; Park, S.; Zhu, Y.; An, J.; Ruoff, R. S. Graphene-Based Ultracapacitors. *Nano Lett.* **2008**, *8* (10), 3498–3502. <https://doi.org/10.1021/nl802558y>.
- (28) Lazar, P.; Karlický, F.; Jurecka, P.; Kocman, M.; Otyepková, E.; Šafářová, K.; Otyepka, M. Adsorption of Small Organic Molecules on Graphene. *J. Am. Chem. Soc.* **2013**, *135* (16), 6372–6377. <https://doi.org/10.1021/ja403162r>.
- (29) Geim, A. K.; Novoselov, K. S. The Rise of Graphene. *Nanosci. Technol. A Collect. Rev. from Nat. Journals* **2009**, 11–19. [https://doi.org/10.1142/9789814287005\\_0002](https://doi.org/10.1142/9789814287005_0002).
- (30) Choi, W.; Lahiri, I.; Seelaboyina, R.; Kang, Y. S. Synthesis of Graphene and Its Applications: A Review. *Crit. Rev. Solid State Mater. Sci.* **2010**, *35* (1), 52–71. <https://doi.org/10.1080/10408430903505036>.
- (31) Li, X.; Yu, J.; Wageh, S.; Al-Ghamdi, A. A.; Xie, J. Graphene in Photocatalysis: A Review. *Small* **2016**, *12* (48), 6640–6696. <https://doi.org/10.1002/sml.201600382>.

## References

- (32) Avouris, P.; Xia, F. Graphene Applications in Electronics and Photonics. *MRS Bull.* **2012**, *37* (12), 1225–1234. <https://doi.org/10.1557/mrs.2012.206>.
- (33) Lee, H.; Paeng, K.; Kim, I. S. A Review of Doping Modulation in Graphene. *Synth. Met.* **2018**, *244* (March), 36–47. <https://doi.org/10.1016/j.synthmet.2018.07.001>.
- (34) Huang, L.; Zhang, M.; Li, C.; Shi, G. Graphene-Based Membranes for Molecular Separation. *J. Phys. Chem. Lett.* **2015**, *6* (14), 2806–2815. <https://doi.org/10.1021/acs.jpcclett.5b00914>.
- (35) Barrer, R. M. Syntheses and Reactions of Mordenite. *J. Chem. Soc.* **1948**, 2158–2163. <https://doi.org/10.1039/JR9480002158>.
- (36) Barrer, R. M.; Riley, D. W. Sorptive and Molecular-Sieve Properties of a New Zeolitic Mineral. *J. Chem. Soc.* **1948**, 133–143.
- (37) Structure Commission of the International Zeolite Association (IZA). Database of Zeolite Structures <http://www.iza-structure.org/> (accessed Nov 15, 2021).
- (38) Yilmaz, B.; Trukhan, N.; Müller, U. Industrial Outlook on Zeolites and Metal Organic Frameworks. *Chinese J. Catal.* **2012**, *33* (1), 3–10. [https://doi.org/10.1016/s1872-2067\(10\)60302-6](https://doi.org/10.1016/s1872-2067(10)60302-6).
- (39) Flanigen, E. M.; Broach, R. W.; Wilson, S. T. *Zeolites in Industrial Separation and Catalysis*; Kulprathipanja, S., Ed.; Wiley, 2010. <https://doi.org/10.1002/9783527629565>.
- (40) Larin, A. V. The Loewenstein Rule: The Increase in Electron Kinetic Energy as the Reason for Instability of Al-O-Al Linkage in Aluminosilicate Zeolites. *Phys. Chem. Miner.* **2013**, *40* (10), 771–780. <https://doi.org/10.1007/s00269-013-0611-7>.
- (41) Loewenstein, W. The Distribution of Aluminum in the Tetrahedra of Silicates and Aluminates. *Am. Mineral.* **1954**, *39* (1–2), 92–96.
- (42) Morris, R. E. Modular Materials from Zeolite-like Building Blocks. *J. Mater. Chem.* **2005**, *15* (9), 931–938. <https://doi.org/10.1039/b415728a>.
- (43) Broach, R. W. Zeolite Types and Structures. In *Zeolites in Industrial Separation and Catalysis*; Wiley-VCH Verlag GmbH & Co. KGaA: Weinheim, Germany, 2010; pp 27–59. <https://doi.org/10.1002/9783527629565.ch2>.
- (44) Smith, J. V. *Tetrahedral Frameworks of Zeolites, Clathrates*; Baur, W. H., Fischer, R. X., Eds.; Landolt-Börnstein - Group IV Physical Chemistry; Springer-Verlag: Berlin/Heidelberg, 2000; Vol. 14A. <https://doi.org/10.1007/b55613>.
- (45) Xue, Z.; Li, Z.; Ma, J.; Bai, X.; Kang, Y.; Hao, W.; Li, R. Effective Removal of Mg<sup>2+</sup> and Ca<sup>2+</sup> Ions by Mesoporous LTA Zeolite. *Desalination* **2014**, *341* (1), 10–18. <https://doi.org/10.1016/j.desal.2014.02.025>.
- (46) Collins, F.; Rozhkovskaya, A.; Outram, J. G.; Millar, G. J. A Critical Review of Waste Resources, Synthesis, and Applications for Zeolite LTA. *Microporous Mesoporous Mater.* **2020**, *291* (July 2019), 109667. <https://doi.org/10.1016/j.micromeso.2019.109667>.
- (47) Moseley, C. G. Eugene Houdry, Catalytic Cracking, and World War II Aviation Gasoline. *J. Chem. Educ.* **1984**, *61* (8), 655–656. <https://doi.org/10.1021/ed061p655>.
- (48) Vogt, E. T. C.; Weckhuysen, B. M. Fluid Catalytic Cracking: Recent Developments on the Grand Old Lady of Zeolite Catalysis. *Chem. Soc. Rev.* **2015**, *44* (20), 7342–7370. <https://doi.org/10.1039/c5cs00376h>.
- (49) Zhou, Y.; Ma, Z.; Tang, J.; Yan, N.; Du, Y.; Xi, S.; Wang, K.; Zhang, W.; Wen, H.; Wang, J. Immediate Hydroxylation of



## References

- Arenes to Phenols via V-Containing All-Silica ZSM-22 Zeolite Triggered Non-Radical Mechanism. *Nat. Commun.* **2018**, *9* (1). <https://doi.org/10.1038/s41467-018-05351-w>.
- (50) Ishida, M.; Suzuki, T.; Ichihashi, H.; Shiga, A. Theoretical Study on Vapour Phase Beckmann Rearrangement of Cyclohexanone Oxime over a High Silica MFI Zeolite. *Catal. Today* **2003**, *87* (1–4), 187–194. <https://doi.org/10.1016/j.cattod.2003.10.021>.
- (51) Yang, W.; Wang, Z.; Sun, H.; Zhang, B. Advances in Development and Industrial Applications of Ethylbenzene Processes. *Chinese J. Catal.* **2016**, *37* (1), 16–26. [https://doi.org/10.1016/S1872-2067\(15\)60965-2](https://doi.org/10.1016/S1872-2067(15)60965-2).
- (52) Degnan, T. F.; Smith, C. M.; Venkat, C. R. Alkylation of Aromatics with Ethylene and Propylene: Recent Developments in Commercial Processes. *Appl. Catal. A Gen.* **2001**, *221* (1–2), 283–294. [https://doi.org/10.1016/S0926-860X\(01\)00807-9](https://doi.org/10.1016/S0926-860X(01)00807-9).
- (53) Thiele, G. F.; Roland, E. Propylene Epoxidation with Hydrogen Peroxide and Titanium Silicalite Catalyst: Activity, Deactivation and Regeneration of the Catalyst. *J. Mol. Catal. A Chem.* **1997**, *117* (1–3), 351–356. [https://doi.org/10.1016/S1381-1169\(96\)00266-X](https://doi.org/10.1016/S1381-1169(96)00266-X).
- (54) Pu, Y.; Xie, X.; Jiang, W.; Yang, L.; Jiang, X.; Yao, L. Low-Temperature Selective Catalytic Reduction of NO<sub>x</sub> with NH<sub>3</sub> over Zeolite Catalysts: A Review. *Chinese Chem. Lett.* **2020**, *31* (10), 2549–2555. <https://doi.org/10.1016/j.ccl.2020.04.012>.
- (55) Purnomo; Setyarini, P. H.; Sulistyarningsih, D. Zeolite-Based Biomaterials for Biomedical Application: A Review. *AIP Conf. Proc.* **2018**, *1977* (June). <https://doi.org/10.1063/1.5042933>.
- (56) Bacakova, L.; Vandrovцова, M.; Kopova, I.; Jirka, I. Applications of Zeolites in Biotechnology and Medicine—a Review. *Biomater. Sci.* **2018**, *6* (5), 974–989. <https://doi.org/10.1039/c8bm00028j>.
- (57) Pavelić, S. K.; Medica, J. S.; Gumbarević, D.; Filošević, A.; Pržulj, N.; Pavelić, K. Critical Review on Zeolite Clinoptilolite Safety and Medical Applications in Vivo. *Front. Pharmacol.* **2018**, *9* (NOV), 1–15. <https://doi.org/10.3389/fphar.2018.01350>.
- (58) Servatan, M.; Zarrintaj, P.; Mahmodi, G.; Kim, S. J.; Ganjali, M. R.; Saeb, M. R.; Mozafari, M. Zeolites in Drug Delivery: Progress, Challenges and Opportunities. *Drug Discov. Today* **2020**, *25* (4), 642–656. <https://doi.org/10.1016/j.drudis.2020.02.005>.
- (59) Lam, A.; Rivera, A. Theoretical Study of the Interaction of Surfactants and Drugs with Natural Zeolite. *Microporous Mesoporous Mater.* **2006**, *91* (1–3), 181–186. <https://doi.org/10.1016/j.micromeso.2005.11.035>.
- (60) Wang, J.; Wang, Z.; Guo, S.; Zhang, J.; Song, Y.; Dong, X.; Wang, X.; Yu, J. Antibacterial and Anti-Adhesive Zeolite Coatings on Titanium Alloy Surface. *Microporous Mesoporous Mater.* **2011**, *146* (1–3), 216–222. <https://doi.org/10.1016/j.micromeso.2011.04.005>.
- (61) Zarrintaj, P.; Mahmodi, G.; Manouchehri, S.; Mashhadzadeh, A. H.; Khodadadi, M.; Servatan, M.; Ganjali, M. R.; Azambre, B.; Kim, S.; Ramsey, J. D.; Habibzadeh, S.; Saeb, M. R.; Mozafari, M. Zeolite in Tissue Engineering: Opportunities and Challenges. *MedComm* **2020**, *1* (1), 5–34. <https://doi.org/10.1002/mco2.5>.
- (62) Kucherenko, I. S.; Soldatkin, O. O.; Kucherenko, D. Y.; Soldatkina, O. V.; Dzyadevych, S. V. Advances in Nanomaterial Application in Enzyme-Based Electrochemical Biosensors: A Review. *Nanoscale Adv.* **2019**, *1* (12), 4560–4577. <https://doi.org/10.1039/c9na00491b>.
- (63) Ikotun, B. D.; Ekolu, S. Strength and Durability Effect of Modified Zeolite Additive on Concrete Properties. *Constr. Build. Mater.* **2010**, *24* (5), 749–757. <https://doi.org/10.1016/j.conbuildmat.2009.10.033>.

## References

- (64) Nakhli, S. A. A.; Delkash, M.; Bakhshayesh, B. E.; Kazemian, H. *Application of Zeolites for Sustainable Agriculture: A Review on Water and Nutrient Retention; Water, Air, & Soil Pollution*, 2017; Vol. 228. <https://doi.org/10.1007/s11270-017-3649-1>.
- (65) Papaioannou, D.; Katsoulos, P. D.; Panousis, N.; Karatzias, H. The Role of Natural and Synthetic Zeolites as Feed Additives on the Prevention and/or the Treatment of Certain Farm Animal Diseases: A Review. *Microporous Mesoporous Mater.* **2005**, *84* (1–3), 161–170. <https://doi.org/10.1016/j.micromeso.2005.05.030>.
- (66) Rangnekar, N.; Mittal, N.; Elyassi, B.; Caro, J.; Tsapatsis, M. Zeolite Membranes - a Review and Comparison with MOFs. *Chem. Soc. Rev.* **2015**, *44* (20), 7128–7154. <https://doi.org/10.1039/c5cs00292c>.
- (67) Suzuki, H. Composite Membrane Having a Surface Layer of an Ultrathin Film of Cage-Shaped Zeolite and Processes for Production Thereof. US4699892A, 1987.
- (68) Tsapatsis, M. Toward High-Throughput Zeolite Membranes. *Science* (80-. ). **2011**, *334* (6057), 767–768. <https://doi.org/10.1126/science.1205957>.
- (69) Snyder, M. A.; Tsapatsis, M. Hierarchical Nanomanufacturing: From Shaped Zeolite Nanoparticles to High-Performance Separation Membranes. *Angew. Chemie - Int. Ed.* **2007**, *46* (40), 7560–7573. <https://doi.org/10.1002/anie.200604910>.
- (70) Pham, T. C. T.; Kim, H. S.; Yoon, K. B. Growth of Uniformly Oriented Silica MFI and BEA Zeolite Films on Substrates. *Science* (80-. ). **2011**, *334* (6062), 1533–1538. <https://doi.org/10.1126/science.1212472>.
- (71) Lewis, M. J.; Jun, S. Thermal Processing. *Food Process. Handb. 2nd Ed.* **2011**, *1* (July), 31–75. <https://doi.org/10.1126/science.1176095>.
- (72) Akhtar, F.; Ojuva, A.; Wirawan, S. K.; Hedlund, J.; Bergström, L. Hierarchically Porous Binder-Free Silicalite-1 Discs: A Novel Support for All-Zeolite Membranes. *J. Mater. Chem.* **2011**, *21* (24), 8822–8828. <https://doi.org/10.1039/c1jm10584a>.
- (73) Korelskiy, D.; Leppäjärvi, T.; Zhou, H.; Grahn, M.; Tanskanen, J.; Hedlund, J. High Flux MFI Membranes for Pervaporation. *J. Memb. Sci.* **2013**, *427*, 381–389. <https://doi.org/10.1016/j.memsci.2012.10.016>.
- (74) Rangnekar, N.; Shete, M.; Agrawal, K. V.; Topuz, B.; Kumar, P.; Guo, Q.; Ismail, I.; Alyoubi, A.; Basahel, S.; Narasimharao, K.; Macosko, C. W.; Mkhoyan, K. A.; Al-Thabaiti, S.; Stottrup, B.; Tsapatsis, M. 2D Zeolite Coatings: Langmuir-Schaefer Deposition of 3 Nm Thick MFI Zeolite Nanosheets. *Angew. Chemie - Int. Ed.* **2015**, *54* (22), 6571–6575. <https://doi.org/10.1002/anie.201411791>.
- (75) Basak, S.; Kundu, D.; Naskar, M. K. Low Temperature Synthesis of NaA Zeolite Membranes: The Effect of Primary and Secondary Crystallizations. *Ceram. Int.* **2014**, *40* (8 PART B), 12923–12930. <https://doi.org/10.1016/j.ceramint.2014.04.152>.
- (76) Boudreau, L. C.; Kuck, J. A.; Tsapatsis, M. Deposition of Oriented Zeolite A Films: In Situ and Secondary Growth. *J. Memb. Sci.* **1999**, *152* (1), 41–59. [https://doi.org/10.1016/S0376-7388\(98\)00166-5](https://doi.org/10.1016/S0376-7388(98)00166-5).
- (77) Huang, A.; Caro, J. Facile Synthesis of LTA Molecular Sieve Membranes on Covalently Functionalized Supports by Using Diisocyanates as Molecular Linkers. *J. Mater. Chem.* **2011**, *21* (30), 11424–11429. <https://doi.org/10.1039/c1jm11549a>.
- (78) Huang, A.; Lin, Y. S.; Yang, W. Synthesis and Properties of A-Type Zeolite Membranes by Secondary Growth Method with Vacuum Seeding. *J. Memb. Sci.* **2004**, *245* (1–2), 41–51. <https://doi.org/10.1016/j.memsci.2004.08.001>.
- (79) Huang, A.; Wang, N.; Caro, J. Synthesis of Multi-Layer Zeolite LTA Membranes with Enhanced Gas Separation Performance by Using 3-Aminopropyltriethoxysilane as Interlayer. *Microporous Mesoporous Mater.* **2012**, *164*, 294–301. <https://doi.org/10.1016/j.micromeso.2012.06.018>.

## References

- (80) Mallada, R. *Encyclopedia of Membranes*; Drioli, E., Giorno, L., Eds.; Springer Berlin Heidelberg: Berlin, Heidelberg, 2020. <https://doi.org/10.1007/978-3-642-40872-4>.
- (81) Conner, W. C.; Tompsett, G.; Lee, K. H.; Yngvesson, K. S. Microwave Synthesis of Zeolites: 1. Reactor Engineering. *J. Phys. Chem. B* **2004**, *108* (37), 13913–13920. <https://doi.org/10.1021/jp037358c>.
- (82) Van Miltenburg, A.; Zhu, W.; Kapteijn, F.; Moulijn, J. A. Adsorptive Separation of Light Olefin/Paraffin Mixtures. *Chem. Eng. Res. Des.* **2006**, *84* (5 A), 350–354. <https://doi.org/10.1205/cherd05021>.
- (83) Caro, J.; Noack, M.; Kölsch, P. Zeolite Membranes: From the Laboratory Scale to Technical Applications. *Adsorption* **2005**, *11* (3–4), 215–227. <https://doi.org/10.1007/s10450-005-5394-9>.
- (84) Morigami, Y.; Kondo, M.; Abe, J.; Kita, H.; Okamoto, K. The First Large-Scale Pervaporation Plant Using Tubular-Type Module with Zeolite NaA Membrane. *Sep. Purif. Technol.* **2001**, *25* (1–3), 251–260. [https://doi.org/10.1016/S1383-5866\(01\)00109-5](https://doi.org/10.1016/S1383-5866(01)00109-5).
- (85) Gallego-Lizon, T.; Edwards, E.; Lobiundo, G.; Freitas Dos Santos, L. Dehydration of Water/t-Butanol Mixtures by Pervaporation: Comparative Study of Commercially Available Polymeric, Microporous Silica and Zeolite Membranes. *J. Memb. Sci.* **2002**, *197* (1–2), 309–319. [https://doi.org/10.1016/S0376-7388\(01\)00650-0](https://doi.org/10.1016/S0376-7388(01)00650-0).
- (86) Yu, C.; Zhong, C.; Liu, Y.; Gu, X.; Yang, G.; Xing, W.; Xu, N. Pervaporation Dehydration of Ethylene Glycol by NaA Zeolite Membranes. *Chem. Eng. Res. Des.* **2012**, *90* (9), 1372–1380. <https://doi.org/10.1016/j.cherd.2011.12.003>.
- (87) Urriaga, A.; Gorri, E. D.; Casado, C.; Ortiz, I. Pervaporative Dehydration of Industrial Solvents Using a Zeolite NaA Commercial Membrane. *Sep. Purif. Technol.* **2003**, *32* (1–3), 207–213. [https://doi.org/10.1016/S1383-5866\(03\)00037-6](https://doi.org/10.1016/S1383-5866(03)00037-6).
- (88) Sato, K.; Aoki, K.; Sugimoto, K.; Izumi, K.; Inoue, S.; Saito, J.; Ikeda, S.; Nakane, T. Dehydrating Performance of Commercial LTA Zeolite Membranes and Application to Fuel Grade Bio-Ethanol Production by Hybrid Distillation/Vapor Permeation Process. *Microporous Mesoporous Mater.* **2008**, *115* (1–2), 184–188. <https://doi.org/10.1016/j.micromeso.2007.10.053>.
- (89) Giannakopoulos, I. G.; Nikolakis, V. Separation of Propylene/Propane Mixtures Using Faujasite-Type Zeolite Membranes. *Ind. Eng. Chem. Res.* **2005**, *44* (1), 226–230. <https://doi.org/10.1021/ie049508r>.
- (90) Mundstock, A.; Wang, N.; Friebe, S.; Caro, J. Propane/Propene Permeation through Na-X Membranes: The Interplay of Separation Performance and Pre-Synthetic Support Functionalization. *Microporous Mesoporous Mater.* **2015**, *215*, 20–28. <https://doi.org/10.1016/j.micromeso.2015.05.019>.
- (91) Sakai, M.; Sasaki, Y.; Tomono, T.; Seshimo, M.; Matsukata, M. Olefin Selective Ag-Exchanged X-Type Zeolite Membrane for Propylene/Propane and Ethylene/Ethane Separation. *ACS Appl. Mater. Interfaces* **2019**, *11* (4), 4145–4151. <https://doi.org/10.1021/acsami.8b20151>.
- (92) Hou, J.; Liu, P.; Jiang, M.; Yu, L.; Li, L.; Tang, Z. Olefin/Paraffin Separation through Membranes: From Mechanisms to Critical Materials. *J. Mater. Chem. A* **2019**, *7* (41), 23489–23511. <https://doi.org/10.1039/c9ta06329c>.
- (93) Roy, A.; Venna, S. R.; Rogers, G.; Tang, L.; Fitzgibbons, T. C.; Liu, J.; McCurry, H.; Vickery, D. J.; Flick, D.; Fish, B. Membranes for Olefin–Paraffin Separation: An Industrial Perspective. *Proc. Natl. Acad. Sci. U. S. A.* **2021**, *118* (37), 1–9. <https://doi.org/10.1073/pnas.2022194118>.
- (94) Sirkar, K. K.; Fane, A. G.; Wang, R.; Wickramasinghe, S. R. Process Intensification with Selected Membrane Processes. *Chem. Eng. Process. Process Intensif.* **2015**, *87*, 16–25. <https://doi.org/10.1016/j.cep.2014.10.018>.

## References

- (95) Koros, W. J.; Ma, Y. H.; Shimidzu, T. General Terms: From: Terminology for Membranes and Membrane Processes. In *IUPAC Standards Online*; De Gruyter, 2016.
- (96) Dudukovic, M. P. Trends in Catalytic Reaction Engineering. *Catal. Today* **1999**, *48* (1–4), 5–15. [https://doi.org/10.1016/S0920-5861\(98\)00353-8](https://doi.org/10.1016/S0920-5861(98)00353-8).
- (97) Dittmeyer, R.; Caro, J. Catalytic Membrane Reactors. In *Handbook of Heterogeneous Catalysis*; American Cancer Society, 2008; pp 2198–2248. <https://doi.org/https://doi.org/10.1002/9783527610044.hetcat0117>.
- (98) Itoh, N. A Membrane Reactor Using Palladium. *AIChE J.* **1987**, *33* (9), 1576–1578. <https://doi.org/10.1002/aic.690330921>.
- (99) Kokugan, T.; Trianto, A.; Takeda, H. Dehydrogenation of Pure Cyclohexane in the Membrane Reactor and Prediction of Conversion by Pseudo Equilibrium Model. *J. Chem. Eng. JAPAN* **1998**, *31* (4), 596–603. <https://doi.org/10.1252/jcej.31.596>.
- (100) Jeong, B. H.; Sotowa, K. I.; Kusakabe, K. Catalytic Dehydrogenation of Cyclohexane in an FAU-Type Zeolite Membrane Reactor. *J. Memb. Sci.* **2003**, *224* (1–2), 151–158. <https://doi.org/10.1016/j.memsci.2003.08.004>.
- (101) Dangwal, S.; Liu, R.; Kim, S. J. High-Temperature Ethane Dehydrogenation in Microporous Zeolite Membrane Reactor: Effect of Operating Conditions. *Chem. Eng. J.* **2017**, *328*, 862–872. <https://doi.org/10.1016/j.cej.2017.07.108>.
- (102) Schäfer, R.; Noack, M.; Kölsch, P.; Stöhr, M.; Caro, J. Comparison of Different Catalysts in the Membrane-Supported Dehydrogenation of Propane. *Catal. Today* **2003**, *82* (1–4), 15–23. [https://doi.org/10.1016/S0920-5861\(03\)00198-6](https://doi.org/10.1016/S0920-5861(03)00198-6).
- (103) Illgen, U.; Schäfer, R.; Noack, M.; Kölsch, P.; Kühnle, A.; Caro, J. Membrane Supported Catalytic Dehydrogenation of Iso-Butane Using an MFI Zeolite Membrane Reactor. *Catal. Commun.* **2001**, *2* (11–12), 339–345. [https://doi.org/10.1016/S1566-7367\(01\)00053-X](https://doi.org/10.1016/S1566-7367(01)00053-X).
- (104) Kong, C.; Lu, J.; Yang, J.; Wang, J. Catalytic Dehydrogenation of Ethylbenzene to Styrene in a Zeolite Silicalite-1 Membrane Reactor. *J. Memb. Sci.* **2007**, *306* (1–2), 29–35. <https://doi.org/10.1016/j.memsci.2007.08.018>.
- (105) Guo, Y.; Lu, G.; Mo, X.; Wang, Y. Vapor-Phase Dehydrogenation of Methanol to Methyl Formate in Catalytic Membrane Reactor with Pd/SiO<sub>2</sub>/Ceramic Composite Membrane. *Chem. Lett.* **2004**, *33* (12), 1628–1629. <https://doi.org/10.1246/cl.2004.1628>.
- (106) Shelepova, E. V.; Ilina, L. Y.; Vedyagin, A. A. Energy-Efficient Dehydrogenation of Methanol in a Membrane Reactor: A Mathematical Modeling. *Chem. Pap.* **2018**, *72* (10), 2617–2629. <https://doi.org/10.1007/s11696-018-0491-x>.
- (107) Zeng, G.; Chen, T.; He, L.; Pinnau, I.; Lai, Z.; Huang, K. W. A Green Approach to Ethyl Acetate: Quantitative Conversion of Ethanol through Direct Dehydrogenation in a Pd-Ag Membrane Reactor. *Chem. - A Eur. J.* **2012**, *18* (50), 15940–15943. <https://doi.org/10.1002/chem.201202005>.
- (108) Keuler, J. N.; Lorenzen, L. The Dehydrogenation of 2-Butanol in a Pd-Ag Membrane Reactor. *J. Memb. Sci.* **2002**, *202* (1–2), 17–26. [https://doi.org/10.1016/S0376-7388\(02\)00072-8](https://doi.org/10.1016/S0376-7388(02)00072-8).
- (109) Basile, A.; Criscuoli, A.; Santella, F.; Drioli, E. Membrane Reactor for Water Gas Shift Reaction. *Gas Sep. Purif.* **1996**, *10* (4), 243–254. [https://doi.org/10.1016/S0950-4214\(96\)00024-2](https://doi.org/10.1016/S0950-4214(96)00024-2).
- (110) Kulprathipanja, A.; Alptekin, G. O.; Falconer, J. L.; Way, J. D. Effects of Water Gas Shift Gases on Pd-Cu Alloy Membrane Surface Morphology and Separation Properties. *Ind. Eng. Chem. Res.* **2004**, *43* (15), 4188–4198. <https://doi.org/10.1021/ie030853a>.
- (111) Kim, C. H.; Han, J. Y.; Kim, S.; Lee, B.; Lim, H.; Lee, K. Y.; Ryi, S. K. Hydrogen Production by Steam Methane Reforming

## References

- in a Membrane Reactor Equipped with a Pd Composite Membrane Deposited on a Porous Stainless Steel. *Int. J. Hydrogen Energy* **2018**, *43* (15), 7684–7692. <https://doi.org/10.1016/j.ijhydene.2017.11.176>.
- (112) Maier, S. M.; Jentys, A.; Lercher, J. A. Steaming of Zeolite BEA and Its Effect on Acidity: A Comparative NMR and IR Spectroscopic Study. *J. Phys. Chem. C* **2011**, *115* (16), 8005–8013. <https://doi.org/10.1021/jp108338g>.
- (113) Feng, X.; Huang, R. Y. M. Liquid Separation by Membrane Pervaporation: A Review. *Ind. Eng. Chem. Res.* **1997**, *36* (4), 1048–1066. <https://doi.org/10.1021/ie960189g>.
- (114) Wang, Q.; Li, N.; Bolto, B.; Hoang, M.; Xie, Z. Desalination by Pervaporation: A Review. *Desalination* **2016**, *387*, 46–60. <https://doi.org/10.1016/j.desal.2016.02.036>.
- (115) Tian, H.; Zheng, H.; Huang, Z.; Qiu, T.; Wu, Y. Novel Procedure for Coproduction of Ethyl Acetate and N- Butyl Acetate by Reactive Distillation. *Ind. Eng. Chem. Res.* **2012**, *51* (15), 5535–5541. <https://doi.org/10.1021/ie202154x>.
- (116) Delgado, P.; Sanz, M. T.; Beltrán, S.; Núñez, L. A. Ethyl Lactate Production via Esterification of Lactic Acid with Ethanol Combined with Pervaporation. *Chem. Eng. J.* **2010**, *165* (2), 693–700. <https://doi.org/10.1016/j.cej.2010.10.009>.
- (117) Yin, P.; Chen, L.; Wang, Z.; Qu, R.; Liu, X.; Xu, Q.; Ren, S. Biodiesel Production from Esterification of Oleic Acid over Aminophosphonic Acid Resin D418. *Fuel* **2012**, *102*, 499–505. <https://doi.org/10.1016/j.fuel.2012.05.027>.
- (118) Ganske, F.; Bornscheuer, U. T. Lipase-Catalyzed Glucose Fatty Acid Ester Synthesis in Ionic Liquids. *Org. Lett.* **2005**, *7* (14), 3097–3098. <https://doi.org/10.1021/ol0511169>.
- (119) Diban, N.; Aguayo, A. T.; Bilbao, J.; Urtiaga, A.; Ortiz, I. Membrane Reactors for in Situ Water Removal: A Review of Applications. *Ind. Eng. Chem. Res.* **2013**, *52* (31), 10342–10354. <https://doi.org/10.1021/ie3029625>.
- (120) Korkmaz, S.; Salt, Y.; Dincer, S. Esterification of Acetic Acid and Isobutanol in a Pervaporation Membrane Reactor Using Different Membranes. *Ind. Eng. Chem. Res.* **2011**, *50* (20), 11657–11666. <https://doi.org/10.1021/ie200086h>.
- (121) Schulz, H. Short History and Present Trends of Fischer–Tropsch Synthesis. *Appl. Catal. A Gen.* **1999**, *186* (1–2), 3–12. [https://doi.org/10.1016/S0926-860X\(99\)00160-X](https://doi.org/10.1016/S0926-860X(99)00160-X).
- (122) Rohde, M. P.; Schaub, G.; Khajavi, S.; Jansen, J. C.; Kapteijn, F. Fischer-Tropsch Synthesis with in Situ H<sub>2</sub>O Removal - Directions of Membrane Development. *Microporous Mesoporous Mater.* **2008**, *115* (1–2), 123–136. <https://doi.org/10.1016/j.micromeso.2007.10.052>.
- (123) Zhou, C.; Wang, N.; Qian, Y.; Liu, X.; Caro, J.; Huang, A. Efficient Synthesis of Dimethyl Ether from Methanol in a Bifunctional Zeolite Membrane Reactor. *Angew. Chemie - Int. Ed.* **2016**, *55* (41), 12678–12682. <https://doi.org/10.1002/anie.201604753>.
- (124) Caro, J.; Noack, M. Zeolite Membranes - Recent Developments and Progress. *Microporous Mesoporous Mater.* **2008**, *115* (3), 215–233. <https://doi.org/10.1016/j.micromeso.2008.03.008>.
- (125) Fontananova, E.; Drioli, E. Membrane Reactors: Advanced Systems for Intensified Chemical Processes. *Chemie-Ingenieur-Technik* **2014**, *86* (12), 2039–2050. <https://doi.org/10.1002/cite.201400123>.
- (126) Wang, H.; Cong, Y.; Yang, W. Continuous Oxygen Ion Transfer Medium as a Catalyst for High Selective Oxidative Dehydrogenation of Ethane. *Catal. Letters* **2002**, *84* (1–2), 101–106. <https://doi.org/10.1023/A:1021088904379>.
- (127) Jiang, H.; Wang, H.; Werth, S.; Schiestel, T.; Caro, J. Simultaneous Production of Hydrogen and Synthesis Gas by Combining Water Splitting with Partial Oxidation of Methane in a Hollow-Fiber Membrane Reactor. *Angew. Chemie -*

## References

- Int. Ed.* **2008**, *47* (48), 9341–9344. <https://doi.org/10.1002/anie.200803899>.
- (128) Zhou, Y.; Ye, H.; Schomäcker, R. Selective Hydrogenation of 1,5-Cyclo-Octadiene over Porous Pd/ $\alpha$ -Al<sub>2</sub>O<sub>3</sub> Active Membrane. *Chinese J. Catal.* **2007**, *28* (8), 715–719. [https://doi.org/10.1016/S1872-2067\(07\)60061-8](https://doi.org/10.1016/S1872-2067(07)60061-8).
- (129) Chommeloux, B.; Cimaomo, S.; Jolimaitre, E.; Uzio, D.; Magnoux, P.; Sanchez, J. New Membrane for Use as Hydrogen Distributor for Hydrocarbon Selective Hydrogenation. *Microporous Mesoporous Mater.* **2008**, *109* (1–3), 28–37. <https://doi.org/10.1016/j.micromeso.2007.04.028>.
- (130) Vankelecom, I. F. J.; Parton, R. F.; Casselman, M. J. A.; Uytterhoeven, J. B.; Jacobs, P. A. Oxidation of Cyclohexane Using FePcY-Zeozymes Occluded in Polydimethylsiloxane Membranes. *J. Catal.* **1996**, *163* (2), 457–464. <https://doi.org/10.1006/jcat.1996.0347>.
- (131) Iojoiu, E. E.; Landrison, E.; Raeder, H.; Torp, E. G.; Miachon, S.; Dalmon, J. A. The “Watercatox” Process: Wet Air Oxidation of Industrial Effluents in a Catalytic Membrane Reactor. First Report on Contactor CMR up-Scaling to Pilot Unit. *Catal. Today* **2006**, *118* (1–2), 246–252. <https://doi.org/10.1016/j.cattod.2006.01.045>.
- (132) Gröschel, L.; Haidar, R.; Beyer, A.; Cölfen, H.; Frank, B.; Schomäcker, R. Hydrogenation of Propyne in Palladium-Containing Polyacrylic Acid Membranes and Its Characterization. *Ind. Eng. Chem. Res.* **2005**, *44* (24), 9064–9070. <https://doi.org/10.1021/ie050426s>.
- (133) Fan, X.; Jiao, Y. *Porous Materials for Catalysis: Toward Sustainable Synthesis and Applications of Zeolites*; Elsevier Inc., 2019. <https://doi.org/10.1016/B978-0-12-814681-1.00005-9>.
- (134) Zoubida, L.; Hichem, B. The Nanostructure Zeolites MFI-Type ZSM5. In *Nanocrystals and Nanostructures*; Simonescu, C. M., Ed.; IntechOpen: Rijeka, 2018. <https://doi.org/10.5772/intechopen.77020>.
- (135) Fernandez, C.; Stan, I.; Gilson, J. P.; Thomas, K.; Vicente, A.; Bonilla, A.; Pérez-Ramírez, J. Hierarchical ZSM-5 Zeolites in Shape-Selective Xylene Isomerization: Role of Mesoporosity and Acid Site Speciation. *Chem. - A Eur. J.* **2010**, *16* (21), 6224–6233. <https://doi.org/10.1002/chem.200903426>.
- (136) Fraenkel, D.; Cherniavsky, M.; Ittah, B.; Levy, M. Shape-Selective Alkylation of Naphthalene and Methyl-naphthalene with Methanol over H-ZSM-5 Zeolite Catalysts. *J. Catal.* **1986**, *101* (2), 273–283. [https://doi.org/10.1016/0021-9517\(86\)90254-X](https://doi.org/10.1016/0021-9517(86)90254-X).
- (137) Matam, S. K.; O'Malley, A. J.; Catlow, C. R. A.; Suwardiyanto; Collier, P.; Hawkins, A. P.; Zachariou, A.; Lennon, D.; Silverwood, I.; Parker, S. F.; Howe, R. F. The Effects of MTG Catalysis on Methanol Mobility in ZSM-5. *Catal. Sci. Technol.* **2018**, *8* (13), 3304–3312. <https://doi.org/10.1039/c8cy00422f>.
- (138) Lu, T.; Yan, W.; Xu, R. Chiral Zeolite Beta: Structure, Synthesis, and Application. *Inorg. Chem. Front.* **2019**, *6* (8), 1938–1951. <https://doi.org/10.1039/c9qi00574a>.
- (139) Bárcia, P. S.; Silva, J. A. C.; Rodrigues, A. E. Adsorption Equilibrium and Kinetics of Branched Hexane Isomers in Pellets of BETA Zeolite. *Microporous Mesoporous Mater.* **2005**, *79* (1–3), 145–163. <https://doi.org/10.1016/j.micromeso.2004.10.037>.
- (140) Qin, Z.; Cychosz, K. A.; Melinte, G.; El Siblani, H.; Gilson, J. P.; Thommes, M.; Fernandez, C.; Mintova, S.; Ersen, O.; Valtchev, V. Opening the Cages of Faujasite-Type Zeolite. *J. Am. Chem. Soc.* **2017**, *139* (48), 17273–17276. <https://doi.org/10.1021/jacs.7b10316>.
- (141) Li, K.; Valla, J.; Garcia-Martinez, J. Realizing the Commercial Potential of Hierarchical Zeolites: New Opportunities in Catalytic Cracking. *ChemCatChem* **2014**, *6* (1), 46–66. <https://doi.org/10.1002/cctc.201300345>.

## References

- (142) Yu, L.; Gong, J.; Zeng, C.; Zhang, L. Synthesis of Binderless Zeolite X Microspheres and Their CO<sub>2</sub> Adsorption Properties. *Sep. Purif. Technol.* **2013**, *118*, 188–195. <https://doi.org/10.1016/j.seppur.2013.06.035>.
- (143) Wang, Y.; Gao, Y.; Chu, W.; Zhao, D.; Chen, F.; Zhu, X.; Li, X.; Liu, S.; Xie, S.; Xu, L. Synthesis and Catalytic Application of FER Zeolites with Controllable Size. *J. Mater. Chem. A* **2019**, *7* (13), 7573–7580. <https://doi.org/10.1039/C8TA09420A>.
- (144) Xu, W. Q.; Yin, Y. G.; Suib, S. L.; Edwards, J. C.; O'Young, C. L. Modification of Non-Template Synthesized Ferrierite/ZSM-35 for n-Butene Skeletal Isomerization to Isobutylene. *J. Catal.* **1996**, *163* (2), 232–244. <https://doi.org/10.1006/jcat.1996.0324>.
- (145) Arletti, R.; Fois, E.; Gigli, L.; Vezzalini, G.; Quartieri, S.; Tabacchi, G. Irreversible Conversion of a Water–Ethanol Solution into an Organized Two-Dimensional Network of Alternating Supramolecular Units in a Hydrophobic Zeolite under Pressure. *Angew. Chemie - Int. Ed.* **2017**, *56* (8), 2105–2109. <https://doi.org/10.1002/anie.201610949>.
- (146) Yilmaz, B.; Müller, U. Catalytic Applications of Zeolites in Chemical Industry. *Top. Catal.* **2009**, *52* (6–7), 888–895. <https://doi.org/10.1007/s11244-009-9226-0>.
- (147) How, H. On Mordeite, a New Mineral from the Trap of Nova Scotia. *J. Chem. Soc* **1864**, *17*, 100–104.
- (148) Godelitsas, A.; Gamaletsos, P.; Roussos-Kotsis, M. Mordeite-Bearing Tuffs from Prassa Quarry, Kimolos Island, Greece. *Eur. J. Mineral.* **2010**, *22* (6), 797–811. <https://doi.org/10.1127/0935-1221/2010/0022-2058>.
- (149) Armbruster, T.; Gunter, M. E.; Bish, D. L.; Ming, D. W. Natural Zeolites; Occurrence, Properties, Applications. *Rev. Mineral. Geochemistry* **2001**, *45*, 1–57.
- (150) Structure Commission of the International Zeolite Association. Framework Type MOR <https://europe.iza-structure.org/IZA-SC/framework.php?STC=MOR> (accessed Feb 15, 2021).
- (151) Narayanan, S.; Tamizhdurai, P.; Mangesh, V. L.; Ragupathi, C.; Santhana krishnan, P.; Ramesh, A. Recent Advances in the Synthesis and Applications of Mordeite Zeolite - Review. *RSC Adv.* **2020**, *11* (1), 250–267. <https://doi.org/10.1039/d0ra09434j>.
- (152) Lotti, P.; Gatta, G. D.; Merlini, M.; Liermann, H. P. High-Pressure Behavior of Synthetic Mordeite-Na: An in Situ Single-Crystal Synchrotron X-Ray Diffraction Study. *Zeitschrift für Krist.* **2015**, *230* (4), 201–211. <https://doi.org/10.1515/zkri-2014-1796>.
- (153) Asuquo, R. A.; Edermirth, G.; Lercher, J. A. N-Butane Isomerization over Acidic Mordeite. *Journal of Catalysis*. 1995, pp 376–382. <https://doi.org/10.1006/jcat.1995.1219>.
- (154) Cañizares, P.; De Lucas, A.; Dorado, F. N-Butane Isomerization over H-Mordeite: Role of the Monomolecular Mechanism. *Appl. Catal. A Gen.* **2000**, *196* (2), 225–231. [https://doi.org/10.1016/S0926-860X\(99\)00477-9](https://doi.org/10.1016/S0926-860X(99)00477-9).
- (155) Wulfers, M. J.; Jentoft, F. C. Mechanism of N-Butane Skeletal Isomerization on H-Mordeite and Pt/H-Mordeite. *J. Catal.* **2015**, *330*, 507–519. <https://doi.org/10.1016/j.jcat.2014.12.035>.
- (156) Tamizhdurai, P.; Ramesh, A.; Krishnan, P. S.; Narayanan, S.; Shanthi, K.; Sivasanker, S. Effect of Acidity and Porosity Changes of Dealuminated Mordeite on N-Pentane, n-Hexane and Light Naphtha Isomerization. *Microporous Mesoporous Mater.* **2019**, *287* (June), 192–202. <https://doi.org/10.1016/j.micromeso.2019.06.012>.
- (157) Zhan, E.; Xiong, Z.; Shen, W. Dimethyl Ether Carbonylation over Zeolites. *J. Energy Chem.* **2019**, *36*, 51–63. <https://doi.org/10.1016/j.jechem.2019.04.015>.

## References

- (158) Liu, J.; Xue, H.; Huang, X.; Wu, P. H.; Huang, S. J.; Liu, S. Bin; Shen, W. Stability Enhancement of H-Mordenite in Dimethyl Ether Carbonylation to Methyl Acetate by Pre-Adsorption of Pyridine. *Cuihua Xuebao/Chinese J. Catal.* **2010**, *31* (7), 729–738. [https://doi.org/10.1016/S1872-2067\(09\)60081-4](https://doi.org/10.1016/S1872-2067(09)60081-4).
- (159) Wahono, S. K.; Stalin, J.; Addai-Mensah, J.; Skinner, W.; Vinu, A.; Vasilev, K. Physico-Chemical Modification of Natural Mordenite-Clinoptilolite Zeolites and Their Enhanced CO<sub>2</sub> Adsorption Capacity. *Microporous Mesoporous Mater.* **2020**, *294*, 109871. <https://doi.org/10.1016/j.micromeso.2019.109871>.
- (160) Sakthinathan, S.; Tamizhdurai, P.; Ramesh, A.; Chiu, T. W.; Mangesh, V. L.; Veerarajan, S.; Shanthi, K. Platinum Incorporated Mordenite Zeolite Modified Glassy Carbon Electrode Used for Selective Electrochemical Detection of Mercury Ions. *Microporous Mesoporous Mater.* **2020**, *292* (September 2019), 109770. <https://doi.org/10.1016/j.micromeso.2019.109770>.
- (161) Reed, T. B.; Breck, D. W. Crystalline Zeolites. II. Crystal Structure of Synthetic Zeolite, Type A. *J. Am. Chem. Soc.* **1956**, *78* (23), 5972–5977. <https://doi.org/10.1021/ja01604a002>.
- (162) Sherman, J. D. Synthetic Zeolites and Other Microporous Oxide Molecular Sieves. *Proc. Natl. Acad. Sci.* **1999**, *96* (7), 3471–3478. <https://doi.org/10.1073/pnas.96.7.3471>.
- (163) Breck, D. W.; Eversole, W. G.; Milton, R. M. NEW SYNTHETIC CRYSTALLINE ZEOLITES. *J. Am. Chem. Soc.* **1956**, *78* (10), 2338–2339. <https://doi.org/10.1021/ja01591a082>.
- (164) García-Sánchez, A.; García-Pérez, E.; Dubbeldam, D.; Krishna, R.; Calero, S. A Simulation Study of Alkanes in Linde Type A Zeolites. *Adsorpt. Sci. Technol.* **2007**, *25* (6), 417–427. <https://doi.org/10.1260/026361707783908274>.
- (165) Boal, B. W.; Schmidt, J. E.; Deimund, M. A.; Deem, M. W.; Henling, L. M.; Brand, S. K.; Zones, S. I.; Davis, M. E. Facile Synthesis and Catalysis of Pure-Silica and Heteroatom LTA. *Chem. Mater.* **2015**, *27* (22), 7774–7779. <https://doi.org/10.1021/acs.chemmater.5b03579>.
- (166) Khajavi, S.; Jansen, J. C.; Kapteijn, F. *Preparation and Performance of H-SOD Membranes: A New Synthesis Procedure and Absolute Water Separation*; Elsevier B.V., 2007; Vol. 170. [https://doi.org/10.1016/S0167-2991\(07\)80956-6](https://doi.org/10.1016/S0167-2991(07)80956-6).
- (167) Pluth, J. J.; Smith, J. V. Accurate Redetermination of Crystal Structure of Dehydrated Zeolite A. Absence of Near Zero Coordination of Sodium. Refinement of Si,Al-Ordered Superstructure. *J. Am. Chem. Soc.* **1980**, *102* (14), 4704–4708. <https://doi.org/10.1021/ja00534a024>.
- (168) Cornelius, M. L. U.; Price, L.; Wells, S. A.; Petrik, L. F.; Sartbaeva, A. The Steric Influence of Extra-Framework Cations on Framework Flexibility: An LTA Case Study. *Zeitschrift fur Krist. - Cryst. Mater.* **2019**, *234* (7–8), 461–468. <https://doi.org/10.1515/zkri-2019-0016>.
- (169) Pluth, J. J.; Smith, J. V. Crystal Structure of Dehydrated Calcium-Exchanged Zeolite A. Absence of near-Zero-Coordinate Calcium(2+) Ion. Presence of Aluminum Complex. *J. Am. Chem. Soc.* **1983**, *105* (5), 1192–1195. <https://doi.org/10.1021/ja00343a019>.
- (170) Lührs, H.; Derr, J.; Fischer, R. X. K and Ca Exchange Behavior of Zeolite A. *Microporous Mesoporous Mater.* **2012**, *151*, 457–465. <https://doi.org/10.1016/j.micromeso.2011.09.025>.
- (171) Zhang, C.; Peng, L.; Jiang, J.; Gu, X. Mass Transfer Model, Preparation and Applications of Zeolite Membranes for Pervaporation Dehydration: A Review. *Chinese J. Chem. Eng.* **2017**, *25* (11), 1627–1638. <https://doi.org/10.1016/j.cjche.2017.09.014>.



## References

- (172) de la Iglesia, Ó.; Mallada, R.; Menéndez, M.; Coronas, J. Continuous Zeolite Membrane Reactor for Esterification of Ethanol and Acetic Acid. *Chem. Eng. J.* **2007**, *131* (1–3), 35–39. <https://doi.org/10.1016/j.cej.2006.12.015>.
- (173) Li, W.; Liu, W.; Xing, W.; Xu, N. Esterification of Acetic Acid and n -Propanol with Vapor Permeation Using NaA Zeolite Membrane. *Ind. Eng. Chem. Res.* **2013**, *52* (19), 6336–6342. <https://doi.org/10.1021/ie3031086>.
- (174) Ameri, E.; Moheb, A.; Roodpeyma, S. Vapor-Permeation-Aided Esterification of Isopropanol/Propionic Acid Using NaA and PERVAP® 2201 Membranes. *Chem. Eng. J.* **2010**, *162* (1), 355–363. <https://doi.org/10.1016/j.cej.2010.05.018>.
- (175) Jafar, J. J.; Budd, P. M.; Hughes, R. Enhancement of Esterification Reaction Yield Using Zeolite A Vapour Permeation Membrane. *J. Memb. Sci.* **2002**, *199* (1), 117–123. [https://doi.org/10.1016/S0376-7388\(01\)00683-4](https://doi.org/10.1016/S0376-7388(01)00683-4).
- (176) Hong, M.; Yu, L.; Wang, Y.; Zhang, J.; Chen, Z.; Dong, L.; Zan, Q.; Li, R. *Heavy Metal Adsorption with Zeolites: The Role of Hierarchical Pore Architecture*; Elsevier B.V., 2019; Vol. 359. <https://doi.org/10.1016/j.cej.2018.11.087>.
- (177) Schwuger, M. J.; Smolka, H. G.; Kurzendörfer, C. P. Zur Verwendung von Na-Al-Silikaten in Waschmitteln: Teil IV: Modelluntersuchungen Zum Ionenaustausch von Schwermetallen Im Bereich Geringer Ionenkonzentrationen. *Tenside Surfactants Deterg.* **1976**, *13* (6), 305–312. <https://doi.org/doi:10.1515/tsd-1976-130601>.
- (178) Smolka, H. G.; Schwuger, M. J. Sodium-Aluminium-Silicates in the Washing Process Part II: Cleansing Action of Natural Zeolites. *Colloid Polym. Sci.* **1978**, *256* (3), 270–277. <https://doi.org/10.1007/BF01550558>.
- (179) Millini, R.; Bellussi, G. Chapter 1. Zeolite Science and Perspectives. In *Zeolites in Catalysis: Properties and Applications*; 2017; pp 1–36. <https://doi.org/10.1039/9781788010610-00001>.
- (180) Grandjean, F. Optical Study of the Absorption of the Heavy Vapors by Certain Zeolites. *CR Acad. Sci* **1910**, *149*, 866–868.
- (181) Weigel, O.; Steinhoff, E. Adsorption of Organic Liquid Vapors by Chabazite. *Z. Krist.* **1925**, *61*, 125–154.
- (182) Passaglia, E. The Crystal Chemistry of Chabazites. *Am. Mineral.* **1970**, *55* (7–8), 1278–1301.
- (183) Barrer, R. M.; Baynham, J. W. The Hydrothermal Chemistry of the Silicates. Part VII. Synthetic Potassium Aluminosilicates. *J. Chem. Soc.* **1956**, 2882–2891.
- (184) Zones, S. I. Zeolite SSZ-13 and Its Method of Preparation. US4544538A, 1985.
- (185) Fahami, A. R.; Günter, T.; Doronkin, D. E.; Casapu, M.; Zengel, D.; Vuong, T. H.; Simon, M.; Breher, F.; Kucherov, A. V.; Brückner, A.; Grunwaldt, J. D. The Dynamic Nature of Cu Sites in Cu-SSZ-13 and the Origin of the Seagull NO<sub>x</sub> Conversion Profile during NH<sub>3</sub>-SCR. *React. Chem. Eng.* **2019**, *4* (6), 1000–1018. <https://doi.org/10.1039/c8re00290h>.
- (186) Bhadra, B. N.; Song, J. Y.; Khan, N. A.; Jun, J. W.; Kim, T. W.; Kim, C. U.; Jhung, S. H. Conversion of Ethylene into Propylene with the Siliceous SSZ-13 Zeolite Prepared without an Organic Structure-Directing Agent. *J. Catal.* **2018**, *365*, 94–104. <https://doi.org/10.1016/j.jcat.2018.06.016>.
- (187) Structure Commission of the International Zeolite Association. Framework Type CHA <http://www.iza-structure.org/IZA-SC/references.php?STC=CHA> (accessed May 14, 2021).
- (188) Kumar, M.; Luo, H.; Román-Leshkov, Y.; Rimer, J. D. SSZ-13 Crystallization by Particle Attachment and Deterministic Pathways to Crystal Size Control. *J. Am. Chem. Soc.* **2015**, *137* (40), 13007–13017. <https://doi.org/10.1021/jacs.5b07477>.
- (189) Paolucci, C.; Di Iorio, J. R.; Ribeiro, F. H.; Gounder, R.; Schneider, W. F. *Catalysis Science of NO<sub>x</sub> Selective Catalytic Reduction With Ammonia Over Cu-SSZ-13 and Cu-SAPO-34*, 1st ed.; Elsevier Inc., 2016; Vol. 59.

## References

- <https://doi.org/10.1016/bs.acat.2016.10.002>.
- (190) Gao, F.; Kwak, J. H.; Szanyi, J.; Peden, C. H. F. Current Understanding of Cu-Exchanged Chabazite Molecular Sieves for Use as Commercial Diesel Engine DeNO<sub>x</sub> Catalysts. *Top. Catal.* **2013**, *56* (15–17), 1441–1459. <https://doi.org/10.1007/s11244-013-0145-8>.
- (191) Bordiga, S.; Regli, L.; Cocina, D.; Lamberti, C.; Bjørgen, M.; Lillerud, K. P. Assessing the Acidity of High Silica Chabazite H-SSZ-13 by FTIR Using CO as Molecular Probe: Comparison with H-SAPO-34. *J. Phys. Chem. B* **2005**, *109* (7), 2779–2784. <https://doi.org/10.1021/jp045498w>.
- (192) Derouane, E. G.; Védrine, J. C.; Ramos Pinto, R.; Borges, P. M.; Costa, L.; Lemos, M. A. N. D. A.; Lemos, F.; Ramôa Ribeiro, F. The Acidity of Zeolites: Concepts, Measurements and Relation to Catalysis: A Review on Experimental and Theoretical Methods for the Study of Zeolite Acidity. *Catal. Rev. - Sci. Eng.* **2013**, *55* (4), 454–515. <https://doi.org/10.1080/01614940.2013.822266>.
- (193) Wang, L.; Zhu, D.; Wang, J.; Cui, W.; Han, J.; Li, B.; Fan, D.; Tian, P.; Liu, Z. Embryonic Zeolite-Assisted Synthesis of SSZ-13 with Superior Efficiency and Their Excellent Catalytic Performance. *J. Mater. Chem. A* **2021**, *9* (27), 15238–15245. <https://doi.org/10.1039/d1ta01452h>.
- (194) Zhao, Z.; Xing, Y.; Li, S.; Meng, X.; Xiao, F. S.; McGuire, R.; Parvulescu, A. N.; Müller, U.; Zhang, W. Mapping Al Distributions in SSZ-13 Zeolites from <sup>23</sup>Na Solid-State NMR Spectroscopy and DFT Calculations. *J. Phys. Chem. C* **2018**, *122* (18), 9973–9979. <https://doi.org/10.1021/acs.jpcc.8b01423>.
- (195) Fischer, M. Water Adsorption in SAPO-34: Elucidating the Role of Local Heterogeneities and Defects Using Dispersion-Corrected DFT Calculations. *Phys. Chem. Chem. Phys.* **2015**, *17* (38), 25260–25271. <https://doi.org/10.1039/c5cp04189a>.
- (196) Wilson, S. T.; Lok, B. M.; Messina, C. A.; Cannan, T. R.; Flanigen, E. M. Microporous Crystalline Inorganic Solids Department of Chemistry. *J. Am. Chem. Soc.* **1982**, *104* (3), 1146–1147.
- (197) Lok, B. M.; Messina, C. A.; Patton, R. L.; Gajek, R. T.; Cannan, T. R.; Flanigen, E. M. Silicoaluminophosphate Molecular Sieves: Another New Class of Microporous Crystalline Inorganic Solids. *J. Am. Chem. Soc.* **1984**, *106* (20), 6092–6093. <https://doi.org/10.1021/ja00332a063>.
- (198) Liu, G.; Tian, P.; Li, J.; Zhang, D.; Zhou, F.; Liu, Z. Synthesis, Characterization and Catalytic Properties of SAPO-34 Synthesized Using Diethylamine as a Template. *Microporous Mesoporous Mater.* **2008**, *111* (1–3), 143–149. <https://doi.org/10.1016/j.micromeso.2007.07.023>.
- (199) Yang, L.; Wang, C.; Zhang, L.; Dai, W.; Chu, Y.; Xu, J.; Wu, G.; Gao, M.; Liu, W.; Xu, Z.; Wang, P.; Guan, N.; Dyballa, M.; Ye, M.; Deng, F.; Fan, W.; Li, L. Stabilizing the Framework of SAPO-34 Zeolite toward Long-Term Methanol-to-Olefins Conversion. *Nat. Commun.* **2021**, *12* (1). <https://doi.org/10.1038/s41467-021-24403-2>.
- (200) Li, S.; Falconer, J. L.; Noble, R. D. SAPO-34 Membranes for CO<sub>2</sub>/CH<sub>4</sub> Separations: Effect of Si/Al Ratio. *Microporous Mesoporous Mater.* **2008**, *110* (2–3), 310–317. <https://doi.org/10.1016/j.micromeso.2007.06.016>.
- (201) Ferri, P.; Li, C.; Millán, R.; Martínez-Triguero, J.; Moliner, M.; Boronat, M.; Corma, A. Impact of Zeolite Framework Composition and Flexibility on Methanol-To-Olefins Selectivity: Confinement or Diffusion? *Angew. Chemie* **2020**, *132* (44), 19876–19883. <https://doi.org/10.1002/ange.202007609>.
- (202) Gale, J. D.; Shah, R.; Payne, M. C.; Stich, I.; Terakura, K. Methanol in Microporous Materials from First Principles. *Catal. Today* **1999**, *50*. [https://doi.org/10.1016/S0920-5861\(98\)00487-8](https://doi.org/10.1016/S0920-5861(98)00487-8).

## References

- (203) Beale, A. M.; Gao, F.; Lezcano-Gonzalez, I.; Peden, C. H. F.; Szanyi, J. Recent Advances in Automotive Catalysis for NO<sub>x</sub> Emission Control by Small-Pore Microporous Materials. *Chem. Soc. Rev.* **2015**, *44* (20), 7371–7405. <https://doi.org/10.1039/c5cs00108k>.
- (204) Zhang, S.; Pang, L.; Chen, Z.; Ming, S.; Dong, Y.; Liu, Q.; Liu, P.; Cai, W.; Li, T. Cu/SSZ-13 and Cu/SAPO-34 Catalysts for DeNO<sub>x</sub> in Diesel Exhaust: Current Status, Challenges, and Future Perspectives. *Appl. Catal. A Gen.* **2020**, *607*, 117855. <https://doi.org/10.1016/j.apcata.2020.117855>.
- (205) Yu, T.; Hao, T.; Fan, D.; Wang, J.; Shen, M.; Li, W. Recent NH<sub>3</sub> - SCR Mechanism Research over Cu/SAPO-34 Catalyst. *J. Phys. Chem. C* **2014**.
- (206) Luo, J.; Gao, F.; Kamasamudram, K.; Currier, N.; Peden, C. H. F.; Yezerets, A. New Insights into Cu/SSZ-13 SCR Catalyst Acidity. Part I: Nature of Acidic Sites Probed by NH<sub>3</sub> Titration. *J. Catal.* **2017**, *348*, 291–299. <https://doi.org/10.1016/j.jcat.2017.02.025>.
- (207) Duan, Y.; Wang, J.; Yu, T.; Shen, M.; Wang, J. The Role and Activity of Various Adsorbed Ammonia Species on Cu/SAPO-34 Catalyst during Passive-SCR Process. *RSC Adv.* **2015**, *5* (19), 14103–14113. <https://doi.org/10.1039/c4ra13984d>.
- (208) Tang, J.; Xu, M.; Yu, T.; Ma, H.; Shen, M.; Wang, J. Catalytic Deactivation Mechanism Research over Cu/SAPO-34 Catalysts for NH<sub>3</sub>-SCR (II): The Impact of Copper Loading. *Chem. Eng. Sci.* **2017**, *168* (II), 414–422. <https://doi.org/10.1016/j.ces.2017.04.053>.
- (209) Fan, D.; Wang, J.; Yu, T.; Wang, J.; Hu, X.; Shen, M. Catalytic Deactivation Mechanism Research over Cu/SAPO-34 Catalysts for NH<sub>3</sub>-SCR (I): The Impact of 950 °C Hydrothermal Aging Time. *Chem. Eng. Sci.* **2018**, *176*, 285–293. <https://doi.org/10.1016/j.ces.2017.10.032>.
- (210) Bower, J. K.; Barpaga, D.; Proding, S.; Krishna, R.; Schaefer, H. T.; McGrail, B. P.; Derewinski, M. A.; Motkuri, R. K. Dynamic Adsorption of CO<sub>2</sub>/N<sub>2</sub> on Cation-Exchanged Chabazite SSZ-13: A Breakthrough Analysis. *ACS Appl. Mater. Interfaces* **2018**, *10* (17), 14287–14291. <https://doi.org/10.1021/acsami.8b03848>.
- (211) Proding, S.; Vemuri, R. S.; Varga, T.; Peter McGrail, B.; Motkuri, R. K.; Derewinski, M. A. Impact of Chabazite SSZ-13 Textural Properties and Chemical Composition on CO<sub>2</sub> Adsorption Applications. *New J. Chem.* **2016**, *40* (5), 4375–4385. <https://doi.org/10.1039/c5nj03205a>.
- (212) Luo, Y.; Funke, H. H.; Falconer, J. L.; Noble, R. D. Adsorption of CO<sub>2</sub>, CH<sub>4</sub>, C<sub>3</sub>H<sub>8</sub>, and H<sub>2</sub>O in SSZ-13, SAPO-34, and T-Type Zeolites. *Ind. Eng. Chem. Res.* **2016**, *55* (36), 9749–9757. <https://doi.org/10.1021/acs.iecr.6b02034>.
- (213) Hong, M.; Li, S.; Falconer, J. L.; Noble, R. D. Hydrogen Purification Using a SAPO-34 Membrane. *J. Memb. Sci.* **2008**, *307* (2), 277–283. <https://doi.org/10.1016/j.memsci.2007.09.031>.
- (214) Li, S.; Falconer, J. L.; Noble, R. D. SAPO-34 Membranes for CO<sub>2</sub>/CH<sub>4</sub> Separation. *J. Memb. Sci.* **2004**, *241* (1), 121–135. <https://doi.org/10.1016/j.memsci.2004.04.027>.
- (215) Segawa, K.; Ilaio, M. C. Methanol Amination over Small-Pore Zeolite Catalysts. *Prog. Zeolite Microporous Mater.* **1997**, *105* (M), 1219–1226. [https://doi.org/10.1016/S0167-2991\(97\)80760-4](https://doi.org/10.1016/S0167-2991(97)80760-4).
- (216) Wu, L.; Hensen, E. J. M. Comparison of Mesoporous SSZ-13 and SAPO-34 Zeolite Catalysts for the Methanol-to-Olefins Reaction. *Catal. Today* **2014**, *235*, 160–168. <https://doi.org/10.1016/j.cattod.2014.02.057>.
- (217) Abrams, L.; Corbin, D. R. Probing Intrazeolite Space; Cambridge University Press, 1995; pp 1–46. [https://doi.org/10.1007/978-94-011-0119-6\\_1](https://doi.org/10.1007/978-94-011-0119-6_1).

## References

- (218) Bosch, M.; Eberhardt, J. K.; Röttger, R.; Krug, T.; Melder, J. Process for the Continuous Synthesis of Methylamines. 7435855, 2008.
- (219) Gredig, S. V.; Koepfel, R. A.; Baiker, A. Comparative Study of Synthesis of Methylamines from Carbon Oxides and Ammonia over Cu/Al<sub>2</sub>O<sub>3</sub>. *Catal. Today* **1996**, 29 (1–4), 339–342. [https://doi.org/10.1016/0920-5861\(95\)00301-0](https://doi.org/10.1016/0920-5861(95)00301-0).
- (220) Bosch, M.; Röttger, R.; Krug, T.; Weber, T.; Ross, K.-H.; Julius, M. Formkörper Enthaltend Ein Alumosilikat and Aluminiumoxid Und Verfahren Zur Kontinuierlichen Herstellung von Methylamine. EP1931466B1, 2012.
- (221) Weigert, F. J. Selective Synthesis and Equilibration of Methylamines on Sodium Mordenite. *J. Catal.* **1987**, 103 (1), 20–29. [https://doi.org/10.1016/0021-9517\(87\)90088-1](https://doi.org/10.1016/0021-9517(87)90088-1).
- (222) Jeon, H. Y.; Shin, C. H.; Jung, H. J.; Hong, S. B. Catalytic Evaluation of Small-Pore Molecular Sieves with Different Framework Topologies for the Synthesis of Methylamines. *Appl. Catal. A Gen.* **2006**, 305 (1), 70–78. <https://doi.org/10.1016/j.apcata.2006.02.044>.
- (223) Dusselier, M.; Davis, M. E. Small-Pore Zeolites: Synthesis and Catalysis. *Chem. Rev.* **2018**, 118 (11), 5265–5329. <https://doi.org/10.1021/acs.chemrev.7b00738>.
- (224) Chu, Y.; Lo, A. Y.; Wang, C.; Deng, F. Origin of High Selectivity of Dimethyl Ether Carbonylation in the 8-Membered Ring Channel of Mordenite Zeolite. *J. Phys. Chem. C* **2019**. <https://doi.org/10.1021/acs.jpcc.9b01874>.
- (225) Li, J. R.; Kuppler, R. J.; Zhou, H. C. Selective Gas Adsorption and Separation in Metal-Organic Frameworks. *Chem. Soc. Rev.* **2009**, 38 (5), 1477–1504. <https://doi.org/10.1039/b802426j>.
- (226) Staelens, N.; Reyniers, M. F.; Marin, G. B. Transalkylation of Methylamines: Kinetics and Industrial Simulation. *Ind. Eng. Chem. Res.* **2004**, 43 (17), 5123–5132. <https://doi.org/10.1021/ie049861x>.
- (227) Hayes, K. S. Industrial Processes for Manufacturing Amines. *Appl. Catal. A Gen.* **2001**, 221 (1–2), 187–195. [https://doi.org/10.1016/S0926-860X\(01\)00813-4](https://doi.org/10.1016/S0926-860X(01)00813-4).
- (228) Guisnet, M. “Coke” Molecules Trapped in the Micropores of Zeolites as Active Species in Hydrocarbon Transformations. *J. Mol. Catal. A Chem.* **2002**, 183, 367–382. [https://doi.org/10.1016/S1381-1169\(01\)00511-8](https://doi.org/10.1016/S1381-1169(01)00511-8).
- (229) Fetting, F.; Dingerdissen, U. Production of Methylamines over ZK-5 Zeolite Treated with Tetramethoxysilane. *Chem. Eng. Technol.* **1992**, 15 (3), 202–212. <https://doi.org/10.1002/ceat.270150309>.
- (230) Chen, D. T.; Zhang, L.; Yi, C.; Dumesic, J. A. Methylamine Synthesis over Solid Acid Catalysts: Microcalorimetric and Infrared Spectroscopic Studies of Adsorbed Species. *J. Catal.* **1994**, 146 (1), 257–267. [https://doi.org/10.1016/0021-9517\(94\)90029-9](https://doi.org/10.1016/0021-9517(94)90029-9).
- (231) Ashina, Y.; Fukatsu, M. Process for Producing Methylamines. US4485261A, 1984.
- (232) Chang, C. D.; Silvestri, A. J. The Conversion of Methanol and Other O-Compounds to Hydrocarbons over Zeolite Catalysts. *J. Catal.* **1977**, 47 (2), 249–259. [https://doi.org/10.1016/0021-9517\(77\)90172-5](https://doi.org/10.1016/0021-9517(77)90172-5).
- (233) *Zeolites and Catalysis*; Čejka, J., Corma, A., Zones, S., Eds.; Wiley, 2010. <https://doi.org/10.1002/9783527630295>.
- (234) Khadzhiev, S. N.; Magomedova, M. V.; Peresypkina, E. G. Kinetic Models of Methanol and Dimethyl Ether Conversion to Olefins over Zeolite Catalysts (Review). *Pet. Chem.* **2015**, 55 (7), 503–521. <https://doi.org/10.1134/S0965544115070063>.
- (235) Song, W.; Marcus, D. M.; Fu, H.; Ehresmann, J. O.; Haw, J. F. An Oft-Studied Reaction That May Never Have Been: Direct

## References

- Catalytic Conversion of Methanol or Dimethyl Ether to Hydrocarbons on the Solid Acids HZSM-5 or HSAPO-34. *J. Am. Chem. Soc.* **2002**, *124* (15), 3844–3845. <https://doi.org/10.1021/ja016499u>.
- (236) Dahl, I. M.; Kolboe, S. On the Reaction Mechanism for Propene Formation in the MTO Reaction over SAPO-34. *Catal. Letters* **1993**, *20* (3–4), 329–336. <https://doi.org/10.1007/BF00769305>.
- (237) Dahl, I. M.; Wendelbo, R.; Andersen, A.; Akporiaye, D.; Mostad, H.; Fuglerud, T. The Effect of Crystallite Size on the Activity and Selectivity of the Reaction of Ethanol and 2-Propanol over SAPO-34. *Microporous Mesoporous Mater.* **1999**, *29* (1–2), 159–171. [https://doi.org/10.1016/S1387-1811\(98\)00328-X](https://doi.org/10.1016/S1387-1811(98)00328-X).
- (238) Olsbye, U.; Svelle, S.; Bjrgen, M.; Beato, P.; Janssens, T. V. W.; Joensen, F.; Bordiga, S.; Lillerud, K. P. Conversion of Methanol to Hydrocarbons: How Zeolite Cavity and Pore Size Controls Product Selectivity. *Angew. Chemie - Int. Ed.* **2012**, *51* (24), 5810–5831. <https://doi.org/10.1002/anie.201103657>.
- (239) Mikkelsen, Ø.; Rønning, P. O.; Kolboe, S. Use of Isotopic Labeling for Mechanistic Studies of the Methanol-to-Hydrocarbons Reaction. Methylation of Toluene with Methanol over H-ZSM-5, H-Mordenite and H-Beta. *Microporous Mesoporous Mater.* **2000**, *40* (1–3), 95–113. [https://doi.org/10.1016/S1387-1811\(00\)00245-6](https://doi.org/10.1016/S1387-1811(00)00245-6).
- (240) Haw, J. F.; Song, W.; Marcus, D. M.; Nicholas, J. B. The Mechanism of Methanol to Hydrocarbon Catalysis. *Acc. Chem. Res.* **2003**, *36* (5), 317–326. <https://doi.org/10.1021/ar020006o>.
- (241) Arstad, B.; Kolboe, S. The Reactivity of Molecules Trapped within the SAPO-34 Cavities in the Methanol-to-Hydrocarbons Reaction. *J. Am. Chem. Soc.* **2001**, *123* (33), 8137–8138. <https://doi.org/10.1021/ja010668t>.
- (242) Svelle, S.; Joensen, F.; Nerlov, J.; Olsbye, U.; Lillerud, K. P.; Kolboe, S.; Bjrgen, M. Conversion of Methanol into Hydrocarbons over Zeolite H-ZSM-5: Ethene Formation Is Mechanistically Separated from the Formation of Higher Alkenes. *J. Am. Chem. Soc.* **2006**, *128* (46), 14770–14771. <https://doi.org/10.1021/ja065810a>.
- (243) Hu, B.; Mao, G.; Wang, D.; Fu, Y.; Wang, B.; Luo, M. Conversion and Coking of Olefins on SAPO-34. *Catal. Sci. Technol.* **2017**, *7* (23), 5785–5794. <https://doi.org/10.1039/c7cy01898c>.
- (244) Rostami, R. B.; Ghavipour, M.; Di, Z.; Wang, Y.; Behbahani, R. M. Study of Coke Deposition Phenomena on the SAPO\_34 Catalyst and Its Effects on Light Olefin Selectivity during the Methanol to Olefin Reaction. *RSC Adv.* **2015**, *5* (100), 81965–81980. <https://doi.org/10.1039/c5ra11288e>.
- (245) Luo, M.; Zang, H.; Hu, B.; Wang, B.; Mao, G. Evolution of Confined Species and Their Effects on Catalyst Deactivation and Olefin Selectivity in SAPO-34 Catalyzed MTO Process. *RSC Adv.* **2016**, *6*, 17651–17658. <https://doi.org/10.1039/c5ra22424a>.
- (246) Zhao, X.; Li, J.; Tian, P.; Wang, L.; Li, X.; Lin, S.; Guo, X.; Liu, Z. Achieving a Superlong Lifetime in the Zeolite-Catalyzed MTO Reaction under High Pressure: Synergistic Effect of Hydrogen and Water. *ACS Catal.* **2019**, *9* (4), 3017–3025. <https://doi.org/10.1021/acscatal.8b04402>.
- (247) Haw, J. F.; Marcus, D. M. Well-Defined (Supra)Molecular Structures in Zeolite Methanol-to-Olefin Catalysis. *Top. Catal.* **2005**, *34* (May), 41–48. <https://doi.org/10.1007/s11244-005-3798-0>.
- (248) Yang, M.; Fan, D.; Wei, Y.; Tian, P.; Liu, Z. Recent Progress in Methanol-to-Olefins (MTO) Catalysts. *Adv. Mater.* **2019**, *31* (50), 1–15. <https://doi.org/10.1002/adma.201902181>.
- (249) Ye, M.; Li, H.; Zhao, Y.; Zhang, T.; Liu, Z. *MTO Processes Development: The Key of Mesoscale Studies*, 1st ed.; Elsevier Inc., 2015; Vol. 47. <https://doi.org/10.1016/bs.ache.2015.10.008>.

## References

- (250) Dincer, I.; Acar, C. Review and Evaluation of Hydrogen Production Methods for Better Sustainability. *Int. J. Hydrogen Energy* **2014**, *40* (34), 11094–11111. <https://doi.org/10.1016/j.ijhydene.2014.12.035>.
- (251) Dincer, I. Green Methods for Hydrogen Production. *Int. J. Hydrogen Energy* **2012**, *37* (2), 1954–1971. <https://doi.org/10.1016/j.ijhydene.2011.03.173>.
- (252) Fujishima, A.; Honda, K. Electrochemical Photolysis of Water at a Semiconductor Electrode. *Nature* **1972**, *238*, 37–38. <https://doi.org/10.1038/238038a0>.
- (253) Nadeem, M. A.; Khan, M. A.; Ziani, A. A.; Idriss, H. An Overview of the Photocatalytic Water Splitting over Suspended Particles. *Catalysts* **2021**, *11* (1), 1–25. <https://doi.org/10.3390/catal11010060>.
- (254) Rao, N. N.; Dubey, A. K.; Mohanty, S.; Khare, P.; Jain, R.; Kaul, S. N. Photocatalytic Degradation of 2-Chlorophenol: A Study of Kinetics, Intermediates and Biodegradability. *J. Hazard. Mater.* **2003**, *101* (3), 301–314. [https://doi.org/10.1016/S0304-3894\(03\)00180-8](https://doi.org/10.1016/S0304-3894(03)00180-8).
- (255) Hu, G.; Yang, J.; Duan, X.; Farnood, R.; Yang, C.; Yang, J.; Liu, W.; Liu, Q. Recent Developments and Challenges in Zeolite-Based Composite Photocatalysts for Environmental Applications. *Chem. Eng. J.* **2021**, *417* (December 2020), 129209. <https://doi.org/10.1016/j.cej.2021.129209>.
- (256) Kärger, J.; Ruthven, D. M.; Theodorou, D. N. *Diffusion in Nanoporous Materials*; Wiley-VCH Verlag GmbH & Co. KGaA: Weinheim, Germany, 2012. <https://doi.org/10.1002/9783527651276>.
- (257) Robeson, L. M. Correlation of Separation Factor versus Permeability for Polymeric Membranes. *J. Memb. Sci.* **1991**, *62* (2), 165–185. [https://doi.org/10.1016/0376-7388\(91\)80060-J](https://doi.org/10.1016/0376-7388(91)80060-J).
- (258) Wicke, E.; Kallenbach, R. Die Oberflächendiffusion von Kohlendioxyd in Aktiven Kohlen. *Kolloid-Zeitschrift* **1941**, No. 97, 135–151. <https://doi.org/10.1007/BF01502640>.
- (259) Varela-Gandía, F. J.; Berenguer-Murcia, A.; Lozano-Castelló, D.; Cazorla-Amorós, D. Hydrogen Purification for PEM Fuel Cells Using Membranes Prepared by Ion-Exchange of Na-LTA/Carbon Membranes. *J. Memb. Sci.* **2010**, *351* (1–2), 123–130. <https://doi.org/10.1016/j.memsci.2010.01.039>.
- (260) Barrer, R. M. Porous Crystal Membranes. *J. Chem. Soc. Faraday Trans.* **1990**, *86* (7), 1123–1130. <https://doi.org/10.1039/FT9908601123>.
- (261) Malek, K.; Coppens, M. O. Knudsen Self- and Fickian Diffusion in Rough Nanoporous Media. *J. Chem. Phys.* **2003**, *119* (5), 2801–2811. <https://doi.org/10.1063/1.1584652>.
- (262) Zito, P. F.; Caravella, A.; Brunetti, A.; Drioli, E.; Barbieri, G. Knudsen and Surface Diffusion Competing for Gas Permeation inside Silicalite Membranes. *J. Memb. Sci.* **2017**, *523*, 456–469. <https://doi.org/10.1016/j.memsci.2016.10.016>.
- (263) Ockwig, N. W.; Nenoff, T. M. Membranes for Hydrogen Separation. *Chem. Rev.* **2007**, *107* (10), 4078–4110. <https://doi.org/10.1021/cr0501792>.
- (264) Zhu, Y.; Gupta, K. M.; Liu, Q.; Jiang, J.; Caro, J.; Huang, A. Synthesis and Seawater Desalination of Molecular Sieving Zeolitic Imidazolate Framework Membranes. *Desalination* **2016**, *385*, 75–82. <https://doi.org/10.1016/j.desal.2016.02.005>.
- (265) Wijmans, J. G.; Baker, R. W. The Solution-Diffusion Model: A Review. *J. Memb. Sci.* **1995**, *107* (1–2), 1–21. [https://doi.org/10.1016/0376-7388\(95\)00102-I](https://doi.org/10.1016/0376-7388(95)00102-I).
- (266) Dechnik, J.; Gascon, J.; Doonan, C. J.; Janiak, C.; Sumbly, C. J. Mixed-Matrix Membranes. *Angew. Chemie - Int. Ed.* **2017**,

## References

- 56, 9292–9310. <https://doi.org/10.1002/anie.201701109>.
- (267) Iulianelli, A.; Liguori, S.; Longo, T.; Tosti, S.; Pinacci, P.; Basile, A. An Experimental Study on Bio-Ethanol Steam Reforming in a Catalytic Membrane Reactor. Part II: Reaction Pressure, Sweep Factor and WHSV Effects. *Int. J. Hydrogen Energy* **2010**, *35* (7), 3159–3164. <https://doi.org/10.1016/j.ijhydene.2009.11.034>.
- (268) Ertl, G. Reactions at Well-Defined Surfaces. *Surf. Sci.* **1994**, *299–300* (C), 742–754. [https://doi.org/10.1016/0039-6028\(94\)90694-7](https://doi.org/10.1016/0039-6028(94)90694-7).
- (269) Baxter, R. J.; Hu, P. Insight into Why the Langmuir-Hinshelwood Mechanism Is Generally Preferred. *J. Chem. Phys.* **2002**, *116* (11), 4379–4381. <https://doi.org/10.1063/1.1458938>.
- (270) Rutkai, G.; Csányi, É.; Kristóf, T. Prediction of Adsorption and Separation of Water-Alcohol Mixtures with Zeolite NaA. *Microporous Mesoporous Mater.* **2008**, *114* (1–3), 455–464. <https://doi.org/10.1016/j.micromeso.2008.01.044>.

# Appendix

## Danksagung

Mein erster Dank geht natürlich an Herrn Prof. Dr. Jürgen Caro für die Möglichkeit diese Arbeit unter seiner Aufsicht in seinem Arbeitskreis durchzuführen. Sie haben mich die letzten Jahre gefordert und gefördert zu dem Punkt, an dem ich mich bestens vorbereitet fühle für meine berufliche Zukunft. Vielen Dank für den fachlichen Input und die lockeren Gespräche nach Feierabend. Es war eine Freude mit Ihnen zu arbeiten. Ich wünsche Ihnen alles Gute im wohlverdienten Ruhestand.

Als nächstes möchte ich meinen Eltern Claudia und Manfred Rieck genannt Best danken. Nicht nur für jegliche Liebe und Hingabe in meinen ersten 27 Lebensjahren aber auch für die Unterstützung in allen Lebenslagen. Ohne euch hätte ich niemals studieren können und ohne euch wäre ich niemals jetzt hier in dieser Position.

An meine Freundin Kimberly Ludewig. Du hast mir meinen Rücken immer freigehalten, es gibt keine Person auf diesem Planeten auf die ich mich mehr verlassen kann und ich kann mir keine Bessere an meiner Seite vorstellen. Ich liebe dich! Und ja der Antrag kommt noch. Irgendwann.

Ich möchte zudem meiner Großmutter Margita Wicke danken, bei der ich die ersten Jahre meines Studiums wohnen durfte, was mir die Umstellung unfassbar erleichtert hat. Ich wäre ohne dich wahrscheinlich nicht so einfach durchs Studium gekommen.

Natürlich muss ich hier auch meine Kollegen nennen. Allen voran Alexander Mundstock, der für mich nicht nur Ansprechpartner Nummer 1 bei jeglichen chemischen Problemen, sondern auch ein guter Freund, mit dem ich über alles quatschen kann, geworden ist. Des Weiteren möchte ich hier namentlich Mario Wolf, Richard Hinterding, Patrick Kißling, Frank Steinbach und Ina Strauß, sowie die Kollegen aus der Werkstatt Peter Mühr, Markus Köhler und Jan Kuckuck erwähnen, die dafür verantwortlich sind, dass der Alltag im Arbeitskreis so viel Spaß gemacht hat.



## List of publications

**Rieck genannt Best, F.;** Mundstock, A.; Dräger, G.; Rusch, P.; Bigall, N. C.; Richter, H.; Caro, J. Methanol-to-Olefins in a Membrane Reactor with in Situ Steam Removal – The Decisive Role of Coking. *ChemCatChem* **2020**, 12 (1), 273–280. <https://doi.org/10.1002/cctc.201901222>.

**Rieck genannt Best, F.;** Mundstock, A.; Kißling, P. A.; Richter, H.; Hindricks, K. D. J.; Huang, A.; Behrens, P.; Caro, J. Boosting Dimethylamine Formation Selectivity in a Membrane Reactor by In Situ Water Removal. *Ind. Eng. Chem. Res.* **2021**. <https://doi.org/10.1021/acs.iecr.1c04149>.

**Rieck genannt Best, F.;** Mundstock, A.; Richter, H.; Kißling, P. A.; Hindricks, K. D. J.; Huang, A.; Behrens, P.; Caro, J. Controlled methylamine synthesis in a membrane reactor featuring a highly steam selective K<sup>+</sup>-LTA membrane. Submitted to *Microporous Mesoporous Mater.* **2022**.

Ombaka, L. M.; McGettrick, J. D.; Oseghe, E. O.; Al-Madanat, O.; **Rieck genannt Best, F.;** Msagati, T. A. M.; Davies, M. L.; Bredow, T.; Bahnemann, D. W. Photocatalytic H<sub>2</sub> Production and Degradation of Aqueous 2-Chlorophenol over B/N-Graphene-Coated Cu<sup>0</sup>/TiO<sub>2</sub>: A DFT, Experimental and Mechanistic Investigation. *J. Environ. Manage.* **2022**, 311 (November 2021), 114822. <https://doi.org/10.1016/j.jenvman.2022.114822>.

## Curriculum vitae



FELIX RIECK GENANNT BEST

## LEBENS LAUF

## AUSBILDUNG

LEIBNIZ  
UNIVERSITÄT  
HANNOVER● **PROMOTIONS VORHABEN Dr. rer. nat.** | seit 02/2018

- Dissertation am Institut für Physikalische Chemie und Elektrochemie, Erstgutachter: Prof. Dr. Jürgen Caro: *Development of Porous Material Dual-Functional Reactors for the Facile Synthesis of Sustainable Chemicals*

● **MASTER OF SCIENCE** | 10/2015 – 12/2017

- Studiengang: Material- und Nanochemie
- Masterarbeit am Institut für Physikalische Chemie und Elektrochemie: *Laser-structured electrodes for electrochemical water splitting*
- Gesamtnote: 1,5

● **BACHELOR OF SCIENCE** | 10/2012 – 08/2015

- Studiengang: Chemie
- Bachelorarbeit am Institut für Anorganische Chemie: *Beschichtung von Platinelektroden mit nanoporösen Kohlenstoffen*
- Gesamtnote: 1,7

GYMNASIUM  
WALSRODE● **ALLGEMEINE HOCHSCHULREIFE** | bis 07/2012

- Schwerpunkt: Chemie, Mathematik, Geschichte
- Gesamtnote: 2,3

## BERUFSPRAKTISCHE ERFAHRUNG

BASF CATALYSTS  
GERMANY● **CHEMIST RESEARCH, DEVELOPMENT AND APPLICATION** | seit 03/2022LEIBNIZ  
UNIVERSITÄT  
HANNOVER● **WISSENSCHAFTLICHER MITARBEITER** | 10/2021 – 12/2021

- Laborarbeit Polymermembranen Evonik Industries

● **WISSENSCHAFTLICHER MITARBEITER** | 02/2018 – 10/2021

- Promotion/Studentenbetreuung

● **STUDENTISCHE BETREUUNG** | 10/2016 – 03/2017

- Leitung Übungsgruppe und Laboraufsicht

● **WISSENSCHAFTLICHE HILFSKRAFT** | 02/2016 – 08/2016

- Laborarbeit Thematik Elektrochemie

## WEITERBILDUNG

TÜV NORD,  
HAMBURG● **PROJEKTMANAGER** | 12/2021

- Zertifikat nach DIN 69900 ff.